High temperature oxidation of slurry coated interconnect alloys

Persson, Åsa Helen

Publication date:
2012

Document Version
Publisher's PDF, also known as Version of record

Ph.D. Thesis

High temperature oxidation of slurry coated interconnect alloys

Åsa H. Persson

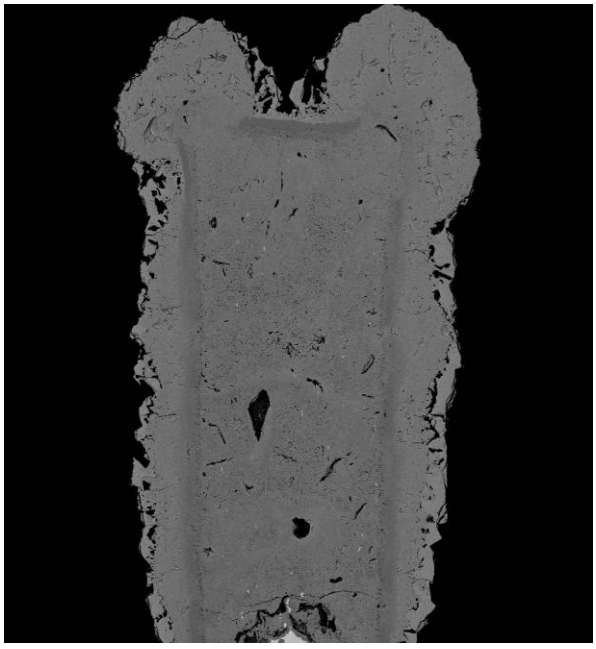

Technical University of Denmark
Department of Energy Conversion and Storage

Abstract

In this project, high temperature oxidation experiments of slurry coated ferritic alloys in atmospheres similar to the atmosphere found at the cathode in an SOFC were conducted. From the observations possible interaction mechanisms between the slurry coatings and the growing oxide scale on the alloy surface were formulated. These mechanisms are a step towards deeper knowledge of how to design a coating/alloy combination with satisfactory performance in an SOFC-stack. A satisfactory performance entails a low growth rate of the forming oxide scale on the alloy surface and a low chromium content and resistance in this oxide scale.

Slurry coated ferritic alloy samples were oxidized long term in air containing 1% water at 900˚C to measure the oxidation rate of the coated samples. The ferritic alloys included in the study were Crofer 22APU and Sandvik 1C44Mo20. Some complementary experiments were also performed on extra Sandvik alloys. The slurry coatings consisted of perovskite, spinel, corundum, and rutile oxides and they were both applied as single layer coatings and as dual layer coatings.

Cross-sections of the oxidized samples were analyzed with scanning electron microscopy, SEM, and energy dispersive spectrometry, EDS. From these analyses information about the microstructures and the compositions of the grown oxide scales were collected.

Based on the oxidation rate measurements for the single layer coated alloy samples three possible interaction mechanisms between the coating and the growing oxide scale were formulated:

A Surface covering coating
B Surface covering coatings with chemical reaction with the forming oxide
C Incorporation of coating particles

In the interaction mechanism A the coating particles are pushed ahead of the outwardly growing oxide scale. Coatings with this interaction mechanism mainly give a geometrical protection against oxidation by blocking oxygen access at the surface of the oxide scale. The protecting effect is gradually reduced as the oxide scale grows thicker than the diameter of the coating particles. Interaction mechanism B entails a chemical reaction between the growing oxide scale and the coating particles at the same time as these are pushed ahead of the growing oxide scale. The chemical reaction leads to a change in the oxide composition. In the third and last interaction mechanism, C, the coating particles are incorporated into the growing oxide scale. The incorporated coating particles create a geometrical protection against oxidation that should not loose their effect after the oxide scale has grown thicker than the diameter of the coating particles.

The two single layer coatings consisting of $(La_{0.85}Sr_{0.15})MnO_3$ + 10% excess Mn, LSM, and $(La_{0.85}Sr_{0.15})CoO_3$ + 10% Co_3O_4, LSC, coatings were found to be relatively successful in decreasing the oxidation rate, the chromium content in the outermost part of

the dense scale, and the electrical resistance in the growing oxide scales when applied onto Crofer 22APU. But, the positive effects of the LSM and LSC coatings were significant enhanced when they were combined with an inner Co_3O_4 coating layer. However, for the Sandvik 1C44Mo20 samples the samples coated with Co_3O_4 + LSM only displayed a slight decrease in the oxidation rate compared to the LSM coated samples. For the Sandvik 1C44Mo20 samples coated with Co_3O_4 + LSC a drastic increase in the oxidation rate was observed compared to the Sandvik 1C44Mo20 samples coated with LSC. A significant amount of chromium in the oxide scale on the Co_3O_4 + LSC coated Sandvik 1C44Mo20 samples was furthermore detected. The cobalt rich coatings' success on Crofer 22APU alloy samples and their failure on Sandvik 1C44Mo20 samples are believed to depend on the manganese access in the coating/alloy system. It appeared that a certain amount of manganese was acquired to stabilize the oxide growth on the alloy samples coated with cobalt rich coatings. This was supported by complementary oxidation of Co_3O_4 + LSC coated Sandvik alloys with varying manganese contents. Based on the microstructures of the formed oxide scales on all Co_3O_4 + LSC coated Fe-22Cr alloys samples included in this study and their observed weight gain, it was established that an optimal manganese content in the alloy on ca. 0.3-0.5 wt.% is a requirement to stabilize and utilize the positive effects of a cobalt rich coating.

Resumé

I dette projekt blev der udført højtemperatur oxidationseksperimenter af slurry-belagte ferrit legeringer i atmosfærer sammenlignelig med atmosfæren ved katoden i en SOFC. Baseret på resultaterne opnået under studiet er der formuleret mulige interaktionsmekanismer mellem slurry-belægninger og de voksende oxidlag på overfladen af legeringsprøverne. Disse mekanismer er et skridt mod en dybere forståelse af, hvordan man skal designe en kombination af belægning/legering med tillfredstillende egenskaber til en SOFC-stak. Tillfredstillende egenskaber indebærer en lav væksthastighed af oxidlaget på legeringsoverfladen og lavt kromindhold samt en lav elektrisk modstand i dette oxidlag.

Slurry-belagte ferrit legeringsprøver blev oxideret under lang tid i luft med 1% vand ved 900˚C for at måle oxidationshastigheden af de belagte prøver. De ferrit-legeringer, som var inkluderet i studiet, var Crofer 22APU og Sandvik 1C44Mo20. Nogle supplerende eksperimenter blev udført på forskellige Sandvik legeringer. Slurry-belægninger bestod af perovskit, spinel, korundum, og rutile oxider og de blev pålagt ved sprøjtning både som enkeltlagsbelægninger og som dobbeltlagsbelægninger i de tilfælde, hvor de blev kombineret.

Tværsnit af de oxiderede prøver blev analyseret med skanning elektron mikroskopi, SEM, og energi dispersiv spektroskopi, EDS. Disse analyser gav informationer om oxidlagenes mikrostruktur og kemiske sammensætning.

Baseret på målingerne af oxidationshastigheden af de enkeltlags belagte legeringsprøver kunne tre mulige interaktionsmekanismer mellem belægning og det voksende oxidlag formuleres:

A Overfladedækkende belægning
B Overfladedækkende belægning med kemisk reaktion med det voksende oxidlag
C Inkorporering af belægningspartikler

I interaktionsmekanisme A skubbes belægningspartiklerne foran det udad voksende oxidlag. Belægninger med denne type af interaktionsmekanisme giver hovedsaglig en geometrisk beskyttelse mod oxidation gennem blokering af ilt tilgang ved overfladen af oxidlaget. Beskyttelseeffekten forsvinder, når oxidlaget vokser tykkere end diameteren af beskyttelsepartiklerne. Interaktionsmekansime B medfører en kemisk reaktion mellem det voksende oxidlag og belægningspartiklerne, samtidigt med at belægningspartiklerne skubbes foran det voksende oxidlag. Den kemiske reaktion fører til en forandring i oxid sammensætningen. I den tredje og sidste interaktionsmekanisme, C, inkorporeres belægsningspartiklerne i det voksende oxidlag. De inkorporerede belægsningspartikler opbygger en geometrisk beskyttelse mod oxidation og denne beskyttelse skulle ikke miste sin effekt, når oxidlaget har vokset sig tykkere end diameteren af belæsgningspartiklerne.

De to enkeltlagsbelægninger bestående af $(La_{0.85}Sr_{0.15})MnO_3$ + 10% overskydende Mn, LSM, og $(La_{0.85}Sr_{0.15})CoO_3$ + 10% Co_3O_4, LSC, var succesfuld m.h.t. at mindske

oxidationshastigheden, krom indholdet og den elektriske modstand i det voksende oxidlag på Crofer 22APU prøverne. Den positive effekt af LSM og LSC belægningerne blev forøget endog mere, når de var i kombination med et indre Co_3O_4-belægningslag. For Sandvik 1C44Mo20 prøverne belagt med Co_3O_4 + LSM blev der kun observeret en lille mindskning i oxidationshastigheden i forhold til den LSM belagte Sandvik 1C44Mo20 prøve. For Sandvik 1C44Mo20 prøverne belagt med Co_3O_4 + LSC blev der observeret en drastisk øgning af oxidationshastigheden i forhold til Sandvik 1C44Mo20 prøver belagt med et enkelt lag af LSC. En signifikant mængde krom blev tillige observeret i oxidlaget på de Co_3O_4 + LSC belagte Sandvik 1C44Mo20 prøver. Forskellen i overskuddet af mangan for Crofer 22APU og Sandvik 1C44Mo20 prøverne er blevet foreslået som en mulig forklaring på, at de kobolt-rige belægningerne giver en positiv effekt på Crofer 22APU legeringsprøverne og deres manglende effekt på Sandvik 1C44Mo20 legeringsprøverne. Det indikerede at der var brug for en vis mængde mangan for at stabilisere oxidlagets vækst på legeringsprøver belagte med en kobolt-rig belægning. Supplerende oxidationseksperimenter for Co_3O_4 + LSC belagte Sandvik legeringsprøver med varierende mangan indhold understøttede denne hypotese. Baseret på mikrostrukturen af de dannede oxidlag på alle Co_3O_4 + LSC belagde Fe-22Cr legeringsprøver i dette studie og deres vægtøgning, forekommer det, at der er brug for et optimalt mangan indhold i legeringen på omkring 0.3-0.5 vægt. % for at kunne udnytte de positive effekter af kobolt-rige belægninger.

Preface

This thesis was written as part of the fulfillment of the requirements for the Ph.D. degree at the Technical University of Denmark. The experimental work was carried out at the Fuel Cells and Solid State Chemistry Department, Risø National Laboratory.

The Ph.D. project was initiated in August 2004 and completed in September 2007, and financed by Energinet.dk project no. 6551, Elkraft system: FU4401, Danish Energy Authority j. no. 79029-0003 and partly by Energinet.dk project no. 2006-1-6342.

For supervision and all the help during the project I would like to thank my supervisors:

- Scientist Lars Mikkelsen, Fuel Cells and Solid State Chemistry Department, Risø National Laboratory

- Senior Scientist and Head of Program Peter V. Hendriksen, Fuel Cells and Solid State Chemistry Department, Risø National Laboratory

- Professor Marcel A. J. Somers, Department of Manufacturing Engineering and Management, Technical University of Denmark

I would also like to acknowledge:
Scientist Ming Chen, Fuel Cells and Solid State Chemistry Department, Risø National Laboratory, for performing the FactSage calculations included in this work

Senior Scientist Karsten A. Nielsen, Fuel Cells and Solid State Chemistry Department, Risø National Laboratory, for inspiring discussions

Cand.jur. Simon Strandholm Rasmussen, Post. Doc. Trine Klemensø, and Ph.D. student Jens Rasmussen for very patiently proof reading my material

The technical staff at Fuel Cells and Solid State Chemistry Department, Risø National Laboratory, for all assistance in the laboratory

The many colleagues and friends at Fuel Cells and Solid State Chemistry Department, Risø National Laboratory and especially the "Jungle office" that have helped with uncountable small and bigger things during the project and made the work so much easier, and the time very enjoyable

Part of chapter 3 and 5 was presented at the conference "2nd International Conference on Diffusion in Solids and Liquids" in Aveiro 2006, and published in the proceedings in Defect and Diffusion Forum Vols. 258-260 (2006) pp. 372-377
"Effect of Perovskite Coating on Oxide Scale Growth on Fe-22Cr"

Å. Persson, P.V. Hendriksen, L. Mikkelsen, and M.A.J. Somers

The material in chapter 2, 3, 4, 5, and 6 is part of a patent submitted in January 2007, EP37840.
"A method of producing a multilayer barrier structure"
K. A. Nielsen, S. Linderoth, P. V. Hendriksen, Å. Persson, and L. Mikkelsen

List of symbols

A	constant/phase in sample cross-section/interaction mechanism
B	constant/phase in sample cross-section/interaction mechanism
C	constant/phase in sample cross-section/interaction mechanism
D	phase in sample cross-section
D^*_{Cr}	diffusion coefficient
D^*_0	pre-exponential factor
E_ρ	activation energy for resistivity
E_{el}	activation energy for oxidation process
i	reaction rate a the interfaces in the oxide scale
K_α, K_β	photon emitted during decay, α: L→K, β: M→K
k_p	the parabolic rate constant
k'_p	constant
k_{log}/ k_{il}	logarithmic rate constants
R	gas constant
S	activity of cation on sample surface
S_0	activity of cation after t_t long diffusion process
Q_V	activation energy for cation diffusion via vacancies
T	temperature in degree K
t	scale thickness
t_t	time
$t_{t,0}$	time$_0$, start of oxidation
x_p	diffusion distance
Δx	diffusion distance
Δw	(measured) weight increase
Δw_0	(measured) weight increase before oxidation process has started
$\Delta w_{theo.}$	calculated theoretical weight increase
Δw_s	weight increase of spinel phase
Δw_c	weight increase of chromia phase
$\Delta\mu_{Mn/Cr}$	gradient in chemical potential
Δ(B)	change in number of unit cells in the chromia phase
Δ(C)	change in number of unit cells in the spinel phase
ρ	relative density/resistivity
I/II/III/IV	interface

List of abbreviations

ASR	area specific resistance
BSE	back-scatter electrons
CCC	cathode current collector
EDS	energy dispersive spectrometry
GIWAXS	grazing incidence wide angle X-ray scattering
LSM	$(La_{0.85}Sr_{0.15})MnO_3$ + 10% Mn excess
LSC	$(La_{0.85}Sr_{0.15})CoO_3$ + 10% Co_3O_4 excess
LSFC	$(La_{0.54}Sr_{0.36})(Fe_{0.8}Co_{0.2})O_3$

PLD	pulse laser deposition
SE	secondary electrons
SEM	scanning electron microscopy
SIMS	secondary ion mass spectrometry
TGA	thermogravimetric analysis
TEM	transmission electron microscopy
RT	Room temperature
XRD	X-ray diffraction
FIB-FEG-SEM	focused ion beam field emission electron gun secondary electron microscope

Table of contents

1. Introduction

1.1 Introduction

The society of today is very much dependent on electricity, and a cheap, effective, and environmental friendly power production has come into focus during the last year's debate regarding global warming. The solid oxide fuel cell, SOFC, is a promising electrical power generator that produces electricity and heat directly from gaseous fuel by electrochemical combination of the fuel with an oxidant. The method bypasses the conversion of chemical energy of fuel into thermal and mechanical energy, and a significantly higher theoretical efficiency is thus achieved compared to conventional methods. In addition fuel cell technology has the characteristics of environmental compatibility, modularity, siting flexibility, and multifuel capability [1-3]. An example on the environmental compatibility is that the amount of pollution (SO_x, NO_x) produced during power generation in a SOFC is reduced compared to traditional power plants [1].

In figure 1.1 below a flat plate design of a SOFC-stack is shown.

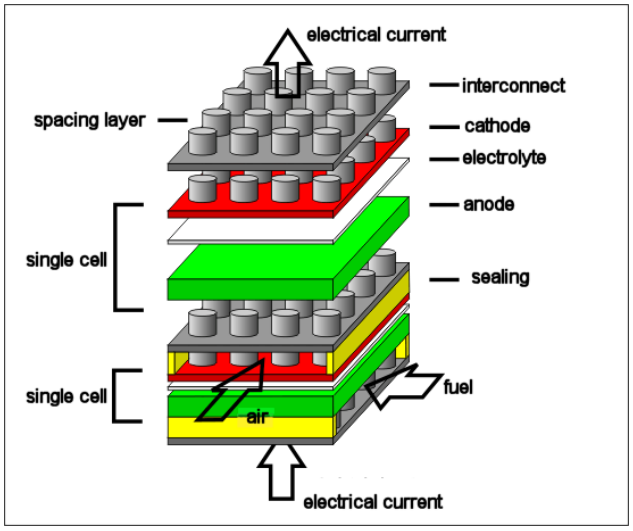

Figure 1.1. Principle sketch of the flat plate design for SOFC-stack.

The interconnect component in a SOFC-stack connects the cathode of one cell to the anode on the next in electrical series as illustrated in figure 1.1 above. The interconnector also separates the air from the fuel cell in adjoining cells of a stack. For the SOFC-stack to be operational the interconnect material has to be chemically and thermally compatible with the other cell components from room temperature up to operational temperature for the fuel cells, ca. 750˚C [2]. Cr_2O_3, chromia, forming ferrous alloys have shown promising results as interconnect materials. They are cheap, easy to shape and handle and they have met several of the requirements on interconnect plates which for example are high electrical conductivity, gas tight, matching thermal expansion with the cell, and chemical stability with other cell components. Chromia forming alloys present a good balance between a slow growth

rate of the oxide scale and electrical conductivity of the oxide scale compared to alumina and silica forming alloys, which have a significantly high electrical resistance in the forming oxide scale [2, 4-6]. However, for the SOFC-stack to present satisfying operational efficiency the growth rate of the chromia scales have to be decreased even further as well as its electrical resistance. The chromium content in the protecting oxide scale also has to decrease, since chromium species evaporating or diffusing via surfaces from the chromia scale, have a detrimental effect on the fuel cell. The elusive chromium species tend to diffuse into the cathode/electrolyte interface where the chromium species are reduced to chromia and come to block the catalytic reactive sites [2, 4, 7-9]. Alloys forming a duplex scale consisting of an inner Cr_2O_3 phase and an outer $MnCr_2O_4$ phase have been developed during the last years and shown promising results in decreasing the available chromium for evaporation [4, 7, 10, 11]. However, the oxidation rate, the electrical conductivity of the oxide scales and the amount of the chromium in the outmost of the oxide scales on the interconnect alloys has still not been decreased enough to achieve an efficiency level of the interconnect material acceptable for use in a commercial SOFC-stack [2, 7, 11, 12]. Applications of coatings on the alloy surface have proven to show promising results, and a few examples are given below:

- Coatings consisting of oxides of the La, Ce, Y, Ni, and Sr metals applied via hot-dipping technique on chromia forming ferrous alloys [13].
- Spinel coating consisting of Co_3O_4 on chromia-forming ferrous alloys applied via spray-painting and plasma-spraying [14, 15].
- $La_{0.85}Sr_{0.15}CoO_3$ coating applied via plasma-spraying on Ni-based alloys [16].
- Ferritic stainless steel coated via screen-printing with a paste of $Mn_{1.5}Co_{1.5}O_4$ spinel powder and heat-treated at 800˚C in an $Ar/3\%H_2O/2.75\%H_2$ atmosphere [10, 17].
- Ferritic stainless steel electroplated with $MnCo_2O_4$ and $Cu_{1.4}Mn_{1.6}O_4$ [18].

1.2 The purpose of this project

The purpose of this work was to study and set up likely interaction mechanisms between an interconnect alloy and an applied coating under conditions similar to the ones found on the cathode side of the interconnector in a SOFC-stack. The coating method used in this project was slurry coating, which is a cheap and easy coating method.

The investigation came to include:

- Investigation of oxidation rates
- Study of microstructure and composition of formed oxide scales
- Measurements of electrical resistance of formed oxide scales

Most of the oxidation tests were performed on alloy samples of Crofer 22APU, an alloy developed specifically for interconnect use, and Sandvik 1C44Mo20, a test alloy. These samples were coated with a range of different slurry coatings, and some complementary oxidation experiments were also performed on slurry coated Sandvik OYC44, Sandvik 350, Sandvik 433, Sandvik 434, and Sandvik 515 alloy samples.

1.3 Structure of present thesis

In chapter 2 the weight gain data/kinetical data collected for all coated/uncoated alloy samples during the project are listed. These weight gain experiments, measuring the oxidation rate of the coated/uncoated alloy samples, functioned as a screening process during the project to find the most successful and interesting alloy/coating combinations.

Chapter 3 is devoted to the oxidation rate and the oxide scale microstructure and composition formed on single layer coated Crofer 22APU samples.

In chapter 4 the favourable effects of combining some of the single layer coatings studied in chapter 3 on Crofer 22APU samples are studied.

Chapter 5 is a comparison of the different oxidation mechanisms found on different chromia forming ferritic alloys coated with identical slurry coatings.

In chapter 6 the electrical resistance of the oxide scales on some of the most successfully coated Crofer 22APU samples are measured and compared. The effects of a mechanical load, an electrical load as well as the oxidation temperature on the growth of the oxide scales are studied.

In the extended appendix 5, tests of a method for measuring the tracer diffusion of chromium in $MnCo_2O_4$ are presented. The tests did not give any conclusive results, but they generated information of how to improve the measuring method into an effective and useful method of measuring the tracer diffusion coefficient of chromium in $MnCo_2O_4$.

1.4 Reference List

1. Minh N.Q. and Takahashi T., *Science and Technology of Ceramic Fuel Cells* (Elsevier Science B.V., Amsterdam, 1995), p. 1
2. Singhal S.C. and Kendall K., *High Temperature Solid Oxide Fuel Cells Fundamentals, Design and Applications* (Elsevier, Cornwall, 2003)
3. Haile, S. M., Acta Materialia, 51, 5981 (2003)
4. Quadakkers, W. J., Piron-Abellan, J., Shemet, V. and Singheiser, L., Materials at High Temperatures, 20, 115 (2003)
5. Linderoth, S., Hendriksen, P. V., Mogensen, M. and Langvad, N., Journal of Materials Science, 31, 5077 (1996)
6. Fergus, J. W., Materials Science and Engineering A-Structural Materials Properties Microstructure and Processing, 397, 271 (2005)
7. Konysheva, E., Penkalla, H., Wessel, E., Mertens, J., Seeling, U., Singheiser, L. and Hilpert, K., Journal of the Electrochemical Society, 153, A765-A773 (2006)
8. Tucker M.C, Kurakawa H., Jacobson C.P., De Jonghe L.C. and Visco S.J., Journal of Power Sources, 160, 130 (2006)
9. Matsuzaki, Y. and Yasuda, I., Solid State Ionics, 132, 271 (2000)
10. Yang, Z. G., Hardy, J. S., Walker, M. S., Xia, G. G., Simner, S. P. and Stevenson, J. W., Journal of the Electrochemical Society, 151, A1825-A1831 (2004)
11. Stanislowski, M., Wessel, E., Hilpert, K., Markus, T. and Singheiser, L., Journal of the Electrochemical Society, 154, A295-A306 (2007)
12. Simner, S. P., Anderson, M. D., Xia, G. G., Yang, Z., Pederson, L. R. and Stevenson, J. W., Journal of the Electrochemical Society, 152, A740-A745 (2005)

13. Huang, K., Hou, P. Y. and Goodenough, J. B., Materials Research Bulletin, 36, 81 (2001)
14. Zahid M., Tietz F., Sebold D. and Buchkremer H.P., in Proceedings of the European SOFC Forum 2004, p. 820
15. Hansson, A. N., Linderoth, S., Mogensen, M. and Somers, M. A. J., Journal of Alloys and Compounds, 433, 193 (2007)
16. Kadowaki, T., Shiomitsu, T., Matsuda, E., Nakagawa, H., Tsuneizumi, H. and Maruyama, T., Solid State Ionics, 67, 65 (1993)
17. Yang, Z. G., Xia, G. G. and Stevenson, J. W., Electrochemical and Solid State Letters, 8, A168-A170 (2005)
18. Bateni, M. R., Wei, P., Deng, X. H. and Petric, A., Surface & Coatings Technology, 201, 4677 (2007)

2. Screening/oxidation rate experiments

2.1 Introduction

As described in chapter 1 the oxidation mechanisms and the interactions between slurry coatings and an interconnect alloy are studied in this project. In the initial stage of this study several different slurry coatings of interest were prepared and applied onto samples of the commercially available interconnect alloy Crofer 22APU and the test alloy Sandvik 1C44Mo20. The samples were long term oxidized in a cycling oxidation experiment where the oxidation rates were calculated by measuring the weight gain of the samples. As the project proceeded Crofer 22APU and Sandvik 1C44Mo20 samples with new slurry coatings were added to the cycling oxidation experiment as well as coated samples of Sandvik OYC44 alloy and model alloys consisting of Sandvik 350, Sandvik 433, Sandvik 434, and Sandvik 515. These weight gain measurements functioned as a screening process to determine the most successful and interesting coating/alloy combinations, which would be analyzed further in scanning electron microscopy, SEM, and exposed to complementary oxidation experiments using thermogravimetric analysis, TGA.

The total list of slurry coatings included in the oxidation experiments is presented in this chapter together with all the curves for the weight gain data collected during the project for the different coating/alloy combinations. Also described in this chapter is the sample preparation of the oxidation samples. Furthermore, the preparation of the cross-sections of the oxidized samples for further analysis in SEM later on in the project is described. It should be noted that not all of the oxidized samples listed in this chapter are further analyzed or discussed in the thesis.

2.2 Experimental

The alloys included in the oxidation study are Crofer 22APU, Sandvik 1C44Mo20, Sandvik OYC44, Sandvik 350, Sandvik 433, Sandvik 434, and Sandvik 515. The compositions of these alloys are displayed in table 2.1.

Table 2.1. Steel compositions of Crofer 22APU, Sandvik 1C44Mo20, Sandvik OYC44, Sandvik 350, Sandvik 433, Sandvik 434 and Sandvik 515 (in wt %) and the foil thicknesses within parenthesis.

Alloy (foil thickness)	**Fe**	**Cr**	**Mn**	**Si**	**C**	**Ni**	**Al**	**La**	**N**	**Mo**	**Ti**	**Add.**
Crofer 22APU (0.3 mm)	Bal.	22.6	0.4	0.1	0.01	0.2	0.1	0.07	0.01	-	0.06	
Sandvik 1C44Mo20 (0.3 mm)	Bal.	22.3	0.1	0.2	-	0.3	-	-	0.03	1.0	-	Zr, Ti, Nb
OYC44 (0.2 mm)	Bal.	21.6	0.3	0.3	0.02	0.2	0.003	-	0.03	-	-	Ce
350 (0.1 mm)	Bal.	22.1	0.1	0.1	-	0.09	-	-	0.08	1.0	0.04	Nb
433 (0.25 mm)	Bal.	22.4	0.6	0.2	-	0.1	0.04	0.05	-	-	-	Ce
434 (0.2 mm)	Bal.	22.2	5.1	0.1	-	0.1	0.01	0.04	-	-	-	Ce
515 (0.2 mm)	Bal.	21.9	0.3	0.1	-	0.07	-	-	0.02	-	0.01	Nb

2.2.1 Sample preparation

From alloy foils of Crofer 22APU, Sandvik 1C44Mo20, Sandvik OYC44, Sandvik 350, Sandvik 433, Sandvik 434, and Sandvik 515 samples for use in the cyclic oxidation experiment were cut. The dimension of the samples cut were 20*20 mm^2 and with a 2 mm hole in the centre of one side ca. 2 mm from the edge. The thicknesses of the alloy foils are listed in table 2.1 above. For the TGA experiments six similar samples were cut from the Crofer 22APU foil. The dimensions of these samples were 20*10*0.3 mm^3 and with a 2 mm hole in the centre of one of the short sides ca. 2 mm from the edge. All the samples for both the cyclic oxidation and the TGA experiments were etched in hydrofluoric acid for 30 minutes to remove any native oxides formed during alloy processing. The samples were rinsed for 10 minutes in water after etching and finally rinsed in alcohol for yet another 10 minutes.

The etched samples were slurry coated, using a hand spray gun, as soon as possible after being etched. As carrier gas technical air at room temperature was used. The slurries consisted of approximately 33 wt.% powder of the coating material dissolved in ethanol with a small amount of polyvinylpyrrolidone, PVP-binder, mixed into it. Before the slurries were applied onto the alloy samples, the slurries were ball-milled until desired particle size distributions were achieved. The slurry coatings were applied on both sides of the samples. In table 2.2 below the total list of used coating slurries are presented. The measured particle sizes in the slurries are also included.

Table 2.2. Description of used coatings, all deposited by slurry coating.

Name	**Content**	**Synthesis**	**Calcination**	**$Ø_{50}$[iv] [μm]**
LSM[a]	$(La_{0.85}Sr_{0.15})MnO_3$ 10% Mn excess	Glycine-nitrate method	5 parts 1200°C/2h 1 part 800°C/2h	1.9
LSM[b]	$(La_{0.85}Sr_{0.15})MnO_3$ 10% Mn excess	Glycine-nitrate method	5 parts 1200°C/2h 1 part 800°C/2h	2.3
LSM[c]	$(La_{0.85}Sr_{0.15})MnO_3$ 10% Mn excess	Glycine-nitrate method	5 parts 1000°C/2h 1 part 800°C/2h	1.3
LSM[d]	$(La_{0.85}Sr_{0.15})MnO_3$ 10% Mn excess	Glycine-nitrate method	5 parts 1000°C/2h 1 part 800°C/2h	1.0
LSM[e]	$(La_{0.85}Sr_{0.15})MnO_3$ 10% Mn excess	Glycine-nitrate method	5 parts 1200°C/2h 1 part 800°C/2h	2.1
Co_3O_4[a]	Co_3O_4	99.7% cobalt (II,III) oxide[i]		2.5
Co_3O_4[b]	Co_3O_4	99.7% cobalt (II,III) oxide[i]		0.7
Co_3O_4[c]	Co_3O_4	99.7% cobalt (II,III) oxide[i]		0.6
Co_3O_4[d]	Co_3O_4	99.7% cobalt (II,III) oxide[i]		1.1
Co_3O_4[e]	Co_3O_4	99.7% cobalt (II,III) oxide[i]		1.3
Co_3O_4[f]	Co_3O_4	99.7% cobalt (II,III) oxide[i]		6.0
Co_3O_4[g]	Co_3O_4	99.7% cobalt (II,III) oxide[i]		1.2
LSC[a]	90 wt% $(La_{0.85}Sr_{0.15})CoO_3$ + 10 wt% Co_3O_4	$LaSrCoO_3$ from Topsø[ii] 99.7% cobalt (II,III) oxide[i]		1.9
LSC[b/c]	90 wt% $(La_{0.85}Sr_{0.15})CoO_3$ + 10 wt% Co_3O_4	$LaSrCoO_3$ from Topsø[ii] 99.7% cobalt (II,III) oxide[i]		1.3
LSC[d]	90 wt% $(La_{0.85}Sr_{0.15})CoO_3$ + 10 wt% Co_3O_4	$LaSrCoO_3$ from Topsø[ii] 99.7% cobalt (II,III) oxide[i]		0.4
LSC[e]	90 wt% $(La_{0.85}Sr_{0.15})CoO_3$ + 10 wt% Co_3O_4	$LaSrCoO_3$ from Topsø[ii] 99.7% cobalt (II,III) oxide[i]		1.9
LSFC[a]	$(La_{0.54}Sr_{0.36})(Fe_{0.8}Co_{0.2})O_3$ + Ce	From Topsø[ii]	850°C/2h	0.6
LSFC[b]	$(La_{0.54}Sr_{0.36})(Fe_{0.8}Co_{0.2})O_3$ + Ce	From Topsø[ii]	850°C/2h	0.7
LSFC[c]	$(La_{0.54}Sr_{0.36})(Fe_{0.8}Co_{0.2})O_3$ obs no Ce	From Topsø[ii]	850°C/2h	1.1
LSFC[d]	$(La_{0.54}Sr_{0.36})(Fe_{0.8}Co_{0.2})O_3$ obs no Ce	From Topsø[ii]	850°C/2h	1.5
$MnCo_2O_4$	$MnCo_2O_4$	Glycine-nitrate method	900°C/8h	1.0
Al_2O_3	Al_2O_3	99.8% aluminum oxide[iii]		3.2
SiO_2	SiO_2			1.3
ZrO_2	ZrO_2			2.7

[i] *from Alfa Aesar*
[ii] *produced in rotating furnace*
[iii] *fine powder from Aldrich*
[iv] *measured by a Beckman coulter I/S particle size analyiser*

Six samples of the Crofer 22APU and Sandvik 1C44Mo20 alloys respectively were left uncoated as reference samples during the oxidation experiments as well as two Crofer 22APU samples for the TGA oxidation tests. As mentioned above the

dimension for the cyclic oxidation sample were 20*20*0.3 mm^3 and for the TGA samples the sample dimension was 20*10*0.3 mm^3.

The thickness of the as-sprayed coating layers were approximately 7, 15, or 30 µm depending on the desired coating design. Outlined in table 2.3 below is the complete list of coating and alloy combinations included in the cyclic oxidation and the TGA experiments.

Table 2.3.a. Description of used coatings on Crofer 22APU samples for cyclic oxidation and TGA experiments.

Sample	*1st layer* **Coating**	**Thickness [µm]**	*2nd layer* **Coating**	**Thickness [µm]**	**Temp. [˚C]**	**Nb. sample**
15 µm LSM	LSM[a]	15	-	-	900	6
30 µm LSM	LSM[b]	30	-	-	900	6
TGA 15 µm LSM	LSM[d]	15			900	2
15 µm LSC	LSC[a]	15	-	-	900	6
15 µm LSC	LSC[b]	15	-	-	900	6
15 µm LSFC	LSFC[a]	15	-	-	900	6
15 µm LSFC	LSFC[b]	15	-	-	900	6
15 µm LSFC	LSFC[c]	15	-	-	900	6
7 µm Co_3O_4	Co_3O_4[a]	7	-	-	900	6
15 µm Co_3O_4	Co_3O_4[b]	15	-	-	900	6
7 µm Co_3O_4 + 15 µm LSM	Co_3O_4[a]	7	LSM[a]	15	900	6
15 µm Co_3O_4 + 15 µm LSM	Co_3O_4[b]	15	LSM[a]	15	900	6
TGA 15 µm Co_3O_4 + 15 µm LSM	Co_3O_4[f]	15	LSM[e]	15	900	2
***950*˚C** 15 µm Co_3O_4 + 15 µm LSM	Co_3O_4[f]	15	LSM[d]	15	950	6
7 µm Co_3O_4 + 15 µm LSC	Co_3O_4[a]	7	LSC[a]	15	900	6
15 µm Co_3O_4 + 15 µm LSC	Co_3O_4[b]	15	LSC[b]	15	900	6
7 µm Co_3O_4 + 15 µm LSFC	Co_3O_4[a]	7	LSFC[a]	15	900	6
15 µm Co_3O_4 + 15 µm LSFC	Co_3O_4[b]	15	LSFC[b]	15	900	6
15 µm Co_3O_4 + 15 µm LSFC	Co_3O_4[c]	15	LSFC[c]	15	900	6
15 µm LSM + 15 µm LSC	LSM[c]	15	LSC[e]	15	900	6
15 µm LSC + 15 µm LSM	LSC[e]	15	LSM[c]	15	900	6
$MnCo_2O_4$	$MnCo_2O_4$	15	-	-	900	6
Al_2O_3	Al_2O_3	15	-	-	900	4
SiO_2	SiO_2	15	-	-	900	4
ZrO_2	ZrO_2	15	-	-	900	4

Table 2.3.b. Description of used coatings on Sandvik 1C44Mo20 for cyclic oxidation experiment.

Sample	*1st layer* **Coating**	**Thickness [µm]**	*2nd layer* **Coating**	**Thickness [µm]**	**Temp. [˚C]**	**Nb. sample**
15 µm LSM	LSM[b]	15	-	-	900	6
15 µm LSC	LSC[c]	15	-	-	900	6
15 µm LSFC	LSFC[d]	15	-	-	900	6
15 µm Co_3O_4	Co_3O_4[d]	15	-	-	900	6
7 µm Co_3O_4 + 15 µm LSM	Co_3O_4[d]	7	LSM[b]	15	900	6
15 µm Co_3O_4 + 15 µm LSM	Co_3O_4[d]	15	LSM[b]	15	900	6
pre-ox. 15 µm Co_3O_4 + 15 µm LSM	Co_3O_4[e]	15	LSM[c]	15	900	4
15 µm Co_3O_4 + 15 µm LSC	Co_3O_4[d]	15	LSC[c]	15	900	6
15 µm Co_3O_4 + 15 µm LSFC	Co_3O_4[d]	15	LSFC[d]	15	900	6

Table 2.3.c. Description of used coatings on Sandvik OYC44, 350, 433, 434 and 515.

Sample	*1st layer* **Coating**	**Thickness [μm]**	*2nd layer* **Coating**	**Thickness [μm]**	**Temp. [˚C]**	**Nb. sample**
15 μm Co_3O_4 + 15 μm LSC	Co_3O_4[d]	15	LSC[d]	15	900	3

Notice that the as-prepared coating thicknesses are approximations. In the cases where a dual coating was applied the base coating was first applied on both sides and left to dry for a few minutes. Thereafter the second coating layer was sprayed on.

Six samples of each coating/alloy combination were prepared for cyclic oxidation experiment, except for the Al_2O_3, SiO_2 and ZrO_2 coated Crofer 22APU samples and the pre-ox. + 15 μm Co_3O_4 + 15 μm LSM coated Sandvik 1C44Mo20 samples. For these coating/alloy combinations only four samples of each were prepared. Furthermore, for the Sandvik OYC44, 350, 433, 434, and 515 samples coated with 15 μm Co_3O_4 + 15 μm LSC only three samples of each coating/alloy combination were prepared for the cyclic oxidation experiment.

In table 2.3b a Sandvik 1C44Mo20 sample is listed as "pre-ox. 15 μm Co_3O_4 + 15 μm LSM". The "pre-ox." notation means that after being etched in hydrofluoric acid according to the procedure described above, four samples of the Sandvik 1C44Mo20 alloy were oxidized in air containing ca. 1% H_2O at 900°C for 24 hours before a 15 μm Co_3O_4 + 15 μm LSM coating was applied. For the pre-oxidation process the heating and cooling ramp were set to 120°C/h.

For the TGA experiments two samples were slurry coated with 15 μm LSM and two samples with 15 μm Co_3O_4 + 15 μm LSM. In table 2.3 the TGA samples are labelled with TGA before the name of the applied coating.

2.2.2 Oxidation procedure for cyclic oxidation and TGA experiments

The coated samples for the cyclic oxidation were weighed before being mounted free-hanging on Pt hooks in a furnace with a volume of ca. $4.32 \cdot 10^{-3}$ m^3. Air containing 1% water was supplied to the furnace with a gas flow of ca. $72 \cdot 10^{-3}$ m^3/h, whereby the gas in the furnace should be completely exchanged about 17 times per hour. The oxidation temperature was set to 900°C or 950˚C depending on the experiment, and the heating and cooling ramps to 120°C/h. The samples were oxidized in 250-hour-long cycles after which they were demounted, weighed and remounted again. This heating program was repeated until the cycling oxidation samples had been oxidized for a total of 4000 hours or as long as possible. With a few exceptions six samples of each alloy/coating combination were introduced in the oxidation furnace when the oxidation started. In general when the samples had been oxidized for 500, 1000, 1500, 2000, and 4000 hours respectively, a sample of each coating/alloy combination was removed from the oxidation furnace for analysis of the samples' cross-sections in SEM, resulting in only one sample of each alloy/coating combination remaining in the furnace for the last 2000 hours oxidation. The alloy/coating combinations not following this procedure were Crofer samples coated with SiO_2, Al_2O_3, and ZrO_2, and the Sandvik alloys OYC44, 350, 433, 434 and 515 coated with Co_3O_4 + LSC. For the Crofer 22APU samples coated with SiO_2, Al_2O_3, and ZrO_2 a total of four samples of each coating type was introduced in the furnace. For the SiO_2 coated samples one

sample was removed after 250 hours oxidation, one after 500 hours oxidation, and two after 4000 hours oxidation. For the Al_2O_3 coated samples one sample was removed after 2000 hours oxidation and three after 4000 hours oxidation. For the ZrO_2 oxide coated samples one sample was removed after 1000 hours oxidation, one after 2000 hours oxidation and two samples after 4000 hours oxidation. For the five special Sandvik alloys a total of three samples was introduced in the oxidation furnace. One sample of each of these special Sandvik alloys was removed from the furnace after 1000, 2000, and 4000 hours of oxidation respectively.

TGA measurements were performed, in a Netzsch, STA 409 CD equipment, to capture the initial oxidation of the uncoated, the 15 µm LSM coated and the 15 µm Co_3O_4 + 15 µm LSM coated Crofer 22APU samples. The oxidation samples were mounted free-hanging in pairs of two on an alumina sample holder shaped like a T. In figure 2.1 a sketch of the TGA furnace and a picture of two oxidation samples mounted on the sample holder are visible. The weight gain measured by the scale in the TGA equipment was the sum of the weight gain for both samples, as the oxidation samples were mounted in pairs of two on the sample holder. The atmosphere in the TGA furnace chamber was set to contain air with 1% water just as the atmosphere in the cyclic oxidation experiment. The furnace chamber in the TGA equipment had a volume of $0.14 \cdot 10^{-3}$ m^3 and a total gas flow of 0.081 m^3/h, whereby the gas in the TGA chamber should be completely exchanged ca. 35 times/hour. The heating profile in the TGA experiments consisted of a heating ramp of 120°C/h up to 900°C, which was held constant for 250 hours where after the furnace chamber was cooled down to RT with a cooling ramp of 120°C/h. To correct the weight gain measurements for buoyancy the weight measurements from alumina samples with the same dimensions as the metal samples were subtracted from the real measurements.

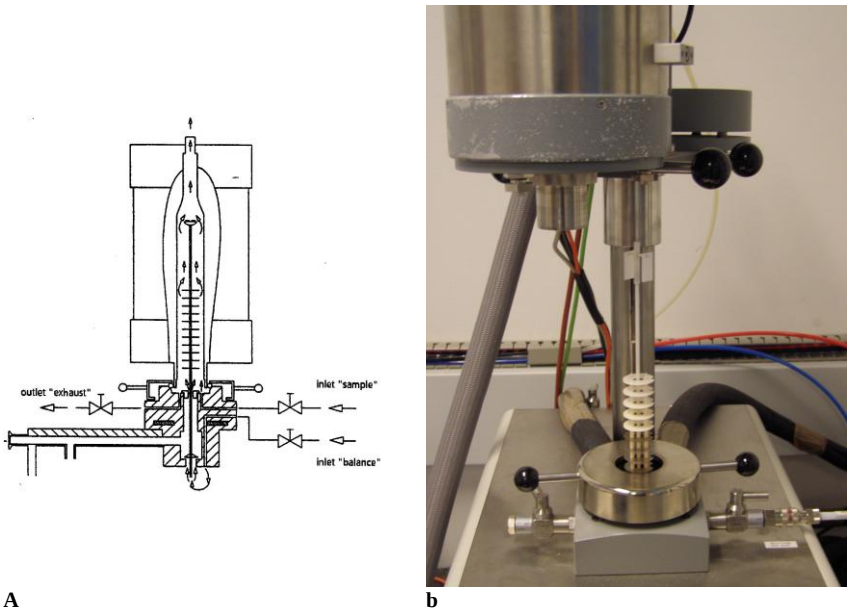

A **b**

Figure 2.1. The TGA set up a) principle sketch [1] and b) sample mounting.

2.2.3 Preparation of cross-sections of the oxidation samples

The samples removed from the cyclic oxidation furnace and the TGA samples were hot-mounted at 180˚C or vacuum-mounted at room temperature in epoxy to prepare cross-sections of the samples. The cross-sections were achieved by grinding 2-3 mm

into the samples using coarse SiC abrasive papers. The cross-sections were thereafter polished using diamond pastes down to 1 μm followed by a finish with OP-S suspension, colloidal silica. The cross-sections were finally carbon coated to avoid charging during SEM investigation at high vacuum in a JEOL JSM 5310 LV microscope. The microstructures of the oxides were captured using back scattered electron, BSE, imaging of the cross-sections, and by performing energy dispersive X-ray spectroscopy, EDS, the approximate cation compositions of oxides were determined. The BSE micrographs and the EDS data collected for the oxidized samples analyzed more in depth are not presented in this chapter but in the following chapters.

2.3 Results

In figure 2.2 the weight gain data collected for the coated Crofer 22APU and Sandvik 1C44Mo20 samples included in the cyclic oxidation experiment at 900˚C and 950˚C are plotted against time.

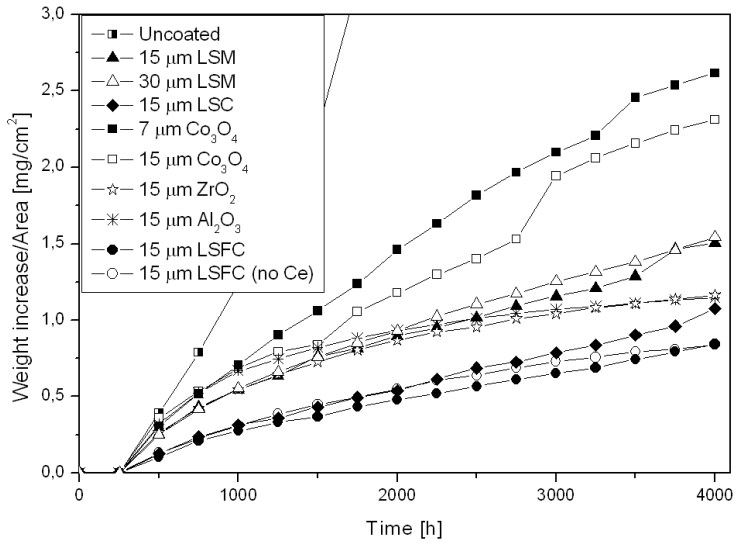

2.2.a. Weight gain-time plot of single layer coated Crofer 22APU oxidized in air containing 1% water at 900˚C.

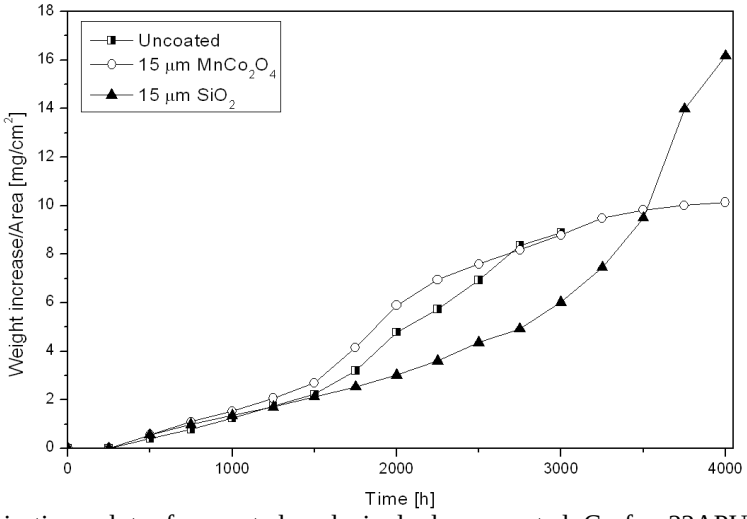

2.2.b. Weight gain-time plot of uncoated and single layer coated Crofer 22APU oxidized in air containing 1% water at 900˚C.

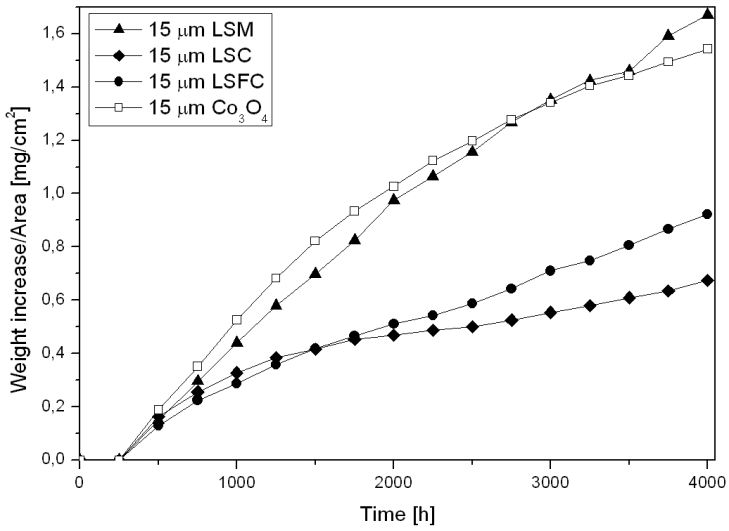

2.2.c. Weight gain-time plot of single layer coated Sandvik 1C44Mo20 oxidized in air containing 1% water at 900˚C.

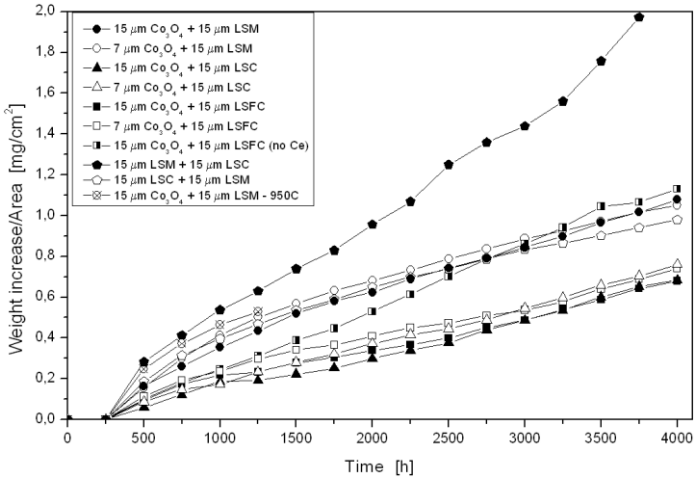

2.2.d. Weight gain-time plot of dual layer coated Crofer 22APU oxidized in air containing 1% water at 900˚C and a single sample at 950˚C.

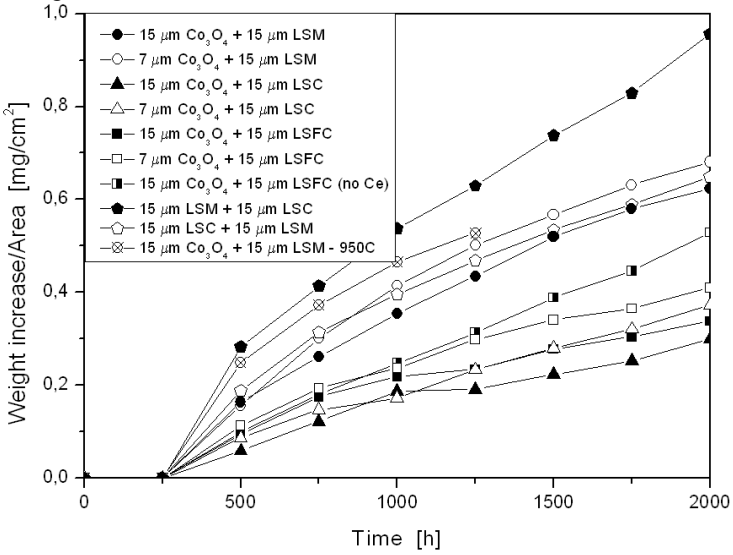

2.2.e. Weight gain-time plot of dual layer coated Crofer 22APU oxidized in air containing 1% water at 900˚C and a single sample at 950˚C.

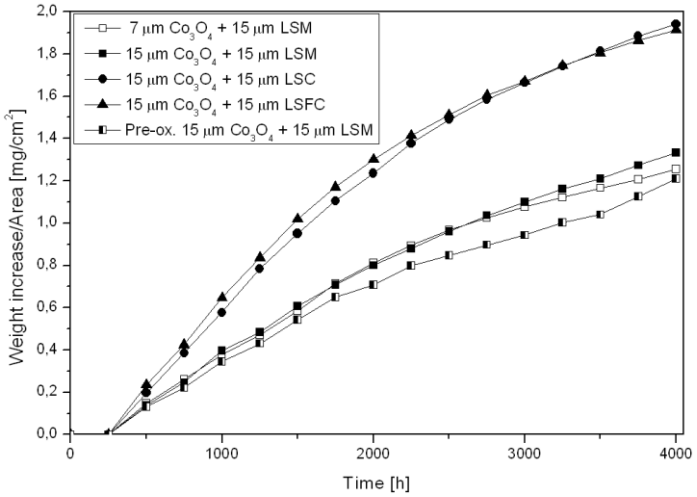

2.2.f. Weight gain-time plot of dual layer coated Sandvik 1C44Mo20 oxidized in air containing 1% water at 900˚C.

In figure 2.3 the weight gain data for the 15 µm Co_3O_4 + 15 µm LSC coated Sandvik OYC 44, Sandvik 350, Sandvik 433, Sandvik 434, and Sandvik 515 samples oxidized at 900˚C in the cyclic oxidation experiment are plotted against time together with the corresponding Crofer 22APU and Sandvik 1C44Mo20 samples.

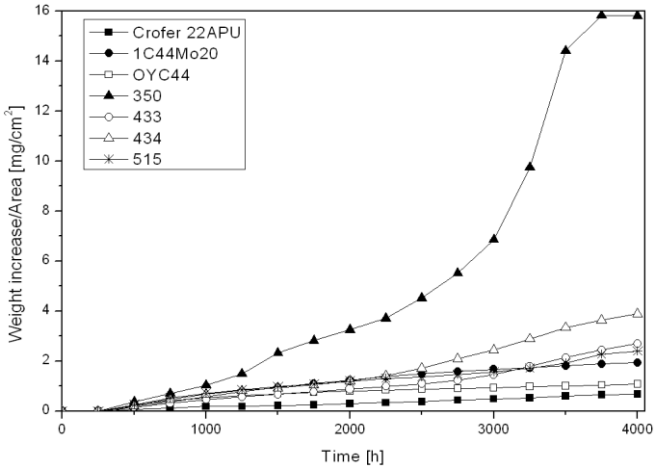

2.3. Weight gain-time plot of 15 µm Co_3O_4 + 15 µm LSM coated Crofer 22APU, Sandvik 1C44Mo20, Sandvik OYC44, Sandvik 350, Sandvik 433, Sandvik 434, and Sandvik 515 samples oxidized in air containing 1% water at 900˚C.

Uncoated and SiO_2 and $MnCo_2O_4$ coated Crofer 22APU samples experienced break away oxidation after ca. 1000 hours oxidation which was observed by a drastic weight increase as observed in the weight gain plots in figure 2.2.b. Sandvik 350 samples coated with 15 µm Co_3O_4 + 15 µm LSC also presented break away tendencies after ca. 2500 hours oxidation as seen in figure 2.3.

During oxidation uncoated Sandvik 1C44Mo20 samples experienced heavy spallation already after 250 hours oxidation and no reliable weight gain data could be collected and consequently no weight gain plot could be constructed.

When plotting the weight gain for the samples against time$^{1/2}$ the weight curves show linear behaviour indicating parabolic oxidation behaviour according to the

mathematical equation 2.1. According to literature, uncoated Crofer 22APU is expected to show parabolic oxidation behaviour [2, 3], and most of the applied slurry coatings do not seem to change this behaviour. The specific oxidation mechanism for each separate sample is discussed in more detail in the following chapters.

Parabolic oxidation behaviour indicates that the growth is governed by a thermal diffusion process, and is commonly found for high temperature oxidation of alloys [4].

$$\Delta w^2 = k_p t_t + C \qquad (2.1)$$

Δw is the weight gain while k_p and t_t stands for the parabolic rated constant and oxidation time respectively. C is an integration constant correcting for the transient oxidation before the protecting oxide scale has formed and steady state parabolic kinetics have been established in the system [5]. In this specific case the integration constant also includes a correction factor compensating for the fact that the data for the first 250 hours of oxidation for the samples are ignored. During the initial heating ramp the organic binder burn off from the coatings, and this results in a weight decrease which masks the weight gain caused by oxidation during the first 250 hours. In appendix 1 more detailed description of how k_p was defined in this study is given.

The parabolic oxidation mechanism is formulated for an ideal system based on several assumptions according to Wagner's theory. The basic assumption is that diffusion of reactants or the transport of electrons across the dense scale is rate determining for the overall oxidation process. This would indicate that the interfacial reactions can be considered to be rapid and it is assumed that thermodynamic equilibrium exists at the interfaces. These assumptions are applicable on an ideal oxide scale that is dense, well adherent, continuous and where the transport of ions occurs via lattice diffusion [4]. In reality these assumptions are not completely fulfilled. In this study oxidation of the uncoated Crofer 22APU samples is closest to an ideal case, and in figure 2.2.b it is illustrated by the weight gain plots that the uncoated Crofer 22APU samples also displayed parabolic oxidation behaviour up to ca. 1000 hours (~ 32 $h^{1/2}$) of oxidation where break away oxidation took place. When coatings are applied on the alloy samples the complexity of the oxidation process increases. The presence of a coating might create porosities in the growing oxide scale. This porosity might change during the oxidation process. The presence of the coating might also cause grain boundary and/or surface diffusion in the oxidizing system and/or facilitate evaporation of oxide species etc. In the presence of a coating a number of interaction mechanisms are made possible in the oxidizing system. The oxidation behaviour visible in weight gain plots for coated samples is a sum of all these interaction mechanisms active during the oxidation. The most dominant mechanism is the one dictating the appearance of the weight gain plot. The general distribution of the weight gain plots in this study for the oxidized samples tends to indicate parabolic oxidation mechanism. However, ZrO_2 and Al_2O_3 coated Crofer 22APU samples and LSC coated Sandvik 1C44Mo20 and Co_3O_4 + LSC coated Sandvik OYC44 samples showed indications on deviation from parabolic oxidation behaviour. As discussed in more detail in chapter 3 and 5 the overall oxidation mechanism of these samples are most likely parabolic, but other oxidation mechanisms in these systems have become significant enough to slightly shift the plots for the weight gain curves.

Since there in most cases were five samples of each alloy/coating combination left in the oxidation furnace for up to 1000 hours of oxidation, an average value of the parabolic rate constant for each alloy/coating was achieved. In table 2.4-5 the calculated parabolic constants are listed, in order of increasing constants. In some cases an alloy/coating combination has two different constants, since the slope of the weight gain-time$^{1/2}$ curve changes as oxidation proceeded. The change in the slope indicates a change of the rate determining process in the oxide scale.

Table 2.4.a. Parabolic rate constants for Crofer after 4000 hours oxidation neglecting the weight gain from the first 250 hours.

	$k_{p,1}\cdot10^{-3}$ $[(mg/(cm^2h^{1/2}))^2]$	Time [h]	$k_{p,2}\cdot10^{-3}$ $[(mg/(cm^2h^{1/2}))^2]$	Time [h]	Remark
15 μm Co_3O_4[b] + 15 μm LSFC[b]	0.13±0.02	3000	0.53	3000-4000	
15 μm Co_3O_4[b] + 15 μm LSC[b]	0.11±0.02	2500	0.57	2500-4000	
7 μm Co_3O_4[a] + 15 μm LSC[a]	0.20±0.05	2750	0.63	3000-4000	
7 μm Co_3O_4[a] + 15 μm LSFC[a]	0.22±0.07	3250	0.67	3250-4000	
15 μm Co_3O_4[c] + 15 μm LSFC[c]	0.21±0.05	1750	1.1	1750-4000	
15 μm LSC[b]	0.35±0.08	4000			
15 μm LSFC[b]	0.37±0.05	4000			
15 μm LSFC[c]	0.46±0.1	4000			
15 μm Co_3O_4[b] + 15 μm LSM[a]	0.49±0.1	3000	0.77	3000-4000	
7 μm Co_3O_4[a] + 15 μm LSM[a]	0.58±0.07	4000			
15 μm LSC[e] + 15 μm LSM[c]	0.56±0.2	4000			
ZrO_2	1.1±0.08	1000	0.29±0.2	1000-4000	Dev. from parabolic
15 μm LSM[c] + 15 μm LSC[e]	0.91±0.2	2250	3.0	2250-3500	
15 μm LSM[a]	1.2±0.2	4000			
30 μm LSM[b]	1.2±0.2	4000			
15 μm Co_3O_4[b]	1.3±0.2	2750	1.9	3000-4000	
Al_2O_3	1.7±0.09	1000	0.25±0.05	1000-4000	Dev. from parabolic
7 μm Co_3O_4[a]	2.9±0.3	4000			
Uncoated	7.5±1.1	1000			Break away ox. 1000h
SiO_2	7.5±0.01	1250			Break away ox. 1250h
$MnCo_2O_4$	9.3±1.0	1250			Break away ox. 1250h

Table 2.4.b. Parabolic rate constants for Sandvik 1C44Mo20 after 4000 hours oxidation neglecting the weight gain from the first 250 hours.

	$k_{p,1}\cdot10^{-3}$ $[(mg/(cm^2h^{1/2}))^2]$	Time [h]	$k_{p,2}\cdot10^{-3}$ $[(mg/(cm^2h^{1/2}))^2]$	Time [h]	Remark
15 μm LSFC[d]	0.33±0.04	4000			
15 μm LSC[c]	0.42±0.06	1250	0.10±0.01	1250-4000	Dev. from parabolic
7 μm Co_3O_4[d] + 15 μm LSM[b]	0.62±0.1	4000			
pre-ox.15 μm Co_3O_4[e] +15 μm LSM[c]	0.63±0.1	4000			
15 μm Co_3O_4[d] + 15 μm LSM[b]	0.66±0.2	4000			
15 μm LSM[b]	0.92±0.3	4000			
15 μm Co_3O_4[d]	1.2±0.1	4000			
15 μm Co_3O_4[d] + 15 μm LSC[c]	1.4±0.5	4000			
15 μm Co_3O_4[d] + 15 μm LSFC[d]	1.7±0.1	4000			

Table 2.4.c. Parabolic rate constants for Sandvik OYC44, 350, 433, 434 and 515 coated with 15 μm Co_3O_4[d] + 15 μm LSC[d] after 4000 hours oxidation neglecting the weight gain from the first 250 hours.

	$k_{p,1}\cdot10^{-3}$ $[(mg/(cm^2h^{1/2}))^2]$	Time [h]	$k_{p,2}\cdot10^{-3}$ $[(mg/(cm^2h^{1/2}))^2]$	Time [h]	Remark
Sandvik OYC44	0.99±0.1	1250	0.27±0.04	1250-4000	Dev. from parabolic
Sandvik 433	0.98±0.1	2750	20	2750-4000	
Sandvik 515	1.7±0.2	3250	14	3250-4000	
Sandvik 434	2.0±0.3	2250	27	2250-4000	
Sandvik 350	5.2±1.3	1250	34±3.0	1250-2500	Break away ox. 2500h

Table 2.5. Parabolic rate constants for 15 μm Co_3O_4 + 15 μm LSM coated Crofer 22APU oxidized in air containing 1% water at 950˚C neglecting the weight gain from the first 250 hours.

	$k_{p,1}\cdot10^{-3}$ $[(mg/(cm^2h^{1/2}))^2]$	Time [h]
15 μm Co_3O_4 + 15 μm LSM	0.77±0.05	1250

In figure 2.2 and table 2.4 it is illustrated that a Crofer 22APU sample coated with a dual coating consisting of Co_3O_4 and a perovskite coating achieves lower oxidation rate in comparison to a Crofer 22APU sample coated with a single layer of Co_3O_4 or with a perovskite coating. When performing the same comparison of coated Sandvik 1C44Mo20 samples it was found that only a dual coating with LSM as the perovskite coating resulted in a decreased oxidation rate relative to the single layer coatings of Co_3O_4 and the perovskite coating. For the LSC and LSFC perovskite a dual coating combination with Co_3O_4 as the inner coating layer resulted in an increased oxidation rate.

In figure 2.4 the weight gain data collected for the uncoated, LSM coated and Co_3O_4 + LSM coated Crofer 22APU samples during the TGA experiment are presented. For both the coated samples a weight decrease is registered in the initial heating ramp due to the burn off of organic binder.

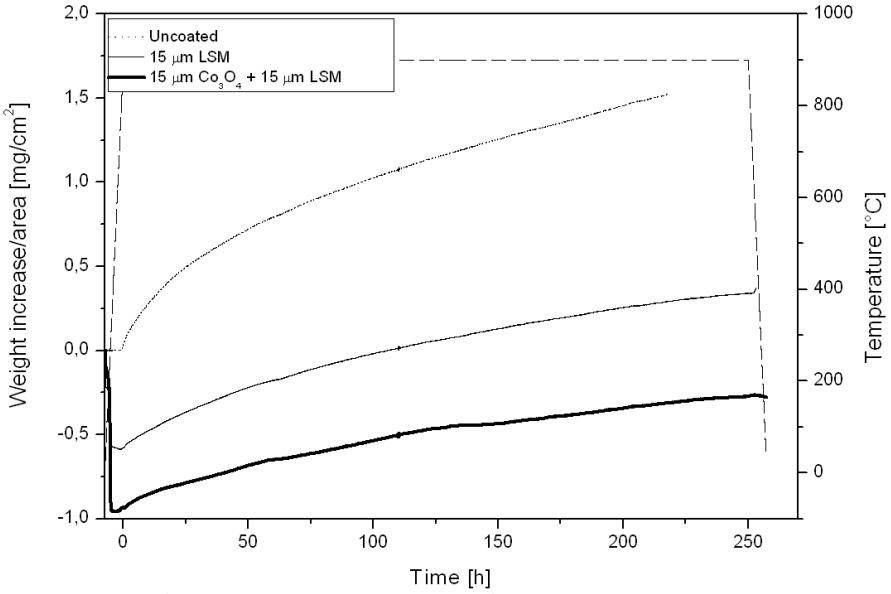

2.4. The weight increase plots from the TG oxidation experiment of uncoated, LSM coated and Co_3O_4 + LSM coated Crofer 22APU.

The calculated parabolic rate constants from these plots are presented in table 2.6.

Table 2.6. Calculated parabolic rate constant for the first 250 hours of oxidation measured using TGA equipment on uncoated, LSM coated and Co_3O_4 + LSM coated Crofer samples.

	$k_{p,1} \cdot 10^{-3}$ $[(mg/(cm^2 h^{1/2}))^2]$
Uncoated	11±0.008
15 μm LSM[d]	4.3±0.008
15 μm Co_3O_4[f] + 15 μm LSM[e]	2.2±0.009

2.4 Further analysis

From the total list of single layer coatings applied on Crofer 22APU the LSM, LSC, Co_3O_4, $MnCo_2O_4$, ZrO_2, and Al_2O_3 coatings were chosen to be further analyzed in the following chapters. The dual coatings consisting of Co_3O_4 + LSM and Co_3O_4 + LSC were also added to this list. The effect of the LSM, LSC, Co_3O_4 + LSM, and Co_3O_4 + LSC coatings on Sandvik 1C44Mo20 samples were also set up to be investigated and compared to the coatings' effect on Crofer 22APU samples. In table 2.7 an overview of the total list of experiments and analyses performed on the different coatings discussed in this thesis is presented.

Table 2.7.a. Overview table of experiment and parameters varied for uncoated and coated Crofer 22APU samples in this thesis.

	Coating thickness	900˚C Cyclic oxidation	950˚C Cyclic oxidation	TGA at 900˚C	ASR measurement at 950˚C	ASR measurement at 900˚C	Oxidation at 900˚C under a mechanical load	SEM Microstructure /composition
Uncoated		x		x				x
LSM	x	x		x	x			x
LSC		x			x			x
LSFC		x						
Co_3O_4	x	x						x
$MnCo_2O_4$		x						x
Al_2O_3		x						x
SiO_2		x						
ZrO_2		x						x
Co_3O_4 + LSM	x	x	x	x	x	x	x	x
Co_3O_4 + LSC	x	x			x		x	x
Co_3O_4 + LSFC	x	x						
LSM + LSC		x						
LSC + LSM		x						

Table 2.7.b. Overview table of experiment and parameters varied for uncoated and coated Sandvik 1C44Mo20 samples in this thesis.

	Coating thickness	Pre-heat treatment at 900˚C	900˚C cyclic oxidation	SEM Microstructure/composition
Uncoated			x	
LSM			x	x
LSC			x	x
LSFC			x	
Co_3O_4			x	
Co_3O_4 + LSM	x	x	x	x
Co_3O_4 + LSC			x	x
Co_3O_4 + LSFC				

Table 2.7.c. Overview table of experiment and parameters varied for Co_3O_4 + LSC coated Sandvik OYC44, 350, 433, 434 and 515.

	900˚C cyclic oxidation	SEM Microstructure/composition
Co_3O_4 + LSC	x	x

2.5 Reference List

1. Mikkelsen L., High Temperature Oxidation of Iron-Chromium Alloys, 2003

2. Kuznecov M., Eichler K., Megel S. and Otschik P., in Proceedings of the European SOFC Forum 2004, p. 1573

3. Yang, Z. G., Hardy, J. S., Walker, M. S., Xia, G. G., Simner, S. P. and Stevenson, J. W., Journal of the Electrochemical Society, 151, A1825-A1831 (2004)

4. Kofstad P, *High Temperature Corrosion* (Elsevier Applied Science Publishers LTD, 1988)

5. Pieraggi, B., Oxidation of Metals, 27, 177 (1987)

3. Single layer coatings on Crofer 22APU

3.1 Introduction

The function of an interconnector in Solid Oxide Fuel Cell (SOFC) stacks is to electrically connect the anode of one fuel cell with the cathode of the next fuel cell in a stack of SOFCs. At the same time it separates the fuel gas on the anode side from the moist air on the cathode side. To ensure satisfactory oxygen ion transport through the electrolyte and to ensure progress of the electrochemical reactions, the fuel cell is operating at high temperature, ~750°C. The high temperature combined with the atmosphere surrounding the interconnector results in an aggressive environment for the interconnect material. Iron-chromium alloys have proven to be successful as interconnect materials [1, 2]. The alloys have a matching thermal expansion coefficient with the other component materials in the fuel cell, and the chromia scale forming alloys have an appropriate balance between growth rate of the protecting chromia scale and its electrical resistance. Crofer 22APU is an iron-chromium alloy designed especially for use as interconnector. When oxidized at high temperatures in a moist oxidizing atmosphere similar to the atmosphere on the cathode side of the interconnector, it forms a duplex oxide scale consisting of an inner Cr_2O_3 layer and a $MnCr_2O_4$ layer on top. The spinel formation decreases the Cr-content in the outermost oxide scale and the amount of chromium that can evaporate as CrO_3 and $Cr(OH)_2O_2$ from the oxide scale [3]. These chromium species diffuse through the cathode to the catalytically reactive sites in the cathode/electrolyte interface where the chromium ions are reduced to chromia that block the catalytic reactive sites. Also, surface diffusion of chromium species along internal surfaces in the cathode may affect the efficiency of the cathode. To further improve the Crofer alloys', and other chromia forming alloys', suitability as interconnect material and make the efficiency level acceptable for use in a commercial SOFC-stack, application of coatings on the alloy surface has shown promising results. The use of some specific coatings has shown to decrease the alloys' oxidation rate, and decrease the electrical resistance of the formed oxides as well as the chromium evaporation and diffusion from the oxide [4-8] surface.

Oxidation experiments with Crofer 22 APU were conducted to get a more detailed understanding of how coatings and steel interact. Ultimately this knowledge contributes to improving the oxidation behaviour of chromia forming iron-based interconnect alloys. Samples of Crofer 22APU were wet coated with slurries consisting of $(La_{0.85}Sr_{0.15})MnO_3$ + 10% Mn excess (LSM), 90 wt% $(La_{0.85}Sr_{0.15})CoO_4$ + 10 wt% Co_3O_4 (LSC), Co_3O_4, $MnCo_2O_4$, ZrO_2, and Al_2O_3. They all showed slightly different interaction mechanisms with the oxide scale forming on the Crofer alloy, and they present different suitability for decreasing the oxidation rate of the alloy and decreasing diffusion/evaporation of chromium containing species from the alloy.

3.2 Experimental

3.2.1 Sample preparation

Crofer 22APU samples with the dimension 20*20*0.3 mm^3 with a 2 mm hole in the centre of one side were etched in hydrofluoric acid for 30 minutes to remove any native oxides formed during alloy processing. The samples were rinsed for 10 minutes

in water after etching and finally rinsed in alcohol for yet another 10 minutes. The samples that were supposed to be coated were slurry coated using a hand-gun spray, so that a ca. 7 μm or a ca. 15 μm thick layer of the coatings was applied on both sides of the samples. The slurries consisted of approximately 33 wt.% powder of the coating material dissolved in ethanol with a small amount of polyvinyl pyrrolidone, PVP-binder, mixed into it. Before sprayed onto the alloy samples, the slurries were ball-milled until a desired particle size distribution around $Ø_{50}$ = 1 μm (in reality $Ø_{50}$ = 0.4-6 μm) was achieved. In chapter 2 the measured particle sized for the different coatings are listed. The added PVP-binder will burn off during the heating ramp when the oxidation is initiated. The coatings included in this study are LSM, LSC, Co_3O_4, $MnCo_2O_4$, ZrO_2, and Al_2O_3. In chapter 2 more details about the coatings and experimental conditions can be found.

3.2.2 Oxidation experiment

The etched uncoated samples and the coated samples were weighed before being mounted as free hanging in an oxidation furnace with a volume of ca. $4.32 \cdot 10^{-3}$ m^3. Air containing 1% water was fed to the furnace with a flow rate ca. $72 \cdot 10^{-3}$ m^3/h, whereby the gas in the furnace chamber should be completely exchanged about 17 times per hour. The samples were oxidized in 250-hour-long cycles at 900°C after which the samples were demounted and weighed. The heating and cooling ramps were set to 120°C/h. When the long term, cyclic oxidation process was started there were between 4-6 samples of each coating type, making it possible to remove samples for further investigation at different points during the oxidation, and still have samples left in the furnace for continued oxidation. Generally a sample of each coating were removed from the furnace after 500, 1000, 2000, and 4000 hours of oxidation for analysis of the samples' cross-sections in SEM. The only exceptions were the ZrO_2 and Al_2O_3 coated samples. The ZrO_2 coated samples were removed from the furnace after 1000, 2000, and 4000 hours of oxidation, while the Al_2O_3 coated samples were removed from the furnace after 2000 and 4000 hours of oxidation. Complementary oxidation experiments at the same temperature and atmosphere as described above were performed for two uncoated and two LSM coated Crofer samples with the dimension 20*10*0.3 mm^3 with a 2 mm hole in the centre of one of the short sides. The alloy samples were etched and coated according to the same procedure as described above and weighed before being mounted free-hanging on a sample holder made of alumina, as seen figure 2.1, in the TGA equipment Netzsch, STA 409 CD. The furnace chamber in the TG equipment had a volume of $0.14 \cdot 10^{-3}$ m^3 and a total gas flow of 0.081 m^3/h, whereby the gas in the chamber should be completely exchanged ca. 35 times/hour. The samples were oxidized for 250 hours to document the initial oxidation behaviour which could not be captured with the cyclic oxidation process. The heating and cooling ramp was just as in the cyclic experiment set to 120°C/h.

3.2.3 Preparation of cross-sections

The samples removed from the oxidation furnace were hot-mounted or vacuum-mounted in epoxy to prepare a cross-section of the sample. The cross-sections were made by grinding 2-3 mm into the samples using course SiC abrasive papers. The cross-sections were thereafter polished using diamond paste down to 1 μm followed by a finish with OP-S suspension, colloidal silica. The cross-sections were finally carbon coated to avoid charging during SEM investigation at high vacuum in a JEOL JSM 5310 LV microscope. The microstructure of the oxides was captured using BSE

imaging on the cross-sections. By performing reference-free EDS the cation compositions of oxides were estimated. The EDS measurements include mappings, line scans and point analysis. For more detailed description of the cross-section preparation, see chapter 2.

3.3 Results

3.3.1 Parabolic oxidation constant and scale thickness

In figure 3.1 the weight gain data collected for the uncoated and single layer coated Crofer sample during the cyclic oxidation experiment is presented as a weight increase-time$^{1/2}$ plot.

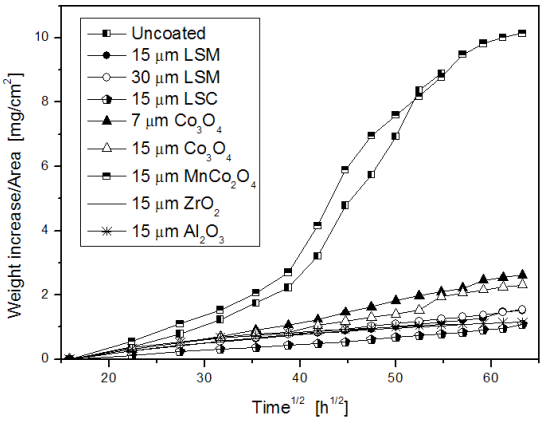

Figure 3.1.a. The weight increase-time$^{1/2}$ plots for uncoated and single layer coated Crofer 22APU samples in the long term, cyclic oxidation experiment at 900˚C in air containing 1% water.

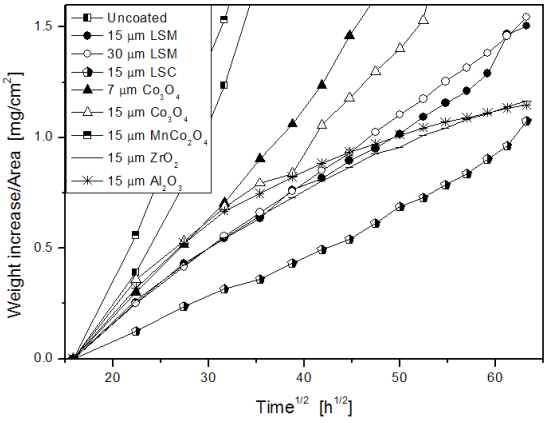

Figure 3.1.b. Enlargement of figure 3.2.a of the weight increase-time$^{1/2}$ plots for uncoated and single layer coated Crofer 22APU samples in the long term, cyclic oxidation experiment at 900˚C in air containing 1% water.

The plots of the LSM, LSC, and the Co_3O_4 coated Crofer samples tended to present a general linearity in figure 3.1 which would indicate parabolic oxidation behaviour. The $MnCo_2O_4$ coated Crofer sample also showed the same tendency towards linearity and parabolic oxidation behaviour up to ca 1000 hours just as the uncoated Crofer sample. Parabolic oxidation can be described by the mathematical formula presented in equation 3.1.

$$\Delta w^2 = k_p \cdot t_t + C \qquad \text{eq. 3.1}$$

Where Δw is the weight gain while k_p and t_t are the parabolic rate constant and oxidation time, respectively. C is an integration constant correcting for the oxidation during the initial stages of oxidation and the evaporation taking place during this period before a dense continuous oxide scale has formed. In an ideal parabolic oxidation mechanism a list of assumptions regarding the conditions of the oxidation system are made according to Wagner's theory. The basic assumptions are that diffusion of reactants or the transport of electrons across the dense scale is rate determining for the overall oxidation process, and this would indicate that the interfacial reactions can be considered to be rapid and it is assumed that thermodynamic equilibrium exists at the interfaces. These assumptions are applicable on an ideal oxide scale that is dense, well adherent, continuous and where the transport of ions occurs via lattice diffusion [9]. In reality these assumptions are not completely fulfilled. Oxidation of the uncoated Crofer 22APU samples is closest to an ideal case in this study, and as mentioned above uncoated Crofer 22APU samples also displayed weight gain indicating parabolic oxidation behaviour up to ca. 1000 hours (~ 32 $h^{1/2}$) of oxidation which is illustrated by the weigh gain plots in figure 3.1. When coatings are applied on the alloy samples the complexity of the oxidation process increases. The presence of a coating might create porosities in the growing oxide scale. This porosity might change during the oxidation process. The presence of the coating might also cause grain boundary and/or surface diffusion in the oxidizing system and/or facilitate evaporation of oxide species etc. In the presence of a coating a number of possible interaction mechanisms are made possible in the oxidizing system. The oxidation behaviour illustrated by the weight gain plots for the coated samples is a sum of all these interaction mechanisms active during the oxidation. The most dominant mechanism is the one dictating the weight gain and thereby the distribution of the weight gain plots.

The LSM, LSC, Co_3O_4, and $MnCo_2O_4$ coated Crofer 22APU samples displayed weight gain plots indicating parabolic oxidation behaviour in figure 3.1, suggesting that a thermally activated diffusion process through the growing oxide scale on the samples was the dominating mechanism during oxidation. The integration constant, C, in equation 3.1 would then include a correction factor compensating for the fact that the first 250 hours of oxidation for the samples are ignored. As mentioned above, the organic binder burn off from the coatings during the initial heating ramp resulting in a weight decrease, which obscure the weight gain caused by oxidation during the first 250 hours.

The weight gain-time$^{1/2}$ curves of the Al_2O_3 and ZrO_2 coated Crofer samples in figure 3.1 have an arced shape rather than linear shape as the other samples. In figure 3.2a magnifications of the weight gain-time$^{1/2}$ plots of the LSM coated samples and the Al_2O_3 and ZrO_2 coated Crofer samples are presented to highlight this. The arced shape of the weigh gain curves might indicate that a reaction mechanism other than a thermally activated diffusion process in the growing oxide scale is becoming significant in the complex oxidation systems of the Al_2O_3 and ZrO_2 coated samples. If the alternative reaction mechanism would become dominating, an oxidation mechanism different from parabolic might be a better summation of the oxidation of the Al_2O_3 and ZrO_2 coated Crofer samples. In figure 3.2b an alternative oxidation

mechanism for the Al_2O_3 and ZrO_2 coated samples is tested by plotting the weight increase against log(time). If the weight gain data form a linear plot in this set up, as the weight gain data for the Al_2O_3 and ZrO_2 coated samples show tendency to do, a logarithmic oxidation mechanism would be a possible description of the oxidation behaviour. The mathematical formula describing logarithmic oxidation is shown in equation 3.2.

Direct logarithmic: $\Delta w = k_{\log} \log(t + t_0) + A$ eq. 3.2a

Inverse logarithmic: $\frac{1}{\Delta w} = B - k_{il} \log t$ eq. 3.2b

Here the letters A and B are integration constants and the $k_{\log}$ and k_{il} are the logarithmic rate constants.
While parabolic oxidation mechanism is relatively well known, and controlled by diffusion processes, logarithmic oxidation mechanisms are not as studied. Logarithmic oxidation behaviour is known to characterize the oxidation of a large number of metals at low temperatures, generally below 300-400 °C, which is well below the oxidation temperature used in this study. Some of the suggested rate-determining mechanisms for logarithmic oxidation behaviour in literature are transport of electrons or ions due to electric fields in or across very thin oxide film, chemisorption, cavity formation in the film, etc [9].

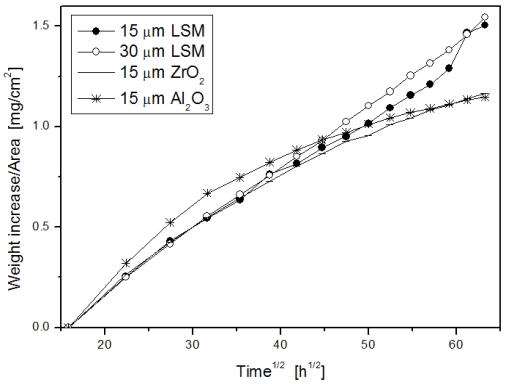

Figure 3.2.a. The weight increase-time$^{1/2}$ plots for LSM, Al_2O_3, and ZrO_2 coated Crofer samples in the long term, cyclic oxidation experiment at 900˚C in air containing 1% water.

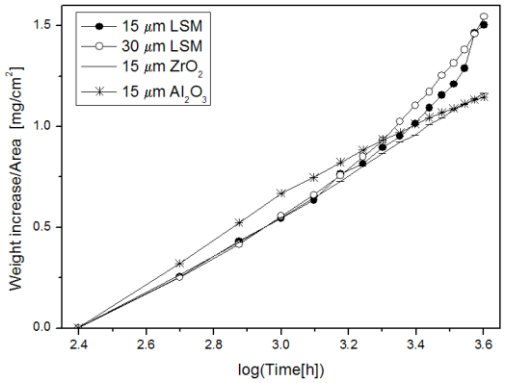

Figure 3.2.b. The weight increase-log(time) plots for LSM, Al_2O_3, and ZrO_2 coated Crofer samples in the long term, cyclic oxidation experiment at 900˚C in air containing 1% water.

The suggested mechanisms for logarithmic oxidation behaviour do not apply very well to the oxidation conditions of the Al_2O_3 and ZrO_2 coated Crofer 22APU samples in this study. It is more likely that the oxidation of the Al_2O_3 and ZrO_2 coated samples is best described by a parabolic oxidation mechanism just as the other coated Crofer 22APU samples. However, due to the possible reaction mechanisms presented in the complex oxidation system on the Al_2O_3 and ZrO_2 coated samples becoming more significant the weight gain plots tend to deviate slightly from characteristic parabolic distribution. The oxidation behaviour of Al_2O_3 and ZrO_2 coated Crofer 22APU samples will be discussed further in section 3.4.5-6.

After ca. 1000 hours of oxidation drastic weight increase was observed for the $MnCo_2O_4$ coated sample and the uncoated sample indicating break away oxidation.

Independent of the oxidation behaviour all the coatings lowered the weight gain compared to the uncoated Crofer 22APU sample except for the $MnCo_2O_4$ coating, which appeared to have an even higher weight increase rate than the uncoated samples. The $MnCo_2O_4$ coated samples were also the only coated samples that showed break away oxidation behaviour, and it took place around the same time as the break away took place at the uncoated samples.

Table 3.1 summarizes the parabolic oxidation constants for the uncoated and the single layer coated Crofer 22APU samples, and the thickness of the formed oxide scales on the samples as determined from the SEM micrographs in figure 3.4-6. The parabolic rate constant decreases after 1000 hours of oxidation for both of the Al_2O_3 and the ZrO_2 coated samples. The decrease in the slope of the weight gain plot for the Al_2O_3 coated sample are as easily discerned on the weight increase-log(time) plot as on the weight increase-time$^{1/2}$ plot.

In table 3.1 the samples are in order of increasing oxidation rate according to the parabolic oxidation constants going downwards. Just as seen in the weight gain plot in figure 3.1 the LSC, LSM and the ZrO_2 coated samples presented the lowest weight gain. For the LSM coating two different coating thicknesses were tested, but no difference in the weight gain was found as illustrated in figure 3.1-2. In comparison the Co_3O_4 coated samples, which had a higher weight gain than the LSM coated samples, showed a difference in weight gain depending on the thickness of the Co_3O_4 coating. The thicker the Co_3O_4 coating was the smaller the weight gain observed. The Al_2O_3 coated samples had a similar weight gain as the Co_3O_4 coated samples during the initial 1500 hours. Hereafter the weight gain rate of the Al_2O_3 coated samples decreases and approaches the level for the LSC, LSM and the ZrO_2 coated samples.

Table 3.1.a. Parabolic rate constants for the coated and uncoated Crofer samples after 4000 hours oxidation neglecting the weight gain from the first 250 hours.

	$k_{p,1}\cdot10^{-3}$ $[(mg/(cm^2h^{1/2}))^2]$	*Time [h]*	$k_{p,2}\cdot10^{-3}$ $[(mg/(cm^2h^{1/2}))^2]$	*Time [h]*	*Remark*
15 μm LSC[b]	0.35±0.08	4000			
ZrO_2	1.1±0.08	1000	0.29±0.2	1000-4000	Deviation from parabolic ox.
15 μm LSM[a]	1.2±0.2	4000			
30 μm LSM[b]	1.2±0.2	4000			
15 μm Co_3O_4[b]	1.3±0.2	2750	1.9	3000-4000	
Al_2O_3	1.7±0.09	1000	0.25±0.05	1000-4000	Deviation from parabolic ox.
7 μm Co_3O_4[a]	2.9±0.3	4000			
Uncoated	8.8±2.7	1000			
$MnCo_2O_4$	9.3±1.0	1250			

Table 3.1.b. Parabolic rate constants for uncoated and LSM coated Crofer samples calculated from oxidation data in the TGA equipment during 250 hours oxidation.

	$k_{p,1}\cdot10^{-3}$ $[(mg/(cm^2h^{1/2}))^2]$
Etched, uncoated	11±0.008
15 μm LSM[d]	4.3±0.008

Table 3.1.c. Measured oxide scale thicknesses, t, on the BSE micrographs.

	t [μm] 500 h	*t [μm] 1000 h*	*t [μm] 2000 h*	*t [μm] 4000 h*	*Remark*
15 μm LSC[b]	4.1±1.2	4.3±1.6	5.4±1.5	9.2±1.9	Tot. ox. scale
ZrO_2		8.3±1.7	9.8±1.8	11.8±2.3	Tot. ox. scale
15 μm LSM[a]	4.7±1.6	6.5±1.7	7.3±1.3	10.6±2.8	Tot. ox. scale
15 μm Co_3O_4[b]	5.6±1.6 (10.6±2.0)	6.8±2.0 (13.3±3.8)	9.2±1.9 (16.2±2.8)	14.5±1.8 (21.0±2.7)	Cr_2O_3 scale (Formed oxide + sintered/reacted coating)
Al_2O_3			10.0±1.5	8.5±2.4	Tot. ox. scale
7 μm Co_3O_4[a]	7.1±1.4 (10.5±2.0)	8.4±1.7 (10.3±1.8)	15.2±3.0 (19.2±7.0)	14.9±4.0 (16.6±4.5)	Cr_2O_3 scale (Formed oxide + sintered/reacted coating)
Uncoated	9.8±3.2	11.9±2.9	15.3±2.0		Tot. ox. scale
$MnCo_2O_4$	8.5±1.0 (15.5±1.4)	13.3±1.5 (21.2±3.1)	19.1±1.8 (26.4±2.7)	25.±3.0 (31.6±3.2)	Cr_2O_3 scale (Formed oxide + sintered/reacted coating)

The weight increase data collected for the uncoated and LSM coated Crofer samples in the TGA equipment are presented below in figure 3.3. These data give information about the initial oxidation during the first 250 hours of oxidation that is lost in the long term, cycling oxidation experiment. The collected data was corrected for buoyancy with a reference sample made of alumina in the same dimensions as the oxidation samples. In the weight increase-time and weight increase-time$^{1/2}$ plots in figure 3.3a and 3.3b respectively it was found that as expected there was great weight loss during the heating ramp for the coated samples due to the organic burn-off. When the temperature in the TGA-chamber reached 900°C all the organic material appeared to have burnt off and a parabolic weight increase was observed. The constants calculated from these weight plots are presented in table 3.1b. When comparing the parabolic rate constants to the ones calculated from the cyclic oxidation experiments, the ones from the TGA-chamber are much higher than the ones from the cyclic

oxidation experiment. Both the uncoated and the LSM coated samples show the same trend.

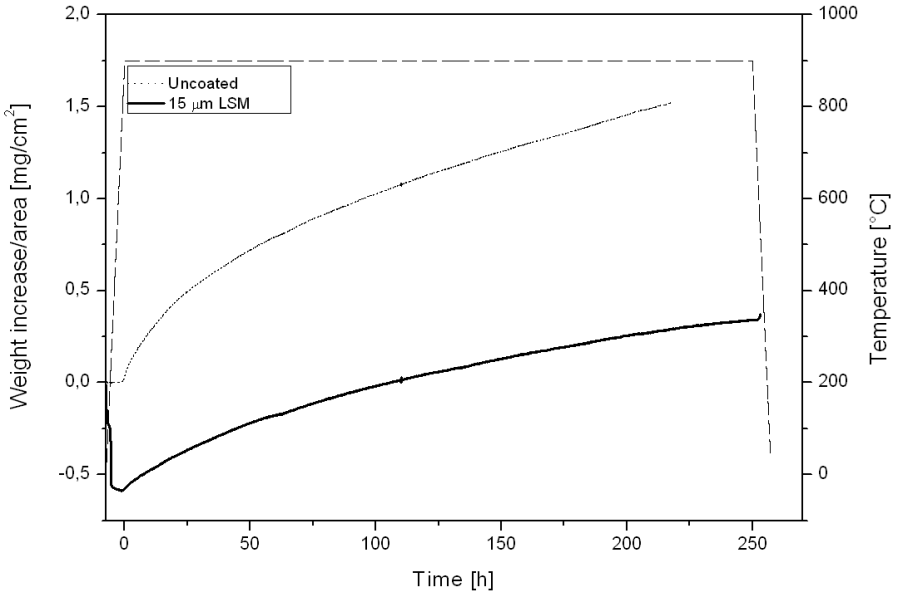

Figure 3.3.a. The weight increase data collect with TGA for uncoated LSM coated Crofer.

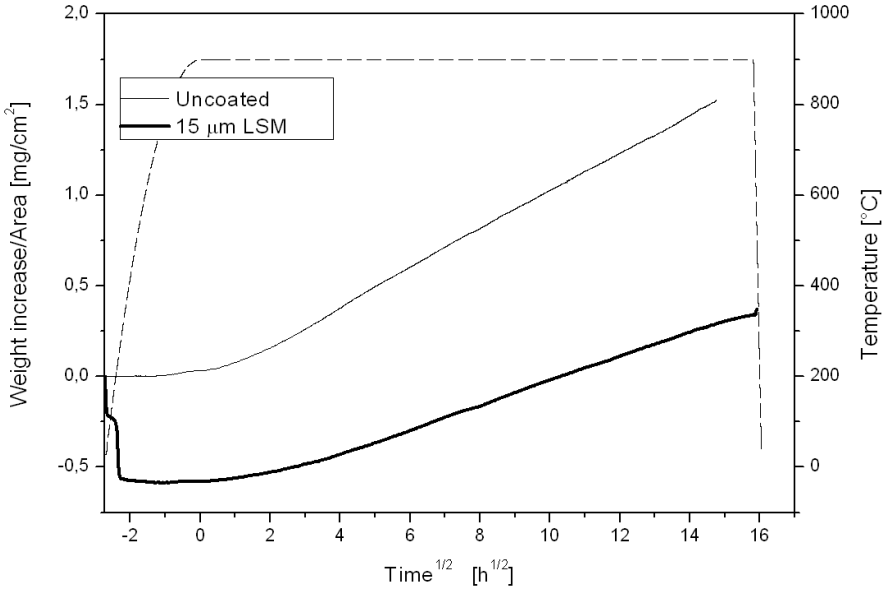

Figure 3.3.b. The weight increase-time$^{1/2}$ plots for uncoated LSM coated Crofer samples from the TGA-measurements.

Micrographs of the cross-sections of the coated and uncoated Crofer samples after different oxidation times are presented in figure 3.4-6. The scale thicknesses presented in table 3.1 are measured on micrographs like these. In the micrographs in figure 3.4 of the uncoated Crofer samples the duplex oxide scale expected to be found is visible [3, 10]. The outer (Mn,Cr)-spinel phase is lighter grey than the inner Cr_2O_3 phase. A number of metal inclusions is observed in the oxide scale. The micrographs of the LSM coated samples in the same figure show a thinner oxide scale than the uncoated ones and fewer metal inclusions. The heavier, bright LSM particles seem to be pushed

in front of the growing oxide scale and are not incorporated into the oxide scale. On the other hand, in the growing oxide scale on the LSC coated samples bright La- and Sr-rich particles appear to be incorporated. These areas probably consist of $LaCrO_3$ and/or $SrCrO_4$ due to dissociation of the LSC coating. The oxide scale on the LSC coated samples are thinner than on the uncoated ones, but the oxide/alloy and oxide/coating interfaces are not as smooth as on the LSM coated samples. In the LSC coating, areas containing high amounts of chromium, cobalt and manganese were also found.

The oxide scale on the Co_3O_4 coated samples in figure 3.5 consists of a Cr_2O_3 layer, which thickness is included in table 3.1, and a spinel phase layer. This spinel phase layer consists of the sintered/reacted Co_3O_4 coating plus the naturally forming spinel phase on Crofer. The Cr_2O_3 phase is slightly darker grey than the spinel phase. Line scans presented in figure 3.9 and appendix 2 support this. For the 15 µm Co_3O_4 coated Crofer 22APU sample oxidized for 500 hours the epoxy has detached from the oxidized sample and the surface of the sample has become visible. In figure 3.6 a similar division of the Cr_2O_3 layer and the spinel phase consisting of the sintered/reacted spinel coating and the forming spinel as found on the Co_3O_4 coated samples were observed on the $MnCo_2O_4$ coated samples. The Cr_2O_3 layer was however significantly thicker than on any of the coated and uncoated samples. After ca. 1000 hours of oxidation the edges of the $MnCo_2O_4$ coated samples started to experience heavy oxidation. This was not observed on any of the other coated or uncoated samples; here the oxide scales on the edges appeared similar to the oxide found along the flat surfaces of the samples.

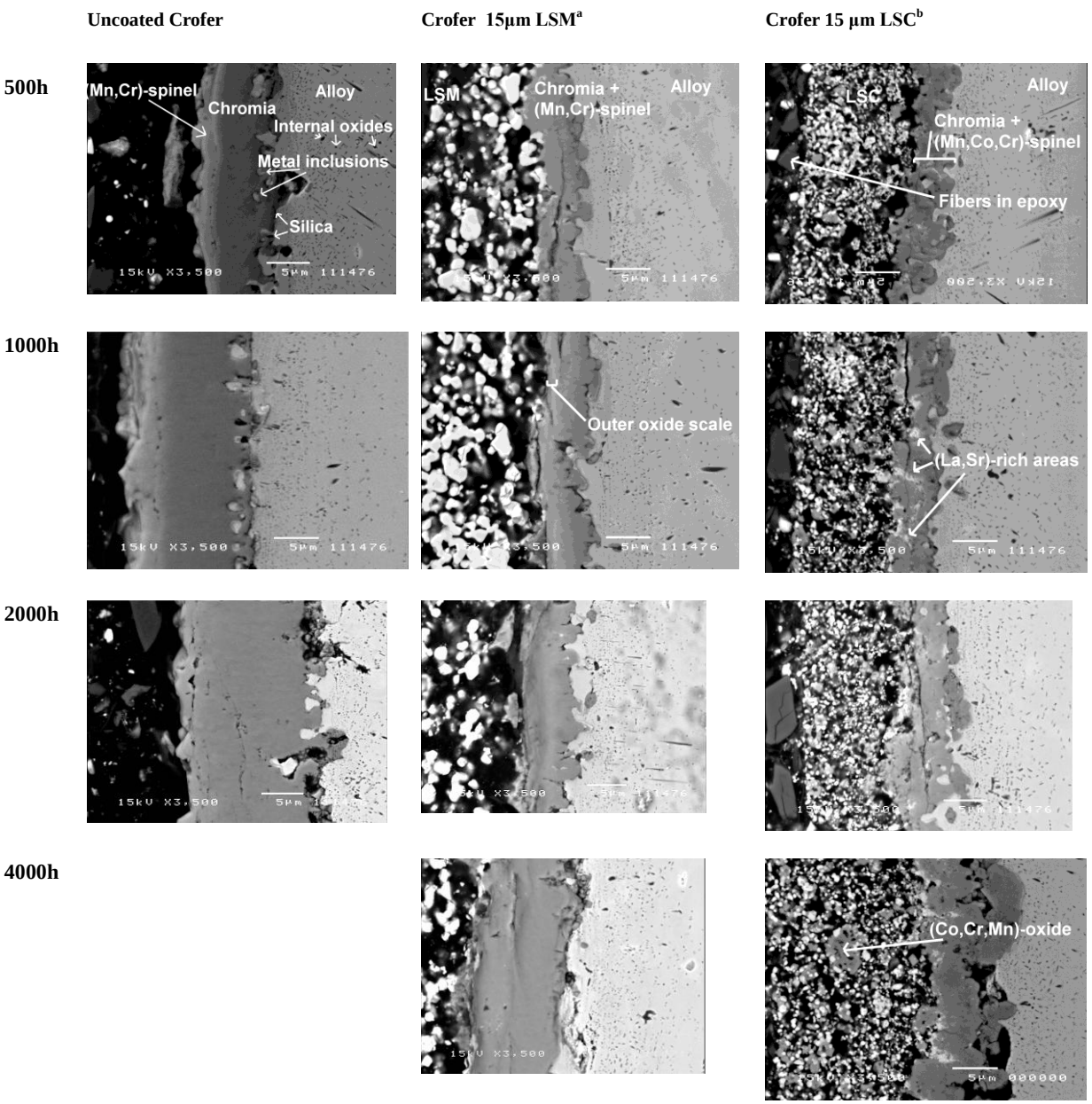

Fig. 3.4. BSE micrographs of the oxide scales in the cross-sections of the samples, with the oxidation times indicated left of the pictures.

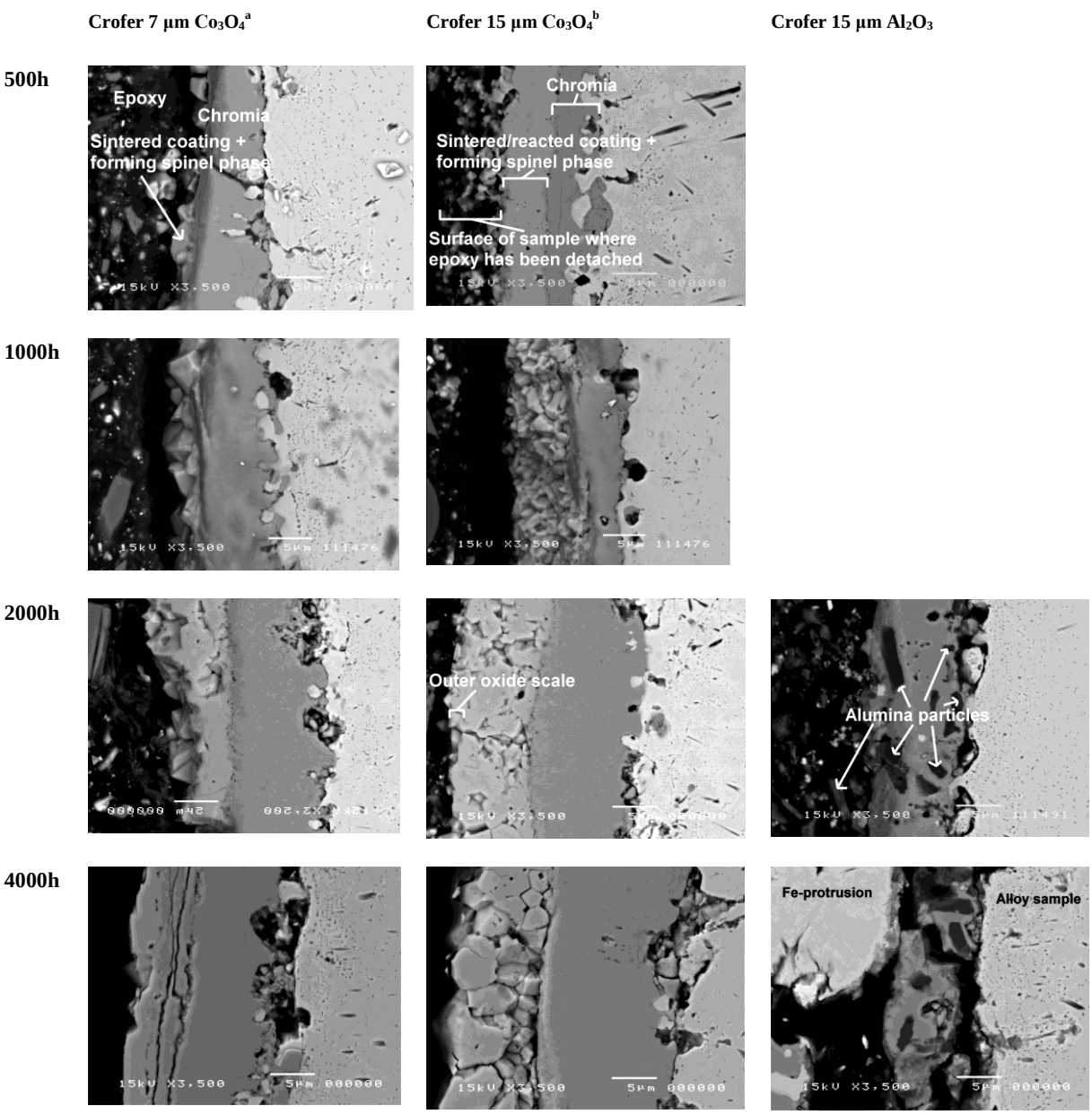

Fig. 3.5. BSE micrographs of the oxide scales in the cross-sections of the samples, with the oxidation times indicated left of the pictures.

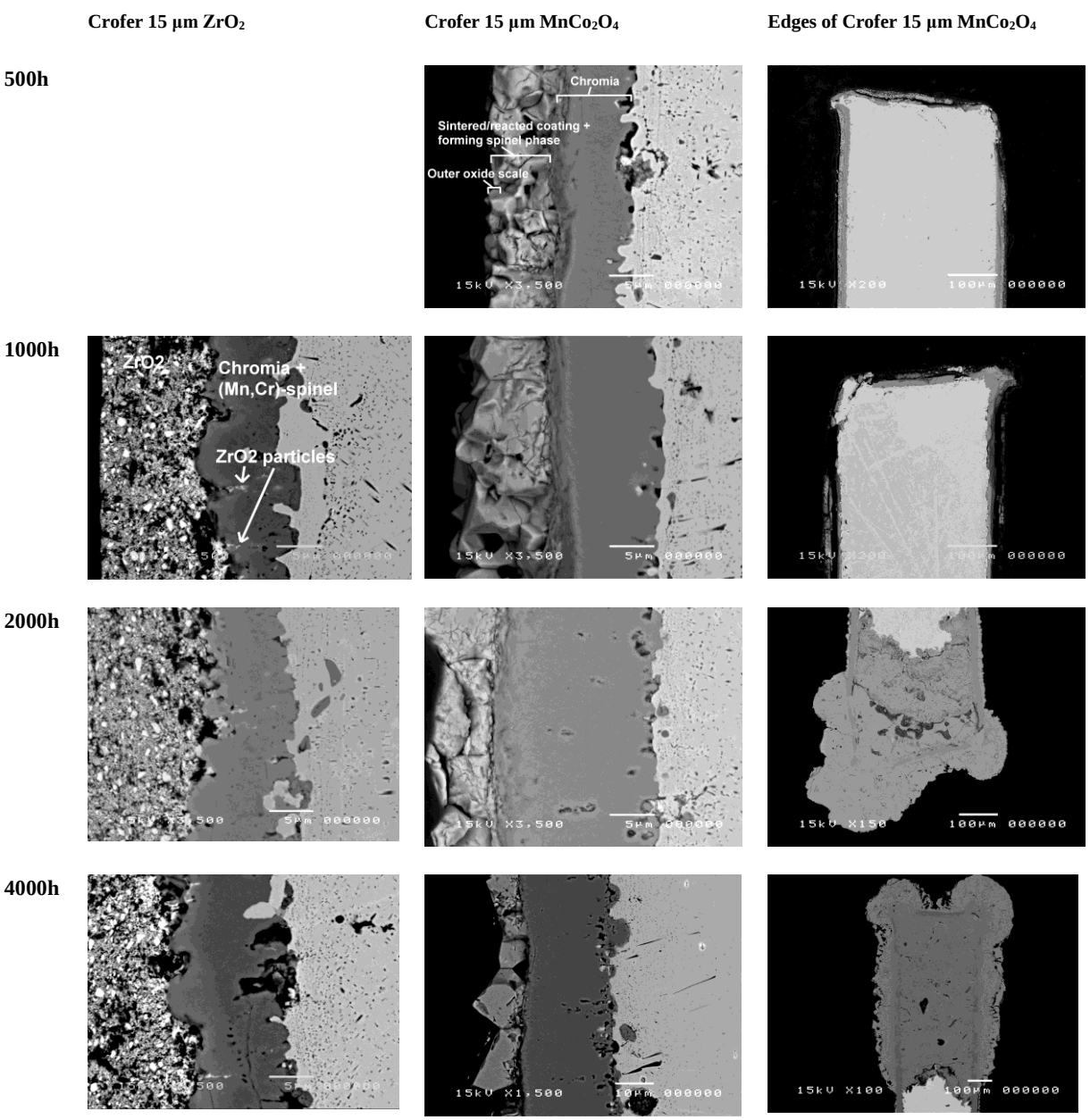

Fig. 3.6. BSE micrographs of the oxide scales in the cross-sections of the samples, with the oxidation times indicated left of the pictures.

Dark Al_2O_3 coating particles were incorporated into the growing oxide scale on the Al_2O_3 coated samples, as can be seen in figure 3.5. On the 2000 hours sample a relatively even and coherent oxide scale is covering the alloy surface as can be seen in figure 3.5 and in figure 3.7a. But, for the 4000 hours sample chips of iron is found sandwiched between an inner oxide scale covering the alloy sample and an oxide scale covering the iron chip's surface. A piece of such an iron chip entirely separated from the alloy sample is visible in the micrograph in figure 3.5, and in figure 3.7b and d micrographs showing such iron chip is visible in lower magnification. In these micrographs the oxide scale is visible on all sides of the chip. In figure 3.7c a micrograph showing an iron chip, which is not yet totally separated from the alloy sample, but presumably is in the process of becoming it, is reproduced.

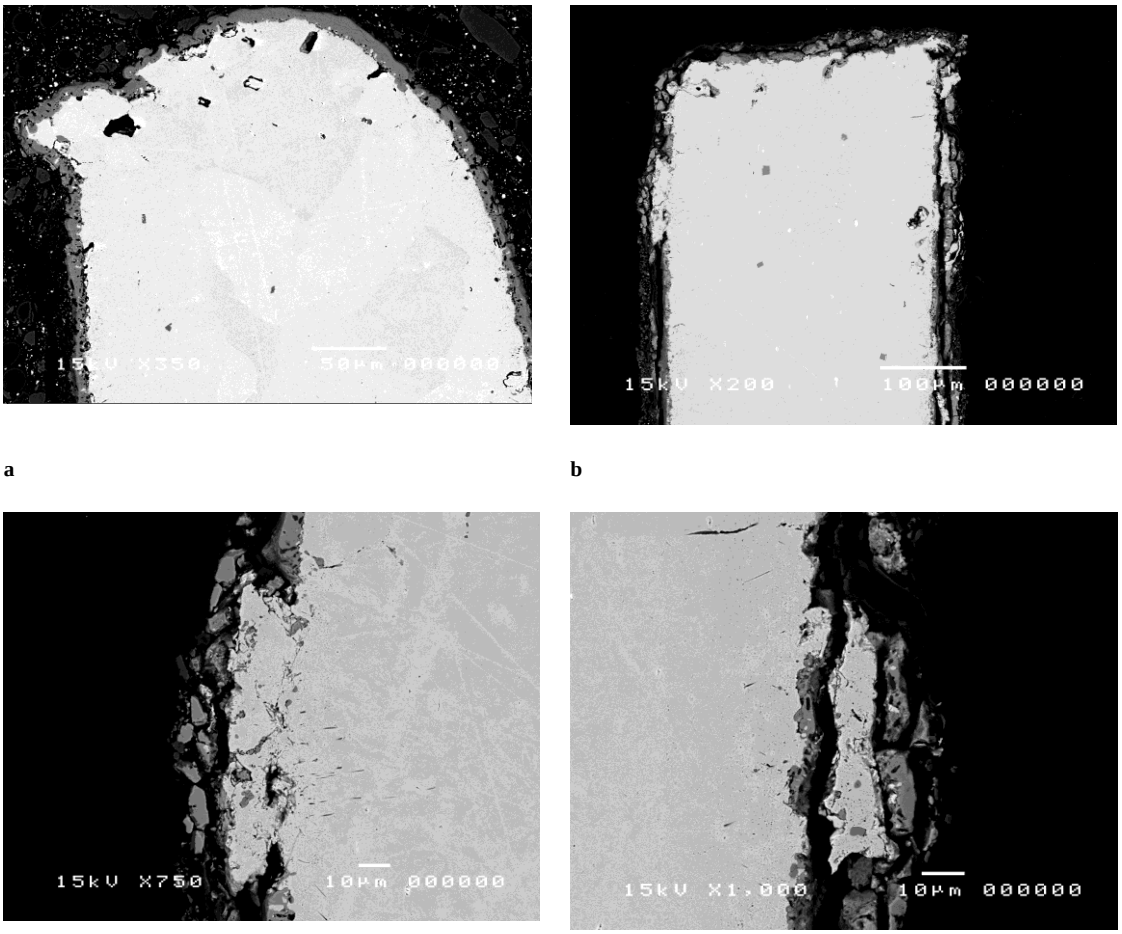

Fig. 3.7. BSE micrographs of the oxide scales on cross-sections of the alumina coated samples oxidized for a) 2000 hours, and b, c, d) 4000 hours.

In the micrographs of the ZrO_2 coated samples in figure 3.6 there is also observed a tendency towards incorporation of ZrO_2 particles in the growing oxide scale. EDS measurements confirmed that the incorporated particles contain high amounts of Zr originating from the coating. But, higher resolutions would have to be used to collect further information about the oxide structure around the embedded particles to get more information to support the assumption that the ZrO_2 coating particles remain chemically inert when they are being incorporated in the oxide scale.

The LSM, LSC, ZrO_2 and Al_2O_3 coatings all appeared porous on the micrographs suggesting free access to oxygen from the atmosphere on the surface of the growing oxide scale. The Co_3O_4 and $MnCo_2O_4$ coatings both sintered/reacted leading to a non-porous coating/spinel phase on the Cr_2O_3 surface. Note, however that there are indications of the $MnCo_2O_4$ coating not being as successfully sintered/reacted as the Co_3O_4 coating, see figure 3.5 and 3.6, and this will also be discussed in more detail in section 3.4.2.

The observed weight gain of the oxidized samples consisted of the oxygen uptake from the atmosphere during the oxidation process. However, if the coatings would contain “oxidizing agents”, these might create oxidation products on the coated

samples during the oxidation process without these being registered as a weight gain. The coatings that might be considered to contain such oxidizing agents are the LSM and LSC coatings. The LSM coating contains 10% extra Mn, which at atmospheric pressure at 900˚C exists as Mn_2O_3, cf. the Mn-O phase diagram in figure 3.8. When this manganese is reacting with Cr originating from the alloy to form a (Mn,Cr)-spinel it would lead to a reduction of the Mn. The $(La_{0.85}Sr_{0.15})MnO_3$ perovskite is stable during the same conditions and should not experience any dissociation. The $(La_{0.85}Sr_{0.15})CoO_3$ perovskite on the other hand would experience dissociation during the same conditions, and when Co reacts with Mn and Cr originating from the alloy, cobalt will be reduced and oxidation products will form, which will not be registered in the weight gain measurements.

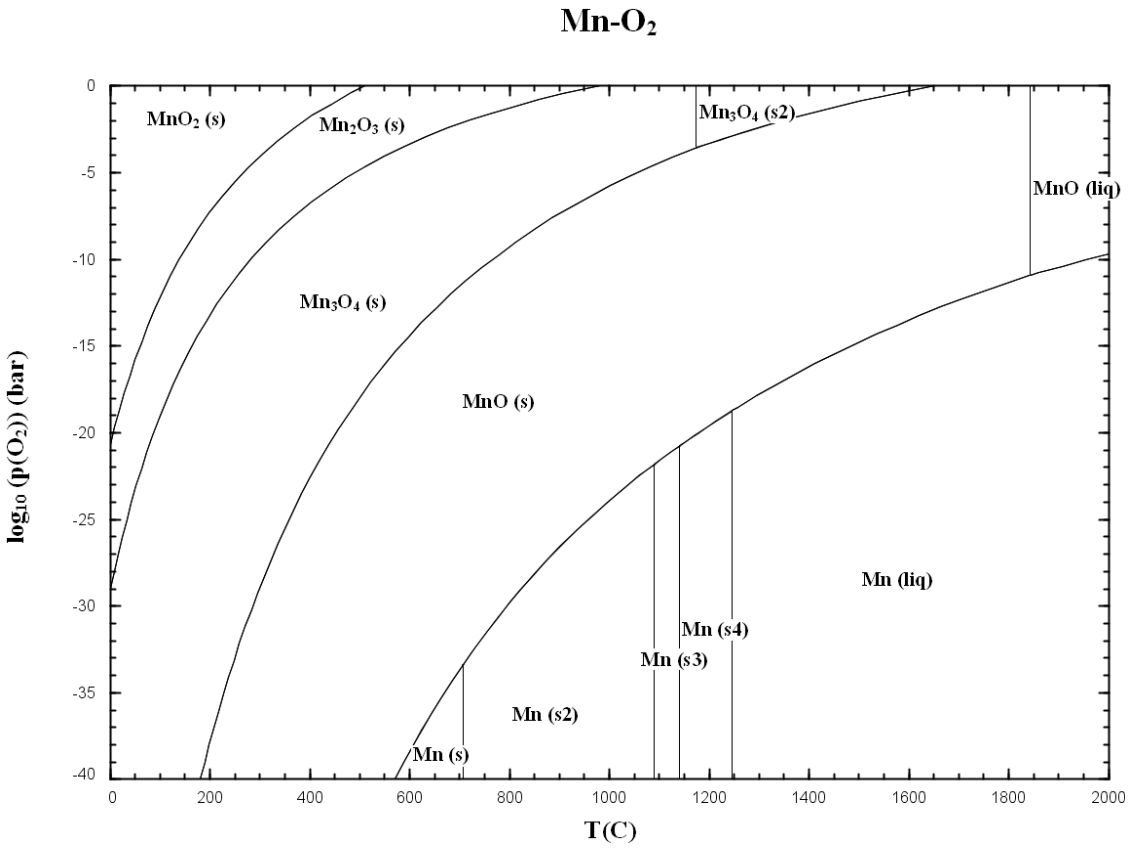

Fig. 3.8. Mn-O phase diagram [11].

3.3.2 EDS data

In figure 3.9 the line scans across the oxide scales on the oxidized samples after 2000 hours are presented.

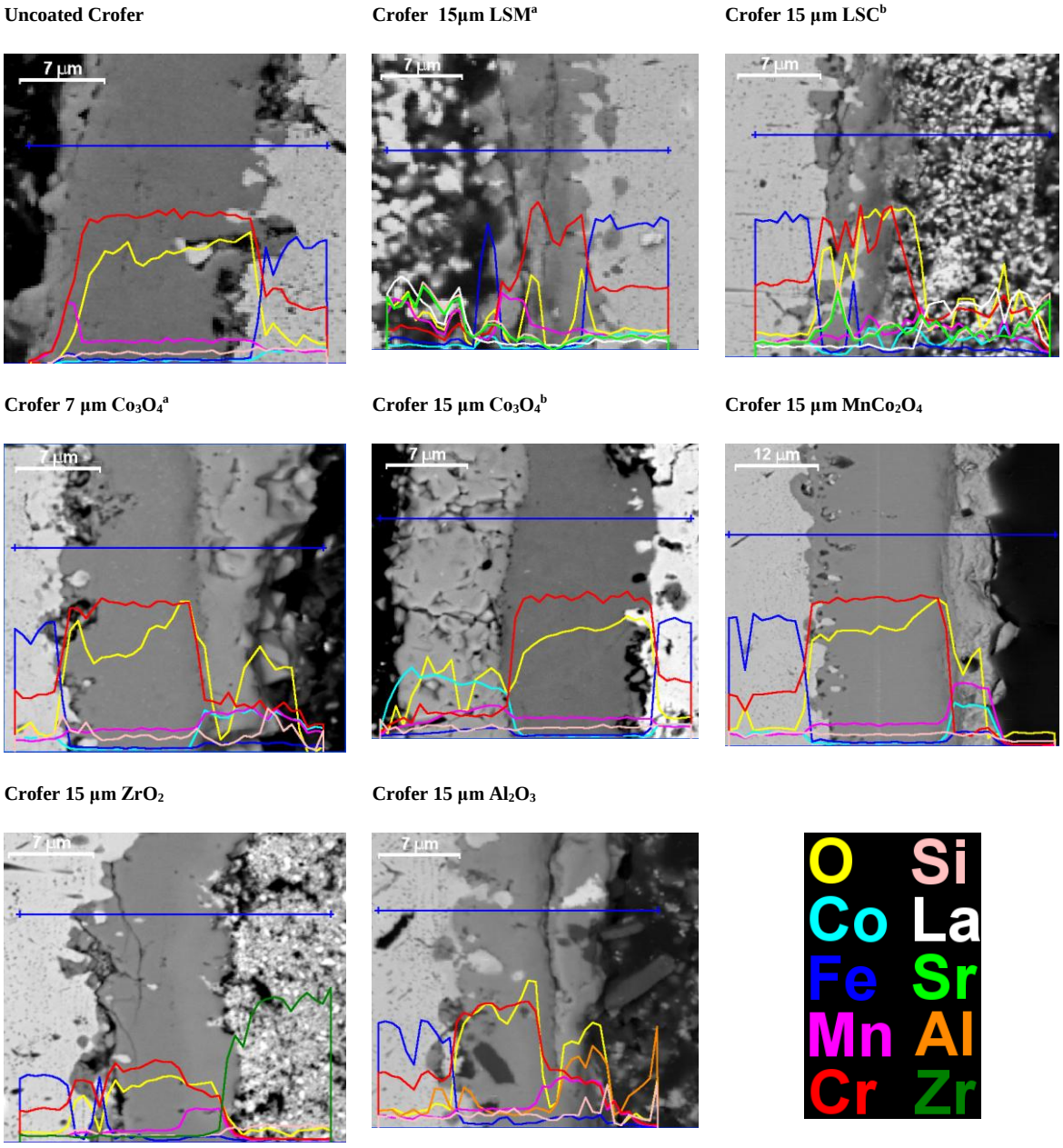

Fig. 3.9. Line scans over the oxide scales on the samples oxidized for 2000 hours.

In the line scans above it was found that the Si and Sr signal follow each other since the Si K_α peak and the Sr L_α peaks overlap. The increase in the signal in the oxide/alloy interface is attributed to the Si K_α peak, and the increase in the signal in the outer oxide scale and in the coating is assigned to the Sr L_α peak.

To determine more precise how much Cr is available in the outer part of the formed, dense oxide scale, point analysis was performed at several points in the outer oxide on all samples. In figure 3.4 in the micrographs of the LSM coated Crofer 22APU sample

oxidized for 1000 hours the area denoted the outer oxide scale is marked as a type example for uncoated, LSM, LSC, ZrO_2, and Al_2O_3 coated samples. For the Co_3O_4 and $MnCo_2O_4$ coated samples, where the coating has sintered/reacted with the forming oxide scale, the outer oxide scale corresponds to the outer part of the sintered/reacted coating layer. In the micrographs for Co_3O_4 and $MnCo_2O_4$ coated samples oxidized for 2000 and 500 hours respectively in figure 3.5 and 3.7 this outer oxide scale area is marked as type examples. This means that any Cr detected in the outer oxide scale on the spinel coated samples must have diffused through both the forming oxide scale and the sintered/reacted spinel coating. The chromium detected here must have diffused a longer distance on these samples compared to on the uncoated and the LSM, LSC, ZrO_2, and Al_2O_3 coated samples and naturally the chromium content is lowered. The cation compositions found in the outer oxide scale on all samples analyzed appear to fall within a spinel phase region according to the Cr-Co-Mn phase diagram in figure 3.10.

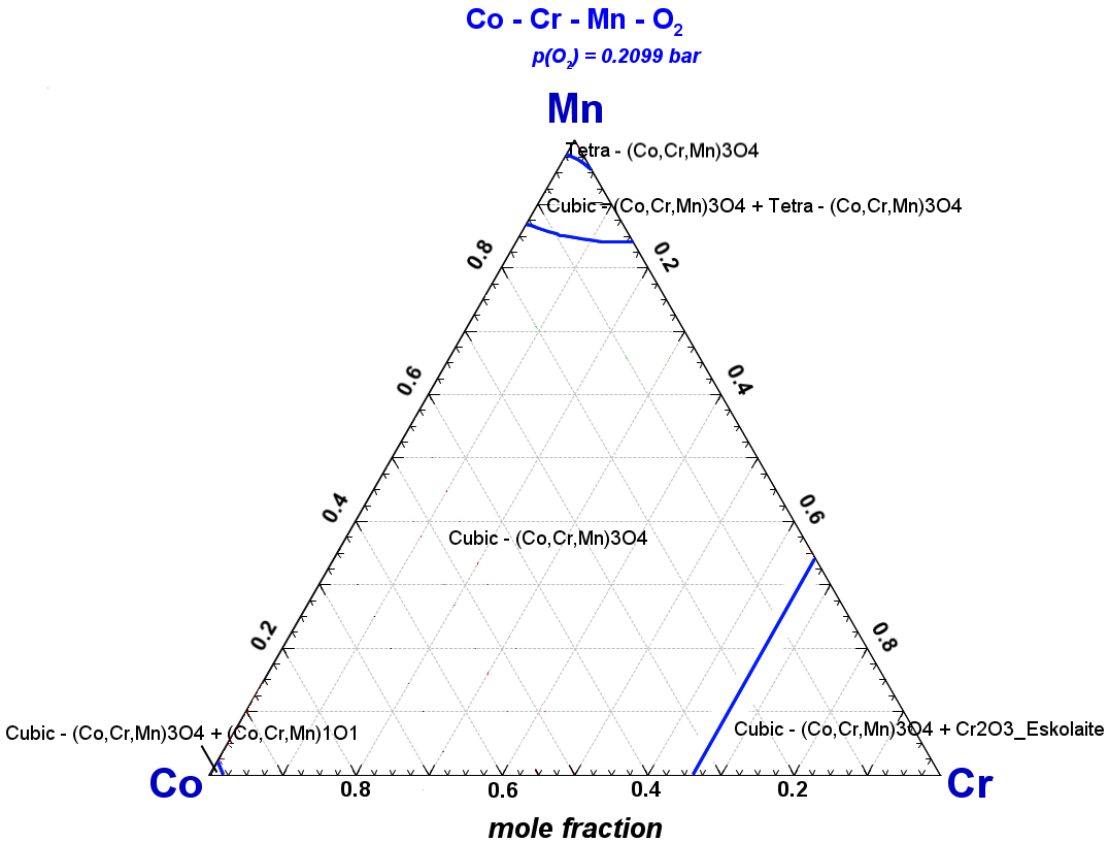

Fig. 3.10. Co-Mn-Cr-O phase diagram [11].

In figure 3.10 it is illustrated that at 900˚C a cubic $(CrMnCo)_3O_4$ spinel is stable with up to 100% cobalt, up to 90% manganese and up to 67% chromium. If the manganese content is above 90% both a cubic and a tetrahedral spinel phase are present. If the chromium content is above 67% the cubic spinel phase falls apart to a spinel phase plus a Cr_2O_3 phase. In table 3.2 below the calculated spinel compositions are listed, and as mentioned earlier they all fall within the stable cubic $(CrMnCo)_3O_4$ spinel composition except the oxide composition found on the Al_2O_3 coated sample oxidized for 4000 hours.

Table 3.2. Spinel composition in the outer oxide scale on the uncoated and coated Crofer samples oxidized in the long term cycling oxidation experiment.

	500 h				*1000 h*				*2000 h*				*4000 h*			
	Cr	**Mn**	**Co**	**Fe**	**Cr**	**Mn**	**Co**	**Fe**	**Cr**	**Mn**	**Co**	**Fe**	**Cr**	**Mn**	**Co**	**Fe**
Uncoated	1.9±0.1	1.1±0.1			1.6±0.2	1.4±0.2			1.7±0.3	1.2±0.4		0.1±0.0				
15 μm LSM[a]	1.4±0.1	1.5±0.1			1.5±0.2	1.4±0.2			1.6±0.2	1.3±0.2			1.6±0.1	1.3±0.1		
15 μm LSC[b]	1.4±0.5	0.6±0.3	0.9±0.2	0.1±0.0	1.5±0.4	0.5±0.2	0.9±0.2	0.1±0.1	1.3±0.4	0.7±0.4	0.9±0.1	0.1±0.1	1.6±0.3	0.5±0.2	0.8±0.1	0.1±0.1
7 μm Co_3O_4[a]	0.3±0.0	1.2±0.2	1.1±0.1	0.4±0.1	0.7±0.1	1.3±0.2	0.9±0.3	0.1±0.0	0.6±0.2	1.2±0.3	1.0±0.2	0.2±0.1	0.8±0.1	1.4±0.1	0.7±0.2	0.2±0.1
15 μm Co_3O_4[b]	0.6±0.1	0.2±0.1	2.1±0.1		0.6±0.1	0.4±0.1	2.0±0.1		0.4±0.1	0.3±0.2	2.2±0.2		0.7±0.3	0.4±0.2	1.9±0.2	0.1±0.0
$MnCo_2O_4$	0.1±0.0	1.2±0.1	1.6±0.2		0.1±0.0	1.3±0.2	1.6±0.2		0.2±0.1	1.3±0.2	1.4±0.2	0.1±0.1	0.5±0.1	1.1±0.1	1.3±0.1	0.1±0.0
ZrO_2					1.8±0.1	1.1±0.1			1.9±0.3	1.0±0.3			1.9±0.1	1.0±0.1		
									Cr	**Mn**	**Al**	**Fe**	**Cr**	**Mn**	**Al**	**Fe**
Al_2O_3									1.4±0.3	1.1±0.3	0.4±0.4	0.1±0.0	2.5±0.6	0.3±0.4	0.2±0.2	0.0±0.1

As shown in table 3.2 a composition close to $MnCr_2O_4$ is observed on the uncoated Crofer samples as expected [3, 10]. The presence of a LSM coating seems to repress the Cr content in the outer spinel in favour for Mn in comparison to the spinel composition found on uncoated Crofer samples. If the coating instead is LSC the same type of suppression of the Cr-content is found as for LSM coating, but the Cr amount is mainly decreased in favour for Co. Studying spinel composition in the outer oxide scale for Co_3O_4 coated samples it is seen that the Cr and Mn contents appear to be lower for the sample with the thicker Co_3O_4 coating layer. When comparing the Cr content in the outer part of the sintered/reacted spinel for Co_3O_4 coated and $MnCo_2O_4$ coated samples, it is found that the Cr content is lower for the $MnCo_2O_4$ coated samples. For the ZrO_2 coated samples the composition of the outer spinel is not much different from the spinel found on uncoated samples. For the Al_2O_3 coated sample oxidized for 2000 hours a spinel with about 40/60 Mn- and Cr-content is found with a slight addition of Al. On the Al_2O_3 coated sample oxidized for 4000 hours there is an oxide scale on the outside as well as on the inside of the iron chips, and the oxide scale observed on areas without any protruded metal chips to consider. The composition presented in table 3.2 is an average of all three types and indicates that the chromium content is significant. A (Mn,Cr)-spinel is observed in the oxide scale found on the areas without any protruded metal chips, and it appears similar to the spinel found on the Al_2O_3 coated samples oxidized for 2000 hours. The oxide scale on the outside of the protruded metal chips also consists of an outer (Mn,Cr)-spinel layer, while the oxide scale below the metal chip seems to mainly consist of chromia. Incorporated alumina particles are found in all three types of the oxide scale on the 4000 hours sample. The incorporated alumina particles are found both in the oxide scale outside and inside a metal chip and in the oxide scale along an alloy surface stretch without any metal chips. If the detected aluminium signal in the outer oxide scale is assumed to originate from incorporated Al_2O_3 particles, the remaining Cr- and Mn-signals give a spinel composition not far from the composition found on uncoated Crofer samples. The measurements made in the chromia rich oxide scale below metal chips are disregarded here.

Mappings are made on the oxide scales to get an overview of the composition of the scales. By combining the mapping signals from Cr, Mn, Co, La, Zr, and Fe an image where the spinel part of the oxide scale is fast and easily discerned form the chromia layer was achieved. On these mappings the relative areas of the spinel and chromia phases can be measured. In table 3.3 the spinel ratios of the oxide scales found for the different samples are presented.

Table 3.3. Spinel ratio of the total oxide scale on uncoated and coated Crofer samples oxidized at 900˚C in air containing 1% water.

	500 h	***1000 h***	***2000 h***	***4000 h***
Uncoated	0.15	0.09	0.10	
15 μm LSM[a]	0.41	0.35	0.43	0.39
15 μm LSC[b]	0.49	0.44	0.40	0.41
7 μm Co_3O_4[a]	0.33	0.34	0.26	0.09
15 μm Co_3O_4[b]	0.53	0.53	0.47	0.34
$MnCo_2O_4$	0.51	0.39	0.30	0.30
Al_2O_3			0.36	<0.20
ZrO_2		0.40	0.30	0.32

The results in table 3.3 clearly show that the presence of a coating increases the spinel ratio of the oxide layer. The Co_3O_4 and $MnCo_2O_4$ coated samples show high spinel ratios at least initially. However, it should be noted that the spinel phase on these samples consists of both sintered/reacted spinel coating and the forming spinel phase during the oxidation process. For the Al_2O_3 coated sample oxidized for 2000 hours a spinel ratio of about 35% is found. When considering the 4000 hours sample the spinel ratio was drastically decreased.

3.4 Discussion

3.4.1 Uncoated

During both the cyclic oxidation and the TGA experiment it was found that etched, uncoated Crofer presents parabolic oxidation behaviour in accordance with literature [3, 10]. After 1000 hours of oxidation at 900°C in air containing 1% water, break away oxidation is displayed by the weight increase plots. Even though the oxidation behaviour was found to be the same for the samples exposed to cyclic oxidation and samples oxidized in the TGA equipment, the samples oxidized in the TGA chamber presented an almost twice as big parabolic oxidation constant as the samples in the cyclic oxidation furnace. In the two oxidation experiments the same heating and cooling ramps, oxidation temperature, and inlet-atmosphere were used, meaning that there should not be any differences in the experimental setup between the cyclic oxidation experiment and the TGA experiment. The higher oxidation rate found in the TGA experiment could be due to faster initial oxidation behaviour that is not possible to capture in the cyclic oxidation experiment due to too few measurements points. A possible explanation could be that the spinel phase of the forming oxide scale was fast growing and dominated the oxide scale growth during the initial 250 hours. Considering the spinel ratios in table 3.3 it is observed that, even though the spinel ratio is relatively stable throughout the oxidation process, there is a small trend of higher spinel ratio after the first 500 hours in comparison to after 1000 and 2000 hours oxidation. This could support the hypothesis that the spinel growth dominates the initial oxidation. This fast spinel growth during the initial 250 hours oxidation should not be confused with the transient oxidation taking place during the very initial oxidation before a protecting oxide scale has formed and steady state parabolic kinetics have been established in the system. A second explanation to the difference in oxidation rate between the two oxidation experiments could be that the gas in the TGA chamber is totally exchanged twice as often during an hour as the gas in the cyclic oxidation furnace. This might create small differences in the water content in the oxidation atmospheres that might affect the oxidation rate.

In figure 3.11 a principle sketch of the diffusive fluxes during the oxidation of uncoated Crofer is presented.

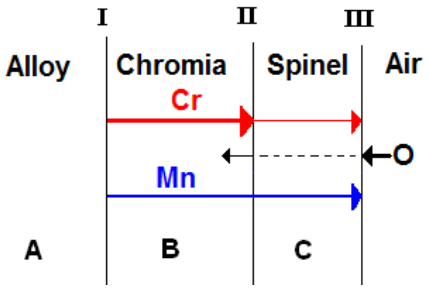

Fig. 3.11. Diffusion model of ions during oxidation of uncoated Crofer.

According to literature the chromia scale on chromia forming alloys grows through counter diffusion of Cr-cations and O-anions with formation of chromia within the chromia scale creating growth stresses which are relaxed via metal inclusions in the oxide [9]. However, the outward diffusing Cr-cations have been shown to be the dominating diffusion species during chromia formation. This should move the growth of the oxide phase closer to the chromia surface. As mentioned earlier and proven in this study, Crofer forms a (Mn,Cr)-spinel phase on top of the Cr_2O_3 scale. The oxygen lattice in spinel is presumed to be fully occupied, and no significant inward oxygen diffusion would be possible to take place since there are no vacancies available for the diffusion process. The presence of the outer spinel layer on oxidized uncoated Crofer should therefore shift the growth of the chromia scale further towards the chromia/spinel interface. However, in some places along the oxide scale on uncoated Crofer, the spinel layer might not be completely stable, continuous or thick enough making it possible for some inward oxygen diffusion to take place on the uncoated Crofer samples. This is noted in figure 3.11 by the dashed oxygen diffusion arrow through the spinel layer. The presence of inward anion diffusion on the uncoated samples is strongly indicated by the presence of metallic inclusions in the oxide scale formed to comply with growth stresses in the oxide caused by the oxide growth taking place within the scale. Alternatively, these metal inclusions may be caused by the thermal cycling, repeated cooling and heating, as a result of a mismatch between the thermal expansion coefficients of oxide and alloy [12]. The small differences in TEC value between the oxide scale and the alloy sample creates stresses in the alloy/oxide interface. To relieve these stresses the alloy might deform and metal inclusions are created in the oxide scale. The presence and growth of (Cr, Mn)-spinel on uncoated samples can only be explained by diffusion of Mn species through the chromia layer as indicated in the diffusion model in figure 3.11. Mn-diffusion through Cr_2O_3 is fast, faster than Cr-diffusion [13]. The presence of the spinel phase on top of the Cr_2O_3 scale ensures the oxygen pressure to be lowered above the Cr_2O_3 layer, and this probably makes the dominating point defect in the chromia phase to consist of cation interstitials [14]. The outward diffusing Cr^{3+} and Mn^{2+} ions are therefore probably diffusing along the grain boundaries in the chromia phase [13-15]. In the chromia/spinel interface the outward diffusing Cr-cations consume oxygen from the spinel phase to form chromia as described in reaction **II**a in table 3.4 below where the possible interface reactions in the growing oxide scale are summarized. When four new unit cells of chromia phase are formed during reaction **II**a three incomplete unit cells of spinel phase are consumed which should suggest that the **II**-interface in figure 3.11 is moving to the right due to reaction **II**a. Since Cr_2O_3 has higher density than $MnCr_2O_4$ there is a volume change in reaction **II**a that might create strains in the **II**-interface and indirectly lead to void formation in the **II**-interface ($\rho(Cr_2O_3)$ = 5.22

gcm^{-3} and $\rho(MnCr_2O_4)$ = 4.93 gcm^{-3} [16, 17]). In the micrographs for uncoated samples figure 3.4 voids can be observed in between the chromia and spinel phases.

As noted above Mn-cations diffuse faster through the chromia scale than the Cr-cations [13]. This would lead to a slight accumulation of Mn in the outer Cr_2O_3 layer that might favour transformation of Cr_2O_3 into $MnCr_2O_4$ with help from oxygen in incomplete spinel units as described in reaction **II**b. The reaction would result in formation of four new, complete spinel unit cells while three unit cells of chromia are consumed. This in turn would move the **II**-interface to the left in figure 3.11. In contrast to reaction **II**a the **II**b reaction might have tendency towards filling possible voids present in the **II**-interface.

A spinel phase might also form according to reaction **II**c in table 3.4. The Mn- and Cr-cations diffusing via interstitials in the chromia phase might react directly with the oxygen in an incomplete unit cell of spinel when reaching the **II**-interface. The **II**c reaction would not move the **II**-interface in any direction, and it would not result in any volume change since the cations simply fill out the vacancies in an incomplete spinel unit cell.

The spinel phase is exposed to atmospheric pressure, which suggests that the available point defects for cation diffusion in the spinel phase consist of cation vacancies [18-23]. The Mn- and Cr-cations are diffusing outward through the spinel phase while the vacancies, created at the spinel surface during oxygen uptake, are diffusing inward. This is described in reaction **III**a. The morphology of the scale on the uncoated samples in figure 3.4 supports the hypothesis that the oxide scale grows mainly by outward cation diffusion. The presence of SiO_2 filled coalesced Kirkendall voids at the alloy/chromia interface [24] and Kirkendall voids at the chromia/spinel interface is a sign of dominating outward cation diffusion.

Table 3.4. Interface reactions on uncoated Crofer with the reactions rates, *i*, and the changes in in number of unit cells in the chromia and spinel phase, $\Delta(B/C)$, where B and C refer to chromia and spinel phase, respectively.

Interface	***Reaction equation***	$\Delta(B)$	$\Delta(C)$	***i***
Ia	$Cr \rightarrow (Cr_I^{\bullet\bullet\bullet} + 3e^{'})_B$	0		i_{Ia}
Ib	$Mn \rightarrow (Mn_I^{\bullet\bullet} + 2e^{'})_B$	0		i_{Ib}
IIa	$8(Cr_I^{\bullet\bullet\bullet} + 3e^{'})_B + 3(2V_M^{'''} + V_M^{''} + 4O_O^x + 8h^{\bullet})_C \rightarrow 4Cr_2O_3$	4	-3	i_{IIa}
IIb	$4Cr_2O_3 + 4(Mn_I^{\bullet\bullet} + 2e^{'})_B + (2V_M^{'''} + V_M^{''} + 4O_O^x + 8h^{\bullet})_C \rightarrow 4MnCr_2O_4$	-4	3	i_{IIb}
IIc	$2(Cr_I^{\bullet\bullet\bullet} + 3e^{'})_B + (Mn_I^{\bullet\bullet} + 2e^{'})_B + (2V_M^{'''} + V_M^{''} + 4O_O^x + 8h^{\bullet})_C \rightarrow MnCr_2O_4$	0	0	i_{IIc}
IIIa	$6O_2 \rightarrow 3(2V_M^{'''} + V_M^{''} + 4O_O^x + 8h^{\bullet})_C$		3	i_{IIIa}

By using the reaction rates for each reaction listed in table 3.4, rate expressions for chromia and spinel phase growth can be formulated. These are displayed in table 3.5. These rate expressions connect the different reactions, but it is impossible to determine the relative rates of the three different reactions and which one is dominating based on the observations made in this chapter. The system is too complex.

Table 3.5. Total rate expressions for chromia and spinel phase formation in the oxide scale growing on oxidizing, uncoated Crofer based on interface reactions listed in table 3.4.

Phase	***Rate expression***
Chromia	$i_{Cr_2O_3} = 4i_{II,a} - 4i_{II,b}$
Spinel	$i_{MnCr_2O_4} = 3i_{II,b} - 3i_{II,a} + i_{II,c}$

3.4.2 Co_3O_4 and $MnCo_2O_4$ coatings

The spinel coated steels showed parabolic oxidation behaviour up to ca 1000 hours of oxidation, where after the $MnCo_2O_4$ coated samples experienced break away oxidation just as uncoated Crofer, see figure 3.1b. The Co_3O_4 coated samples on the other hand continued to present parabolic oxidation behaviour during the whole 4000 hours cyclic oxidation process, and with a lower parabolic rate constant than uncoated Crofer. The positive effect of a porous Co_3O_4 coating on decreasing the oxidation rate of a Fe-22Cr alloy during oxidation at 900˚C has been observed before [25]. For the Co_3O_4 coated samples it was also found that based on weight gain data an increased coating thickness decreased the oxidation rate. The micrographs in figure 3.5-6 show that both the Co_3O_4 coating and the $MnCo_2O_4$ coating in principle have sintered/reacted already after 500 hours of oxidation.

The differences in the effect of the Co_3O_4 and the $MnCo_2O_4$ coatings on the oxidation rate should be found in the different properties of the spinel phases formed in the presence of the two coatings, and the conditions the Co_3O_4 and $MnCo_2O_4$ coatings enforce on the oxidation process. Four significant properties and conditions important for the effect of the coating and the corrosion rate are:

- The $\Delta\mu_{Mn/Cr}$ established across the Cr_2O_3 scale
- The relative density, ρ, of the formed spinel phase
- Number of grain boundaries in the formed spinel phase
- The effective diffusion coefficients for Mn-, Cr-, Co-, and O-ions through the formed spinel phase

For the Co_3O_4 coated samples the concentration profile of Mn- and Cr-cations across the chromia scale is the same as for uncoated Crofer since no addition of the two cations are made on the outside of the chromia layer. The spinel phase in the oxide scale consists of the formed spinel and the sintered/reacted Co_3O_4 coating and it appears to be relatively dense in the micrographs in figure 3.5. This might partly be explained by the $Co_3O_4 \rightarrow CoO$ phase transition the Co_3O_4 coating undergoes at around 900˚C [25-30]. The phase diagram for Co-O is presented in figure 3.12 below.

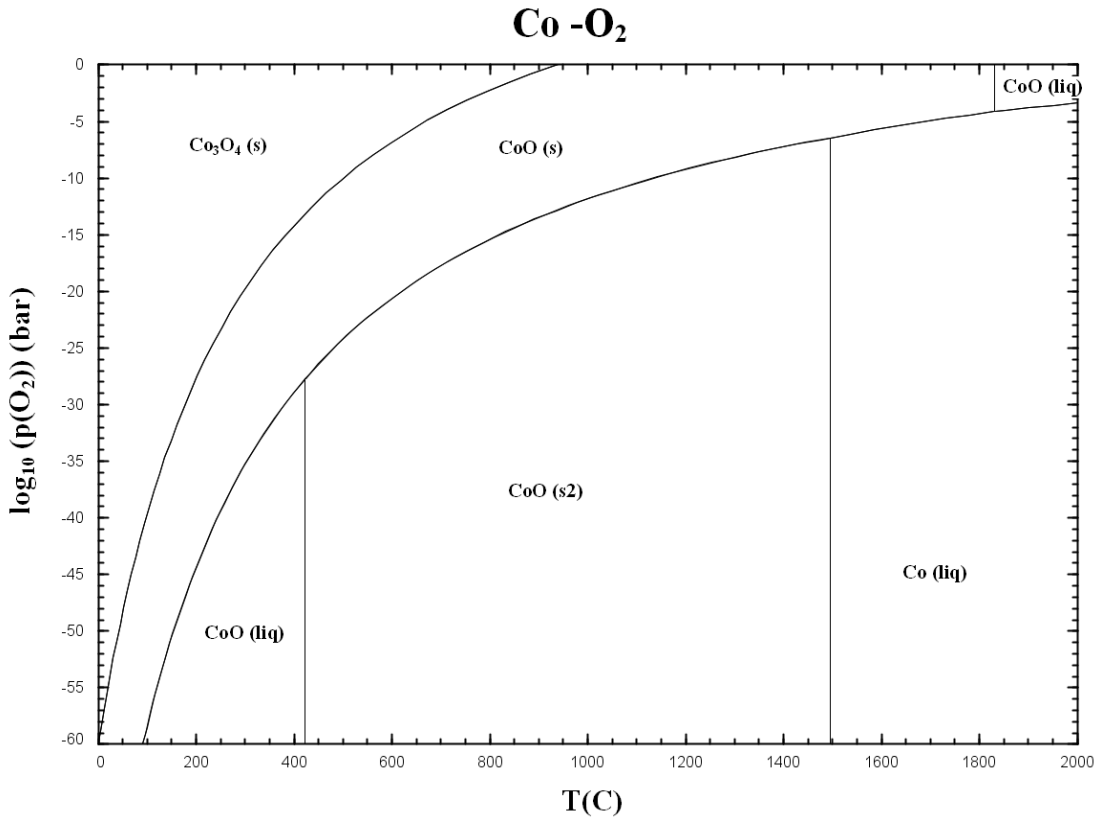

Fig. 3.12. Co-O phase diagram [11].

The Co_3O_4 → CoO phase transition involves a volume change that based on crystal parameter data should be a volume decrease [16]. When outward diffusing Mn- and Cr-ions reaches the CoO phase, a spinel phase is reformed and the volume of the coating layer is once again increased [16]. Due to the volume decrease during the Co_3O_4 → CoO phase transition a denser spinel layer than the original Co_3O_4 layer might form during the reformation of the spinel phase. Z. Yang, G. Xia, and J. W. Stevenson also used a change in volume to densify a $Mn_{1.5}Co_{1.5}O_4$ coating on Crofer 22APU alloy through heat treatment in reducing atmosphere before oxidizing the samples at 800˚C in air [31, 32]. However, dilatometery experiment show in contrast large expansion when heating Co_3O_4 to the phase transition temperature [33] suggesting that the CoO phase formed from heating of Co_3O_4 exhibits pore and/or cation vacancies. The explanation to why a denser spinel layer than the originally applied Co_3O_4 may instead be the larger driving force for the reaction with outward diffusing Cr- and Mn-cation and a CoO phase (the change in Gibbs free energy forming (Mn,Cr,Co)-spinel is larger when the starting point is CoO rather than Co_3O_4). Perhaps the highly defect nature of the CoO phase (possible pores and cation vacancies) somehow favours formation of a more dense layer. The exact temperature for the Co_3O_4 → CoO phase transition is slightly varying in literature, 922˚C according to a study by X. Liu *et* al. [29], 907˚C according to a study by H. St. C. O'Neill *et* al. [34], ca. 900˚C according to a study by G. M. Kale *et* al. [27], and ca. 897˚C according to a study by Sreedharan *et* al. [30]. Due to this it is difficult to be certain that the phase transition has taken place during the 900˚C oxidation in this study. Also there is a temperature variation of about 3-4˚C in the oxidation furnace during the cyclic oxidation experiment performed in this study which suggests that the

temperature needed for the phase transition to take place might not be reached all over the surface of all the Co_3O_4 coated samples mounted in the oxidation furnace. But assuming that a temperature high enough is reached for the $Co_3O_4 \rightarrow CoO$ phase transition to take place it is most likely that the CoO-phase is transformed back to a spinel phase rather quickly due to the outward diffusing Mn- and Cr-ions. The (Mn,Cr,Co)-spinel formed will not be able to undergo any phase transition at the oxidation temperature as long as the manganese and chromium contents do not reach too high values as can be seen in the Cr-Mn-Co-O phase diagram in figure 3.10. The spinel compositions listed in table 3.2 show that the spinel composition is well inside the area for stable cubic spinel phase on the Co_3O_4 coated samples. This suggests that the chromia scale established on the alloy surface due to oxidation will be interacting with a spinel phase during the rest of the oxidation process. This leads to the interface reaction between the forming oxide scale and the applied coating on Co_3O_4 coated Crofer samples to be similar to the interface reactions observed on uncoated Crofer, see table 3.4. But in the spinel layer consisting of the forming spinel and the sintered/reacted residues of the Co_3O_4 coating a concentration profile of Co is established, inducing inward diffusion of Co in the spinel phase via cation vacancies. Line scans across the oxide scales confirm the presence of the Co-concentration profile as seen in figure 3.9. The Co-cations might to some degree continue to diffuse into the chromia phase as illustrated via a dashed line in figure 3.13 which is a sketch over the possible diffusive fluxes on the Co_3O_4 coated samples.

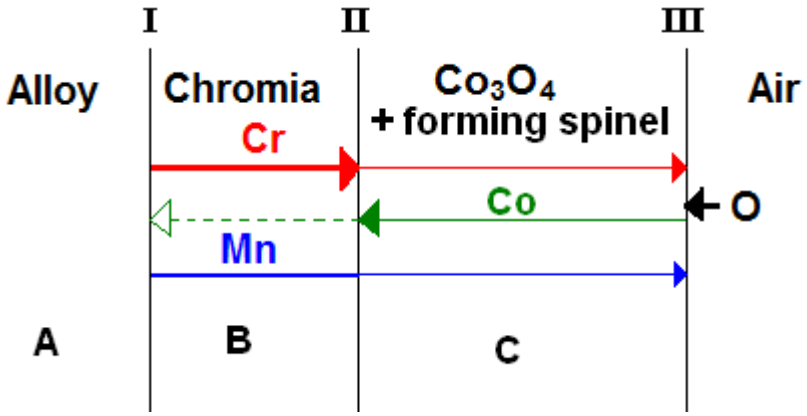

Fig. 3.13. Diffusive fluxes of ions during oxidation of Co_3O_4 coated Crofer.

The Co-content in the spinel phase makes a fourth interface reaction in interface **II** possible when cobalt containing spinel phase reacts with chromia. In table 3.6 below a type example of such a reaction is listed.

Table 3.6. The extra interface reaction at interface **II** on Co_3O_4 coated Crofer.

Interface	***Reaction equation***	$\Delta(B)$	$\Delta(C)$	***i***
IId	$12Cr_2O_3 + 8Cr_{0.6}Mn_{1.2}Co_{1.2}O_4 \rightarrow$ $16Cr_{1.8}Mn_{0.6}Co_{0.6}O_4 + (2V_{Cr}^{'''} + V_{Mn}^{''} + 4O_O^x + 8h^{\bullet})$	-4	3	i_{IId}

In the figure 3.1 and table 3.1 it is illustrated that a thicker layer of the Co_3O_4 coating reduced the oxidation rate. According to table 3.2 the chromium and manganese content in the outmost spinel phase are slightly lowered for a thicker Co_3O_4 coating layer. This could be due to the longer diffusion distance for the outwardly diffusing cations and inwardly diffusing vacancies that is a consequence of the thicker Co_3O_4 layer, which in turn leads to a lowered oxidation rate. A second explanation could be that the larger amount of Co present in the spinel phase has the effect of reducing the effective diffusion of chromium in the layer and therefore both the chromium content in the outmost spinel phase is lowered and the oxidation rate is decreased.

The $MnCo_2O_4$ coating increased rather than decreased the oxidation rate of the Crofer samples when comparing the weight gain and the parabolic rate constants for uncoated and $MnCo_2O_4$ coated Crofer samples in figure 3.1 and in table 3.1, respectively. Considering the micrographs in figure 3.6 and the measured scale thicknesses in table 3.1 the $MnCo_2O_4$ coating appeared to enhance the growth rate of the Cr_2O_3 scale.

The diffusion and interface reaction conditions on the $MnCo_2O_4$ coated sample are as on the Co_3O_4 coated samples assumed to be similar to the ones found on uncoated Crofer however with some modifications. In figure 3.14 a sketch over the diffusive fluxes likely to occur in the parabolic oxidation process of $MnCo_2O_4$ coated samples are presented.

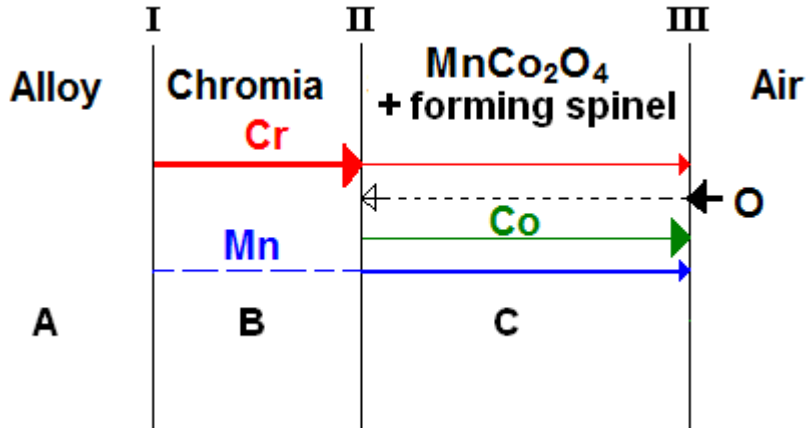

Fig. 3.14. Diffusive fluxes of ions during oxidation of $MnCo_2O_4$ coated Crofer.

The possible interface reactions on the $MnCo_2O_4$ coated samples are believed to be the same as those on uncoated Crofer plus the extra **II**d interface reaction in table 3.4 and 3.6. However, instead of decreasing the oxidation rate the interface reaction on the $MnCo_2O_4$ coated samples increases the oxidation rate of the Crofer alloy. The list of significant properties and conditions that should be important for the effect of the coating and the corrosion rate described above first mentions the concentration profile of Mn and Cr across the chromia scale. Due to the presence of the $MnCo_2O_4$ coating the concentration profile of Mn across the chromia scale is decreased while the concentration profile of Cr has not changed. Also mentioned on the list is the relative density of the spinel phase and the number of grain boundaries in the spinel phase. In the micrographs in figure 3.5 and 3.6 the spinel phase on the $MnCo_2O_4$ coated

samples seems slightly less dense than for example the phase observed on the Co_3O_4 coated samples discussed above. In figure 3.15 the micrographs of the $MnCo_2O_4$ and Co_3O_4 coated samples oxidized for 4000 hours are magnified, and it is possible to see that the areas between cracks in the spinel phase on the Co_3O_4 coated samples has an even and dense surface. On the corresponding areas on the $MnCo_2O_4$ coated samples wrinkles and small holes are visible as shadows on the micrograph. In the spinel phase/chromia phase interface, that is interface **II**, large holes shaped after the chromia scale surface and the spinel crystals in the spinel scale are observed on the $MnCo_2O_4$ coated samples. Tendencies towards the same type of holes can be seen in interface **II** on the Co_3O_4 coated samples, but these are smaller and tend to be relatively well filled out with smaller spinel crystals.

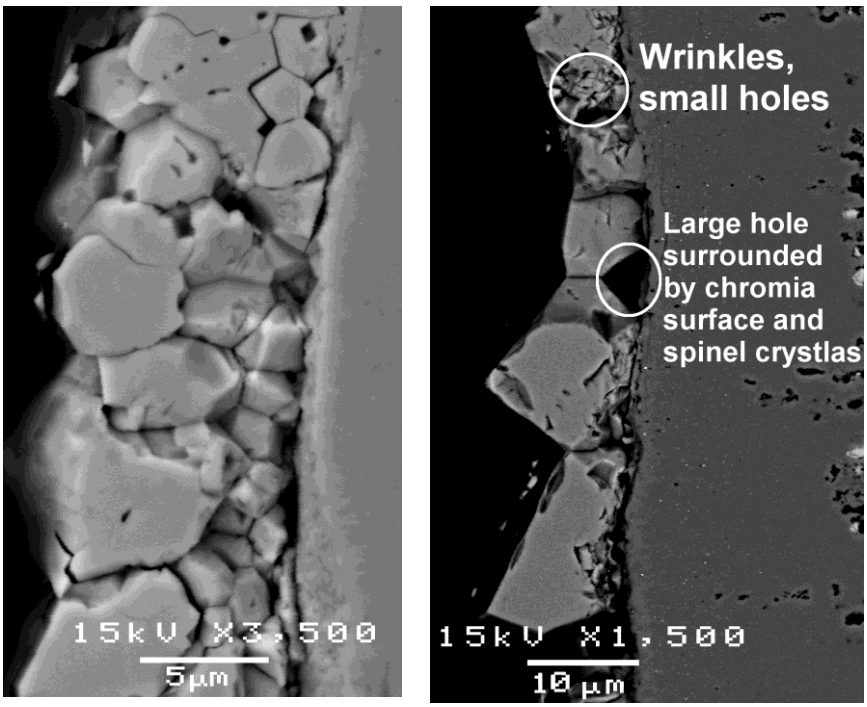

a b

Fig. 3.15. The a) 15 µm Co_3O_4 and b) $MnCo_2O_4$ coated Crofer 22APU samples oxidized for 4000 hours in air containing 1% water at 900˚C.

The slightly larger amount and size of holes and cracks in the spinel phase on the $MnCo_2O_4$ coated samples might be caused by the fact that the $MnCo_2O_4$ coating does not undergo any densifying phase transition as the Co_3O_4 coating does. The larger amount of grain boundaries, cracks etc. would be fast and easy diffusion paths for inward diffusing oxygen and a fifth interface reaction at interface **II** might be taking place where oxygen is directly reacting with chromium cations at the chromia surface, or slightly within the chromia phase as described in table 3.7. This chromia formation might induce stresses in the oxide scale due to uneven growth which would create more cracks and easy diffusion paths for inward diffusing oxygen. If the spinel phase on the $MnCo_2O_4$ coated samples also possesses a significantly high surface diffusion of oxygen along open grain boundaries the effect of the more numerous grain boundaries would be even more reinforced.

Table 3.7. The extra interface reaction at interface **II** on $MnCo_2O_4$ coated Crofer.

Interface	*Reaction equation*	$\Delta(B)$	$\Delta(C)$	*i*
IIe	$4(Cr_i^{\bullet\bullet\bullet} + 3e^{'})_B + 3O_2 \rightarrow 2Cr_2O_3$	2		i_{IIIe}

It is also possible that the Mn- and Co-cations in the spinel phase on the $MnCo_2O_4$ coated samples have a significantly higher mobility which would suggest that the effective inward oxygen diffusion as a consequence of the cation vacancy transport described in reaction **II**a and **III**a in table 3.4 in the spinel phase is fast and feeds the growth of the chromia phase below. The Mn- and Co-cations would have to diffuse outward towards the oxide surface as illustrated in figure 3.14 to provide interface **II** with oxygen. This last explanation to the bad oxidation protection of the $MnCo_2O_4$ coating gives the following three possible explanations:

- Formation of numerous cracks and grain boundaries in the spinel phase
- Fast surface diffusion in grain boundaries
- High cation mobility in the spinel phase leading to fast inward transport of oxygen

A fourth explanation, not listed here, explaining the increased oxidation rate on the $MnCo_2O_4$ coated Crofer samples compared to uncoated Crofer samples cannot be ruled out.

The heavy edge oxidation observed on the edges of the $MnCo_2O_4$ coated sample oxidized for 2000 and 4000 hours in figure 3.6 might explain the observed break away oxidation behaviour after 1000 hours oxidation. For chromia forming alloys where the chromium content in the alloy drops below 16 wt.% due to consumption of the chromium during chromia scale formation, iron will start to oxidize. EDS measurements in the alloy just below the oxidized area on the sample's edges show a chromium content even below 10 wt.% at some places close to the heavy oxidized areas, and the oxide within the residues of the earlier formed chromia scale contains high amounts of iron. Just a few microns away from the heavily oxidized areas the chromium content is again established on a level high enough to favour chromia formation. The reason why these heavy oxidation areas are taking place at specifically the sample's edges is probably because this is where the oxygen exposed area per bulk sample is the largest, making chromium depletion the most likely here. The geometry of the samples at the corners further favours a detachment of the oxide scale here. As seen in table 3.1 the oxide scales on the $MnCo_2O_4$ coated samples are the thickest ones in the study. The thicker the oxide scale gets the higher the risk of stress induced break away oxidation [9].

3.4.3 LSM coating

Based on the weight gain data collected the LSM coated Crofer samples presented parabolic oxidation behaviour with a parabolic rate constant six times lower than the rate constant found for uncoated Crofer. As can be observed in the micrographs in figure 3.4 the LSM coating giving this effect was porous. An estimation of the porosity of the LSM coating based on the micrographs gives a value of ca 30% with pore sizes of ca. 1 µm. This suggests that during oxidation unlimited access to oxygen is to be expected at the surface of the forming oxide scale. A second observation supporting this statement is that samples coated with 15 µm LSM had the same parabolic rate constant as samples coated with 30 µm LSM. If an oxygen access at the surface of the growing oxide scale would have been affected by the presence of the

LSM coating a thicker LSM coating should have resulted in a lower oxidation rate due to the longer diffusion distance. After establishing the free access to oxygen at the oxide surface a sketch over the likely diffusive fluxes in the oxide scale on LSM coated Crofer samples could be assembled, and it is presented in figure 3.16.

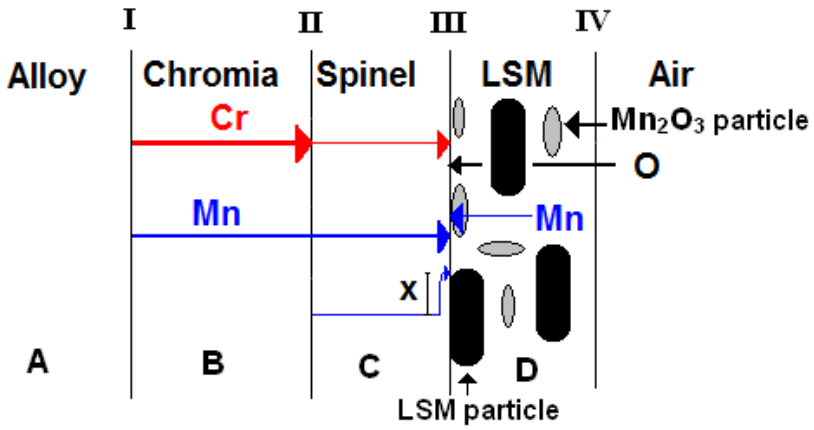

Fig. 3.16. Diffusive fluxes during oxidation of LSM coated Crofer.

The interface reactions taking place on the LSM coated Crofer samples are assumed to be similar to the interface reactions on the uncoated Crofer listed in table 3.4 and the extra **II**-interface reaction in table 3.6 above. Just as for uncoated Crofer there is grain boundary diffusion of Mn- and Cr-cations through the chromia scale. At interface **II** Cr_2O_3 is formed by consuming oxygen from the oxygen lattice in the neighbouring spinel. The formed Cr_2O_3 phase can be transformed into $MnCr_2O_4$ according to reaction **II**b, or outwardly diffusing Cr- and Mn-cations might directly form a spinel phase by filling up an incomplete unit cell consisting of oxygen and cation vacancies as described in reaction **II**c. The Cr_2O_3 phase might also react with the spinel phase according to reaction **II**d creating a spinel phase with higher chromium content. The Mn- and Cr-cations continue to diffuse outward through the spinel phase via cation vacancies formed on the spinel surface according to reaction **III**a. At interface **III** the growing oxide scale also reacts with the LSM coating. As mentioned in section 3.3.1 above it is the Mn_2O_3 phase in the coating that reacts with the growing oxide scale, and the thermodynamically stable $(La_{0.85}Sr_{0.15})MnO_3$ perovskite particles are pushed in front of the oxide scale as seen in figure 3.4. The Mn_2O_3 phase is probably present as particles spread out in the LSM coating and they are illustrated in figure 3.16 as smaller, greyish particles. It is probably the Mn_2O_3 particles placed next to the alloy/oxide surface that will contribute to the interface reaction. The oxidation number for the Mn-cation in the Mn_2O_3 phase is +3 while it is $+2\frac{1}{3}$ in the $Cr_{1.5}Mn_{1.5}O_4$ spinel found on the LSM coated sample according to the spinel compositions listed in table 3.2 for LSM coated samples. Since the Mn-content is ca. 17% higher in this spinel phase than in the $MnCr_2O_4$ spinel phase found on uncoated Crofer sample, it is suggested that the extra Mn is originating from the LSM coating. When the Mn_2O_3 phase is reacting with the outer spinel layer on the growing oxide scale to form the spinel composition seen in table 3.2, the Mn-cations from the Mn_2O_3 might contribute with oxygen to the oxide scale growth that will not be registered in the weight gain of the oxidizing sample. The reaction between the $MnCr_2O_4$ spinel on the alloys sample and the Mn_2O_3 is described in table 3.8 below.

Table 3.8. The extra interface reaction at interface **III** on LSM coated Crofer.

Interface	***Reaction equation***	$\Delta(C)$	$\Delta(D)$	***i***
IIIb	$6(Mn_2O_3)_D + 12(MnCr_2O_4)_C \rightarrow 16(Mn_{1.5}Cr_{1.5}O_4)_C + O_2$	4	-6	i_{IIIb}

In appendix 3 the effect of oxygen uptake from the coating on the weight gain is calculated. In figure 3.17 the weight increase-time$^{1/2}$ plot for the single coated Crofer samples are presented together with the calculated theoretical weight gain curve for the LSM coated Crofer sample. The calculated theoretical weight gain, where the oxygen uptake from the coating is incorporated, for the LSM coated sample is mistakable similar to the actually measured weight gain.

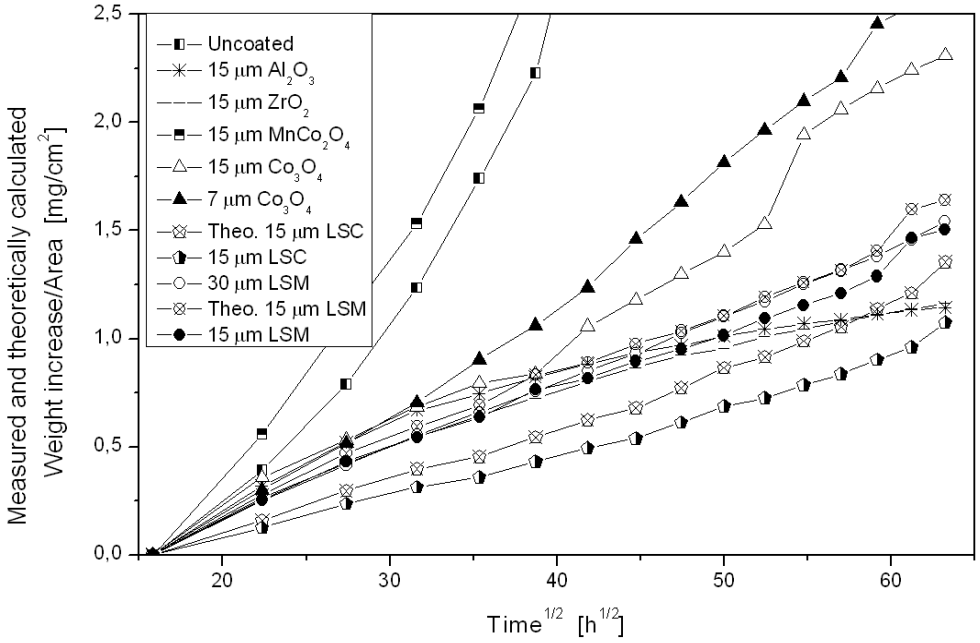

Figure 3.17. The measured weight gain for the uncoated and single layer coated Crofer samples and the theoretically calculated weigh gain for the LSM and LSC coated Crofer samples in the long term, cyclic oxidation experiment at 900˚C in air containing 1% water plotted against time$^{1/2}$.

After the Mn_2O_3 phase has transformed into a spinel phase the spinel composition changes in the oxide scale due to diffusion processes.

The extra uptake of Mn from the LSM coating leads to a decreased chromium content in the outer spinel phase compared to uncoated Crofer. The chromium content did however increase as oxidation proceeded, indicating continued outward chromium diffusion. The presence of the LSM coating also increased the spinel ratio in the oxide scale to ca. 40% in comparison to ca. 10% on uncoated Crofer. Furthermore, fewer metallic inclusions in the chromia layer on the LSM coated samples are observed, when comparing the microstructure of the oxides formed on uncoated samples and on

LSM coated samples. The increase of the relative thickness of the spinel layer would be consistent with a net flux of Cr species from spinel into LSM and/or the contribution of Mn from LSM to spinel development. The thicker spinel layer on the LSM coated samples would reinforce the ability to hinder inward oxygen diffusion in the oxide scale. This would reduce the overall oxidation rate and the oxidation process becomes more controlled by outward cation diffusion. The reduced number of metallic inclusions in the coated samples could be an indication on this.

In figure 3.16 the thermodynamically stable $(La_{0.85}Sr_{0.15})MnO_3$ particles are illustrated by the larger, black figures in phase D. During the initial stages of the oxidation these $(La_{0.85}Sr_{0.15})MnO_3$ particles will implement a geometrical protection against oxidation. The outwardly diffusing cations will be forced to diffuse an extra distance, x, along the particle to reach the oxide surface and accessible oxygen which is illustrated in figure 3.16 as well. The effect of the geometrical protection of the coating particles on the surface will slowly loose its importance as the thickness of the oxide scale grows larger than the diameter of the coating particles, and the extra diffusion distance implemented by the coating particles on the oxide surface is negligible compared to the total diffusion distance through the oxide scale.

TGA measurements on LSM coated Crofer resulted in a parabolic rate constant four times higher than the parabolic rate constant calculated from the recorded weight gain in the cyclic oxidation experiment. The parabolic rate constant for uncoated Crofer samples was also found higher in the TGA measurements compared to the cyclic oxidation experiment. Here the rate constant was only twice as high, and it could be that a fast spinel formation during the initial oxidation stage could explain the difference in rate constant from the TGA experiment and the cyclic oxidation experiment. A second explanation could be a difference in water content in the oxidation atmospheres. However, the first explanation involving the initial fast spinel formation is supported by the fact that the weight gain rate is increased twice as much for the LSM coated sample compared to the uncoated sample in the TGA experiment. It is observed that the LSM coated samples have a higher spinel ratio than the uncoated ones in table 3.3, which might be caused by the extra access to Mn from the coating. If a fast spinel formation exists during the initial oxidation it is quite likely that this spinel formation would be even faster on the LSM coated sample due to the larger ability to form spinel

To summarize, the LSM coating decreased the oxidation rate, increased the spinel ratio in the oxide scale and decreased the chromium content in the outer oxide scale. Studying the microstructure of the oxide scale both the chromia and spinel phase appeared to have high density, even higher than the density observed for the oxide phases on Co_3O_4 coated samples. The bright LSM coating particles were also observed to remain on the oxide surface during the whole oxidation process being pushed in front of the growing oxide scale. At the same time the excess Mn in the LSM coating is chemically changing the chemical composition of the growing oxide scale.

3.4.4 LSC coating

The LSC coated Crofer samples presented parabolic oxidation behaviour with a parabolic rate constant 18 times lower than the corresponding rate constant for uncoated Crofer. The scale thicknesses displayed in table 3.1 also showed that the

scale on the LSC coated samples was clearly thinner compared to uncoated Crofer. Comparing the microstructures of the oxide scales on the two perovskite coated samples it is seen that the alloy/oxide interface is smoother on the LSM coated sample than on the LSC coated samples. For the LSC coated sample there are also bright $LaCrO_3$ and $SrCrO_4$ containing areas within the oxide scale, mainly in the spinel layer. These bright particles originate from the LSC coating. Also visible in the micrographs in figure 3.4 is that the LSC coating is porous and should not create any hindrance for oxygen diffusion to the surface of the forming oxide scale. During the oxidation process, oxide products form in the LSC coating that might create a geometrical blockage against O_2 penetration. However, based on the appearance of the LSC coatings in the micrographs in figure 3.4, the porosity of the LSC coating is not decreased enough during the oxidation process to significantly limit the oxygen penetration. The outmost part of this forming oxide scale, which is assumed to consist of a spinel phase, had chromium content almost as high as the corresponding spinel phase on the LSM coated samples. But, the Mn content was decreased in favour for Co in the spinel on the LSC coated samples. The area ratio of this spinel phase on the LSC coated sample was almost 50% after the first 500 hours of oxidation. As oxidation proceeded the spinel ratio decreased to ca. 40% after 4000 hours oxidation. Based on these observations plausible diffusive fluxes are illustrated in figure 3.18.

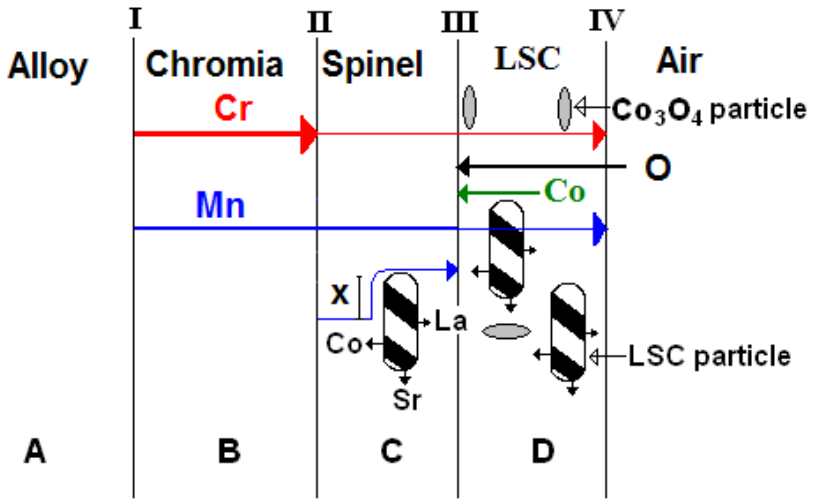

Fig. 3.18. Diffusive fluxes during oxidation of LSC coated Crofer.

The interface reactions are assumed to be similar to the ones listed for uncoated Crofer in table 3.4 and the extra **II**-interface reaction in table 3.6 when the spinel phase has another composition than the on Crofer naturally forming $MnCr_2O_4$. Cr and Mn diffuse through the Cr_2O_3 scale via the grain boundaries, and at interface **II** a Cr_2O_3 phase is formed according to reaction **II**a and a spinel phase according to the reactions **II**b and/or **II**c and/or a version of **II**d. The manganese uptake in the spinel might be slightly hindered owing to the presence of Co in the spinel phase. At interface **III** oxygen uptake is taking place. One possible reaction would be reaction **III**a in table 3.4. A second interface reaction at interface **III** might include oxygen uptake from the LSC in contact with the (Cr,Mn)-oxide. The $(La_{0.85}Sr_{0.15})CoO_3$ perovskite is not thermodynamically stable at the oxidation conditions and dissociates into $LaCrO_3$, $SrCrO_4$ and (Co,Cr,Mn)-spinel in contact with outward diffusing chromium and manganese ions. The Co-cations in the LSC perovskite are reduced

during this dissociation/reaction and might therefore contribute with oxygen originating from the coating to the oxide scale growth. In table 3.9 a type reaction of the dissociation and reaction between the $MnCr_2O_4$ spinel phase and the $(La_{0.85}Sr_{0.15})CoO_3$ perovskite is suggested.

Table 3.9. The extra interface reaction at interface **III** on LSC coated Crofer.

Interface	***Reaction equation***	***i***
IIIc	$40(La_{0.85}Sr_{0.15})CoO_3 + 40MnCr_2O_4 + 3O_2 \rightarrow 34LaCrO_3 + 6SrCrO_4 + 40CrMnCoO_4$	i_{IIIc}

In appendix 3 calculation of possible oxygen contribution form the LSC coating to the growth of the oxide scale are presented. In figure 3.17 both measured and theoretically calculated weight increase data for LSC coated Crofer samples is presented. It is shown that only minor changes, almost negligible, in the order of precedence in the weight gain of the oxidized samples are observed when considering the calculated theoretical weight gain for the LSC coated sample. That is the oxygen uptake from the LSC coating instead of the atmosphere is not a significant effect on the lowered oxidation rate.

When the LSC coating dissociate and reacts into $LaCrO_3$, $SrCrO_4$ and (Co,Cr,Mn)-spinel via reaction with outward diffusing chromium and manganese, the thermodynamically stable $LaCrO_3$ and $SrCrO_4$ particles appear to be incorporated into the growing oxide scale. The incorporated $SrCrO_4$ and $LaCrO_3$ particles would provide a geometrical protection against oxidation, since outward diffusing Mn- and Cr-cation are forced to diffuse an extra distance, x, around them as illustrated in figure 3.18 to reach the oxide surface. This geometrical hindrance for oxidation will not become negligible after the oxide scale has grown thicker than the diameter of the incorporated particles as was the case for the geometrical protection provided by LSM coating particle on the surface of the growing oxide scale. As the oxide scale grows thicker, more coating particles will become incorporated and the extra diffusion distance, implemented by their presence, will be of the same dimension as the thickness of the oxide scale. However, as seen in figure 3.4 there are still coating particles present on the surface of the oxide scale also providing a geometrical protection just as the LSM coating particles did.

The spinel phase on the LSC coated samples appeared denser than the spinel phases on the Co_3O_4 and $MnCo_2O_4$ coated samples. Compared to the spinel phase on the LSM coated samples the spinel phase on the LSC coated samples might appear slightly less dense. This might be due to the incorporation of the $LaCrO_3$ and $SrCrO_4$ particles originating from the LSC coating that might create porosity during the incorporation process. Once the particles have been incorporated into the oxide scale they might increase the mechanical stresses in the oxide scale and in the alloy/oxide interface. It was for example observed that the alloy/oxide interface on the LSM coated samples were smoother than the same interface on the LSC coated samples, and on the LSM samples no inclusions of coating particles were observed.

3.4.5 Al_2O_3 coating

The weight gain data from the Al_2O_3 coated samples showed deviation from a parabolic oxidation behaviour, and the parabolic rate constant in the mathematical

expression for parabolic oxidation would have to change for the equation to fit the collected weight gain data. But, independent of the oxidation mechanism the coating decreased the weight gain compared to the uncoated Crofer samples. In the micrograph in figure 3.5 incorporation of the Al_2O_3 coating particles was observed. Incorporation of the coating particles in both the chromia and the spinel phase was observed. These coating particles should provide a continuous geometrical protection effect against oxidation through out the oxidation process even after the scale thickness has grown larger than the diameter of the coating particles. The extra diffusion path, x, implemented by the presence of the coating particle within the forming oxide is illustrated in figure 3.19 where the possible diffusive fluxes in the oxide scale are presented.

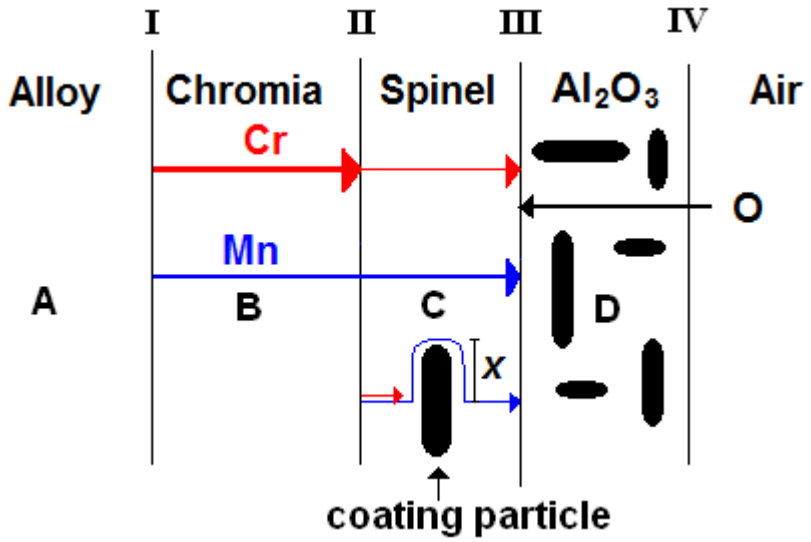

Fig. 3.19. Diffusive fluxes during oxidation of Al_2O_3 coated Crofer.

Al_2O_3 is more thermodynamically stable than both $MnCr_2O_4$ and Cr_2O_3 and is therefore unlikely to dissociate when incorporated into the growing oxide scale. The aluminium signals detected in the outer spinel phase on the forming oxide scale in table 3.2 is therefore believed to originate from Al_2O_3 coating particles embedded in the oxide scale not visible on the micrographs, and not from dissolved aluminium in the oxide. The (Mn,Cr)-spinel composition remaining if the aluminium signal is ignored is similar to the spinel composition formed on uncoated Crofer samples, only with a slightly higher Mn-content. Since there is no chemical effect of the Al_2O_3 coating on the growing oxide scale, the interface reactions on the Al_2O_3 coated samples are based on the same assumptions as for the uncoated Crofer sample listed in table 3.4. Instead, the slight variations in the spinel composition compared to uncoated Crofer samples are believed to be caused by diffusion effects. It has been shown that surface diffusion of chromium on Al_2O_3 proceeds relatively slowly [35], suggesting that the faster diffusing manganese probably is diffusing around the Al_2O_3 coating particles before chromium is, forming a Mn-rich oxide phase. The Al_2O_3 coating appears to increase the spinel ratio to ca. 30% compared to 10% for the uncoated Crofer samples after 2000 hours oxidation. The explanation to this is again believed to be the geometrical diffusion hindering of the Cr-cations and the accumulation of fast diffusing Mn closer to the alloy surface in large enough amounts

to form (Mn,Cr)-spinel. Visible proof of the faster diffusion of Mn around the Al_2O_3 coating particles and the formation of a spinel phase closer to the alloy surface can be seen in figure 3.20.

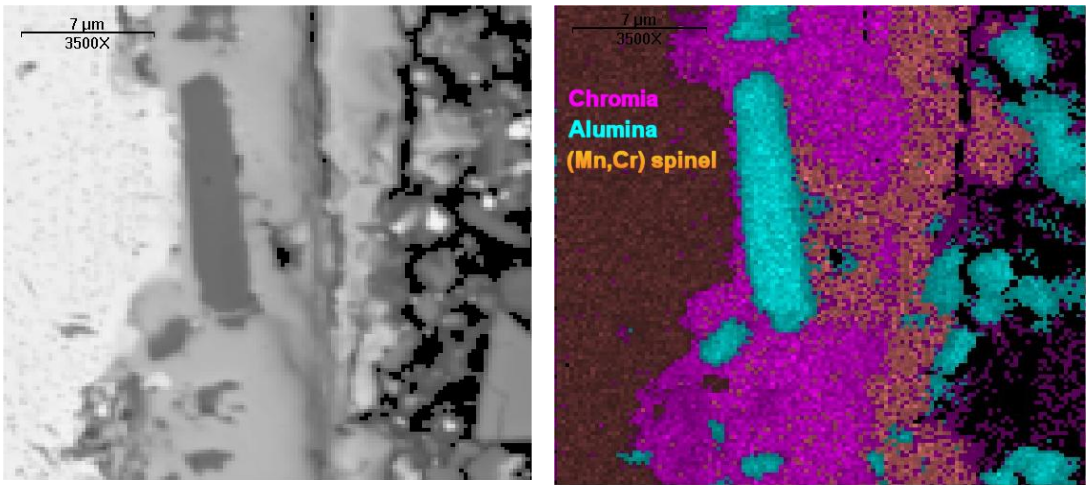

Figure 3.20. Mapping of the alumina coated sample oxidized for 2000h.

The pale orange area in the EDS map symbolises a Mn containing spinel phase, and this phase is as expected found on top of the chromia phase. However, the spinel phase is also found closer to the alloy/oxide interface on the outer side of the large Al_2O_3 coating particle incorporate in the oxide scale along side the oxide/alloy interface. In section 3.3.1 it was suggested that the weight gain data collected for the Al_2O_3 coated samples indicated that an alternative oxidation mechanism to parabolic oxidation can describe the oxidation of these samples, but that it was more likely that a parabolic description was the best summation of the complex oxidation reaction active on the oxidizing samples. During ideal parabolic oxidation the oxidation rate decreases with time due to the oxide scale growing thicker creating longer diffusion distance for the ions [9]. On the Al_2O_3 coated samples the above described and discussed extensive incorporation of coating particles introduces longer diffusion distances for the ions in a manner that might explain the deviation from parabolic oxidation behaviour in the weight increase plot.

The large and thermodynamically stable Al_2O_3 coating particles might be responsible for creating large stresses in the oxide scale and in the oxide/alloy interface. These stresses might be causing the iron protrusions observed in the micrographs in figure 3.5 and 3.7. No other coated samples presented similar iron chip formation after 4000 hours oxidation. These protrusions might be a way to relieve the stresses built up in the oxide scale or in the alloy/oxide scale interface. A second possible explanation could be that extensive internal oxidation with larger volume than the original alloy components is taking place just below the chromia/alloy interface. These internal oxides would then create extensive compressive stresses in the alloy that would initiate metal protrusion through the oxide scale. However, the number of and the appearance of the internal oxidation on the Al_2O_3 coated samples do not differ in any significant way from the internal oxidations found on the other samples in the study. This suggests that the internal oxidation probably is not the explanation to the observed metal protrusions.

3.4.6 ZrO_2 coating

As displayed in figure 3.1-2 the ZrO_2 coated samples appear to show similar deviation from parabolic oxidation behaviour as the Al_2O_3 coated samples. However, just as the Al_2O_3 coating the ZrO_2 coating decreases the oxidation rate of the Crofer 22APU samples compared to the uncoated samples, independent of the oxidation mechanism. The micrographs in figure 3.6 show small tendencies of the incorporation of bright ZrO_2 particles in the outer part of the growing oxide scale. The performed point analyses of the outer oxide scale presented in table 3.2 show a spinel composition similar to the spinel composition found on uncoated samples. The ZrO_2 coating does not affect the oxide composition. Instead it functions simply as a geometrical protection against oxidation. In figure 3.21 a sketch over the possible diffusive fluxes during oxidation is presented.

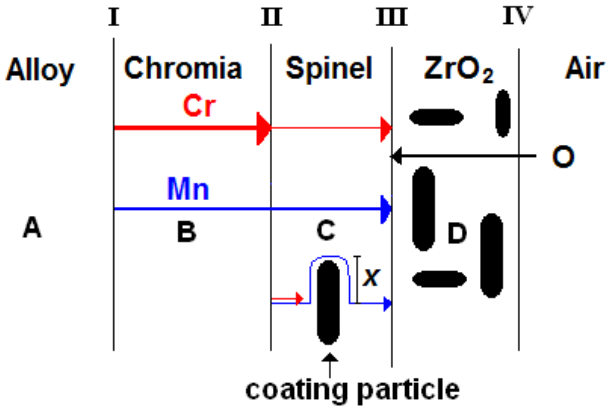

Fig. 3.21. Diffusive fluxes during oxidation of ZrO_2 coated Crofer.

The ZrO_2 coating is porous as can be seen in the micrographs in figure 3.6 which means that there is an unhindered access to oxygen at the surface of the forming spinel phase, in this case $MnCr_2O_4$ spinel. The interface reactions on the ZrO_2 coated samples are assumed to be similar to the ones for uncoated Crofer listed in table 3.4. The composition of the outmost spinel on the ZrO_2 coated samples is even the same as the composition found on the uncoated Crofer.

The ZrO_2 coating particles do not affect the chemical composition of the forming oxide, but it does appear to affect the spinel ratio of the oxide scale. In comparison to the uncoated samples the ratio has increased from 10% to 30-40%. The incorporation of the coating particles makes it possible for the coating particles to remain a geometrical diffusion obstacle throughout the oxidation for both outward diffusing cations and any possible inward diffusion of oxygen ions that might take place. The longer diffusion path, x, around the incorporated coating particles is illustrated in figure 3.21. Studies have shown that Cr presents a low surface diffusion on ZrO_2 [35], which means that when the outwardly diffusing cations of Mn and Cr reach the ZrO_2 particles, the Cr-ions will have difficulties diffusing around them and incorporating the particles into the oxide scale. Instead it is likely to assume that the Mn-ions, which also diffuse faster through the forming oxide scale than the Cr-ions [13], will be responsible for the initial incorporation of the ZrO_2 particles. The formed Mn-rich oxide phase around the ZrO_2 particles creates a diffusing path for the slower diffusing chromium ions. The geometrical diffusion obstacles these incorporated ZrO_2 particles

form, might make it possible for a (Mn,Cr)-spinel phase to form closer to the alloy surface compared to uncoated Crofer samples. According to the data in table 3.3 the spinel ratio of the total oxide scale is at least increased by about 20% compared to the uncoated samples. The incorporated ZrO_2 particles are unlikely to dissociate in the oxide scale, since they are thermodynamically very stable, which agrees with the observation of an unchanged spinel composition in the oxide compared to the uncoated sample. All these effects were also listed for the Al_2O_3 coated samples, and the impact of these effects is probably larger for the Al_2O_3 coated samples than for the ZrO_2 coated samples since the deviation from parabolic oxidation behaviour is larger for the Al_2O_3 coated samples. Just as for the Al_2O_3 coated Crofer 22APU samples the incorporation of the thermodynamically stable ZrO_2 coating particles and the increase in diffusion distance for the cations this creates might explain the deviation from parabolic oxidation behaviour in the weight gain plots.

3.4.7 Interaction mechanisms

Based on the observations above the interaction mechanisms between the coatings and the forming oxides could be divided into three main groups.

A Surface covering coating
B Surface covering coatings with chemical reaction with the forming oxide
C Incorporation of coating particles

Group A contains coatings which appear to be pushed in front of the outwardly growing oxide scale. The protecting effect of this type of coating is mainly a geometrical effect, since the coating might hinder oxygen access to the oxidizing cations on the alloy surface in the initial state of the oxidation and then on the oxide surface as the oxidation proceeds. However, no real chemical reaction takes place between the forming oxide scale and the coating components.

Group B contains almost the same type of coatings as group A with the exception that these coatings also tend to have a chemical reaction with the outmost of the forming oxide and introduce composition changes in the forming oxide at the same time as the main part of the coating particles are pushed in front of the oxide scale.

Group C consists of coatings which are incorporated into the forming oxide scale. The oxide scale grows around the coating particles, which therefore continue to implement a geometrical protection of significance for oxidation even after the oxidation has led to the formation of a thicker oxide layer than the diameter of the coating particles.

The interaction model between the growing oxide scale and the Co_3O_4 coating is best described as a B type, since the composition of the spinel phase changed compared to the spinel composition found on uncoated Crofer, and the coating is being pushed in front of the oxide scale. The interaction mechanism between the growing oxide scale and the $MnCo_2O_4$ coating can also be classified as a type B. However, the chemical effect is limited and the spinel coating appears to be pushed in front of the growing oxide scale.

For the LSM coating the interaction mechanism between the oxide scale and the coating can be described as a combined A and B type. The $(La_{0.85}Sr_{0.15})MnO_3$ perovskite particles are responsible for the A part of the mechanism since they are

being pushed in front of the growing oxide scale and do not dissociate or react. The Mn_2O_3 phase in the LSM coating is responsible for chemically changing the composition of the growing oxide scale, and therefore implements an interaction mechanism of type B.

The interaction mechanism between the growing oxide scale and the LSC coating is classified as a combined type of B and C. The $(La_{0.85}Sr_{0.15})CoO_3$ perovskite dissociates and react with the growing oxide scale changing its composition according to the interaction mechanism B. During the dissociation of the $(La_{0.85}Sr_{0.15})CoO_3$ perovskite and the reaction with the outwardly diffusing chromium thermodynamically stable $SrCrO_4$ and $LaCrO_3$ particles are formed. These particles are incorporated into the growing oxide scale, according to interaction mechanism C, and create geometrical diffusion obstacles in the oxide scale for both outwardly diffusing cation and anions/O_2-gas on the oxide scale surface.

The interaction mechanisms between the growing oxide scale and the Al_2O_3 and ZrO_2 coatings are type C mechanisms. Coating particles are incorporated into the growing oxide scale, but they are not reacting with the oxide phase surrounding them. They are however implementing a geometrical diffusion obstacle that reduces the oxidation rate and facilitates spinel formation creating a larger spinel ratio, which decreases the chromium content in the surface of the dense oxide.

3.5 Conclusions

In this study the Co_3O_4, $MnCo_2O_4$, LSM, LSC, Al_2O_3, and ZrO_2 coated Crofer 22APU samples in general presented parabolic oxidation. However, the Al_2O_3 and ZrO_2 coating samples presented weight gain plots showing deviations from parabolic oxidation behaviour. These deviations are assumed to be due to the changes in the diffusion conditions in the growing oxide scales because of the incorporations of the Al_2O_3 and ZrO_2 coating particles in the oxide scales. All the coatings except the $MnCo_2O_4$ coating seemed to decrease the weight gain compared to uncoated samples independent of the oxidation behaviour. All the coatings were also observed to increase the spinel ratio in the growing oxide scales, and the dense, well adherent spinel phase outside the chromia layer is believed to be one of the possible characteristics that cause the lowered oxidation rate. In a spinel phase the oxygen lattice is assumed to be full and therefore unable to transport oxygen ions via vacancies. The presence of such a spinel phase on top of the chromia layer in the growing oxide scales forces the oxidation process in the oxide scale to be dominated by outwardly diffusing cations with no or negligible contributions from inwardly diffusing oxygen. This would, as mentioned earlier, be one possible contribution to the lowered oxidation rate. The presence of a spinel on top of the chromia layer also lowers the chromium content in the outmost oxide on the oxidation samples. When applying a Mn containing coating, such as LSM, the concentration gradient of Mn across the growing oxide scale is decreased. A decreased concentration gradient of Mn leads to a decreased driving force for outwardly diffusing Mn, which might decrease the oxidation rate. A third explanation to the lowered oxidation rate of the coated samples might be that the coatings insert particles in the growing oxide scale that give a geometrical protection against oxidation. Examples of such coatings are ZrO_2, Al_2O_3, and LSC. A fourth possible explanation to the lowered oxidation rate on coated samples might be that the coating initiates formation of a spinel phase with a composition that has especially unfavourable diffusion conditions. All four possible

explanations to the lowered oxidation rate are probably present to different extent depending on the coating type. However, the relative importance of the contributions is unknown.

Three different interaction mechanisms between the growing oxide scale and the applied slurry coatings were observed. Which of the interaction mechanisms is the most successful is difficult to say, but an optimal solution would probably consist of a coating providing a combination of the three interaction mechanism. The Co_3O_4 and $MnCo_2O_4$ coated samples presented interaction mechanisms of type B, surface covering coatings with chemical reaction with the forming oxide scale. Both coatings provided low chromium content in the outer spinel phase, but the chromia layer was noticeable thick and in a SOFC-stack the electrical resistance across the oxide scale would be too high. The Al_2O_3 and ZrO_2 coated samples presented an interaction mechanism of type C, incorporation of coating particles in the growing oxide scale. The scale thicknesses on these samples were still relatively high and the chromium content in the outer oxide was not significantly decreased compared to uncoated Crofer. For the LSM coating the interaction between the oxide scale and the coating consist of two mechanisms. First there is a chemical change of the oxide composition that decreases the chromium content in the outer oxide, type B. Secondly there is a geometrical oxidation protection on the oxide surface that might have an effect during the initial oxidation, type A. Besides lowered chromium content in the outer oxide scale the oxide scale is significantly thinner than the oxide scale found on uncoated Crofer. The LSC coated samples also present a significantly thinner oxide scale and lowered chromium content in the outer oxide scale. But the interaction mechanisms between the growing oxide scale and the LSC coating is of type B and C instead. That is besides a chemical change of the growing oxide scale there is also a geometrical protection against oxidation due to incorporated coating particles in the growing oxide scale.

In this study the most suited coatings for use as a protection against oxidation on an interconnector in a SOFC-stack was found to be the LSM or the LSC coating. Both had a combination of interaction mechanism between the growing oxide scale and the coating.

The spinel compositions found in the outer oxide scales on the oxidized samples in this chapter were determined by kinetics, since thermodynamics is not able to affect the compositions due to the large range of stable cubic spinel compositions in the Co-Mn-Cr-O system, cf. figure 3.10.

3.5 Reference List

1. Quadakkers, W. J., Piron-Abellan, J., Shemet, V. and Singheiser, L., Materials at High Temperatures, 20, 115 (2003)

2. Quadakkers, W. J., Piron-Abellan, J. and Shemet, V., Material Research, 7, 203 (2004)

3. Yang, Z. G., Hardy, J. S., Walker, M. S., Xia, G. G., Simner, S. P. and Stevenson, J. W., Journal of the Electrochemical Society, 151, A1825-A1831 (2004)

4. Larring, Y. and Norby, T., Journal of the Electrochemical Society, 147, 3251 (2000)

5. Zhu, W. Z. and Deevi, S. C., Materials Research Bulletin, 38, 957 (2003)

6. Huang, K., Hou, P. Y. and Goodenough, J. B., Materials Research Bulletin, 36, 81 (2001)

7. Linderoth, S., Surface & Coatings Technology, 80, 185 (1996)

8. Chen, X., Hou, P. Y., Jacobson, C. P., Visco, S. J. and De Jonghe, L. C., Solid State Ionics, 176, 425 (2005)

9. Kofstad P, *High Temperature Corrosion* (Elsevier Applied Science Publishers LTD, 1988)

10. Kuznecov M., Eichler K., Megel S. and Otschik P., in Proceedings of the European SOFC Forum 2004, p. 1573

11. Calculated using FactSage 5.5,1-5-2007

12. Evans, H. E., International Materials Reviews, 40, 1 (1995)

13. Sabioni, A. C. S., Huntz, A. M., Borges L.C and Jomard F., Philosophical Magazine, 87, 1921 (2007)

14. Kofstad, P., Oxidation of Metals, 44, 3 (1995)

15. Lobnig, R. E., Schmidt, H. P., Hennesen, K. and Grabke, H. J., Oxidation of Metals, 37, 81 (1992)

16. *CRC Handbook of Chemistry and Physics* (CRC Press LLC, New York, 2004)

17. Hastings, J. M. and Corliss, L. M., Physical Review, 126, 556 (1962)

18. Dieckmann, R., Journal of Physics and Chemistry of Solids, 59, 507 (1998)

19. Topfer, J., Aggarwal, S. and Dieckmann, R., Solid State Ionics, 81, 251 (1995)

20. Lu, F. H., Tinkler, S. and Dieckmann, R., Solid State Ionics, 62, 39 (1993)

21. Lu, F. H. and Dieckmann, R., Solid State Ionics, 53-6, 290 (1992)

22. Lu, F. H. and Dieckmann, R., Solid State Ionics, 59, 71 (1993)

23. Lu, F. H. and Dieckmann, R., Solid State Ionics, 67, 145 (1993)

24. Hansson A.N. and Somers M.A.J., in Proceedings of the 6th International Conference on the Microscopy of Oxidation, p. 49

25. Hansson A.N., PhD.-thesis, Oxides in the Co-Cr-Fe-O system and oxidation behaviour of coated Fe-22Cr steel, 2004

26. Jankowski, J., Thomas, G. and Camby, L. P., Solid State Ionics, 101, 1321 (1997)

27. Kale, G. M., Pandit, S. S. and Jacob, K. T., Transactions of the Japan Institute of Metals, 29, 125 (1988)

28. Oneill, H. S. C., Physics and Chemistry of Minerals, 12, 149 (1985)

29. Xing, L. and Prewitt, C. T., Physics and Chemistry of Minerals, 17, 168 (1990)

30. Sreedharan, O. M., Chandrasekharaiah, M. S. and Karkhanavala, M. D., High Temperature Science, 9, 109 (1977)

31. Yang, Z. G., Xia, G. G. and Stevenson, J. W., Electrochemical and Solid State Letters, 8, A168-A170 (2005)

32. Yang, Z. G., Xia, G. G., Simner, S. P. and Stevenson, J. W., Journal of the Electrochemical Society, 152, A1896-A1901 (2005)

33. Zahid, M., Tietz, F., Sebold, D. and Buchkremer, H. P., in Proceedings of the European SOFC Forum 2004, p. 820

34. Oneill, H. S. C., Physics and Chemistry of Minerals, 12, 149 (1985)

35. Tucker M.C, Kurakawa H., Jacobson C.P., De Jonghe L.C. and Visco S.J., Journal of Power Sources, 160, 130 (2006)

4. Dual layer coatings on Crofer 22APU

4.1 Introduction

In a Solid Oxide Fuel Cell, SOFC, stack the interconnector separates the fuel gas on the anode side and the moist air on the cathode side, while transporting the electrical current between the cells and the external circuit. All this is taking place at high temperatures. Oxidation resistant Fe-Cr alloys have been developed as interconnect material since the chromia scale that forms on these alloys has a good balance between growth kinetics and electrical conductivity [1]. However, Cr-species evaporated from the surface of the chromia scale and diffuse into the cathode and contaminate it as well as the cathode/electrolyte interface. Due to this contamination and blockage the electrochemical properties of the cathode will be severely degraded [2]. Crofer 22APU, which is a Fe-Cr alloy designed for interconnect use, forms a protective duplex oxide layer consisting of Cr_2O_3, alloy side, and $MnCr_2O_4$, surface side, under SOFC operating conditions [3, 4]. The outer spinel phase decreases the Cr-content in the outer oxide scale and the amount of evaporating Cr-species is decreased. However, even if the Crofer 22APU alloy presents promising results regarding growth rate of the oxide scale, electrical resistance of the growing oxide scale and the chromium content in the outer oxide scale, the three characteristics are not satisfactorily low enough for an acceptable durability of the SOFC stacks. The growth rate, the electrical resistance and the Cr-content of the oxide scale must be reduced further. Application of spinel forming coatings on the surface of interconnect alloys has been demonstrated to reduce the growth rate, to reduce Cr concentration in the spinel and to increase the electrical conductivity [5-8].

The different coatings and coating methods show different advantages. It has been observed that Crofer 22APU coated with a single layer of Co_3O_4 via wet powder spraying has a significantly lower chromium content in the outer oxide scale compared to uncoated Crofer 22APU when oxidized at 800˚C [9]. Also observed is that a single layer coating of LSM or LSC on Crofer 22APU samples form an oxide scale with lower chromium content in the outmost part during oxidation as well as a lower oxidation rate [8, 10]. The two successful coating types were combined in this study to investigate if their favourable effect on the oxidation of Crofer samples can be increased when combined. Dual coatings, consisting of an inner Co_3O_4 coating layer and an outer coating layer of LSM or LSC, were applied onto Crofer 22APU alloy samples via slurry coating. The samples were oxidized at 900˚C in air containing 1% water for 4000 hours. The oxidation rates and the chromium contents in the outer oxide scales formed on these dual coated samples were analyzed and compared to the performance of the single layer coated samples.

4.2 Experimental

4.2.1 Sample preparation

Crofer 22APU samples with the dimension 20*20*0.3 mm^3 were etched in hydrofluoric acid to remove any native oxides formed during alloy processing. The samples were rinsed in water and alcohol after etching. The samples were thereafter slurry coated using a hand-gun spray, so that a ca. 7 μm or a ca. 15 μm thick layer of Co_3O_4 coating was applied on both sides of the samples. The samples were left to dry

for a few minutes where after the second coating layer with a thickness of ca. 15 μm was applied. The coating slurries consisted of approximately 33 wt.% powder of the coating material dissolved in ethanol with a small amount of PVP-binder mixed into it. The binder will burn off during the heating ramp when the oxidation is initiated. The coatings included in this study are 7/15 μm Co_3O_4 + 15 μm LSM and 7/15 μm Co_3O_4 + 15 μm LSC, and they are compared to uncoated Crofer. The uncoated samples were etched using the same procedure as described above. In chapter 2 more details about the coatings can be found.

4.2.2 Oxidation experiment

The etched uncoated samples and the coated samples were weighed before being mounted free-hanging in an oxidation furnace with a volume of $4.32 \cdot 10^{-3}$ m^3. The samples were oxidized for 250 hours long cycles at 900°C in air containing 1% water after which the samples are demounted and weighed. The gas flow into the furnace was set to $72 \cdot 10^{-3}$ m^3/h, which meant the atmosphere in the furnace should be completely exchanged ca. 17 times every hour. The heating and cooling ramps were both set to 120°C/h. When the long term, cyclic oxidation process were started there were six samples of each coating type, making it possible to remove samples for further investigation at different points during the oxidation, and still have samples left in the furnace for continued oxidation. For all coating types, samples were removed form the oxidation furnace after 500, 1000, 2000, and 4000 hours. Complementary oxidation experiments at the same temperature and atmosphere as described above were performed in a TGA-equipment for two uncoated and two 15 μm Co_3O_4 + 15 μm LSM coated Crofer samples with the dimension 20*10*0.3 mm^3. The alloy samples were etched and coated according to the same procedure as described above before being mounted as described in figure 2.1 on a sample holder made of alumina in TGA equipment Netzsch, STA 409 CD. The furnace chamber in the TGA-equipment had a volume of $0.14 \cdot 10^{-3}$ m^3 and a total gas flow of 0.081 m^3/h, which meant the gas in the furnace chamber was completely exchanged ca. 35 times/hour. The samples were oxidized for 250 hours to investigate the initial oxidation behaviour, which could not be captured with the long term cyclic oxidation process. The heating and cooling ramp was just as in the cyclic experiment set to 120°C/h. For more detailed description on the oxidation conditions and the sample preparation of the cross-sections see chapter 2.

4.3 Results

4.3.1 Weight gain

In figure 4.1 the weight gain data collected for the Co_3O_4 + LSM and Co_3O_4 + LSC coated Crofer samples are plotted together with the weight gain data for uncoated Crofer samples in a weight increase-$time^{1/2}$ plot.

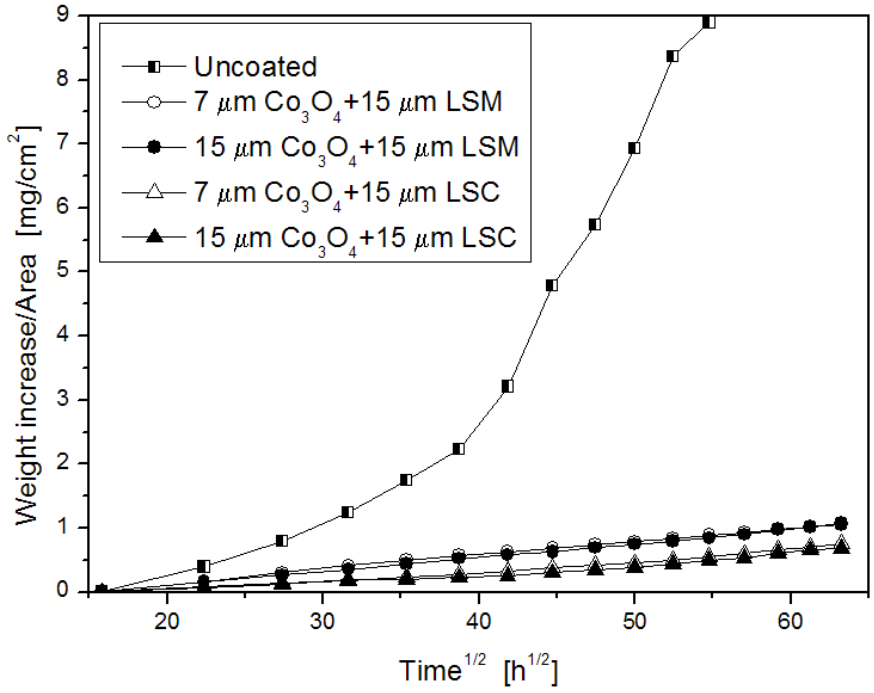

Figure 4.1.a. The weight increase-time$^{1/2}$ plots for uncoated and dual layer coated Crofer samples in air containing 1% water at 900˚C for 4000 hours.

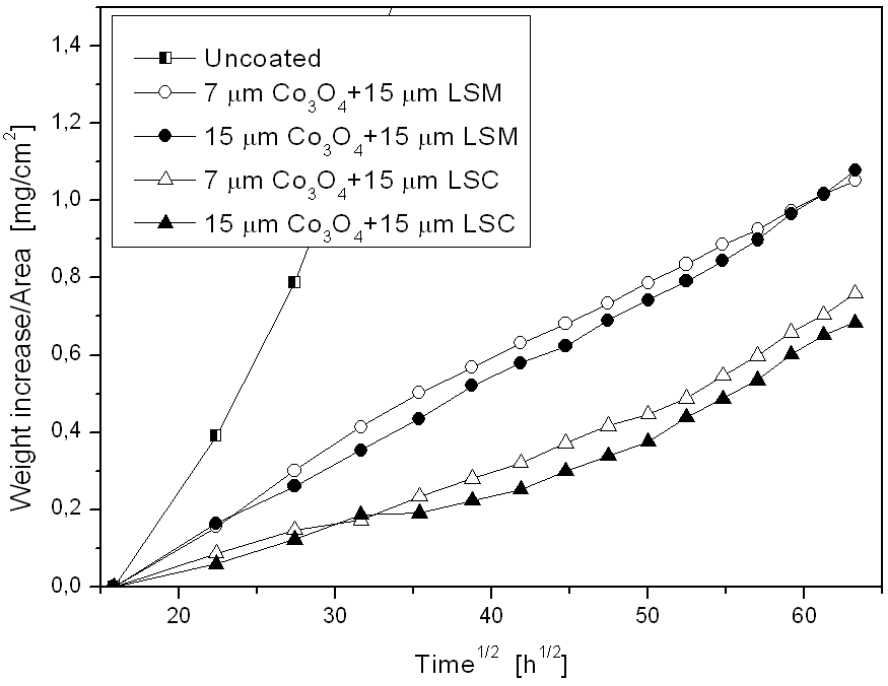

Figure 4.1.b. Enlargement of the weight increase-time$^{1/2}$ plots for uncoated and dual layer coated Crofer samples in air containing 1% water at 900˚C for 4000 hours.

The uncoated Crofer samples present a linear plot of the weight gain in figure 4.1, indicating parabolic oxidation behaviour, up to ca 1000 hours of oxidation [3, 4]. The rate determining process at high temperature parabolic oxidation is as a rule a thermal diffusion process [11]. After that the weight gain deviates from parabolic oxidation behaviour by increasing drastically. This phenomenon indicates break away oxidation.

All the dual coated samples present linear curves in the weight gain plots, indicating parabolic oxidation behaviour. No signs of break away oxidation are observed on the plots of the coated samples. In table 4.1 the calculated parabolic rate constants for the dual coated samples and the uncoated samples are presented.

Table 4.1.a. Parabolic rate constant for uncoated and dual coated Crofer after 4000 hours oxidation neglecting the weight gain from the first 250 hours.

	$k_{p,1}\cdot10^{-3}$ $[(mg/(cm^2h^{1/2}))^2]$	*Time [h]*	$k_{p,2}\cdot10^{-3}$ $[(mg/(cm^2h^{1/2}))^2]$	*Time [h]*
15 μm Co_3O_4[b] + 15 μm LSC[b]	0.11±0.02	2500	0.57	2500-4000
7 μm Co_3O_4[a] + 15 μm LSC[a]	0.20±0.05	2750	0.63	3000-4000
15 μm Co_3O_4[b] + 15 μm LSM[a]	0.49±0.1	3000	0.77	3000-4000
7 μm Co_3O_4[a] + 15 μm LSM[a]	0.58±0.07	4000		
Uncoated	7.5±1.1	1000		

Table 4.1.b. Parabolic rate constant for the first 250 hours oxidation measured using TGA equipment.

	$k_{p,1}\cdot10^{-3}$ $[(mg/(cm^2h^{1/2}))^2]$
Uncoated	11±0.008
15 μm Co_3O_4[f] + 15 μm LSM[e]	2.2±0.009

Table 4.1.c. Average oxide scale thickness, t, measured on the SEM micrographs of the uncoated and coated Crofer samples oxidized for 500, 1000, 2000, and 4000 hours.

	t [μm] 500 h	*t [μm] 1000 h*	*t [μm] 2000 h*	*t [μm] 4000 h*	*Remark*
15 μm Co_3O_4[b] + 15 μm LSC[b]	2.6±0.9	3.6±0.9 *(27.3±3.4)*	5.8±2.2 *(26.2±3.5)*	8.1±1.8 *(26.1±12.6)*	Ox. scale (Heavily ox. areas)
7 μm Co_3O_4[a] + 15 μm LSC[a]	2.4±0.9	4.4±1.3	6.5±2.3		Ox. scale
15 μm Co_3O_4[b] + 15 μm LSM[a]	4.4±1.4	5.2±1.4	6.0±2.6	8.5±1.8	Ox. scale
7 μm Co_3O_4[a] + 15 μm LSM[a]	4.8±1.7	4.9±1.4	7.2±2.4	10.8±2.0	Ox. scale
Uncoated	9.8±3.2	11.9±2.9	15.3±2.0		Ox. scale

From the weight gain plots in figure 4.1 it is observed that the thickness of the inner Co_3O_4 coating does not affect the oxidation behaviour since all four present parabolic distribution of the weight gain data. But based on the weight gain plots in figure 4.1 and the parabolic rate constants listed in table 4.1 it appears as if a thicker inner Co_3O_4 coating layer leads to a lower weight gain rate.

In figure 4.2 the weight gain plots for 15 μm Co_3O_4 + 15 μm LSM coated samples and the uncoated Crofer samples oxidized in the TGA equipment are presented. The parabolic oxidation rate constants calculated from these curves are presented in table 4.1.

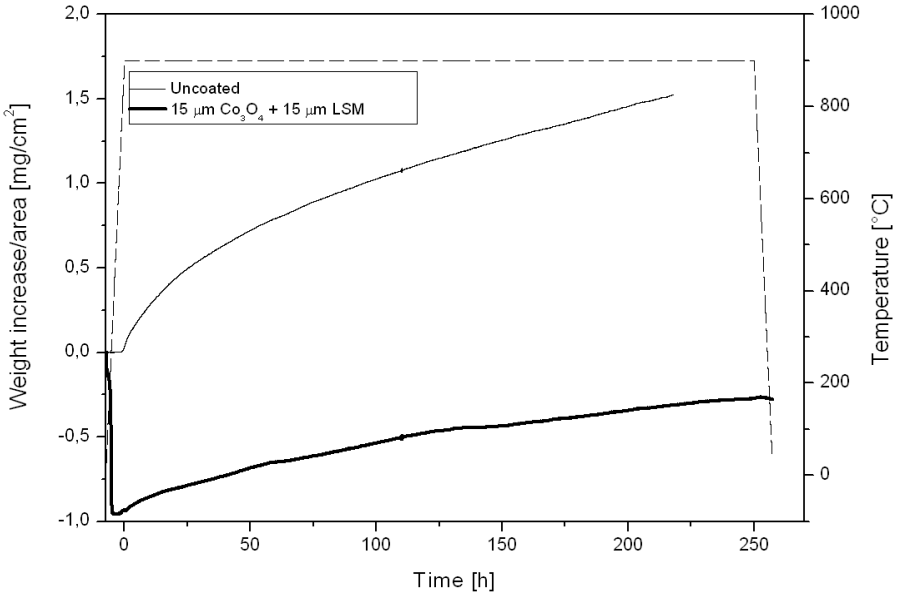

Figure 4.2.a. The weight increase data collected with TGA for uncoated and 15 μm Co_3O_4 + 15 μm LSM coated Crofer

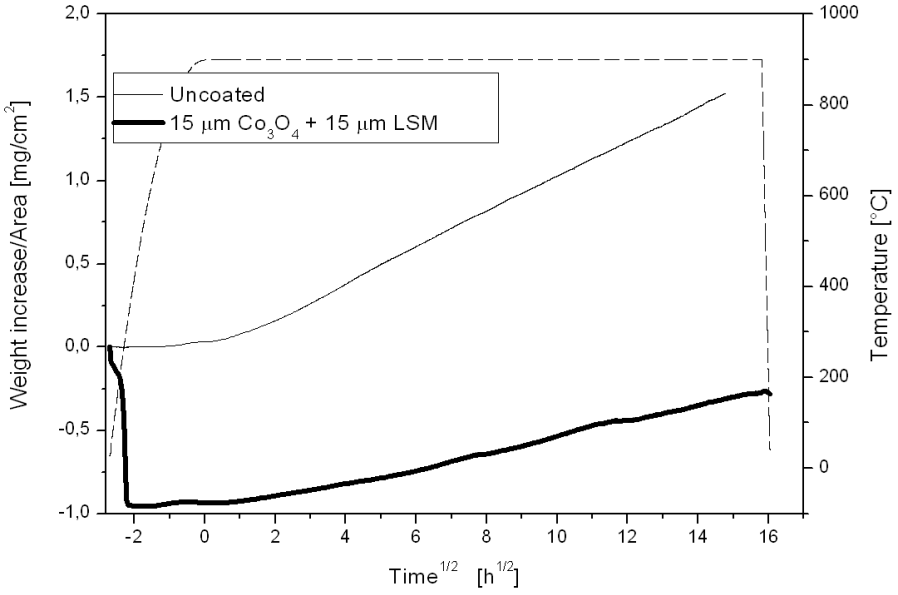

Figure 4.2.b. The weight increase-time$^{1/2}$ plots for uncoated and 15 μm Co_3O_4 + 15 μm LSM coated Crofer samples from the TGA-measurements.

The samples in the TGA-experiment appear to be oxidized faster in comparison to the samples included in the cyclic oxidation experiment. The 15 μm Co_3O_4 + 15 μm LSM coated samples oxidized five times faster in the TGA-equipment than in the cyclic oxidation furnace, while the uncoated Crofer sample only oxidizes twice as fast in the TGA experiment compared to the cyclic oxidation experiment.

4.3.1 Microstructure

In figure 4.3-4.4 below the cross-sections of the uncoated and dual coated samples are displayed.

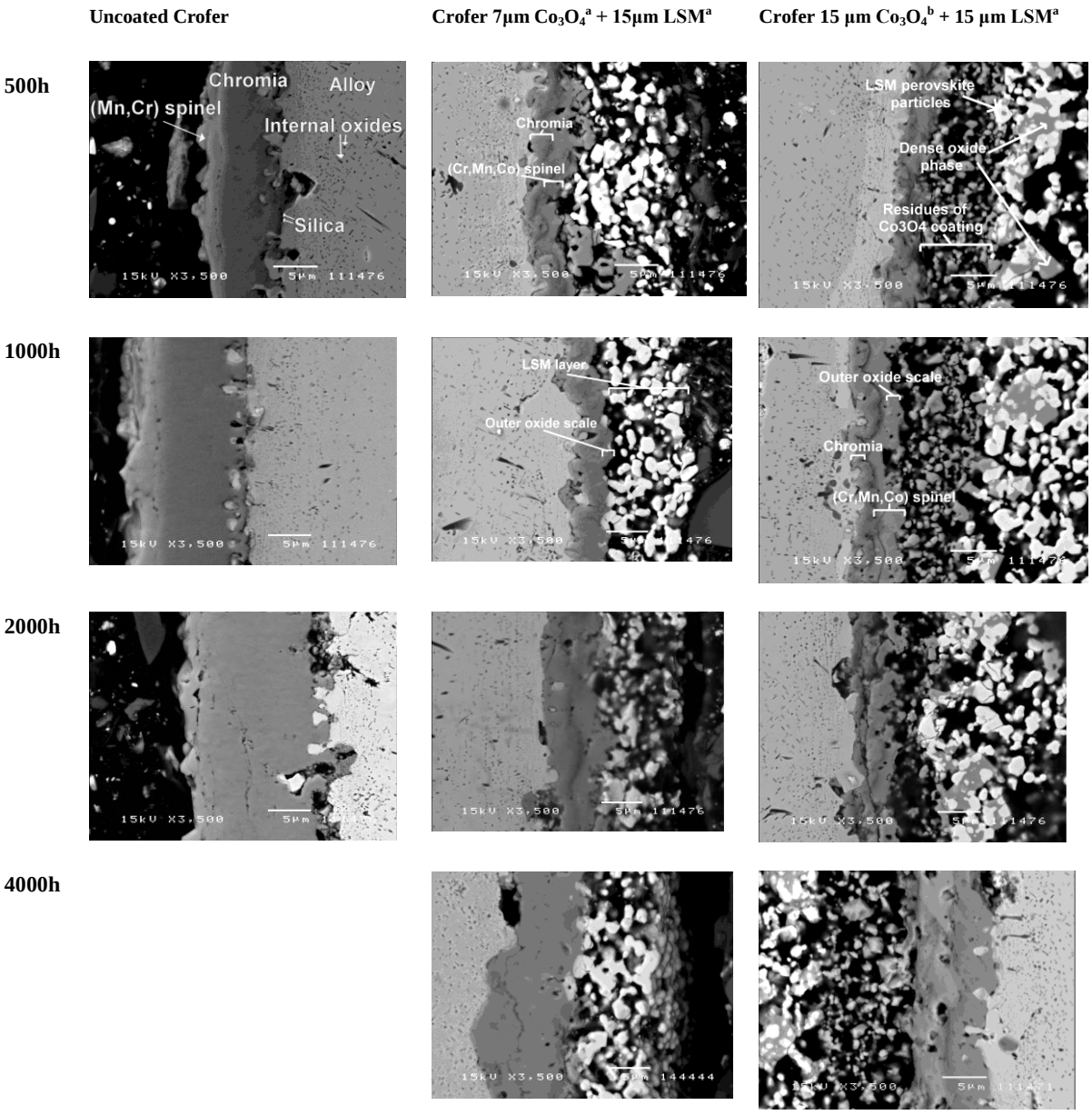

Fig. 4.3. BSE micrographs of cross-sections of the samples, with the oxidation times indicated left of the pictures.

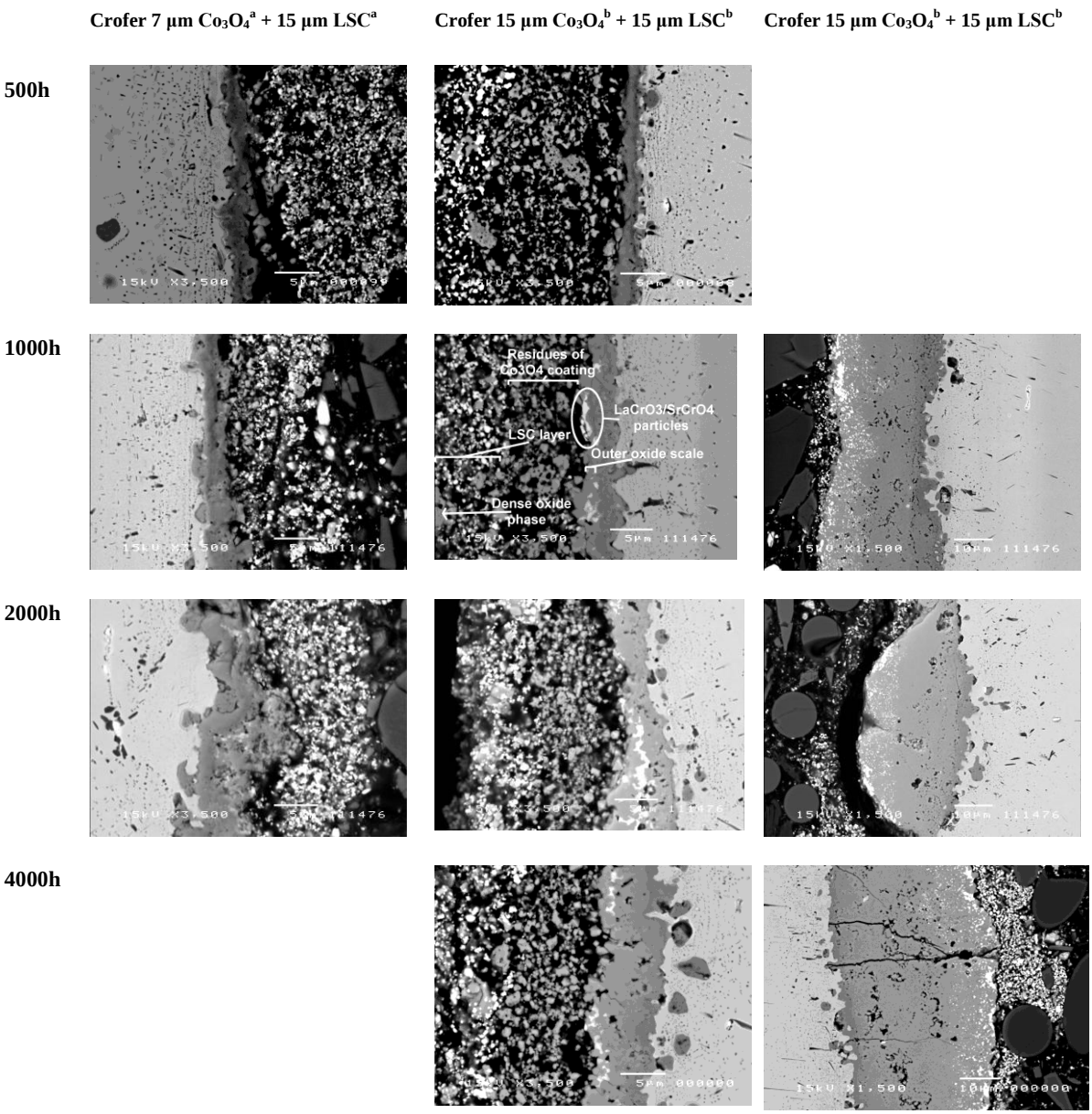

Fig. 4.4. BSE micrographs of cross-sections of the samples, with the oxidation times indicated left of the pictures.

The scale thicknesses measured on micrographs like these are listed in table 4.1c above. For all the coated samples the oxide scales were generally significantly thinner than the oxide scale on the uncoated Crofer sample. The oxide scales formed on the uncoated and the Co_3O_4 + LSM and Co_3O_4 + LSC coated samples all tended to present a relatively constant thickness except for the 15 µm Co_3O_4 + 15 µm LSC coated samples, which had a few heavily oxidized areas along the sample surface on each of the cross-sections from the 1000, 2000, and 4000 hours samples. Examples of these areas are presented in figure 4.4 and the thicknesses of these areas are included in table 4.1 within brackets. But despite these heavily oxidized areas the 15 µm Co_3O_4 + 15 µm LSC coated sample presented the lowest weight gain during the first 2000 hours of oxidation, and when the heavily oxidized areas are ignored these samples also present the thinnest oxide scales. The 15 µm Co_3O_4 + 15 µm LSC coated samples had lower weight gain than the 15 µm Co_3O_4 + 15 µm LSM coated samples, cf. figure

4.1. During these first 2000 hours of oxidation the general thickness of the oxide scale on the 15 µm Co_3O_4 + 15 µm LSC coated samples are significantly smaller than the oxide scale thickness observed on the 15 µm Co_3O_4 + 15 µm LSM coated samples. As oxidation continues the differences in the parabolic rate constant and the thickness of the oxide scale for the two samples decreased.

The oxide/alloy interface on the Co_3O_4 + LSC coated samples show a tendency towards being slightly less smooth and more wavy than the corresponding interface on the Co_3O_4 + LSM coated samples. The chromia/spinel interface within the oxide scale on the Co_3O_4 + LSC coated samples also appears wavier than the corresponding chromia/spinel interface on the Co_3O_4 + LSM coated samples. That is the lateral position of the chromia/spinel interface is varying much more on the Co_3O_4 + LSC coated samples than on the Co_3O_4 + LSM coated samples.

Both on the Co_3O_4 + LSM and the Co_3O_4 + LSC coated samples it was observed that the inner Co_3O_4 coating layer appeared completely consumed after oxidation if it had been applied with a thickness of about 7 µm. When the inner Co_3O_4 coating layer was twice as thick, residues of it were still easily discernable after oxidation even though EDS data indicated changes in the composition. The original Co_3O_4 coating appeared to have transformed into a (Cr,Mn,Co)-oxide. The composition of the spinel varies depending on how close to the surface of the growing oxide scale the analysing probe is positioned. The oxide was presumed to consist of a spinel and the cation composition was quantified accordingly. The average compositions in the residues of the Co_3O_4 coating across the layer on the 15 µm Co_3O_4 + 15 µm LSM and 15 µm Co_3O_4 + 15 µm LSC coated samples are presented in table 4.2. By consulting the Co-Mn-Cr-O phase diagram in figure 3.10 it is established that the assumption that the residues of the Co_3O_4 coating layer remain a spinel phase after oxidation, most likely is correct when considering the compositions presented in table 4.2.

Table 4.2. Average spinel composition across the residues of the Co_3O_4 coating on the 15 µm Co_3O_4 + 15 µm LSM and 15 µm Co_3O_4 + 15 µm LSC coated samples.

	15 µm Co_3O_4[b] + 15 µm LSM[a]				***15 µm Co_3O_4[b] + 15 µm LSC[b]***			
	Cr	**Mn**	**Co**	**Fe**	**Cr**	**Mn**	**Co**	**Fe**
500 h	0.4±0.3	0.3±0.2	2.4±0.4		0.4±0.3	0.1±0.2	2.4±0.4	
1000 h	*Lack of data*				0.3±0.1	0.4±0.2	2.2±0.3	0.1±0.1
2000 h	0.3	0.7	1.9		0.5±0.1	0.4±0.2	2.0±0.1	0.1±0.1
4000 h	0.5±0.2	0.8±0.1	1.6±0.2		0.6±0.1	0.3±0.2	2.1±0.3	

For the 15 µm Co_3O_4 + 15 µm LSM coated Crofer 22APU sample oxidized for 1000 hours there was not enough EDS data collected in the inner Co_3O_4 coating layer to calculate an oxide composition. For the 15 µm Co_3O_4 + 15 µm LSM coated Crofer 22APU sample oxidized for 2000 hours not enough EDS data was collected to calculate standard deviation in the composition.

When the outer coating consisted of LSM the Mn content was approximately twice as high compared to the composition found on the samples with a second layer consisting of LSC. The chromium and manganese content tend to increase while the cobalt content decrease over time.

The outmost part of the oxide scales on the coated and uncoated samples was analyzed with EDS to determine the oxide composition, and in figure 4.5 line scans across the oxide scales on the Co_3O_4 + LSM and Co_3O_4 + LSC coated samples oxidized for 2000 hours are presented. In appendix 4 line scans across the formed oxide scales on the uncoated and the Co_3O_4 + LSM and Co_3O_4 + LSC coated samples oxidized for 500, 1000, 2000, and 4000 hours are summarized.

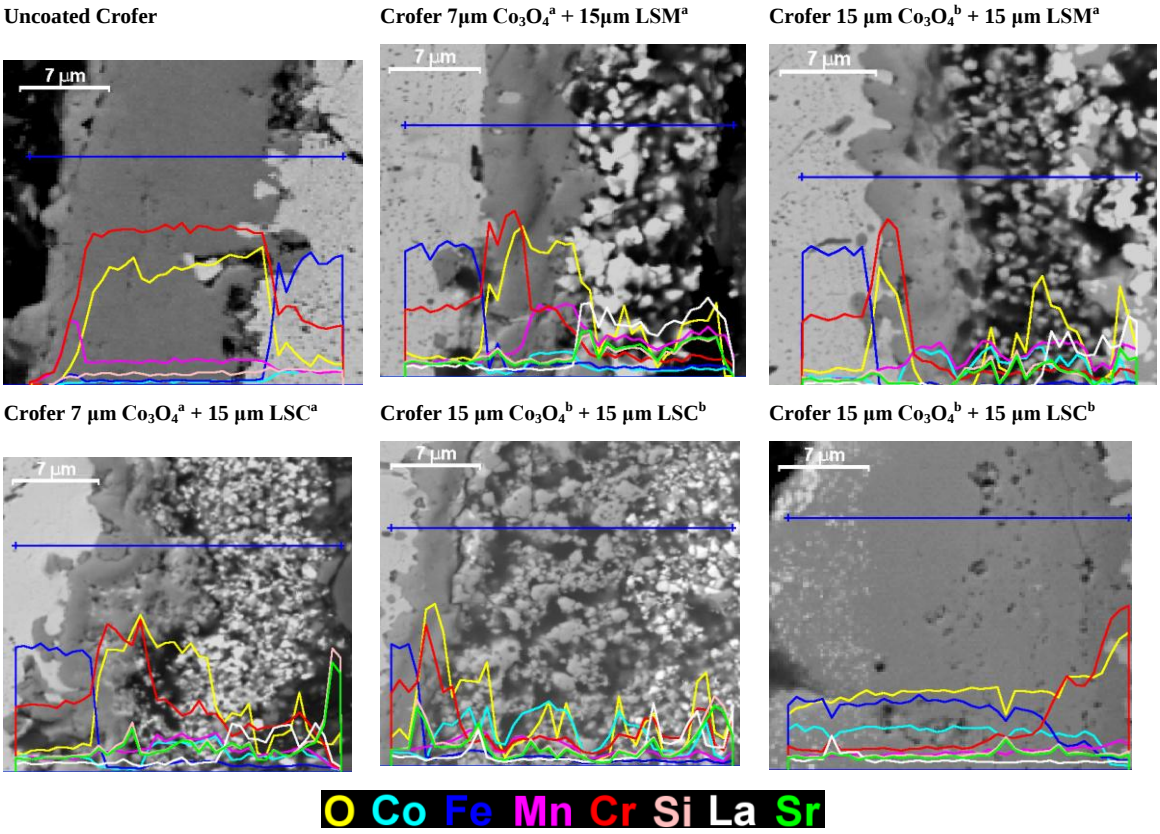

Fig. 4.5. Line scans over the oxide scale on uncoated an dual coated Crofer 22APU samples, oxidized for 2000 hour in air containing 1% water at 900˚C..

The line scans show that the chromia phase of the forming oxide scale is decreased in thickness in the presence of the Co_3O_4 + LSM and Co_3O_4 + LSC dual coatings compared to uncoated and LSM, LSC, and Co_3O_4 single coated Crofer 22APU samples in chapter 3. Additionally the chromium signal is decreased in the outmost part of the growing oxide scale, presumably consisting of a spinel phase. As the thickness of the Co_3O_4 layer was increased, the cobalt content in the forming spinel phase of the oxide scale seemed to increase at the same time as the chromium content decreased.

To get statistically better measurements of the chromium amount in the outer part of the forming oxide scale, point analyses were performed at several points in this outer part of the forming oxide scale on each sample. On the micrographs in figure 4.4 of the 7/15 µm Co_3O_4 + 15 µm LSM and 15 µm Co_3O_4 + 15 µm LSC coated Crofer 22APU samples oxidized for 1000 hours the area denoted the outer oxide scale is marked as type examples. In table 4.3 the calculated spinel compositions are presented.

Table 4.3. Spinel composition in the outer part of the dense oxide layer for samples of uncoated and coated Crofer that have been oxidized for 500, 1000, 2000 and 4000 hours.

	500 h				*1000 h*				*2000 h*				*4000 h*			
	Cr	**Mn**	**Co**	**Fe**	**Cr**	**Mn**	**Co**	**Fe**	**Cr**	**Mn**	**Co**	**Fe**	**Cr**	**Mn**	**Co**	**Fe**
Uncoated	1.9±0.1	1.1±0.1			1.6±0.2	1.4±0.2			1.7±0.3	1.2±0.4		0.1±0.0				
7 μm Co_3O_4[a] + 15 μm LSM[a]	0.7±0.2	1.5±0.2	0.8±0.1	0.1±0.0	0.7±0.1	1.7±0.1	0.6±0.0	0.1±0.0	0.9±0.2	1.5±0.2	0.5±0.1	0.1±0.0	1.3±0.2	1.2±0.3	0.5±0.1	
15 μm Co_3O_4[b] + 15 μm LSM[a]	0.5±0.2	0.6±0.1	1.8±0.1	0.1±0.0	0.4±0.1	0.9±0.2	1.7±0.2	0.1±0.0	0.5±0.2	1.1±0.2	1.4±0.1		0.7±0.1	0.8±0.1	1.5±0.2	
7 μm Co_3O_4[a] + 15 μm LSC[a]	0.7±0.2	0.8±0.1	1.4±0.1	0.1±0.0	0.9±0.1	0.9±0.1	1.2±0.2	0.1±0.1	1.3±0.4	0.6±0.3	1.0±0.1	0.1±0.1				
15 μm Co_3O_4[b] + 15 μm LSC[b]	0.4±0.2	0.7±0.1	1.6±0.1	0.3±0.1	0.4±0.1	0.7±0.1	1.7±0.1	0.2±0.1	0.5±0.2	0.6±0.1	1.7±0.2	0.2±0.1	0.5±0.2	0.4±0.1	1.8±0.1	0.2±0.1

For all the dual coatings the chromium content was lowered in the outer spinel phase compared to the chromium content in the spinel phase on the uncoated and the LSM and LSC single coated Crofer 22APU samples in chapter 3. As noticed in the line scans the cobalt content in the spinel phase increased with increased thickness of the inner Co_3O_4 coating layer. A thicker inner Co_3O_4 coating layer also appeared to lower the chromium content in the outer oxide scale to the same level as the chromium content detected on the Crofer samples coated with a single layer of Co_3O_4 coating in chapter 3. The lower chromium content was held more stable during the total oxidation period of 4000 hours when the inner Co_3O_4 coating layer was thicker.

Comparing the spinel compositions in table 4.2 for the 15 μm Co_3O_4 + 15 μm LSC and 15 μm Co_3O_4 + 15 μm LSM coated samples there are only small differences in the compositions. There is a slight tendency towards higher cobalt content and lower manganese content in the sample with the LSC perovskite. In the same sample there is also a higher amount of iron registered in the outer spinel. The iron content could even be neglected for the 2000 and 4000 hours sample for the 15 μm Co_3O_4 + 15 μm LSM coated samples. The iron registered in the spinel on the samples should be considered with some scepticism since there exists some risk that the iron signal has been caused by an overlap of the K_β for Mn over the K_α for Fe.

EDS mapping was performed on the oxide scales on some of the oxidized samples to get an overview of the chromia and spinel distribution in the oxide scale. By combining the Mn-, Cr-, Co-, Fe-, and La-element maps, images were created where the chromia and spinel phases in the growing oxide scale could be easily separated. On these images the area fraction of the spinel phase in the oxide scales were calculated for the different samples. The area fractions are presented in table 4.4.

Table 4.4. Spinel ratio of the total oxide scale.

	500 h	***1000 h***	***2000 h***	***4000 h***
Uncoated	0.15	0.09	0.10	
7 μm Co_3O_4[a] + 15 μm LSM[a]	0.57	0.63	0.53	0.54
15 μm Co_3O_4[b] + 15 μm LSM[a]	0.69	0.61	0.57	0.46
15 μm Co_3O_4[b] + 15 μm LSC[b]	0.84	0.81	0.81	0.75

From table 4.4 it is apparent that the spinel ratio in the oxide scale increases drastically in the presence of a dual coating.

For the Co_3O_4 + LSM coated samples where the spinel ratio was calculated on both samples with a thick and a thin inner Co_3O_4 coating layer it appeared as if a thicker inner Co_3O_4 coating layer increased the spinel ratio in the oxide scale. However, it also seemed as if the spinel ratio decreased the most as oxidation proceeded when the inner Co_3O_4 coating layer was thicker. In general the spinel ratios in the oxide scales tended to decrease as oxidation proceeded.

The highest spinel ratio was found for the 15 μm Co_3O_4 + 15 μm LSC coated sample.

In the oxide scales on the Co_3O_4 + LSC coated samples bright La- and/or Sr-containing areas are incorporated. These bright areas are mainly visible in the chromia/spinel interface within the oxide scale or in the forming spinel phase. The La

and Sr are originating from the LSC coating. These areas probably consist of $LaCrO_3$ and/or $SrCrO_4$ due to dissociation of the LSC coating. No bright La- and/or Sr-rich areas were observed in the oxide scale formed on the Co_3O_4 + LSM coated samples which might be explained by the fact that LSM is more thermodynamically stable than LSC and will not dissociate and react with Cr during the oxidation experiment.

In the micrographs of the 15 μm Co_3O_4 + 15 μm LSM coated samples a dense light grey phase surrounding some of the bright perovskite particles in the outer LSM layer was observed. When performing EDS on these spots high signals indicating a (Cr,Mn,Co)-oxide were detected. If the oxide phase is assumed to consist of spinel the compositions presented in table 4.5 are acquired.

Table 4.5. Spinel composition in oxide phase surrounding the perovskite particles in the LSM coating layer on 15 μm Co_3O_4 + 15 μm LSM coated samples.

	Cr	***Mn***	***Co***	***Fe***
500 h	0.3	0.9	1.8	
1000 h	0.3	0.8	1.9	
2000 h	0.4	1.1	1.6	
4000 h	0.4	0.8	1.8	

As illustrated in table 4.5 there was no significant change in the composition of the spinel phase over time, indicating that it might have formed early on in the oxidation process. The high amounts of Co show that Co-cations both diffuse inward towards the alloy and outward into the LSM coating during the oxidation process. However, the spinel phase was not as easily spotted on the 7 μm Co_3O_4 + 15 μm LSM coated samples indicating that not enough Co was available for its formation. For the Co_3O_4 + LSC coated samples similar oxide phases are observed. However, these oxide phase areas are not as dense, continuous, or large as the ones observed in the LSM coating. The small size of the oxide phases in the LSC coating complicates analysis via point analysis, and only a few point analyses were successfully performed. Based on these the spinel compositions listed in table 4.6 were achieved. The chromium and cobalt content is higher in this spinel phase than in the corresponding spinel phase in the LSM coating on the Co_3O_4 + LSM coated samples. The manganese content in the spinel phase in the LSC coating is low and is negligible during the first 1000 hours of oxidation.

Table 4.6. Spinel composition in the oxide phase surrounding the perovskite particles in the LSC coating layer on the 15 μm Co_3O_4 + 15 μm LSC coated samples.

	Cr	***Mn***	***Co***	***Fe***
500 h	0.7		2.3	
1000 h	0.4		2.6	
2000 h	0.6	0.1	2.2	
4000 h	0.8	0.2	2.0	

Based on the line scans in figure 4.5 it appeared as if the LSC coating layer presented a higher Cr content than the corresponding LSM coating. This agrees with the observation that LSC is less thermodynamically stable than LSM and would dissociate into (Co,Cr)-oxides, $LaCrO_3$ and $SrCrO_4$ during interaction with Cr_2O_3.

4.4 Discussion

4.4.1 Co_3O_4 + LSM coated samples

The Co_3O_4 + LSM coating decreased the weight gain compared to uncoated Crofer 22APU samples. The measured weight gain during the oxidation is a measurement of oxygen uptake from the atmosphere that takes place during the oxidation. If cations in the coating are able to be reduced during reaction with the growing oxide scale and/or the outwardly diffusing Cr- and Mn-cations originating from the alloy, oxygen originating from the coating might also contribute to the growth of the oxide scale. If no compensating oxygen uptake into the coating from the atmosphere would take place, this oxygen contribution to the oxide scale growth would not be detected as weight gain on the samples. That is the observed lowered weight gain in the presence of a reducable coating might in an extreme case only be a result of oxygen uptake from the coating instead of the atmosphere. According to the micrographs in figure 4.3 the oxide scales on the Co_3O_4 + LSM coated samples are thinner than the oxide scales grown on uncoated Crofer samples, indicating a real protecting effect against oxidation of the Co_3O_4 + LSM coating. The excess Mn in the LSM coating might however be reduced during reaction with the growing oxide scale and the outwardly diffusing Cr- and Mn-cations, and thereby contribute with some oxygen to formation of oxidation products either on the growing oxide scale and/or outside in the coating. The excess Mn in the LSM coating is present as a Mn_2O_3 phase, see Mn-O phase diagram in figure 3.8, and will be reduced when it transforms into a (Cr,Mn,Co)-spinel phase. The $(La_{0.85}Sr_{0.15})MnO_{3-\delta}$ perovskite phase is thermodynamically stable under the same conditions and should not be able to dissociate and contribute with Mn for oxidation reactions.

Both uncoated and 15 μm Co_3O_4 + 15 μm LSM coated samples presented higher oxidation rate in the TGA experiment than in the long term, cyclic oxidation experiment. A possible explanation for this difference in oxidation rate could be a faster initial oxidation process that is not possible to capture in the long term oxidation experiment due to too few data points. It was observed that the spinel ratio of the oxide scales in table 4.4 tended to decrease as oxidation proceeded. This could indicate that the spinel phase is growing faster during the initial oxidation than during the rest of the oxidation process. The establishment of this spinel phase in the oxide scale might take place during the initial 250 hours of oxidation, causing a higher oxide scale growth. For uncoated Crofer the parabolic rate constant was close to twice as high in the TGA experiment compared to the long term oxidation experiment. For the 15 μm Co_3O_4 + 15 μm LSM coated sample the parabolic rate constant was five times larger than the constant observed in the long term cycling oxidation experiment. This suggests that in the presence of the 15 μm Co_3O_4 + 15 μm LSM coating the initial spinel formation is faster than on the uncoated samples. This is supported by the observations presented in table 4.4 that show that the presence of a dual coating increases the spinel ratio in the oxide scale. If the initial oxidation consists of the establishment of the spinel phase, the difference in the oxidation rate during the initial oxidation process and the long term oxidation process would be significantly larger on the coated samples than on the uncoated sample as also observed in the TGA experiment.

In the micrographs of the Co_3O_4 + LSM coated samples it was observed that the dual coating was porous which ensures that there is free access to oxygen at the surface of the oxide scale.

From the EDS analysis it was found that cobalt must have diffused both inward and outward since high amounts of cobalt were detected in the forming spinel phase in the oxide scale as well as in the oxide phase found around the perovskite particles in the LSM coating. Manganese originating form the alloy is diffusing outward through the forming oxide scale. Inward diffusion of manganese originating from the Mn_2O_3 phase in the LSM coating is probably also taking place through the dual coating. From these observations a sketch over the diffusion processes taking place across the forming oxide scale and the coatings on the Co_3O_4 + LSM coated samples are constructed and displayed in figure 4.6 below.

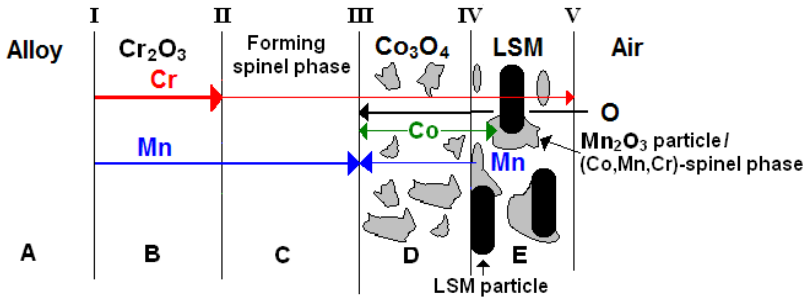

Fig. 4.6. Diffusive fluxes during oxidation of Co_3O_4 + LSM coated Crofer.

The interface reactions in the oxide scale on the Co_3O_4 + LSM coated samples can be assumed to be similar to the ones listed in table 3.4 for uncoated Crofer 22APU in chapter 3. However, the uncoated and dual coated samples should differ significantly in the initial reactions which are not included in table 3.4. Co_3O_4 undergoes a phase transition into CoO at around 900˚C as seen in the Co-O phase diagram in figure 3.12 [12-16].

As discussed in chapter 3 in section 3.4.2 the $Co_3O_4 \rightarrow CoO$ phase transition may affect and favour the formation of a denser spinel phase than the originally applied Co_3O_4 spinel. A single layer of Co_3O_4 coating on Crofer 22APU has shown to form a totally sintered/reacted and dense spinel phase on the alloy surface, cf. chapter 3. The formed spinel phase in the oxide scale on the Co_3O_4 + LSM coated samples appears even denser on the micrographs in figure 4.3, but unlike the single layer Co_3O_4 coated Crofer samples there are separated oxide particles, residues of the inner Co_3O_4 coating layer, on the 15 µm Co_3O_4 + 15 µm LSM coated samples. The inwardly diffusing Mn-cations originating from the LSM coating might be part of a possible explanation to why the inner Co_3O_4 coating layer is not completely sintered/reacted on the dual coated samples as on the single layer coated samples. However, when the inner Co_3O_4 coating layer was only 7 µm thick it appeared completely consumed since no residues were seen on the micrographs in figure 4.3.

The Mn_2O_3 particles in the LSM coating are made visible in the sketch in figure 4.6 as the light grey particles. During the initial oxidation these particles would react with CoO and the quickly outwardly diffusing Cr-cations and transform into a (Mn,Co,Cr)-

spinel phase surrounding the perovskite particles. This suggests that after the initial oxidation process the changes in the oxide/spinel composition of the oxide products in phase D and E and interface **III** and **IV** in figure 4.6 are mainly caused by diffusion via cation vacancies as expected in spinel phases at atmospheric pressure [17-22].

Comparing the weight gain data for the Co_3O_4 + LSM coated samples with the ones found for the LSM and Co_3O_4 layer single coated Crofer 22APU samples in chapter 3 there was a clear decrease in the weight gain when the LSM and Co_3O_4 coating layers were combined into a dual coating. A Crofer sample coated with a single layer of LSM presented a spinel composition close to $Cr_{1.5}Mn_{1.5}O_4$ and a spinel ratio of ca. 40% according to chapter 3. The presence of the inner Co_3O_4 coating layer resulted in a ca. 60% decrease of the chromium content in the spinel phase and a ca. 50% increase in the spinel ratio. This suggests that by adding cobalt to the growing spinel phase in the oxide scale, the total oxide scale becomes thinner at the same time as the spinel phase grows faster and chromium diffusion is reduced.

4.4.2 Co_3O_4 + LSC coated samples

Just as for the Co_3O_4 + LSM coating the Co_3O_4 + LSC coating appears porous in the micrographs in figure 4.4. This suggests that there is unhindered oxygen access to the surface of the forming oxide scale. With this in mind a sketch over the diffusion processes in the Co_3O_4 + LSC coated sample during oxidation is assembled in figure 4.7 below.

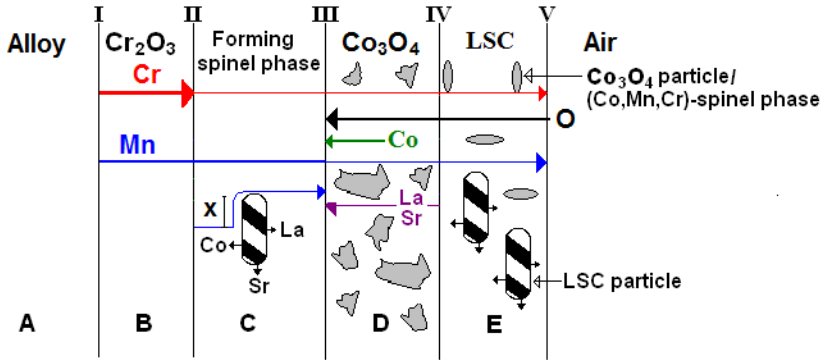

Fig. 4.7. Diffusion model of ions during oxidation of Co_3O_4 + LSC coated Crofer.

The interface reactions in the oxide scale on the Co_3O_4 + LSC coated samples are assumed to be the same as the ones listed in table 3.4 for uncoated Crofer. Cr- and Mn-cations are diffusing through the chromia layer probably mainly along the grain boundaries. In interface **II** chromia is forming via consumption of oxygen from the spinel phase. Spinel phase formation in interface **II** could take place via transformation of the chromia phase as described in interface reaction **II**b. The chromium uptake into the spinel phase seems to be lowered due to the high amount of Co present in the spinel phase. This cobalt is originating from the coatings and has been diffusing inward. As described in the section above Co_3O_4 transforms into CoO at ca 900˚C [12-16]. The phase transition is however probably reversed very quickly due to outward diffusion of Cr and Mn that would form a (Cr,Mn,Co)-spinel when reacting with CoO, cf. figure 3.10. The cation exchange at the interface **III** would thereafter take place via cation vacancy diffusion as expected in a spinel phase at

atmospheric pressure. At interface **III** oxygen uptake into the forming spinel phase would take place via the **III**a reaction which also introduces the cation vacancies that will be diffusing inwardly as the Cr- and Mn-cations are diffusing outward.

In comparison to the $(La_{0.85}Sr_{0.15})MnO_{3-\delta}$ perovskite the $(La_{0.85}Sr_{0.15})CoO_{3-\delta}$ perovskite dissociates and reacts with chromium at the conditions for the oxidation which results in formation of (Cr,Co)-spinel, $LaCrO_3$ and $SrCrO_4$. The (Cr,Co)-spinel phase formed in the LSC coating incorporated Mn during longer oxidation, but the spinel phase still has approximately double the amount of Cr as compared to the spinel phase observed surrounding the LSM perovskite particles in the LSM coating on the Co_3O_4 + LSC coated samples. On the Co_3O_4 + LSC coated samples $LaCrO_3$ and $SrCrO_4$ were detected in the oxide scale, mainly in the spinel phase, below the inner Co_3O_4 coating layer. This suggests that La- and Sr-ions diffuse inwardly through the Co_3O_4 coating layer as illustrated in figure 4.7. The incorporation of the $LaCrO_3$ and $SrCrO_4$ particles into the growing oxide scale might inflict a geometrical protection effect against oxidation since the outwardly diffusing cations would have to diffuse the extra distance around the stable $LaCrO_3$ and $SrCrO_4$ particles to reach the surface of the oxide scale.

Just as for the Co_3O_4 + LSM coated samples residues of the inner Co_3O_4 coating layer are only found on the Co_3O_4 + LSC coated samples if the inner Co_3O_4 coating layer was 15 µm thick. If the inner Co_3O_4 coating layer was 7 µm thick it appeared completely consumed. In this study no exact explanation can be formulated for the lack of sintering/reaction of the inner Co_3O_4 coating when it was applied as 15 µm thick, but as mentioned above it might be possible that the inward diffusion of La and Sr affects the sintering ability of the coating layer just as the inward diffusion of Mn might explain the lack of sintering/reaction of the inner Co_3O_4 coating on the Co_3O_4 + LSM coated samples.

In the LSC coating a (Co,Cr,Mn)-spinel phase was observed surrounding the brighter $LaCrO_3$ and $SrCrO_4$ particles. This phase was probably formed partly by the reduction of the Co when the LSC perovskite dissociated and reacted with Cr. The reduction process would lead to the formation of oxidation products without any measurable oxygen uptake from the atmosphere taking place. The reduction of the LSC coating might also provide the growing oxide scale with oxygen which means that the oxide scale might be growing faster than the measured weight gain indicates. There is probably a contribution of oxygen from the Co_3O_4 + LSC coating, but the scale thicknesses on the Co_3O_4 + LSC coated samples are smaller than the scale thicknesses measured on the uncoated Crofer samples indicating a real protection effect of the Co_3O_4 + LSC coating.

Even though the oxide scale on the Co_3O_4 + LSC coated samples generally is thin and contains low amounts of chromium, heavily oxidized areas are observed with high iron and chromium contents. These areas might create easy and fast diffusion paths for chromium that might poison the cathode/electrolyte interface in the fuel cell. These heavily oxidized areas were only observed on the Co_3O_4 + LSC coated samples when the inner Co_3O_4 coating layer was 15 µm thick. Between the 7 µm Co_3O_4 + 15 µm LSC, 15 µm Co_3O_4 + 15 µm LSC, 7 µm Co_3O_4 + 15 µm LSM, and 15 µm Co_3O_4 + 15 µm LSM coated samples the 15 µm Co_3O_4 + 15 µm LSC had the highest Co content in the coating/oxide system relative to the Mn content. Based on this it is

suggested that a certain amount of Mn would have to be present in the coating to stabilize the (Co,Cr)-oxides forming in the presence of a cobalt rich coating. A similar observation was done by D. L. Douglass, who showed that a minor amount of Mn indicated to slow down the (Cr,Co)-spinel growth on a Co-20Cr alloy [23]. During large access to Co and limited access to Mn fast forming (Co,Cr)-oxides might function as a drain for chromium that delays the formation of a protecting oxide scale which in turn leads to making outward iron diffusion possible. The 15 µm Co_3O_4 + 15 µm LSC coated Crofer 22APU samples are also the samples with the largest iron content in the outer oxide scale in table 4.3. But, the iron signals detected here might also be a result of overlap of the K_β for Mn over the K_α for Fe as mentioned in section 4.3.1. A third explanation could be that the small amounts of iron that are detected in the outer oxide scale are the residues of the iron oxide that form initially before a protection oxide scale has established.

Comparing the weight gain data for the Co_3O_4 + LSC coated samples with the ones found for a single layer coatings consisting of LSC and Co_3O_4 in chapter 3 there is a significant decrease in the weight gain when the LSC and Co_3O_4 coatings are combined into a dual layer coating. Crofer samples coated with a single layer of LSC in chapter 3 presented a spinel composition close to $Cr_{1.5}Mn_{0.5}CoO_4$ and a spinel ratio of ca. 40%. When an inner Co_3O_4 coating layer was applied under the LSC coating, the chromium content was decreased with ca. 60% and the spinel ratio in the oxide scale was increased 100%. The spinel ratio was also increased and the chromium content in the outer oxide scale slightly lowered compared to the spinel ratio and the chromium content found on the single layer Co_3O_4 coated Crofer 22APU samples in chapter 3. Just as for the Co_3O_4 + LSM coated samples the inner Co_3O_4 coating layer seems to provide an extra Co-source that will make the spinel phase in the oxide scale grow faster and lower the chromium diffusion.

4.5 Conclusions

Crofer 22APU samples coated with a dual coating consisting of Co_3O_4 + LSM/LSC present lower weight gain during oxidation than Crofer samples coated with LSM, LSC or Co_3O_4. The presence of an inner Co_3O_4 coating also seems to decrease the chromium content in the outmost oxide scale and at the same time increase the spinel ratio in the oxide scale compared to the single coated samples. The effect on the weight gain, chromium content and spinel ratio was improved if the thickness of the inner Co_3O_4 coating layer was increased from 7 to 15 µm. A thicker inner Co_3O_4 coating layer also seemed to stabilize the chromium content at a low level in the forming spinel phase on the oxide scale. However, when the outer perovskite coating consisted of LSC there are indications of a need for manganese in the oxide/coating-system to stabilize the forming oxides. Heavily oxidized spots along the cross-section containing high amounts of iron and chromium were observed on the 15 µm Co_3O_4 + 15 µm LSC coated samples; these might function as fast and easy diffusion paths for Cr. Added to this the spinel phase found in the LSC layer, on the Co_3O_4 + LSC coated samples, has almost twice the Cr-content compared to a similar spinel phase found in the LSM layer, on the Co_3O_4 + LSM coated samples.

In chapter 3 classifications of three different interaction mechanisms between the growing oxide scale and the applied single coating were formulated.

A Surface covering coating

B Surface covering coatings with chemical reaction with the forming oxide
C Incorporation of coating particles

A single coating consisting of Co_3O_4 was classified to have interaction mechanisms of type B with the growing oxide scale. For a single coating layer of LSM a combination of interaction mechanisms A and B appeared to provide the best description of the system. Finally the interaction mechanism for a single coating layer of LSC was classified to consist of a combination of type B and C. Based on the observations in this chapter of the Co_3O_4 + LSM and Co_3O_4 + LSC dual coatings, it is presumed that when creating the dual coatings the interaction mechanisms found for the single layer coatings are preserved. Meaning, the interaction mechanism for the Co_3O_4 + LSM coating is classified as a combination of type A and B, and the interaction mechanism for the Co_3O_4 + LSC coating is classified as a combination of type B and C.

It appeared as if the larger reactivity the coating had the lower weight increase and indirectly oxidation rate were observed for the Crofer 22APU samples. However, a too large reactivity of the coating system also seemed to be unfavourable for stabilizing the growing oxide scale as seen on the Co_3O_4 + LSC coated samples where fast and easy diffusion paths for degrading chromium were created in the heavily oxidized areas.

As noted in chapter 3 the spinel compositions registered on the oxidation samples in this chapter are kinetically determined due to the extensive range of stable spinel compositions in the Co-Mn-Cr-O system, cf. figure 3.10.

For Crofer 22APU alloy in use in an SOFC-stack as interconnect material there appear to be several advantages with a dual coating consisting of either Co_3O_4 + LSM or Co_3O_4 + LSC. The double layer coatings lowered the oxidation rate of the alloy noticeably more than the corresponding single layer coatings. The lowered oxidation rate would lead to a thinner oxide scale, which would improve the electrical conductivity across the interconnector. The dual coatings also lowered the chromium content in the formed oxide scales successfully. This would indirectly lead to a lowered degree of chromium poisoning of the cathode/electrolyte interface in a SOFC and less degradation of the SOFC efficiency. However, the Co_3O_4 + LSC coated Crofer 22APU samples presented heavily oxidized areas with high amounts of iron and chromium along the surface of the samples. These areas would create fast and easy diffusion paths for chromium that would poison the cathode/electrolyte interface.

4.6 Reference List

1. Hilpert, K., Quadakkers, W., and Singheiser, L., in *Handbook of Fuel Cells - Fundamentals, Technology and Applications*, Edited by W. Vielstich, A. Lamm, and H. Gasteiger (John Wiley & Sons, Chicester, UK, 2003), Vol. 4, p. 1037

2. Badwal, S. P. S., Deller, R., Foger, K., Ramprakash, Y. and Zhang, J. P., Solid State Ionics, 99, 297 (1997)

3. Kuznecov M., Eichler K., Megel S. and Otschik P., in Proceedings of the European SOFC Forum 2004, p. 1573

4. Yang, Z. G., Hardy, J. S., Walker, M. S., Xia, G. G., Simner, S. P. and Stevenson, J. W., Journal of the Electrochemical Society, 151, A1825-A1831 (2004)

5. Quadakkers, W. J., Greiner, H., Hansel, M., Pattanaik, A., Khanna, A. S. and Mallener, W., Solid State Ionics, 91, 55 (1996)

6. Yang, Z. G., Xia, G. G. and Stevenson, J. W., Electrochemical and Solid State Letters, 8, A168-A170 (2005)

7. Chen, X., Hou, P. Y., Jacobson, C. P., Visco, S. J. and De Jonghe, L. C., Solid State Ionics, 176, 425 (2005)

8. Larring, Y. and Norby, T., Journal of the Electrochemical Society, 147, 3251 (2000)

9. Zahid M., Tietz F., Sebold D. and Buchkremer H.P., in Proceedings of the European SOFC Forum 2004, p. 820

10. Persson, Å., Hendriksen, P. V., Mikkelsen, L. and Somers M.A.J., Defect andDiffusion Forum, 258-260, 372 (2006)

11. Kofstad P, *High Temperature Corrosion* (Elsevier Applied Science Publishers LTD, 1988)

12. Hansson A.N., PhD.-thesis, Oxides in the Co-Cr-Fe-O system and oxidation behaviour of coated Fe-22Cr steel, 2004

13. Jankowski, J., Thomas, G. and Camby, L. P., Solid State Ionics, 101, 1321 (1997)

14. Kale, G. M., Pandit, S. S. and Jacob, K. T., Transactions of the Japan Institute of Metals, 29, 125 (1988)

15. Oneill, H. S. C., Physics and Chemistry of Minerals, 12, 149 (1985)

16. Xing, L. and Prewitt, C. T., Physics and Chemistry of Minerals, 17, 168 (1990)

17. Dieckmann, R., Journal of Physics and Chemistry of Solids, 59, 507 (1998)

18. Topfer, J., Aggarwal, S. and Dieckmann, R., Solid State Ionics, 81, 251 (1995)
19. Lu, F. H., Tinkler, S. and Dieckmann, R., Solid State Ionics, 62, 39 (1993)
20. Lu, F. H. and Dieckmann, R., Solid State Ionics, 53-6, 290 (1992)
21. Lu, F. H. and Dieckmann, R., Solid State Ionics, 59, 71 (1993)
22. Lu, F. H. and Dieckmann, R., Solid State Ionics, 67, 145 (1993)
23. Douglass, D. L. and Armijo, J. S., Oxidation of Metals, 3, 185 (1971)

5. Comparison of coated alloys with varying manganese content

5.1 Introduction

Various coatings have been tested on some promising types of interconnect alloys in literature [1-4], but a coating that is successful on one type of steel might not be as successful on another steel type. In this study LSM, LSC, Co_3O_4, Co_3O_4 + LSM, and Co_3O_4 + LSC coatings were applied as slurry coatings on Crofer 22APU and Sandvik 1C44Mo20 alloys, which is a designed interconnect alloy and a test alloy respectively [5]. The samples were oxidized in air containing 1% water at 900˚C for a maximum of 4000 hours. The observed oxidation behaviours of the two coated alloys were analyzed and compared.

The Crofer 22APU and the Sandvik 1C44Mo20 alloys had among other things different manganese content. By applying a Co_3O_4 + LSC coating on five additional model alloys, with different manganese contents, the effect of the manganese content in the alloy on the interaction between the alloy and the Co-rich coating was investigated. This is interesting since manganese access has shown to have an effect on the behaviour of the dual coatings discussed in chapter 4.

5.2 Experimental

5.2.1 Sample preparations and oxidation experiment

Samples with the dimension 20*20*0.3 mm^3 were cut from foils of Crofer 22APU, Sandvik 1C44Mo20, Sandvik OYC44, Sandvik 350, Sandvik 433, Sandvik 434 and Sandvik 515. The compositions of the different alloys are listed in table 2.1. The samples were etched in hydrofluoric acid to remove any native oxides before they were slurry coated on both sides using a hand gun spray. The slurries consisting of approximately 33 wt.% powder of the coating material dissolved in ethanol with a small amount of PVP-binder. In table 5.1, the different coating types deposited on the different alloy samples and the number of each alloy/coating combination prepared, are listed. Besides the coated samples in table 5.1, six etched Crofer 22APU and six etched Sandvik 1C44Mo20 samples were left uncoated. For more detailed information about sample preparation see chapter 2.

Table 5.1. Overview of alloy/coating combinations prepared for cyclic oxidation in air containing 1% water at 900˚C.

	15 μm LSM	**15 μm LSC**	**15 μm Co_3O_4**	**15 μm Co_3O_4 + 15 μm LSM**	**15 μm Co_3O_4 + 15 μm LSC**
Crofer 22APU	6	6	6	6	6
Sandvik 1C44Mo20	6	6	6	6	6
Sandvik OYC44	-	-	-	-	6
Sandvik 350	-	-	-	-	6
Sandvik 433	-	-	-	-	6
Sandvik 434	-	-	-	-	6
Sandvik 515	-	-	-	-	6

The coated and uncoated samples were weighed and mounted free-hanging on Pt-hooks in a furnace with a volume of ca. 4.3 $\cdot 10^{-3}$ m^3. The samples were oxidized for 4000 hours in air containing 1% water at 900˚C. Every 250th hour the furnace was cooled down and the samples were weighed at RT. The heating and cooling ramps were set to 120˚C/h. The gas flow in the furnace was set to ca. 72 $\cdot 10^{-3}$ m^3/h, whereby the gas in the furnace chamber should be completely exchanged around 17 times per hour.

After 500, 1000, 2000, and 4000 hours of oxidation, uncoated and coated Crofer 22APU and Sandvik 1C44Mo20 samples were removed from the furnace to prepare cross-sections of the oxidized samples, as described in detail in chapter 2. For the Sandvik OYC44, Sandvik 350, Sandvik 433, Sandvik 434 and Sandvik 515 samples, there were only prepared cross-sections of the samples oxidized for 1000 hours.

5.3 Results

5.3.1 Oxidation behaviour and microstructure

The weight gain data for LSM, LSC, Co_3O_4, Co_3O_4 + LSM, and Co_3O_4 + LSC coated Crofer 22APU and Sandvik 1C44Mo20 are plotted against the square rote of time in figure 5.1 below. The weight gain plots for both uncoated and coated Crofer 22APU samples in figure 5.1.a-b show parabolic oxidation behaviour as discussed in detail in chapters 3 and 4. In chapter 3 it is also discussed that the integral constant, C, in equation 3.1, which is a mathematical description of parabolic oxidation, also corrects for the first 250 hours of oxidation that is ignored in this study for the oxidized samples. The organic binder in the coatings burns off during the first 250 hours of oxidation, and this leads to unreliable weight gain data during these initial hours of oxidation.

In figure 5.1.c only weight gain plots of coated Sandvik 1C44Mo20 are included since the oxide scales on the uncoated Sandvik 1C44Mo20 samples spalled off already after 250 hours oxidation, and no reliable weight gain data could be collected. The coated Sandvik 1C44Mo20 samples on the other hand, all showed well-adhering oxide scales, and no signs of break away oxidation tendencies were observed in the weight gain data collected as can be seen from the curves in figure 5.1.c. Most of the coated Sandvik 1C44Mo20 samples also presented weight gain plots indicating parabolic oxidation behaviour just as the coated Crofer samples. Only the LSC coated Sandvik 1C44Mo20 samples showed indications on deviation from parabolic oxidation behaviour. As discussed in chapter 3 the oxidation of coated alloys is a complex system due to interaction between the alloy and the coating. The LSC coated Sandvik 1C44Mo20 samples are assumed to follow an overall parabolic oxidation behaviour. However, due to the possible reaction mechanisms present in the complex oxidation system becoming more noticeable, the weight gain plot tends to deviate slightly from characteristic parabolic oxidation behaviour. These are the same arguments used for the oxidation behaviour of ZrO_2 and Al_2O_3 coated Crofer 22APU samples in chapter 3.

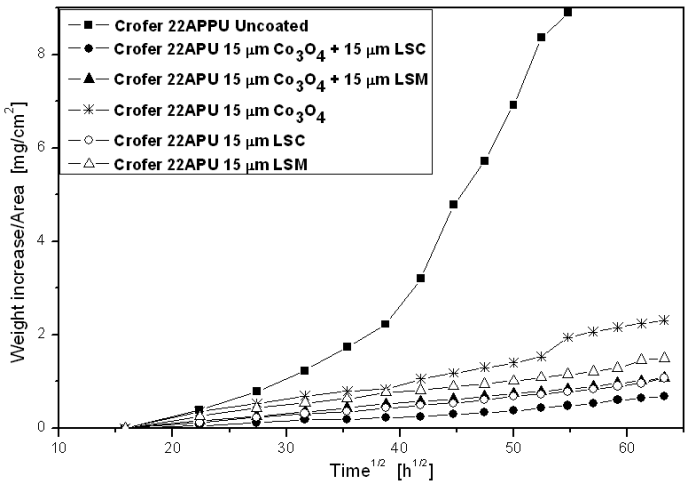

Figure 5.1.a. The weight increase-time$^{1/2}$ plots neglecting the first 250 hours of oxidation for uncoated and coated Crofer samples in the long term, cyclic oxidation experiment at 900˚C in air containing 1% water.

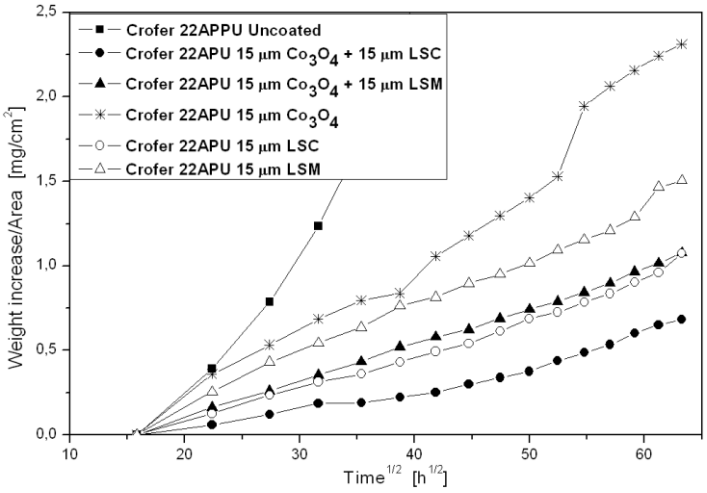

Figure 5.1.b. The weight increase-time$^{1/2}$ plots neglecting the first 250 hours of oxidation for uncoated and coated Crofer samples in the long term, cyclic oxidation experiment at 900˚C in air containing 1% water, enlargement of figure 5.1.a.

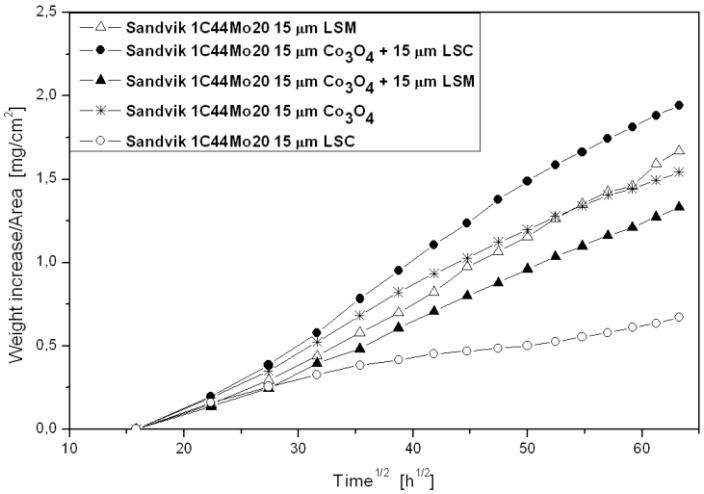

Figure 5.1.c. The weight increase-time$^{1/2}$ plots neglecting the first 250 hours of oxidation for coated Sandvik 1C44Mo20 samples in the long term, cyclic oxidation experiment at 900˚C in air containing 1% water.

The calculated parabolic rate constants for the samples in figure 5.1 are presented in table 5.2. For the LSC coated Sandvik 1C44Mo20 sample, two parabolic constants are listed since the slope of the weight increase – time$^{1/2}$ plot tends to decrease after ca. 1000 hours of oxidation.

Table 5.2.a. Parabolic rate constants for uncoated and coated Crofer 22APU samples after 4000 hours oxidation neglecting the weight gain from the first 250 hours.

	$k_{p,1}\cdot10^{-3}$ $[(mg/(cm^2h^{1/2}))^2]$	Time [h]	$k_{p,2}\cdot10^{-3}$ $[(mg/(cm^2h^{1/2}))^2]$	Time [h]
15 μm Co_3O_4[b] + 15 μm LSC[b]	0.11±0.02	2500	0.57	2500-4000
15 μm Co_3O_4[b] + 15 μm LSM[a]	0.49±0.1	3000	0.77	3000-4000
15 μm LSC[b]	0.35±0.08	4000		
15 μm LSM[a]	1.2±0.2	4000		
15 μm Co_3O_4[b]	1.3±0.2	2750	1.9	3000-4000
Uncoated	7.5±1.1	1000		

Table 5.2.b. Parabolic rate constants for coated Sandvik 1C44Mo20 samples after 4000 hours oxidation neglecting the weight gain from the first 250 hours.

	$k_{p,1}\cdot10^{-3}$ $[(mg/(cm^2h^{1/2}))^2]$	Time [h]	$k_{p,2}\cdot10^{-3}$ $[(mg/(cm^2h^{1/2}))^2]$	Time [h]	Remark
15 μm LSC[c]	0.42±0.06	1250	0.10±0.01	1250-4000	Dev. from parabolic ox.
15 μm Co_3O_4[d] + 15 μm LSM[b]	0.66±0.2	4000			
15 μm LSM[b]	0.92±0.3	4000			
15 μm Co_3O_4[d]	1.2±0.1	4000			
15 μm Co_3O_4[d] + 15 μm LSC[c]	1.4±0.5	4000			

The weight gain plots in figure 5.1 and the parabolic rate constants in table 5.2 show that on Crofer 22APU samples dual layer coatings, consisting of an inner Co_3O_4 coating layer and an outer LSM or LSC coating layer, significantly decrease the oxidation rate compared to single layer LSM, LSC or Co_3O_4 coatings. The coated Crofer 22APU samples with the lowest weight gain are the samples coated with a Co_3O_4 + LSC dual coating. More details about the coated Crofer samples can be found in chapters 3 and 4.

For the coated Sandvik 1C44Mo20 sample the lowest oxidation rate was observed for the LSC coated samples. When an inner Co_3O_4 coating layer was applied below the LSC coating, the oxidation rate was drastically increased compared to LSC and Co_3O_4 single coated Sandvik 1C44Mo20 samples. The oxidation mechanism also appeared to change into a more pronounced parabolic oxidation mechanism compared to the LSC coated Sandvik 1C44Mo20 samples. When the Co_3O_4 and LSM coatings were combined to a Co_3O_4 + LSM dual coating on Sandvik 1C44Mo20 samples the oxidation rate was decreased ca. 20% compared to the LSM and Co_3O_4 single layer coated Sandvik 1C44Mo20 samples. The same effect was observed on the Crofer 22APU samples, but on these alloy samples the Co_3O_4 + LSM dual layer coating decreased the oxidation rate by ca. 60% compared to the single layer LSM and Co_3O_4 coatings.

In figure 5.2-5, micrographs of the oxidized Crofer 22APU and Sandvik 1C44Mo20 samples coated with LSM, LSC, Co_3O_4 +LSM, and Co_3O_4 +LSC are displayed.

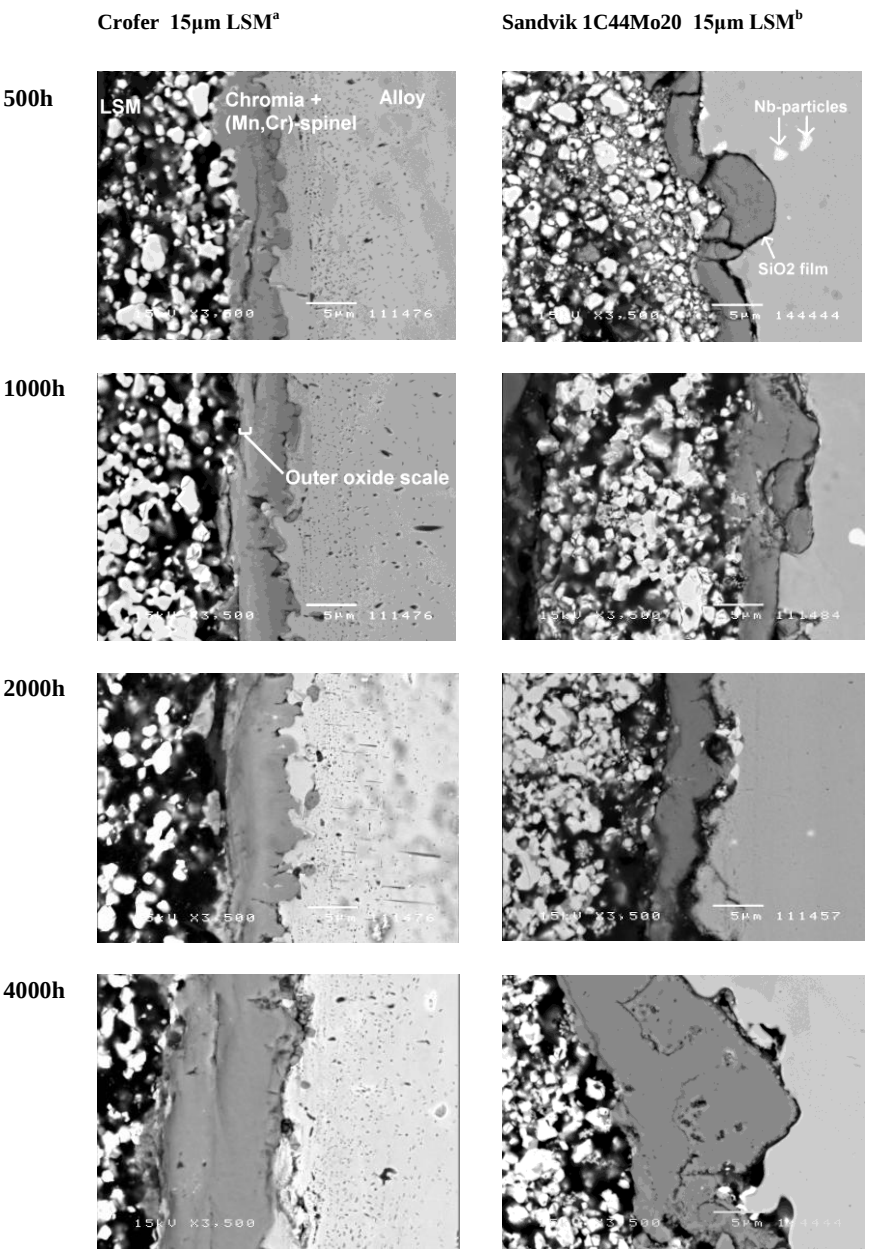

Fig. 5.2. BSE micrographs of cross-sections of the 15 µm LSM coated Crofer 22APU and Sandvik 1C44Mo20 samples, with the oxidation times indicated to left of the pictures.

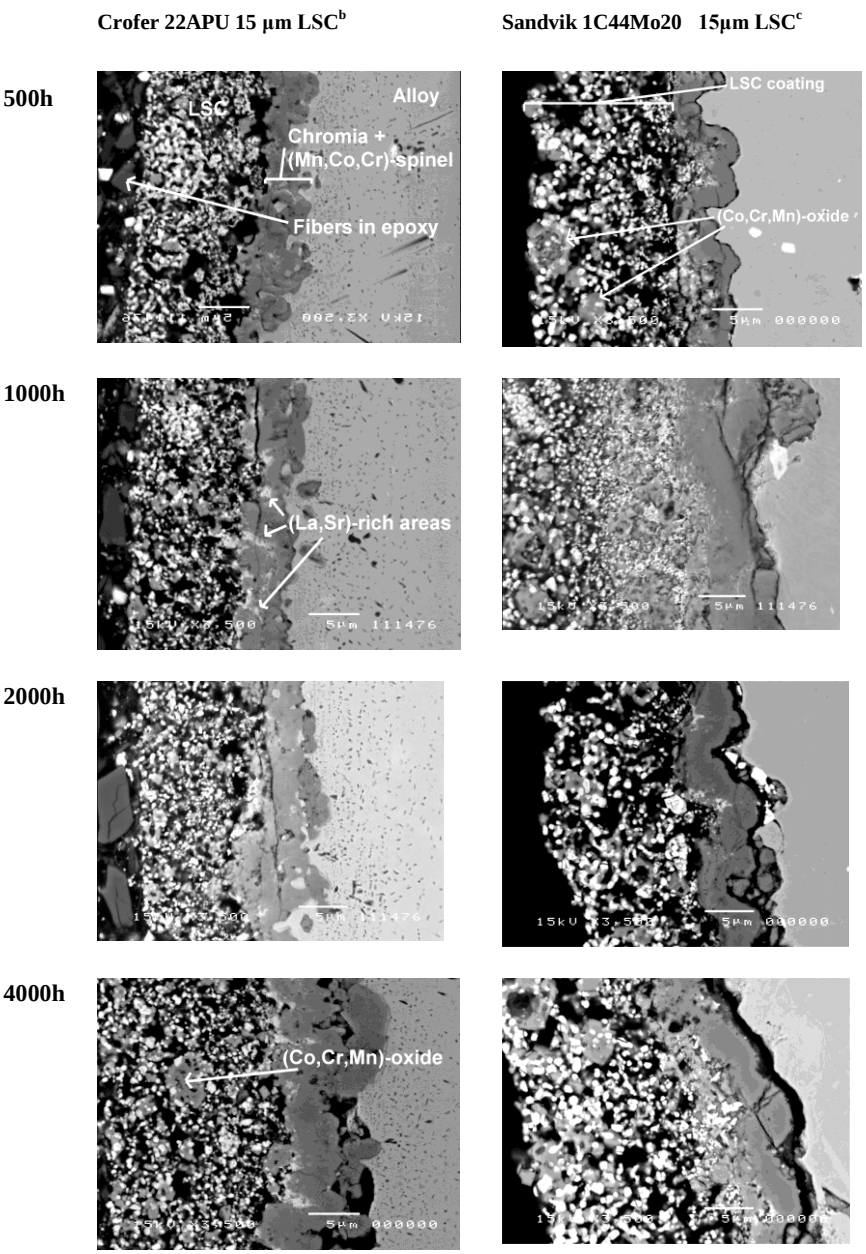

Fig. 5.3. BSE micrographs of cross-sections of the 15 µm LSC coated Crofer 22APU and Sandvik 1C44Mo20 samples, with the oxidation times indicated to left of the pictures.

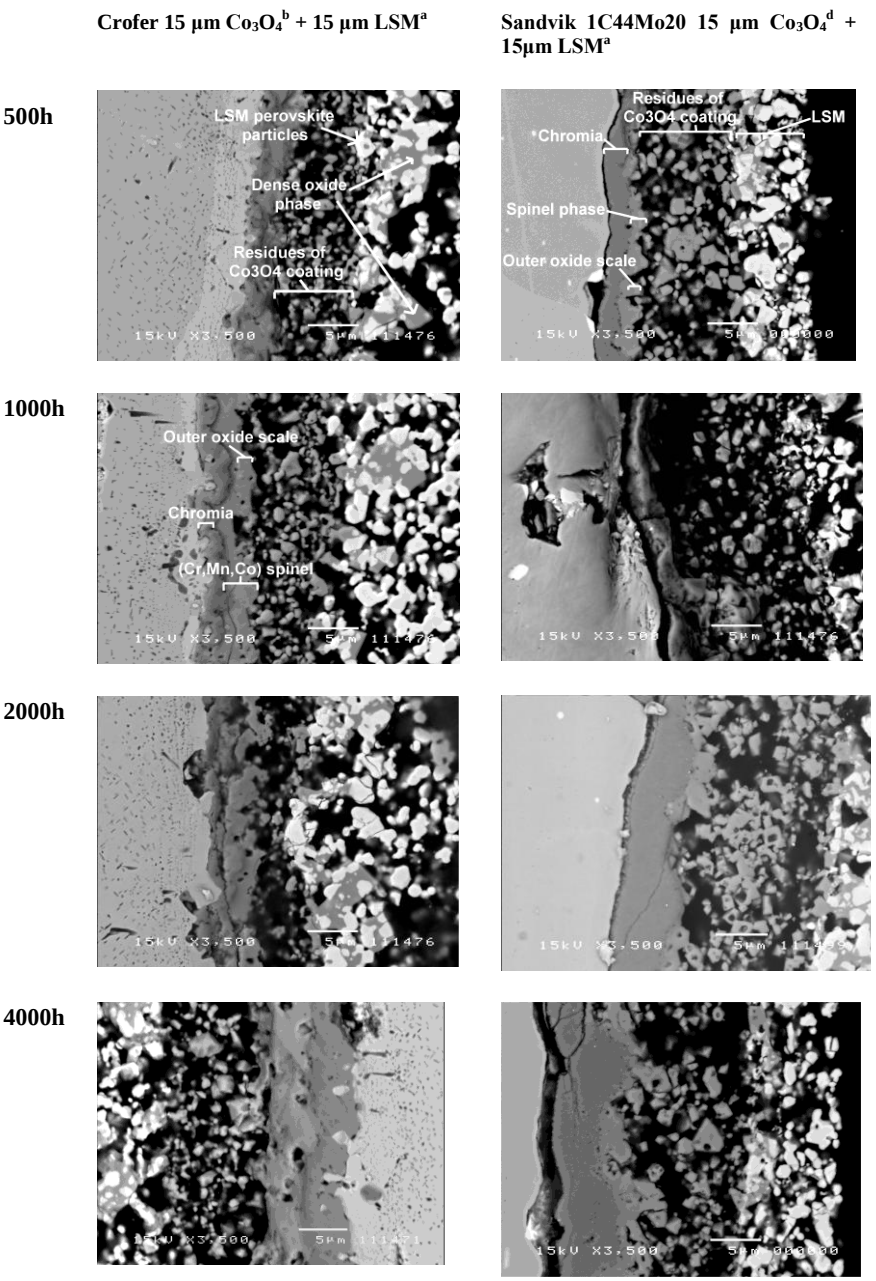

Fig. 5.4. BSE micrographs of cross-sections of the 15 µm Co_3O_4 + 15 µm LSM coated Crofer 22APU and Sandvik 1C44Mo20 samples, with the oxidation times indicated to left of the pictures.

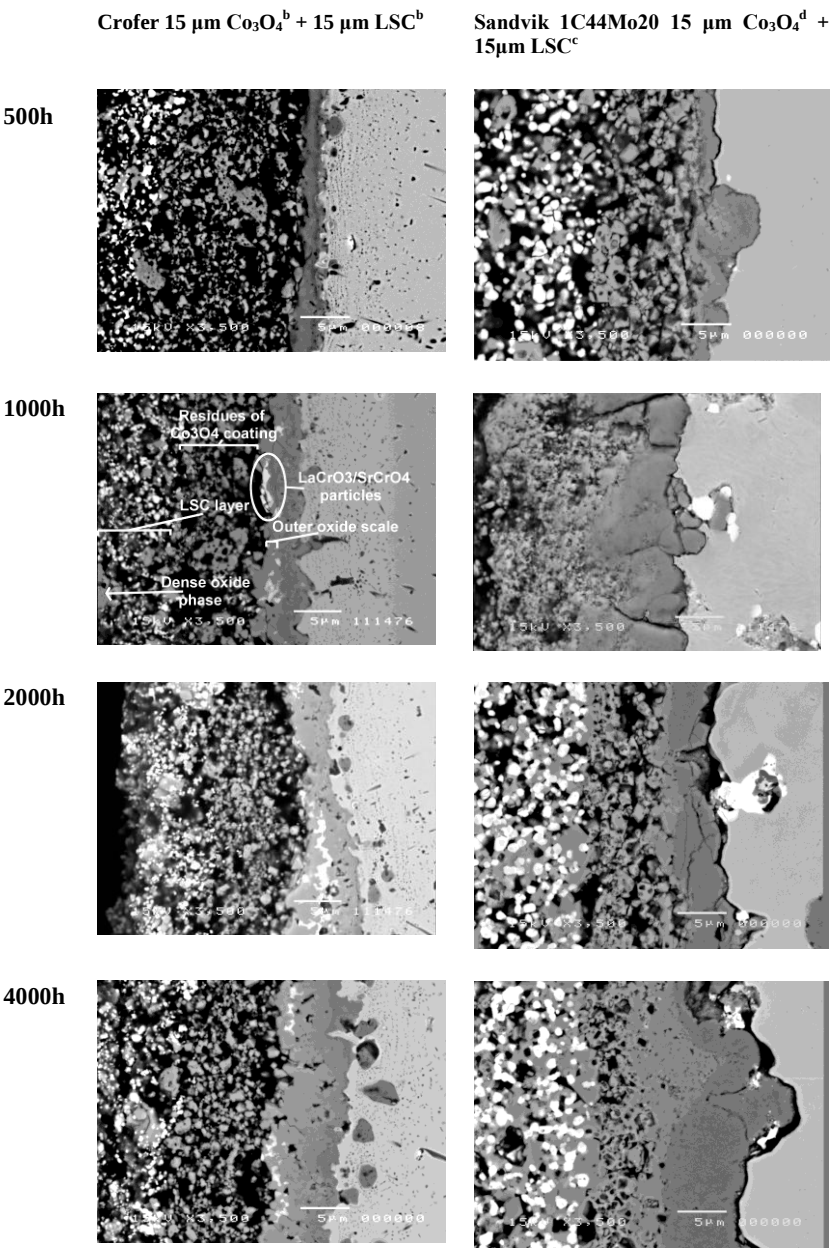

Fig. 5.5. BSE micrographs of cross-sections of the 15 µm Co_3O_4 + 15 µm LSM coated Crofer 22APU and Sandvik 1C44Mo20 samples, with the oxidation times indicated to the left of the pictures.

The micrographs of the Crofer 22APU samples have been presented earlier in this thesis in chapter 3 and 4, and for more detailed comments and discussion regarding these micrographs these chapters should be consulted.

When studying the Sandvik 1C44Mo20 samples it becomes apparent that no signs of internal oxidation of Al_2O_3 or TiO_2 are found in the alloy beneath the oxide scale as on the Crofer 22APU samples. Instead bright areas, both within the alloy and in the oxide scale/alloy interface, can be seen. These areas were identified as Nb-rich areas by EDS analysis. Similar Nb-rich areas were not found on the Crofer 22APU samples. Also noted in the oxide/alloy interface on the Sandvik 1C44Mo20 samples is a dark, thin, relatively continuous Si-rich film, which most likely consists of SiO_2. On the Crofer 22APU samples only traces of SiO_2 was observed at the oxide/alloy interface, and it occurred in the shape of small particles instead of a continuous film.

When comparing the oxide/perovskite coating interface on the LSM and LSC coated Crofer 22APU and Sandvik 1C44Mo20 samples, it was found that bright particles originating from the coating tended to be incorporated into the growing oxide scale, when the perovskite coating consisted of LSC. When the perovskite coating consisted of LSM the bright perovskite particles instead seemed to be pushed ahead of the oxide scale. For the Sandvik 1C44Mo20 samples the incorporation of heavy particles originating from the LSC coating was more extensive than on the Crofer 22APU samples.

On the Co_3O_4 + LSM coated Crofer 22APU and Sandvik 1C44Mo20 samples, residues of the inner Co_3O_4 coating are visible as separated oxide particles, cf. figure 5.4. On the Co_3O_4 + LSM coated samples in the LSM coating layer dense, light grey oxide phases are observed, surrounding the heavier perovskite particles on both the Crofer 22APU and Sandvik 1C44Mo20 samples.

Comparing the micrographs of the Co_3O_4 + LSC coated Crofer 22APU and Sandvik 1C44Mo20 samples in figure 5.5 it was found that the inner Co_3O_4 coating layer had sintered/reacted extensively on the Sandvik 1C44Mo20 samples while still consisting of well separated and defined particles on the corresponding Crofer 22APU samples. On the Sandvik 1C44Mo20 samples the sintered/reacted inner Co_3O_4 coating layer appeared to have completely incorporated the LSC coating in an oxide phase after ca. 2000 hours of oxidation. The extensive sintering/reaction of the inner Co_3O_4 coating layer on the Sandvik 1C44Mo20 samples created problems when determining the borders of the oxide scale to measure the oxide scale thickness. Therefore, the scale thicknesses on the Co_3O_4 + LSC coated Sandvik 1C44Mo20 samples are left out in table 5.3 below where the scale thicknesses on the oxidized samples are presented. On the Co_3O_4 + LSC coated Crofer 22APU samples bright $LaCrO_3$ and $SrCrO_4$ particles were observed in the oxide scales below the residues of the inner Co_3O_4 coating. These La- and Sr-rich areas seemed to mainly be situated in the outer spinel phase of the oxide scales. No such $LaCrO_3$ and $SrCrO_4$ particles were observed on the Co_3O_4 + LSC coated Sandvik 1C44Mo20 samples.

Table 5.3.a. Measured oxide scale thickness, t, for uncoated and coated Crofer after 4000 hours oxidation.

	t [μm] 500 h	**t [μm] 1000 h**	**t [μm] 2000 h**	**t [μm] 4000 h**	**Remark**
15 μm LSC[b]	4.1±1.2	4.3±1.6	5.4±1.5	9.2±1.9	Ox. scale
15 μm LSM[a]	4.7±1.6	6.5±1.7	7.3±1.3	10.6±2.8	Ox. scale
15 μm Co_3O_4[b] + 15 μm LSC[b]	2.6±0.9	3.6±0.9 *(27.3±3.4)*	5.8±2.2 *(26.2±3.5)*	8.1±1.8 *(26.1±12.6)*	Ox. scale (Heavily ox. areas)
15 μm Co_3O_4[b] + 15 μm LSM[a]	4.4±1.4	5.2±1.4	6.0±2.6	8.5±1.8	Ox. scale
Uncoated	9.8±3.2	11.9±2.9	15.3±2.0		Ox. scale

Table5.3.b. Measured oxide scale thickness, t, for coated Sandvik 1C44Mo20 after 4000 hours oxidation.

	t [μm] 500 h	**t [μm] 1000 h**	**t [μm] 2000 h**	**t [μm] 4000 h**	**Remark**
15 μm LSM[b]	3.0±0.7	5.3±1.8	5.8±1.8	10.2±2.8	Ox. scale
15 μm LSC[c]	3.6±1.1	7.9±2.0	5.4±1.6	6.9±2.3	Ox. scale
15 μm Co_3O_4[d] + 15 μm LSM[b]	4.5±1.9	5.5±2.1	6.8±2.2	10.9±3.6	Ox. scale

For all the coated Crofer 22APU samples and for the LSM and Co_3O_4 + LSM coated Sandvik 1C44Mo20 samples, a continuous increase in the thickness of the oxide scales were observed which agrees well with the continuous increase in weight gain. However, for the LSC coated Sandvik 1C44Mo20 samples, the measured oxide scale thicknesses varied in an irregular way over time and did not increase continuously as the weight gain of the samples indicated it should. This irregularity in the scale thicknesses is probably caused by the difficulties in determining the boarders of the oxide scale due to incorporation of particles originating from the LSC coating into the oxide scale.

Comparing the weight gain data for the LSM and Co_3O_4 + LSM coated Sandvik 1C44Mo20 samples it was found that the presence of an inner Co_3O_4 coating layer slightly decreased the oxidation rate. This could indicate the formation of a thinner oxide scale on the Co_3O_4 + LSM coated samples compared to the LSM coated samples. However, when considering the measured oxide scale thicknesses in table 5.3 above, the thicker scale was found on the dual coated samples. This might be caused by the fact that parts of the Co_3O_4 coating is merged together with the growing oxide scale. It could also be possible that the growing oxide scale has an oxygen uptake from the coating which would lead to an oxide growth not registered in the total weight gain of the sample.

The scale thicknesses discussed above are measured on the most consistent oxide scale microstructure found on the coated Crofer 22APU and Sandvik 1C44Mo20 samples. However, there are some characteristics found on some of the samples which are not included in the measured and calculated average scale thicknesses in table 5.3. In figure 5.6 below some heavy oxidized areas found on Co_3O_4 + LSC coated Crofer 22APU samples are present. These areas were not found on the 500 hours oxidized sample, but for the 1000, 2000, and 4000 hours sample ca. 5 areas on each cross-section were observed. The average thicknesses of these areas are presented in table 5.3 within parentheses. Also included in figure 5.6 are micrographs of characteristics found for the Co_3O_4 + LSC coated Sandvik 1C44Mo20 samples oxidized for 2000 and 4000 hours. It appears as if the oxide scale grows into the alloy at "oxide pits"

along the whole cross-section. This characteristic only becomes prominent after ca. 1000 hours of oxidation, but the initialized "oxide pits" are visible already after 500 hours of oxidation.

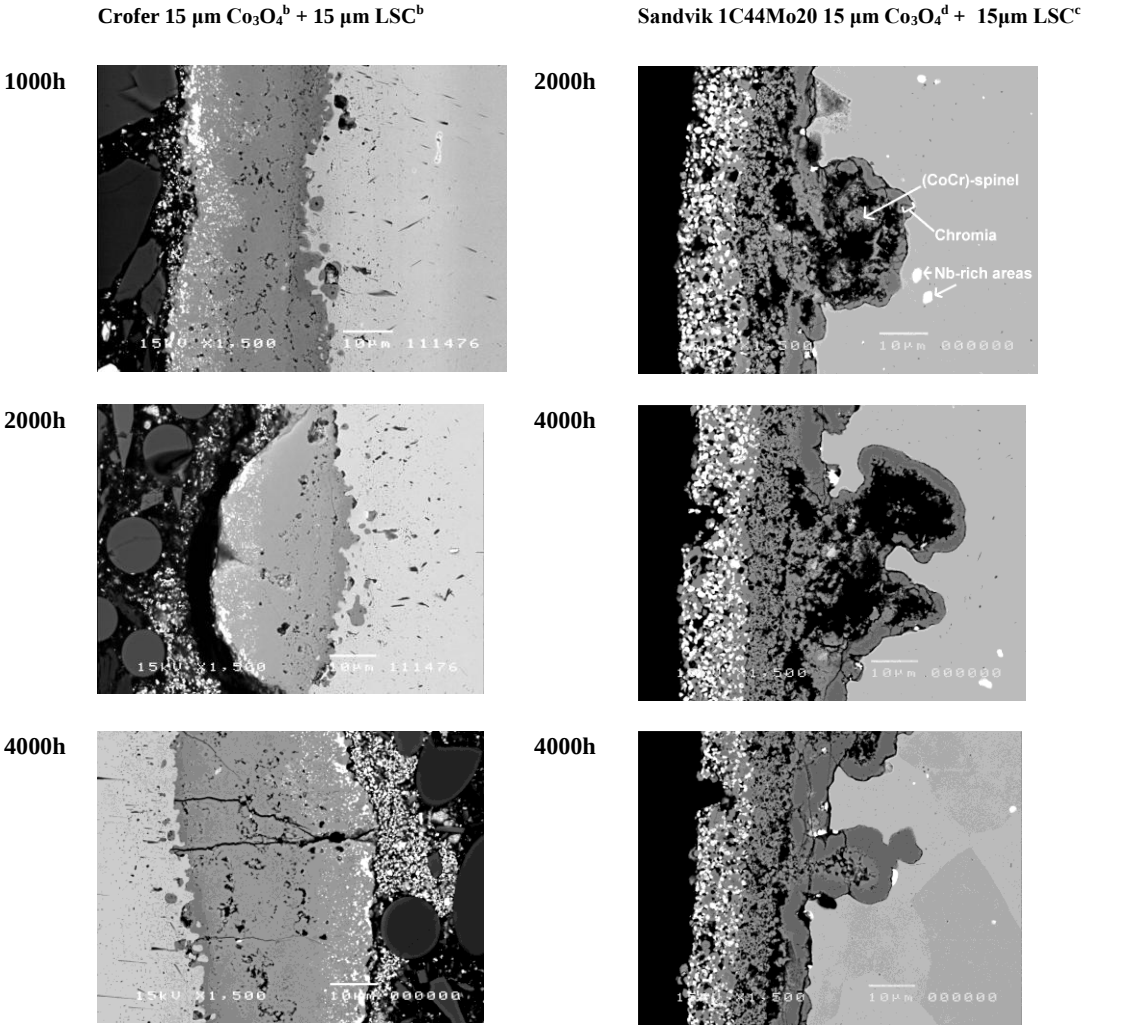

Fig. 5.6. BSE micrographs of cross-sections of the samples, with the oxidation times indicated to the left of the pictures.

In figure 5.6 two different types of "oxide pits" from the Co_3O_4 + LSC coated Sandvik 1C44Mo20 sample oxidized for 4000 hours are visible. One of the "oxide pits" consists of a void in the middle and the other one is filled up with an oxide phase. These characteristic "oxide pits" were not observed on any of the LSM, Co_3O_4 + LSM, or LSC coated Sandvik 1C44Mo20 samples.

5.3.2 EDS data

In figure 5.7, line scans across the oxide scales on the LSM, LSC, Co_3O_4 + LSM, and Co_3O_4 + LSC coated Crofer 22APU and Sandvik 1C44Mo20 samples oxidized for 2000 hours are presented. Also included in figure 5.7 are a line scan across one of the heavily oxidized areas on the Co_3O_4 + LSC coated Crofer 22APU sample oxidized for 2000 hours and an "oxide pit" on Co_3O_4 + LSC coated Sandvik 1C44Mo20 sample oxidized for 4000 hours.

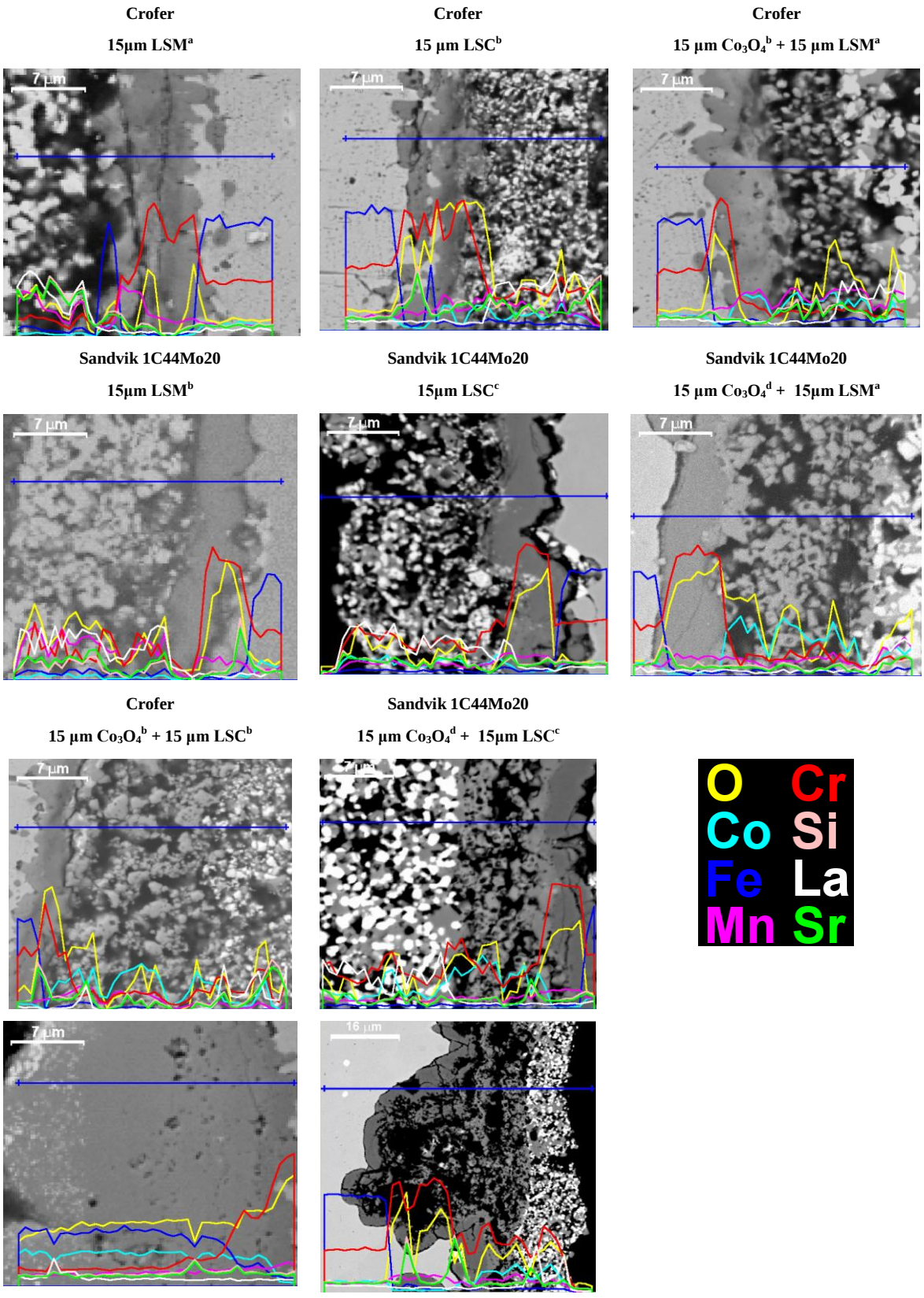

Fig. 5.7. Line scans across the oxide scales formed on coated Crofer 22APU and Sandvik 1C44Mo20 samples oxidized for 2000 hours and across a heavily oxidized spot on Co_3O_4 + LSC coated Crofer 22APU oxidized for 2000 hours and an "oxide pit" on Co_3O_4 + LSC coated Sandvik 1C44Mo20 oxidized for 4000 hours.

When studying the line scans across the outer oxide scale on the coated Crofer 22APU samples, and specifically the LSM coated sample, the Mn-signal increases significantly while the Cr-signal decreases, cf. figure 5.7. In figure 5.2-5 type examples of the outer oxide scale are marked. For the Crofer 22APU samples coated with LSC, Co_3O_4 + LSM, or Co_3O_4 + LSC an increase in the Co-signal is also detected in the outer oxide scale. In the heavily oxidized area on the Co_3O_4 + LSC coated Crofer 22APU sample, the most prominent signal is iron. The iron oxide on these heavily oxidized spots also contains high amounts of Co and some Cr. A more detailed discussion of the coated Crofer 22APU samples is given in chapter 3 and 4.

Studying the line scans across the oxide scales on the Sandvik 1C44Mo20 samples it is observed that the characteristic increase of the Mn signal in the outer oxide scale found on the Crofer 22APU samples, is hardly seen on the Sandvik 1C44Mo20 samples. For the LSC, Co_3O_4 + LSM and Co_3O_4 + LSC coated Sandvik 1C44Mo20 samples the Co-signal increased as the Cr-signal decreased. The line scan across the "oxide pit" on the Co_3O_4 + LSC coated Sandvik 1C44Mo20 sample indicated high amounts of Cr-rich oxides within the "oxide pit".

In table 5.4 the spinel compositions in the outer oxide scales, based on point analysis on the coated Crofer 22APU and Sandvik 1C44Mo20 samples, are presented. It was found that the spinel phase in the outer oxide scale on the LSM coated Crofer samples consists of a (Cr,Mn)-spinel with a Cr/Mn-ratio of ca. 50/50. For the LSC coated Crofer samples a (Cr,Co,Mn)-spinel is detected and the relation between the cations in the spinel is ca. 50/33/17. When a Co_3O_4 coating layer is applied below the LSM and LSC coating layers on the Crofer samples, a significant decrease in the chromium content in the outer oxide scale is observed compared to the single layer coated samples. The Mn content in the outer oxide scale was twice as high for the Co_3O_4 + LSM coated Crofer than for the Co_3O_4 + LSC coated Crofer samples after 2000 hours oxidation.

Table 5.4.a. Spinel composition in the outer oxide scale on the Crofer 22APU samples.

	500 h				*1000 h*				*2000 h*				*4000 h*			
	Cr	**Mn**	**Co**	**Fe**	**Cr**	**Mn**	**Co**	**Fe**	**Cr**	**Mn**	**Co**	**Fe**	**Cr**	**Mn**	**Co**	**Fe**
15 µm LSM[a]	1.4±0.1	1.5±0.1			1.5±0.2	1.4±0.2			1.6±0.2	1.3±0.2			1.6±0.1	1.3±0.1		
15 µm LSC[b]	1.4±0.5	0.6±0.3	0.9±0.2	0.1±0.0	1.5±0.4	0.5±0.2	0.9±0.2	0.1±0.1	1.3±0.4	0.7±0.4	0.9±0.1	0.1±0.1	1.6±0.3	0.5±0.2	0.8±0.1	0.1±0.1
15 µm Co_3O_4[b] **+ 15 µm LSM**[a]	0.5±0.2	0.6±0.1	1.8±0.1	0.1±0.0	0.4±0.1	0.9±0.2	1.7±0.2	0.1±0.0	0.5±0.2	1.1±0.2	1.4±0.1		0.7±0.1	0.8±0.1	1.5±0.2	
15 µm Co_3O_4[b] **+ 15 µm LSC**[b]	0.4±0.2	0.7±0.1	1.6±0.1	0.3±0.1	0.4±0.1	0.7±0.1	1.7±0.1	0.2±0.1	0.5±0.2	0.6±0.1	1.7±0.2	0.2±0.1	0.5±0.2	0.4±0.1	1.8±0.1	0.2±0.1

Table 5.4.b. Spinel composition in the outer oxide scale on the Sandvik 1C44Mo20 samples, but on the LSC coated sample the oxide most likely consists of a corundum structure.

	500 h				*1000 h*				*2000 h*				*4000 h*			
	Cr	**Mn**	**Co**	**Fe**	**Cr**	**Mn**	**Co**	**Fe**	**Cr**	**Mn**	**Co**	**Fe**	**Cr**	**Mn**	**Co**	**Fe**
15 µm LSM[b]	1.9±0.2	1.0±0.2		0.1±0.1	2.0±0.4	0.9±0.4			2.2±0.6	0.7±0.6		0.1±0.1	2.0±0.1	1.0±0.1		
15 µm LSC[c]	2.4±0.5	0.1±0.1	0.5±0.4		2.6±0.3		0.3±0.3		2.6±0.5		0.4±0.4		2.6±0.5		0.3±0.4	0.1±0.2
15 µm Co_3O_4[d] **+ 15 µm LSM**[b]	0.4±0.6	0.3±0.2	2.3±0.6		0.5±0.3	0.3±0.1	2.2±0.3		0.9±0.5	0.2±0.1	1.8±0.5	0.1±0.1	1.1±0.4	0.2±0.1	1.7±0.3	

In table 5.4.b it is seen that the spinel compositions found in the outer oxide scale on the LSM coated Sandvik 1C44Mo20 samples are close to $MnCr_2O_4$ during the whole 4000 hours long oxidation process.

For the Co_3O_4 + LSM coated Sandvik 1C44Mo20 samples the spinel is dominated by cobalt. During the first 1000 hours of oxidation the chromium and manganese contents are almost equally small, but as the oxidation continues the chromium content grows significantly. After 4000 hours oxidation the Mn content is almost negligible and the spinel composition is close to $CrCo_2O_4$.

For the LSC coated samples the Mn content is negligible in the spinel, and the cobalt content small, which suggests that the outer oxide consists of a corundum phase instead of a spinel phase according to the Co-Mn-Cr-O phase diagram in figure 3.10. No spinel composition in the outer oxide scale for the Co_3O_4 + LSC coated Sandvik 1C44Mo20 samples are listed in table 5.4 above, since there are difficulties determining where the forming oxide scale ends and the sintered/reacted inner Co_3O_4 coating layer begins. However, it was observed that the spinel phase close to the growing chromia scale had a composition close to $CoCr_2O_4$ with only a few percent Mn.

Comparing the spinel compositions found on the coated Crofer 22APU samples and the coated Sandvik 1C44Mo20 samples in the outer oxide scale it is obvious that the chromium content generally is higher on the Sandvik 1C44Mo20 samples. At the same time it was observed that the spinel phases formed on the Crofer 22APU samples has higher Mn content than the corresponding spinel phases on the Sandvik 1C44Mo20 samples, cf. figure 4.3.

The residues of the inner Co_3O_4 coating layer on the dual coated Crofer 22APU and Sandvik 1C44Mo20 samples changed composition after oxidation independent of how extensively the layer had merged with the growing oxide scale. The composition depends on the distances from the alloy surface. In table 4.2 the average spinel composition across the residues of the inner Co_3O_4 coating layer on the dual coated Crofer 22APU samples are presented. In table 5.5 the corresponding measurements are presented for the dual coated Sandvik 1C44Mo20 samples.

Table 5.5. Average spinel composition across the residues of the Co_3O_4 coating on the 15 µm Co_3O_4 + 15 µm LSM and 15 µm Co_3O_4 + 15 µm LSC coated Sandvik 1C44Mo20 samples.

	15 µm Co_3O_4[d] + 15 µm LSM[b]				***15 µm Co_3O_4[d] + 15 µm LSC[c]***			
	Cr	**Mn**	**Co**	**Fe**	**Cr**	**Mn**	**Co**	**Fe**
500 h	0.1±0.0	0.1±0.2	2.8±0.2		0.1±0.1		2.8±0.1	
1000 h	*Lack of data*				*Lack of data*			
2000 h	0.5±0.3	0.3±0.1	2.2±0.3		0.6±0.3		2.3±0.3	
4000 h	0.5±0.2	0.4±0.1	2.2±0.1		1.6±0.3	0.1±0.1	1.4±0.3	

The amount of manganese in the residues of the inner Co_3O_4 coating layer was lower on the Sandvik 1C44Mo20 samples than on the Crofer 22APU samples. For the Co_3O_4 + LSC coated Sandvik 1C44Mo20 samples hardly any manganese was detected, instead a drastic increase in the chromium content was observed after 4000 hours of oxidation. For the Co_3O_4 + LSM coated Sandvik 1C44Mo20 samples, small

amounts of manganese were observed in the residues of the inner Co_3O_4 coating layer. However, it was only twice the amount of manganese registered on the corresponding Crofer 22APU sample.

In the LSM and LSC coating layer on the Co_3O_4 + LSM and Co_3O_4 + LSC coated Crofer 22APU samples, particles of dense oxide phases surrounding the bright perovskite particles were observed. The spinel compositions found in these areas on the Crofer 22APU samples are listed in table 4.5 and 4.6. In table 5.6.a the spinel compositions found in the dense oxide particles surrounding the bright perovskite particles in the LSM coating layer on the Co_3O_4 + LSM coated Sandvik 1C44Mo20 samples, are listed. The spinel composition found in the dense oxide phase surrounding the perovskite particles in the LSC coating on the Co_3O_4 + LSC coated Sandvik 1C44Mo20 samples are listed in table 5.6.b.

Table 5.6.a. Spinel composition in the oxide particles surrounding the perovskite particles in the LSM coating layer on the 15 μm Co_3O_4 + 15 μm LSM coated Sandvik 1C44Mo20 samples.

	Cr	**Mn**	**Co**	**Fe**
500 h	0.2	0.9	1.9	
1000 h				
2000 h	0.4	0.6	2.0	
4000 h	0.3	0.6	2.2	

Table 5.6.b. Spinel composition in the oxide phase surrounding the perovskite particles in the LSC coating layer on the 15 μm Co_3O_4 + 15 μm LSC coated Sandvik 1C44Mo20 samples.

	Cr	**Mn**	**Co**	**Fe**
500 h	0.1		2.9	
1000 h				
2000 h	1.6		1.4	
4000 h	1.8		1.2	

The chromium content in the oxide phase in the LSC coating layer on the Co_3O_4 + LSC coated Sandvik 1C44Mo20 samples was significantly higher than in the oxide phase in the LSM coating layer on the Co_3O_4 + LSM coated Sandvik 1C44Mo20 samples. The chromium content in the oxide phase in the LSC coating layer on the Co_3O_4 + LSC coated Sandvik 1C44Mo20 samples was also twice as high compared to the chromium content found in the oxide phase in the LSC coating layer on the corresponding Crofer 22APU samples, cf. table 4.6.

The oxide compositions found in the heavily oxidized spots on the Co_3O_4 + LSC coated Crofer 22APU samples were found to contain large amounts of iron, cobalt and some chromium. When the same investigation of the characteristic "oxide pits" on the Co_3O_4 + LSC coated Sandvik 1C44Mo20 samples was performed, no iron rich oxides were found. The oxide scale along the side of the "oxide pits" consists of a chromia phase, and any oxide present in the middle of an "oxide pit" tend to consist of a $(CrCo)_3O_4$ spinel phase close to $CoCr_2O_4$ composition and with only traces of manganese.

EDS mappings of the growing dense oxide scales on the LSM coated Sandvik 1C44Mo20 samples were collected to get an overview of the composition of the

scales. By combining the mapping signals from Cr, Mn, La, and Fe, images where the spinel part of the oxide scale is easily discerned form the chromia layer was achieved. On these mappings the relative areas of the spinel and chromia phases was measured, and in table 5.7 below the spinel ratios of the oxide scales found for the LSM coated Sandvik 1C44Mo20 samples are presented with the spinel ratios found for the corresponding Crofer 22APU samples. For the Crofer 22APU samples a spinel ratio of ca. 40% was found. For the LSM coated Sandvik 1C44Mo20 samples a spinel ratio around ca. 20% was observed.

Table 5.7. Spinel ratio of the total oxide scale on LSM coated Crofer 22APU and Sandvik 1C44Mo20 samples oxidized in air with 1% water at 900˚C for a total of 4000 hours.

	500 h	**1000 h**	**2000 h**	**4000 h**
Crofer 22APU + 15 μm LSM[a]	0.41	0.35	0.43	0.39
Sandvik 1C44Mo20 + 15 μm LSM[b]	0.25	0.28	0.27	0.18

5.3.3 Oxidation data on the complementary Sandvik samples

In figure 5.8 the weight increase data collected during the oxidation experiment for the Co_3O_4 + LSC coated Sandvik model alloys, OYC44, 350, 433, 434, 515, and 1C44Mo20, and Crofer 22APU samples are presented in a weight increase-time$^{1/2}$ plot.

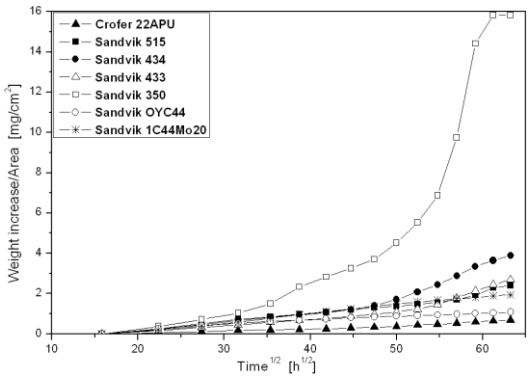

Figure 5.8.a. The weight increase-time$^{1/2}$ plots for Co_3O_4 + LSC coated Crofer 22APU and Sandvik model alloys, OYC44, 350, 433, 434, 515, and 1C44Mo20, samples in the long term, cyclic oxidation experiment at 900˚C in air containing 1% water.

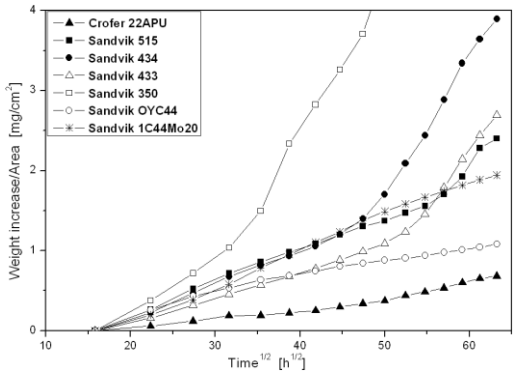

Figure 5.8.b. The weight increase-time$^{1/2}$ plots for Co_3O_4 + LSC coated Crofer 22APU and Sandvik model alloys, OYC44, 350, 433, 434, 515, and 1C44Mo20, samples in the long term, cyclic oxidation experiment at 900˚C in air containing 1% water, enlargement of figure 5.8.a.

Most of the weight gain curves in figure 5.8 tend to appear linear, indicating parabolic oxidation behaviour, and in table 5.8 below the calculated parabolic rate constants are presented. In table 5.8 the Mn content in the alloys is presented next to the parabolic rate constants. The OYC44 sample is the only sample that shows slight deviations from a linear weight gain plot. Just as discussed for the LSC coated Sandvik 1C44Mo20 sample in section 5.3.1, the Sandvik OYC44 samples are most likely oxidizing predominantly via a parabolic growth rate. However, the other oxidation reactions present in the complex system have become noticeable which results in a slight deviation from parabolic distribution in the weight gain plot. The Sandvik 350 samples appear to experience drastic increase in the weight gain rate after ca. 1250 hours of oxidation indicating break away oxidation. The Sandvik 433, 434, and 515 samples also appear to experience some increase in the oxidation rate after ca. 2000 hours oxidation, but the increase is much less drastic than for the 350 samples and is probably indicating a change in the rate determining diffusion process. The lowest weight gain was observed for the Crofer 22APU samples. Second lowest weight gain was observed for the Sandvik 433 and Sandvik OYC44 samples.

Table 5.8. Parabolic rate constants for Sandvik 1C44Mo20, Sandvik OYC44, Sandvik 350, Sandvik 433, Sandvik 434, Sandvik 515, and Crofer 22APU alloy samples coated with 15 µm Co_3O_4 + 15 µm LSC together with the corresponding Mn contents in the alloys.

15 µm Co_3O_4 + 15 µm LSC on:	**Mn [wt.%]**	**$k_{p,1}\cdot10^{-3}$ [(mg/(cm^{2}h$^{1/2}$))^2]**	**Time [h]**	**$k_{p,2}\cdot10^{-3}$ [(mg/(cm^{2}h$^{1/2}$))^2]**	**Time [h]**	**Remark**
Crofer 22APU	0.4	0.11±0.02	2500	0.57	2500-4000	
Sandvik OYC44	0.3	0.99±0.1	1250	0.27±0.04	1250-4000	Dev. from parabolic ox.
Sandvik 433	0.6	0.98±0.1	2750	20	2750-4000	
Sandvik 1C44Mo20	0.1	1.4±0.5	4000			
Sandvik 515	0.3	1.7±0.2	3250	14	3250-4000	
Sandvik 434	5.1	2.0±0.3	2250	27	2250-4000	
Sandvik 350	0.1	5.2±1.3	1250	34±3.0	1250-2500	

According to the results in table 5.8 it seems as if there is a trend towards lower oxidation rate when the manganese content is above 0.3 wt.%, and increasing oxidation rate for manganese contents above ca. 0.5 wt.%.

The microstructure for the six alloys coated with Co_3O_4 + LSC and oxidized for 1000 hours are presented below in figure 5.9.

Sandvik 1C44Mo20 (0.1 wt.%)
15 µm Co_3O_4[d] + 15 µm LSC[c]

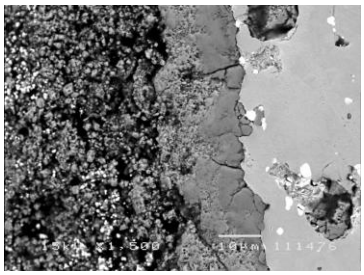

Sandvik 350 (0.1 wt.%)
15 µm Co_3O_4[d] + 15 µm LSC[d]

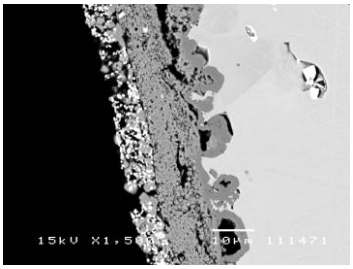

Sandvik OYC44 (0.3 wt.%)
15 µm Co_3O_4[d] + 15 µm LSC[d]

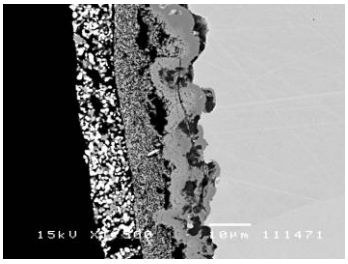

Sandvik 515 (0.3 wt.%)
15 µm Co_3O_4[d] + 15 µm LSC[d]

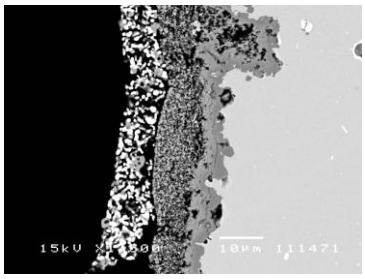

Crofer 22APU (0.4 wt.%)
15 µm Co_3O_4[b] + 15 µm LSC[b]

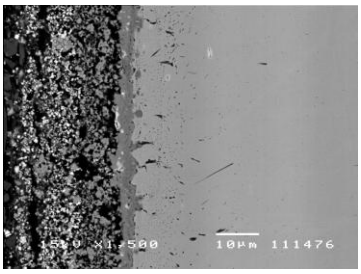

Crofer 22APU Local heavy oxidation area
15 µm Co_3O_4[b] + 15 µm LSC[b]

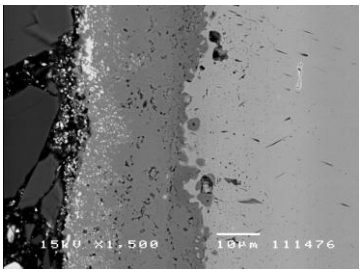

Sandvik 433 (0.6 wt.%)
15 µm Co_3O_4[d] + 15 µm LSC[d]

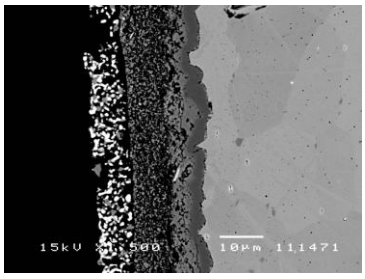

Sandvik 434 (5.1 wt.%)
15 µm Co_3O_4[d] + 15 µm LSC[d]

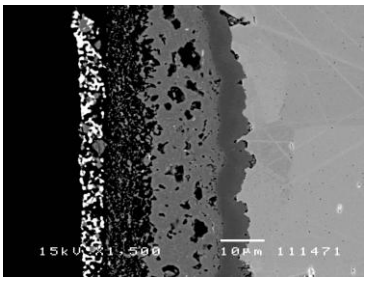

Sandvik 434 Local heavy oxidation area
15 µm Co_3O_4[d] + 15 µm LSC[d]

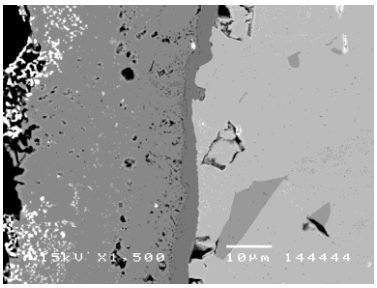

Fig. 5.9. BSE micrographs of cross-sections of the 15 µm Co_3O_4 + 15 µm LSC coated Sandvik 1C44Mo20, Sandvik OYC44, Sandvik 350, Sandvik 433, Sandvik 434, Sandvik 515, and Crofer 22APU oxidized for 1000 hours.

When comparing the micrographs of the different samples it appears as if the oxide scale becomes more and more discernable and the merging of the coating and the oxide scale decreases as the Mn content increases in the alloy. At the same time, the thicknesses of the oxide scales also appear to increase, when the Mn content in the alloy reaches a certain amount. On the Sandvik 434 samples, which contains ca. 5 wt.% Mn, the oxide scale is thicker in comparison to the oxide scales on the other samples. This is in accordance with literature that has shown that a too high Mn content in the alloy leads to increased oxidation rate due to the high diffusion rate of Mn in chromia [6, 7]. The Sandvik 434 samples displays the same type of local heavily oxidized areas as the Crofer 22APU samples as seen in figure 5.9. The Co_3O_4 + LSC coated Sandvik 1C44Mo20 samples displays “oxide pits” along the cross-section as visible in figure 5.6, and similar “oxide pits” could be found along the

cross-section on the Sandvik 350 samples. Tendencies towards "oxide pit" formation were also observed on Sandvik OYC44 and Sandvik 515 alloys.

In figure 5.10 the line scans across the oxide scales formed after 1000 hours oxidation on the different Sandvik alloy samples and the Crofer 22APU sample coated with Co_3O_4 + LSC are presented.

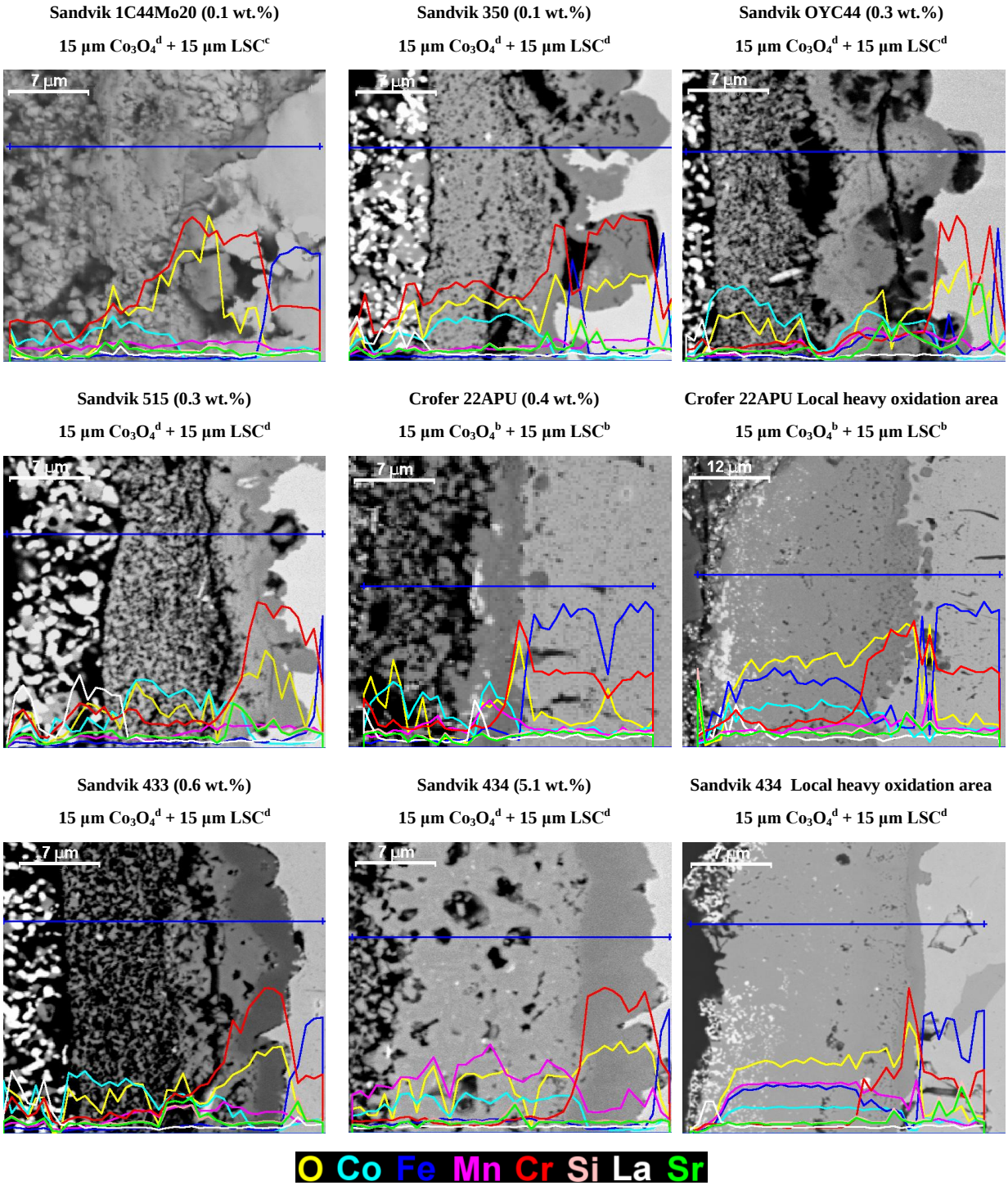

Fig. 5.10. Line scans across cross-sections of the 15 µm Co_3O_4 + 15 µm LSC coated Sandvik 1C44Mo20, Sandvik OYC44, Sandvik 350, Sandvik 433, Sandvik 434, Sandvik 515, and Crofer 22APU oxidized for 1000 hours.

The Sandvik 1C44Mo20 and Sandvik 350 samples, which are the alloy samples with the lowest Mn content, had significant amounts of chromium in the layer that originally was the inner Co_3O_4 coating layer. As the Mn content in the alloy increases, the Cr amount in the inner Co_3O_4 coating layer decreases and at the same time the Mn content in the outer dense growing oxide scale increases. Crofer 22APU and Sandvik 434 both presented heavily oxidized areas, and when performing line scans across these areas, significant iron content was observed in both. For Sandvik 434 with over 5 wt.% Mn content, the Mn signal was equally significant as the iron signal in the heavily oxidized spots. On the Crofer 22APU sample the Mn signal on the other hand was even smaller than the Co signal in heavily oxidized spots.

5.4 Discussion

5.4.1 Crofer 22APU versus Sandvik 1C44Mo20

For the Crofer 22APU alloy it was found that dual coatings consisting of Co_3O_4 + LSM and Co_3O_4 + LSC resulted in lower oxidation rate than the single layer coatings consisting of Co_3O_4, LSM and LSC, as seen in figure 5.1. The dual layer coatings also presented lower chromium content in the outer oxide scales than the corresponding single layer coatings according to the spinel compositions listed in table 5.4. The oxide scales were all generally well defined on the coated Crofer 22APU samples irrespectively of what coating was applied. The only exception would be the Co_3O_4 + LSC coated Crofer 22APU samples which display a few heavily oxidized areas along the cross-section on each oxidized sample as seen in figure 5.6. These heavily oxidized areas contained dominantly iron and cobalt as well as relatively high amounts of chromium. These heavily oxidized areas would function as fast and easy diffusion paths for outward diffusing chromium in an SOFC stack which is detrimental for the fuel cells in the stack [8-10]. A possible explanation to why these heavily oxidized areas form could be that the cobalt originating from the Co_3O_4 + LSC coating reacts rapidly with the forming Cr_2O_3 scale on the alloy surface to form a $(CrCo)_3O_4$ spinel. The rapid spinel formation compared to the Cr_2O_3 growth might result in the Cr_2O_3 scale being used up during the spinel formation faster than new Cr_2O_3 can form and iron is able to oxidize [11]. D. L. Douglass and J. S. Armijo showed in a study of a Co-20Cr alloy that addition of manganese tends to slow down the spinel growth [11]. Assuming that this effect also is present for a Fe-20Cr alloy with Mn addition coated with a cobalt rich coating it might explain why the oxide scale generally is thin on the Co_3O_4 + LSC coated Crofer 22APU samples. The outward diffusing manganese originating from the Crofer 22APU alloy might in general be enough to stabilize the spinel formation, but at a few spots along the cross-section the Co-rich spinel formation is able to take off and consume the Cr_2O_3 scale.

Sandvik 1C44Mo20 samples coated with a dual layer coating consisting of Co_3O_4 + LSM presented a slightly lower weight gain than Sandvik 1C44Mo20 samples coated with a single layer of Co_3O_4 or LSM. Sandvik 1C44Mo20 samples coated with a dual coating consisting of Co_3O_4 + LSC on the other hand presented significantly higher weight gain than Sandvik 1C44Mo20 samples coated with a single layer of Co_3O_4 or LSC. In comparison to the Crofer 22APU samples the oxide scale on the coated Sandvik 1C44Mo20 samples only appeared relatively well defined when the coating contained LSM either as a single layer or as a second layer in a dual coating. On the LSC and Co_3O_4 + LSC coated Sandvik 1C44Mo20 samples the growing oxide scales tended to merge with the applied coatings, making it difficult to determine where the

growing dense oxide scale ended and formation of oxide products in the residues of the coatings started. The inner Co_3O_4 coating layer on the Co_3O_4 + LSC coated Sandvik 1C44Mo20 samples was totally reacted and merged with the growing oxide scale and the outer LSC coating layer. In table 5.5 and 5.6 it was seen that the residues of the inner Co_3O_4 coating layer and the oxide phase surrounding the bright perovskite particles in the outer LSC layer contained large amounts of chromium. Accordingly there is a large reactivity between the growing oxide scale and the Co_3O_4 + LSC coating on the Sandvik 1C44Mo20 samples that might explain the large weight gain during oxidation. In addition to this, "oxide pits" were observed in the chromia/alloy interface on the Co_3O_4 + LSC coated Sandvik 1C44Mo20 samples as seen in figure 5.6. Along the alloy surface in these "oxide pits" a thin Cr_2O_3 scale was observed, in the middle a spinel with a composition close to $CoCr_2O_4$ and only a minor addition of Mn was found.

Based on the summarized observations above, the Sandvik 1C44Mo20 samples coated with LSM or Co_3O_4 + LSM appeared to be more successful in forming a protective oxide scale with relatively low chromium content than Sandvik 1C44Mo20 samples coated with LSC or Co_3O_4 + LSC. The explanation might be that there is not enough outward diffusing manganese originating from the Sandvik 1C44Mo20 alloy through the chromia scale to form Mn-containing spinel in the presence of a LSC or Co_3O_4 + LSC coating and the large amounts of cobalt these coatings entails. As mentioned above, previous studies have shown that formation of a $(CrCo)_3O_4$ spinel phase from CoO and Cr_2O_3 is a rapid process but can be slowed down by the presence of Mn [11]. The Mn content in the Sandvik 1C44Mo20 alloy is only ca. 0.1 wt.%, which might be too small a Mn-source, or it could be that the relatively continuous SiO_2 film formed in the alloy/oxide interface function as a diffusion barrier for the outwardly diffusing manganese. The SiO_2 film is formed due to the high silicon content in the alloy. When manganese is present in the coating this might compensate to some degree for the lack of manganese access from the alloy. However, when comparing the summarized observations for the LSM coated Crofer 22APU and Sandvik 1C44Mo20 samples it appears as if manganese originating from the coating is not as efficient in stabilizing the growing spinel phase as manganese originating from the alloy. Crofer 22APU contains 0.4 wt.% manganese and does not develop a continuous silica film in the oxide/alloy interface, which ensures at least a four times larger manganese access in the oxide scale than on the Sandvik 1C44Mo20 samples. The chromium content is lower in the outer oxide scale on the Crofer 22APU samples as seen in table 5.4, and the spinel ratio in the total oxide scale is larger on the Crofer 22APU samples as seen in table 5.7. The oxide scale on the Crofer 22APU samples are thinner and more well defined than the corresponding oxide scales on the Sandvik 1C44Mo20 samples.

The "oxide pits" formed on the Co_3O_4 + LSC coated Sandvik 1C44Mo20 is probably another effect of the low Mn access. It is possible that when there is not enough Mn diffusing outwardly through the growing oxide scale to block and bind the inward diffusing Co in a (Co,Mn,Cr)-spinel phase, cobalt might be able to diffuse further into the Cr_2O_3 scale and initiate a rapid $(CrCo)_3O_4$ spinel phase formation closer to the alloy surface.

5.4.2 The effect of Mn

When the coated Crofer 22APU and Sandvik 1C44Mo20 samples are compared, it appears as if the manganese content/access from the alloy has crucial importance as to whether the applied coatings are successful or not. Samples of five additional alloys were coated with 15 µm Co_3O_4 + 15 µm LSC to investigate this further. No Mn was present in the Co_3O_4 + LSC coating, and any Mn needed to form slower growing Mn-containing and Cr-lean phase as a layer structure on top of the chromia scale would have to originate from the alloy itself.

Considering the weight gain data it was observed that the lowest weight gain was observed for the Crofer 22APU (0.4 wt.% Mn) sample. Second lowest weight gain was observed for the Sandvik OYC44 (0.3 wt.% Mn) and Sandvik 433 (0.6 wt.% Mn) samples. Larger weight gain was observed for the Sandvik 515 (0.3 wt.% Mn), Sandvik 1C44Mo20 (0.1 wt.% Mn), Sandvik 434 (5.1 wt.% Mn), and Sandvik 350 (0.1 wt.% Mn) samples. The microstructure of the oxide scales grown on samples oxidized for 1000 hours were studied and compared. From this it was found that on the Sandvik 1C44Mo20 (0.1 wt.% Mn), Sandvik 350 (0.1 wt.% Mn), Sandvik OYC44 (0.3 wt.% Mn), and Sandvik 515 (0.3 wt.% Mn) samples the growing oxide scales and the coatings tended to merge and tendencies towards "oxide pit" formation at the alloy/oxide interface were observed. The oxide scales on the Crofer 22APU (0.4 wt.% Mn), Sandvik 433 (0.6 wt.% Mn), and Sandvik 434 (5.1 wt.% Mn) samples appeared more well defined, and merging of the growing oxide scales and the coatings and "oxide pit" formation was hardly seen on these samples. Instead the Crofer 22APU (0.4 wt.% Mn) and Sandvik 434 (5.1 wt.% Mn) samples presented a few heavily oxidized spots with high content of iron along the cross-sections. The Sandvik 434 (5.1 wt.% Mn) also presented the generally thickest, dense oxide scale of the oxidized samples. The oxide scale consisted of an inner Cr_2O_3 scale and an outer thick, Mn-rich spinel phase. This is in agreement with observations in literature that ferrous Fe-Cr alloys containing high amounts of manganese tend to show high oxidation rate due to the fast diffusion of Mn through the chromia scale and formation of a Mn-rich oxide on top of the chromia scale [7].

Based on these observations it appears that an optimal Mn content in the alloy is in the range of 0.3-0.5 wt.% when considering protection with the here studied coatings. The Co_3O_4 + LSC coated samples with the lowest weight gain has a Mn content in this range. These samples also present well defined oxide scales that do not merge with the coating layers via a chromium rich oxide phase. The Crofer 22APU, Sandvik 1C44Mo20, Sandvik OYC44, Sandvik 350, Sandvik 433, Sandvik 434, and Sandvik 515 alloys all differ on many more element contents than the manganese content which complicates a direct comparison between the seven samples. However, the comparison still shows a trend indicating that an optimal manganese content between 0.3-0.5 wt.% in the alloy is recommended for a cobalt rich coating on the alloys to be successful.

5.5 Conclusions

The comparison of the oxidation data for the LSM, LSC, Co_3O_4, Co_3O_4 + LSM, and Co_3O_4 + LSC coated Crofer 22APU and Sandvik 1C44Mo20 samples showed that a coating successful on one type of Fe-Cr alloy not necessarily will be successful on another type of Fe-Cr alloy. A lower oxidation rate and a lower chromium content in the outer oxide scale was observed for oxidizing Crofer 22APU samples if they were

coated with dual coatings of Co_3O_4 + LSM or Co_3O_4 + LSC compared to single layer coatings of LSM, LSC, and Co_3O_4. Basically, the reverse was observed for Sandvik 1C44Mo20 samples. Sandvik 1C44Mo20 samples coated with a dual coating of Co_3O_4 + LSM had almost the same weight gain as the Sandvik 1C44Mo20 samples coated with a single layer coating of LSM or Co_3O_4, only a slightly lower oxidation rate was observed for the dual coating. The Co_3O_4 + LSM dual coating did however appear to be more successful in decreasing the chromium content in the outer oxide scale than the LSM single layer coating on Sandvik 1C44Mo20 samples. Sandvik 1C44Mo20 samples coated with a dual coating consisting of Co_3O_4 + LSC presented significantly higher oxidation rate than the Sandvik 1C44Mo20 samples coated with a single layer of Co_3O_4 or LSC. The SEM micrographs of the cross-sections of the Co_3O_4 + LSC coated Sandvik 1C44Mo20 samples revealed a total merging of the growing oxide scale and the two coating layers via a chromium rich $(CrCo)_3O_4$ spinel phase. The lower manganese access in the Sandvik 1C44Mo20 samples compared to the Crofer 22APU samples is a possible explanation to the failure of a cobalt rich coating on the Sandvik 1C44Mo20 samples. It appeared as if a certain amount of manganese is acquired to stabilize the oxide growth on the oxidizing samples. Oxidation data from Co_3O_4 + LSC coated Sandvik 350, Sandvik OYC44, Sandvik 433, Sandvik 434, and Sandvik 515 samples support this theory and indicate that an optimal manganese content in the ferrous Fe-22Cr alloy probably lies somewhere around 0.3-0.5 wt.%.

For a Fe-22Cr interconnect alloy at use in an SOFC-stack there appear to be several advantages with a dual coating design with relatively high levels of cobalt content. The oxidation rate of the alloy is lowered which improves the electrical conductivity across the interconnector. The lowered chromium content in the formed oxide scales indirectly leads to a lowered degree of chromium poisoning of the cathode/electrolyte interface in the SOFC and less degradation of the SOFC efficiency. However, if the interconnect alloy does not contain around 0.3-0.5 wt.% manganese the positive effects of a cobalt rich dual coatings are lost and turns unfavourable instead. If the second coating layer contains manganese, this might compensate to some degree for the lack of manganese in the alloy.

5.6 Reference List

1. Zhu, J. H., Zhang, Y., Basu, A., Lu, Z. G., Paranthaman, M., Lee, D. F. and Payzant, E. A., Surface & Coatings Technology, 177, 65 (2004)

2. Kadowaki, T., Shiomitsu, T., Matsuda, E., Nakagawa, H., Tsuneizumi, H. and Maruyama, T., Solid State Ionics, 67, 65 (1993)

3. Chen, X., Hou, P. Y., Jacobson, C. P., Visco, S. J. and De Jonghe, L. C., Solid State Ionics, 176, 425 (2005)

4. Bateni, M. R., Wei, P., Deng, X. H. and Petric, A., Surface & Coatings Technology, 201, 4677 (2007)

5. Yang, Z. G., Hardy, J. S., Walker, M. S., Xia, G. G., Simner, S. P. and Stevenson, J. W., Journal of the Electrochemical Society, 151, A1825-A1831 (2004)

6. Sabioni, A. C. S., Huntz, A. M., Borges L.C and Jomard F., Philosophical Magazine, 87, 1921 (2007)

7. Marasco, A. L. and Young, D. J., Oxidation of Metals, 36, 157 (1991)

8. Sakai, N., Horita, T., Xiong, Y. P., Yamaji, K., Kishimoto, H., Brito, M. E., Yokokawa, H. and Maruyama, T., Solid State Ionics, 176, 681 (2005)

9. Singhal S.C. and Kendall K., *High Temperature Solid Oxide Fuel Cells Fundamentals, Design and Applications* (Elsevier, Cornwall, 2003)

10. Fujita, K., Hashimoto, T., Ogasawara, K., Kameda, H., Matsuzaki, Y. and Sakurai, T., Journal of Power Sources, 131, 270 (2004)

11. Douglass, D. L. and Armijo, J. S., Oxidation of Metals, 3, 185 (1971)

6. Measurement of ASR of oxide scales grown on single layer and dual layer coated Crofer 22APU

6.1 Introduction

The growth rate of the oxide scales on LSM, LSC, Co_3O_4 + LSM, and Co_3O_4 + LSC coated Crofer 22APU samples were studied measuring the weight gain of these samples during oxidation in air containing 1% water at 900˚C, see chapter 3 and 4. The area specific resistance, ASR, of these oxide scales forming in the interface between the coated interconnect and cathode materials in a SOFC-stack in operation is an important parameter for SOFC application. The object of the present work was therefore to investigate the ASR between the LSM, LSC, Co_3O_4 + LSM, and Co_3O_4 + LSC coated Crofer 22APU samples and adjacent plates of cathode current collector, CCC, material consisting of 95% dense ($La_{0.85}Sr_{0.15}Mn_{1.1}O_{3-\delta}$), LSM15, during oxidation. The ASR measurements on the coated Crofer 22APU samples were done at 950˚C. To determine the effect of oxidation temperature on the ASR and growth rate of the oxide scales on the coated Crofer 22APU samples, complementary ASR measurements were conducted on a Co_3O_4 + LSM coated sample at 900˚C and a weight gain experiment at 950˚C for another Co_3O_4 + LSM coated sample. Furthermore, the effect of an applied mechanical load, and an applied current density on the oxide scale growth was investigated in the ASR measurement set-up running at 900˚C.

6.2 Experimental

6.2.1 Sample preparation of cycling 950˚C oxidation samples

Crofer 22APU samples with the dimension 20*20*0.3 mm^3 with a 2 mm hole in the centre of one side were etched in hydrofluoric acid to remove any native oxides formed during alloy processing. Using a hand spray gun with technical air as carrier gas the slurry coatings were applied on both sides of the Crofer 22APU samples. Six samples were coated with 15 μm Co_3O_4 + 15 μm LSM. For more detailed description of etching and coating procedure see chapter 2.

6.2.2 Sample preparation of ASR measurements

The Crofer 22APU samples used for the ASR measurements were cut in the dimension 20*40*0.3 mm^3 and were perforated at both ends with holes, Ø = 6mm, having a centre distance of 28 mm, as shown in figure 6.1 below. The samples were etched in hydrofluoric acid according to the same etching procedure used for the free-hanging oxidation samples above to remove any native oxides. The coatings of interest where thereafter applied on both sides of the samples on a squared area, 20 x 20 mm^2, centred where the two orthogonal symmetry axes of the samples cross as indicated in figure 6.1. The sample design is adjusted to fit the stack configuration.

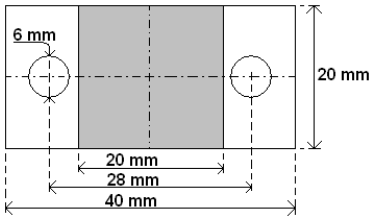

Figure 6.1. Principle sketch of the dimensions of interconnect-stack samples.

In table 6.1 an overview of the number of coated Crofer 22APU samples prepared for the ASR measurements are presented.

Table 6.1. Overview of Crofer 22APU samples prepared for ASR measurements.

Coating	Number of samples
30 µm LSM[a]	1
20 µm LSC[a]	1
15 µm Co_3O_4[e] + 15 µm LSM[c]	2
20 µm Co_3O_4[b] + 18 µm LSM[a]	1
15 µm Co_3O_4[e] + 15 µm LSC[e]	1
20 µm Co_3O_4[b] + 18 µm LSC[b]	1

More Crofer 22APU samples with alternative coatings for ASR measurements were prepared parallel to the ones listed in table 6.1. They are however not further discussed in this chapter even though they were included in one of the ASR measurement set-ups in this study.

6.2.3 Free-hanging oxidation experiment

The 15 µm Co_3O_4 + 15 µm LSM coated Crofer 22APU samples prepared for cyclic oxidation at 950°C were weighed before being mounted free-hanging on Pt-hooks in the oxidation furnace. The samples were thereafter oxidized in air containing 1% water at 950˚C. Every 250th hour of oxidation they were cooled down to room temperature to be weighed. The heating and cooling ramps were set to 120˚C/h. The oxidation furnace had a volume of ca 4.32 $\cdot 10^{-3}$ m^3 and a gas flow of ca 72 $\cdot 10^{-3}$ m^3/h, which means that the gas in the furnace chamber should be completely exchanged about 17 times per hour.

6.2.4 Interconnect-stack experiments

To be able to simultaneously measure the ASR at the interface between the different coated Crofer 22APU samples and the LSM15 contacting layers, units of LSM15 CCC-layer/coated Crofer 22APU sample/LSM15 CCC-layer are set up in a vertical stack with a power supply and Pt-wires to follow the resistance across the interfaces. A stack like this is in the following text denoted an interconnect-stack, and the more detailed experimental set-up is described below.

The interconnect-stack running at 950°C was set up to contain a total of 10 different interconnect samples. In the experimental set-up thin platinum wires, d = 0.3 mm, were spot welded onto the non-coated part of the metal samples, and connected to a data acquisition setup. Contact components of the dimensions 20*20*1 mm^3 of LSM15 were placed on both sides of each metal sample, covering the coated areas. A

voltage probe of rolled down platinum wire was placed on top of the contact layers before also being connected to the data collection setup. 10 units like this built from the 10 metal samples included in the 950°C interconnect-stack were gathered with 0.3 mm thick gold current probes connected to a power supply at both ends of the assembled stack. Through out the oxidation experiment a mechanical load of 0.3 MPa ensured an intimate contact between the various components. A constant current of ca. 0.5 A/cm^2 caused a voltage difference to be established over the interfaces of the alloy samples. The interface resistances were thereafter calculated from these voltage differences between the interconnectors and the platinum probes on the other side of the LSM15 contact component. The measured resistance across the interface consisted of resistance contribution from the LSM15 component, the growing oxide scale and the alloy samples. The resistance in the alloy sample is assumed to be negligible due to the high electrical conductivity in metals [1]. A reference value of the resistance over the LSM15 layer was measured over a LSM15 plate sandwiched between two other LSM15 plated in the interconnect-stack. This reference value for the resistance over the LSM15 plate is subtracted from the total resistance measured across the coated Crofer sample/LSM15 interface and an area specific resistance of the growing oxide scale is achieved. Since each alloy sample in the 950°C interconnect-stack was coated with an identical coating on both sides of the sample, a double determination of the individual interface resistances could be made as well as an evaluation of any possible effect the current direction might have on the oxidation process. The oxidation experiment was carried out in stagnant air in a vertical kiln, built together from two symmetrical half-shell furnaces. In figure 6.2.a a sketch explaining the stacking principle visually is presented.

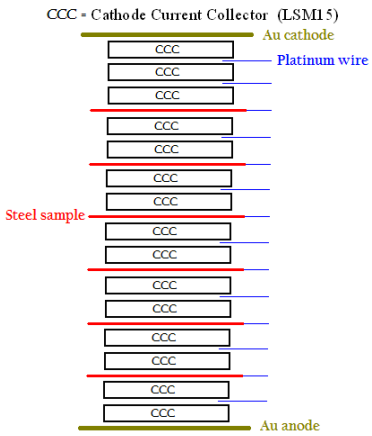

a

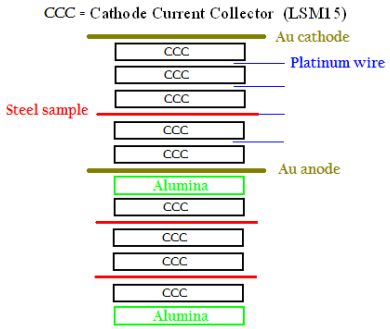

B

c

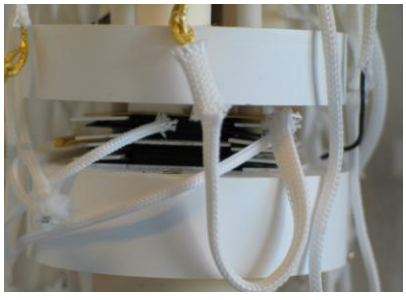

D

Figure 6.2. Principle sketch of the stack experiments, a) the 950°C-stacks, b) the 900°C-stack and c,d) photos of the furnace used for the stack experiments, here with the 900°C-stack set up.

The temperature profile for the 950°C interconnect-stack experiment included a heating ramp of 180°C/h to a binder burn-off step at 430°C, held for 10 hours, followed by further heating up to 950˚C with a ramp of 180°C/h. The test temperature, 950°C, was held for approximately 1000 hours. The temperature was thereafter reduced stepwise to evaluate the temperature dependency of the electrical resistance in the oxide scale. With a cooling ramp of 100°C/h the furnace temperature was lowered in 50°C-steps and held there to stabilize the temperature in the furnace and the interface resistances at the specific temperatures. Finally, five thermal cycles between the test temperature, 950°C, and room temperature were performed to evaluate how large temperature variations affected the electrical resistance in the samples. In figure 6.3.a the detailed temperature profile is presented. The current direction was reversed in the stack for about 300 hours after ca half of the experiment had been conducted to investigate possible effects of the current direction on the degradation rate of the electrical conductivity of the samples.

The momentary ASR values for the degraded samples in the interconnect-stack are read after 1000 hours oxidation before the stepwise cooling starts. The ASR values for the samples at 750˚C after 1000 hours oxidation at 950˚C are read as the momentarily ASR values at the last measurement point at the 750˚C cooling step.

As mentioned above there were a total of 10 different metal samples included in the 950°C stack experiment, but only the four interconnect samples consisting of LSM, LSC, Co_3O_4 + LSM, and Co_3O_4 + LSC coated Crofer 22APU will be studied in more detail in this chapter.

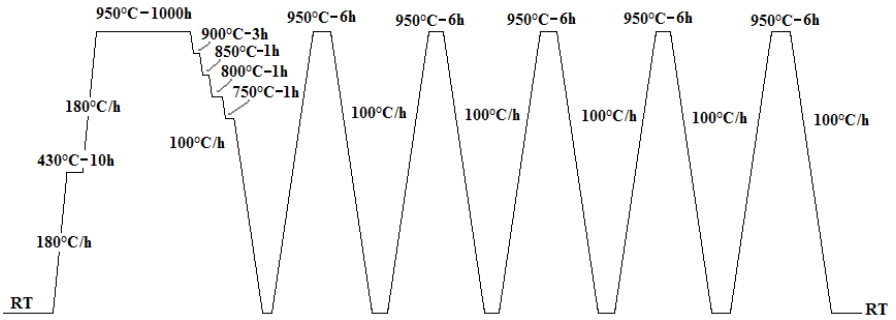

A

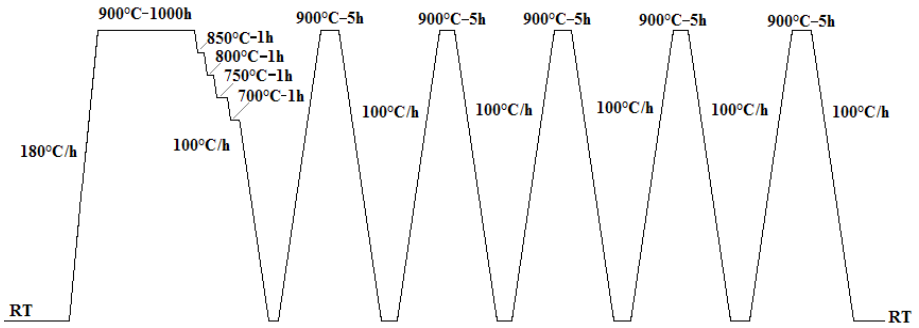

B

Figure 6.3. Temperature profile for the a) 950°C interconnect-stack experiment and b) 900°C interconnect-stack experiment.

The interconnect-stack set to run at 900°C was set up in the same vertical kiln used for the 950°C interconnect-stack experiment. In the 900°C interconnect-stack only three Crofer 22APU samples were included, two 15 μm Co_3O_4 + 15 μm LSM and one 15 μm Co_3O_4 + 15 μm LSC coated samples. Only one of the 15 μm Co_3O_4 + 15 μm LSM coated samples was built into a current resistance measurement unit as described above for the 950°C interconnect-stack. The other two coated Crofer 22APU samples were also mounted in LSM15 CCC-layer/coated Crofer 22APU sample/LSM15 CCC-layer units. The two units were isolated from the electrical current applied on the single current resistance measurement unit by alumina plates that had been inserted under the negative gold current probe, which supplies the power to the current resistance measurement. In figure 6.2.b the 900°C interconnect-stack setup is illustrated with a principle sketch and in figure 6.2.c-d pictures of the real 900˚C interconnect-stack set up in the vertical kiln can be seen. The 900°C interconnect-stack was heated directly up to 900°C with a ramp of 180°C/h without any stop for organic burn-off. The temperature was held at 900°C for 1000h whereafter the temperature was lowered in 50°C steps to 700°C and then directly down to room temperature with a cooling ramp of 100°C/h. Finally the stack was exposed to five thermal cycles between room temperature and 900°C with a heating and cooling ramp of 100°C/h. The temperature profile for the 900°C interconnect-stack is presented in detail in figure 6.3.b.

Just as for the 950˚C interconnect-stack the momentary ASR value for the degraded sample in the interconnect-stack is read after 1000 hours oxidation before the stepwise cooling starts. The ASR value for the sample at 750˚C, after 1000 hours oxidation at 900˚C, is read as the momentary ASR values at the last measurement point at the 750˚C cooling step.

6.2.5 Preparation of cross-sections

The 950˚C free-hanging oxidation sample was vacuum-mounted in epoxy. The cross-sections of the samples were then prepared by grinding 2-3 mm into the samples using course SiC abrasive papers. These cross-sections were then polished down to 1 μm using diamond pastes followed by a finish with OP-S suspension, colloidal silica. The cross-sections were finally carbon coated to avoid charging during SEM investigation in JEOL JSM 5310 LV microscope. For more detailed description of the cross-section preparation see chapter 2.

The 950°C interconnect-stack and the 900°C interconnect-stack were detached from the Pt-wires and power supply cables and taped together to remain compact while being vacuum-mounted in epoxy. The interconnect-stacks were sectioned so that a cross-section of the LSM15 CCC-layer/coated Crofer 22APU sample/LSM15 CCC-layer interfaces was achieved. The cross-section was polished using diamond pastes down to 1 μm followed by a finish with OP-S suspension, colloidal silica and carbon coated to avoid charging during analysis in JEOL JSM 5310 LV microscope.

The microstructures of the formed oxide scales were captured using BSE imaging and via EDS analysis the compositions of the oxide scales were determined.

6.3 Results

6.3.1 Weight gain and ASR data

The weight gain for the 15 µm Co_3O_4 + 15 µm LSM coated Crofer 22APU samples oxidized in air containing 1% water at 950˚C are plotted against time$^{1/2}$ together with the weight gain data for the corresponding sample oxidized at 900˚C in figure 6.4. The curves adopt an appearance close to linear in the weight gain-time$^{1/2}$ plot and are therefore assumed to follow parabolic oxidation behaviour. For further discussion of this see chapter 4.

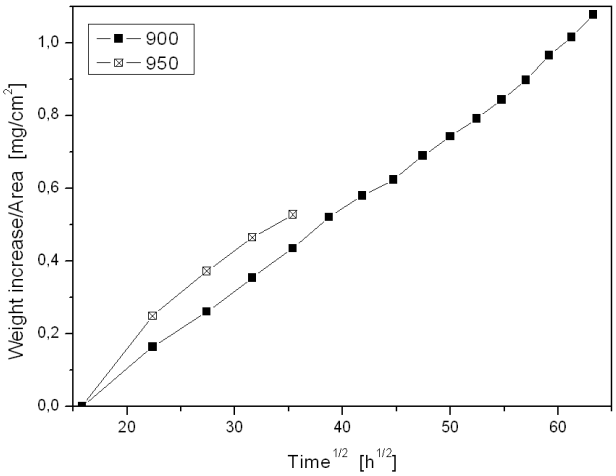

Figure 6.4. The weight increase – time$^{1/2}$ plot for Co_3O_4 + LSM coated Crofer 22APU samples oxidized in air containing 1%water at 900˚C and 950˚C.

The parabolic rate constants calculated from these curves are listed in table 6.2 below.

Table 6.2. Parabolic rate constants for 15 µm Co_3O_4 + 15 µm LSM coated Crofer 22APU oxidized in air containing 1% water at 900˚C and 950˚C neglecting the weight gain from the first 250 hours. The samples oxidized at 900˚C have been oxidized for a total of 4000 hours while the sample oxidized at 950˚C only have oxidized for a total of 1250 hours.

	$k_{p,1}\cdot10^{-3}$ [(mg/(cm^{2}h$^{1/2}$))^2]	Time [h]	$k_{p,2}\cdot10^{-3}$ [(mg/(cm^{2}h$^{1/2}$))^2]	Time [h]
900˚C	0.49±0.1	3000	0.77	3000-4000
950˚C	0.77±0.05	1250		

As seen in figure 6.4 and in table 6.2 the increased oxidation temperature leads to an increased oxidation rate.

In table 6.3 below the ASR values for the oxide scales after 1000 hours oxidation of the oxidized samples in the 950˚C and 900˚C interconnect-stacks are listed. The values consist of averages of the ASR values measured on the two interfaces on each sample and are corrected for contribution from the LSM15 plates. If the oxide scales are assumed to be continuous and uniform the ASR for the oxide scale can be mathematically described with equation 6.1.

$$ASR = \rho \cdot t \qquad \text{eq. 6.1}$$

In equation 6.1, ρ is the resistivity of the oxide scale and t the oxide scale thickness. The resistivity, ρ, is assumed to follow an Arrhenius expression according to equation 6.2 below [1, 2];

$$\rho = T \cdot \rho_0 \cdot e^{\left(-\frac{E_\rho}{RT}\right)} \qquad \text{eq. 6.2}$$

where R is the gas constant, T is temperature in K, and E_ρ is the activation energy of the resistivity. Based on the ASR values collected during the stepwise cooling of the interconnect-stacks the activation energies for the oxide scales on the coated Crofer 22APU samples were calculated, and they are also included in table 6.3 below. A mathematical expression for the thickness, t, of the oxide scale can be formulated by re-arranging the equation for parabolic oxidation presented in equation 3.1 and adding a constant correcting for the density of the growing oxide scale and the number of oxygen atoms per formula unit oxide. In equation 6.3 below the mathematical expression for oxide scale thickness is presented.

$$t = B \cdot \sqrt{k_p \cdot t_t} \qquad \text{eq. 6.3}$$

The constant B summarizes the density of the oxide scale and the number of oxygen atoms per formula unit oxide, and t_t is time. The parabolic rate constant follows an Arrhenius type expression as described in equation 6.4.

$$k_p = k_{p_0} \cdot e^{\left(-\frac{E_{el}}{RT}\right)} \qquad \text{eq. 6.4}$$

The E_{el} term stands for activation energy of the oxidation process. By combining equation 6.1-4 an expression for how ASR changes with time and temperature is achieved as presented in equation 6.5 below.

$$ASR = B \cdot \frac{\sqrt{k_{p_0} t_t}}{\rho_0} \cdot T \cdot e^{\left(-\frac{E_{ox}}{2RT} - \frac{E_{el}}{RT}\right)} \qquad \text{eq. 6.5}$$

Table 6.3. The ASR values for the coated Crofer 22APU samples in the 950˚C and 900˚C interconnect-stacks after 1000 hours oxidation at the actual oxidation temperature and at the cooling step 750˚C and the calculated activation energy.

Coating	**ASR at oxidation temp. [mΩ*cm^2]**	**ASR at 750ºC [mΩ*cm^2]**	**E_ρ [kJmol^{-1}]**	**Temp. [˚C]**
30 µm LSM[a]	9.1	40	78.1	*950*
20 µm Co_3O_4[b] + 18 µm LSM[a]	6.5	44	100.8	*950*
20 µm LSC[a]	3.4	23	100.3	*950*
20 µm Co_3O_4[b] + 18 µm LSC[b]	2.9	20	101.4	*950*
15 µm Co_3O_4[f] + 15 µm LSM[d]	3.0	10	86.5	*900*

The ASR for the LSM and LSC coated samples in the 950˚C interconnect-stack were lowered when an inner Co_3O_4 coating layer was placed below the LSM/LSC coating

layers. The effect on the inner Co_3O_4 coating layer was the largest when the perovskite coating was LSM. The lowest ASR values in the 950˚C interconnect-stack were measured for the LSC and Co_3O_4 + LSC coated samples.

When the temperature was step-wise decreased from the oxidation temperatures 950˚C/900˚C down to 750˚C in the interconnect-stacks the ASR values increased. It is noted that the Co_3O_4 + LSM coated samples in the 900˚C interconnect-stack had lower ASR values than the Co_3O_4 + LSM coated samples in the 950˚C interconnect-stack.

The activation energy for resistivity of the oxide scales on the LSC, Co_3O_4 + LSM, and Co_3O_4 + LSC coated samples in the 950˚C interconnect-stack were almost identical, while the oxide scale grown on LSM coated samples in the same interconnect stack presented ca. 20% lower activation energy. The activation energy for the oxide scale grown on the Co_3O_4 + LSM coated sample in the 900˚C interconnect-stack was somewhere in between the activation energies for the oxide scales on Co_3O_4 + LSM and LSM coated samples in the 950˚C interconnect-stack.

During the thermal cycling of the interconnect-stacks the ASR values for the samples were stable which indicated that the grown oxide scales were mechanically stable during the thermal cycling.

6.3.2 Microstructure of oxide scales

In figure 6.5-7 micrographs of the formed oxide scales on the LSM, LSC, Co_3O_4 + LSM and Co_3O_4 + LSC coated Crofer 22APU samples after 1000 hours oxidation at 900˚C and 950˚C free-hanging and in interconnect-stacks are presented. Micrographs of the oxide scale on both sides of the Crofer 22APU samples included in the interconnect-stacks are presented. On the one side of the sample the electrical current ran through the growing oxide scale in the same direction the electrical current would in a SOFC-stack in operation. On the other side of the samples the electrical current ran in the opposite direction through the growing oxide scales. This direction of the electrical current would correspond to the reactions in a SOFC-stack being reversed so that a Solid Oxide Electrolysis Cell-stack, SOEC-stack, is created [3, 4].

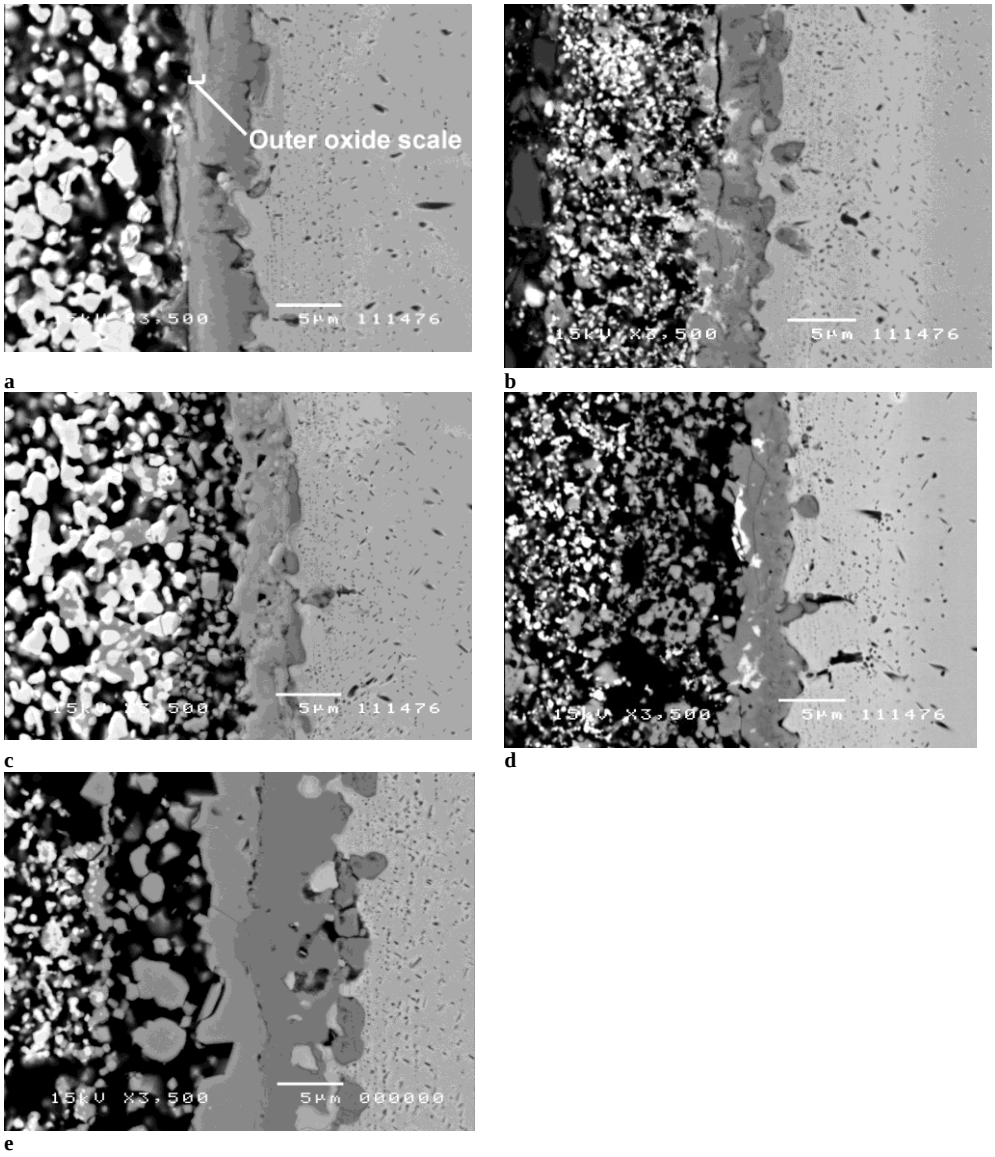

Figure 6.5. Micrographs of a) 15 µm LSM, b) 15 µm LSC, c) 15 µm Co_3O_4 + 15 µm LSM, d) 15 µm Co_3O_4 + 15 µm LSC coated Crofer 22APU samples oxidized free-hanging for 1000 hours in air containing 1% water at 900˚C and e) a 15 µm Co_3O_4 + 15 µm LSM coated Crofer 22APU samples oxidized for 1000 hours in air containing 1% water at 950˚C.

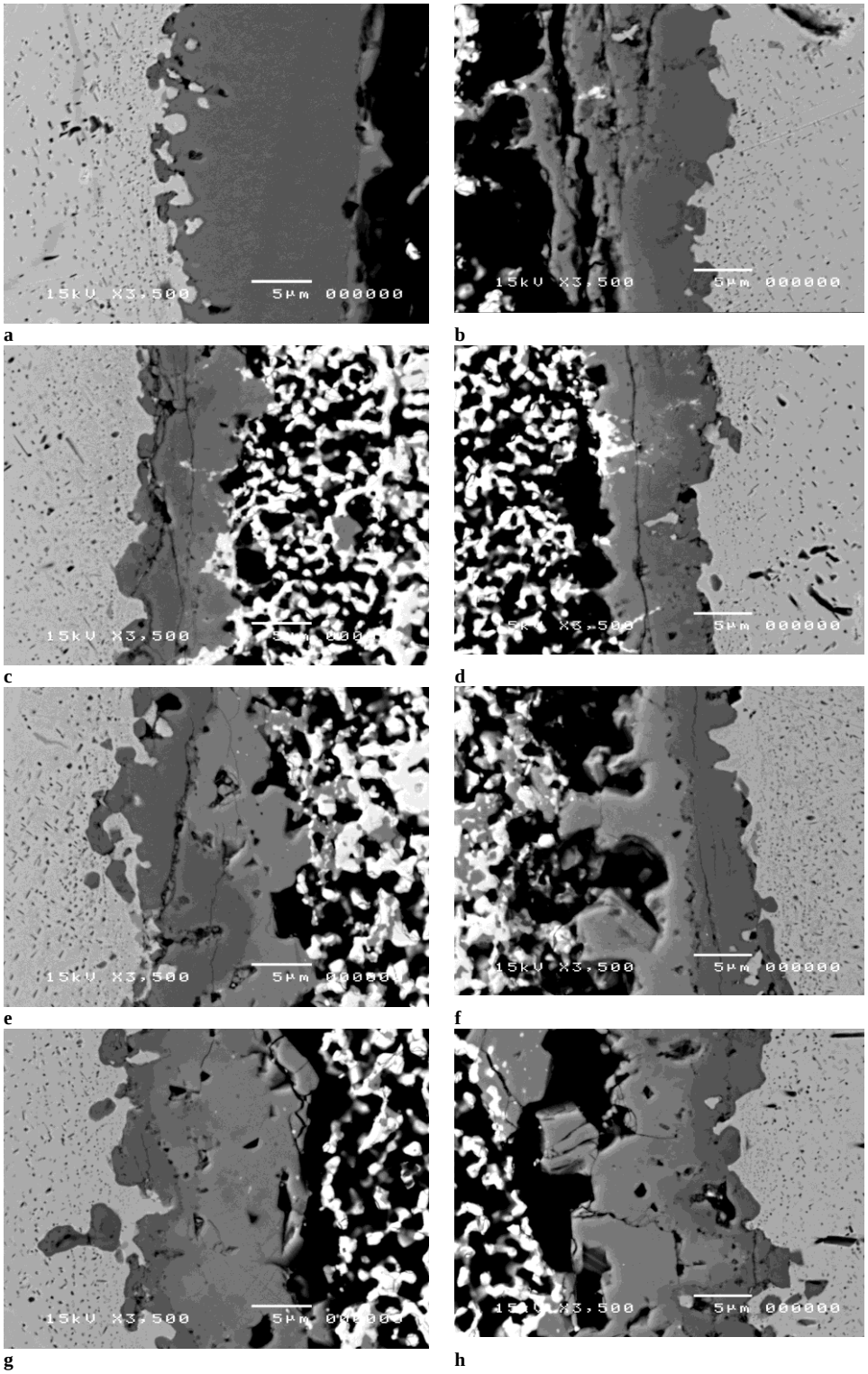

Figure 6.6. Micrographs of the oxide scales grown on coated Crofer 22APU samples oxidized for 1000 hours at 950˚C in the 950˚C interconnect-stack in the different current directions, a) 30 µm LSM – fuel cell direction, b) 30 µm LSM – electrolysis direction, c) 20 µm LSC – fuel cell direction, d) 20 µm LSC – electrolysis direction, e) 20 µm Co_3O_4 + 18 µm LSM – fuel cell direction, f) 20 µm Co_3O_4 + 18 µm LSM – electrolysis direction, g) 20 µm Co_3O_4 + 18 µm LSC – fuel cell direction, and h) 20 µm Co_3O_4 + 18 µm LSC – electrolysis direction

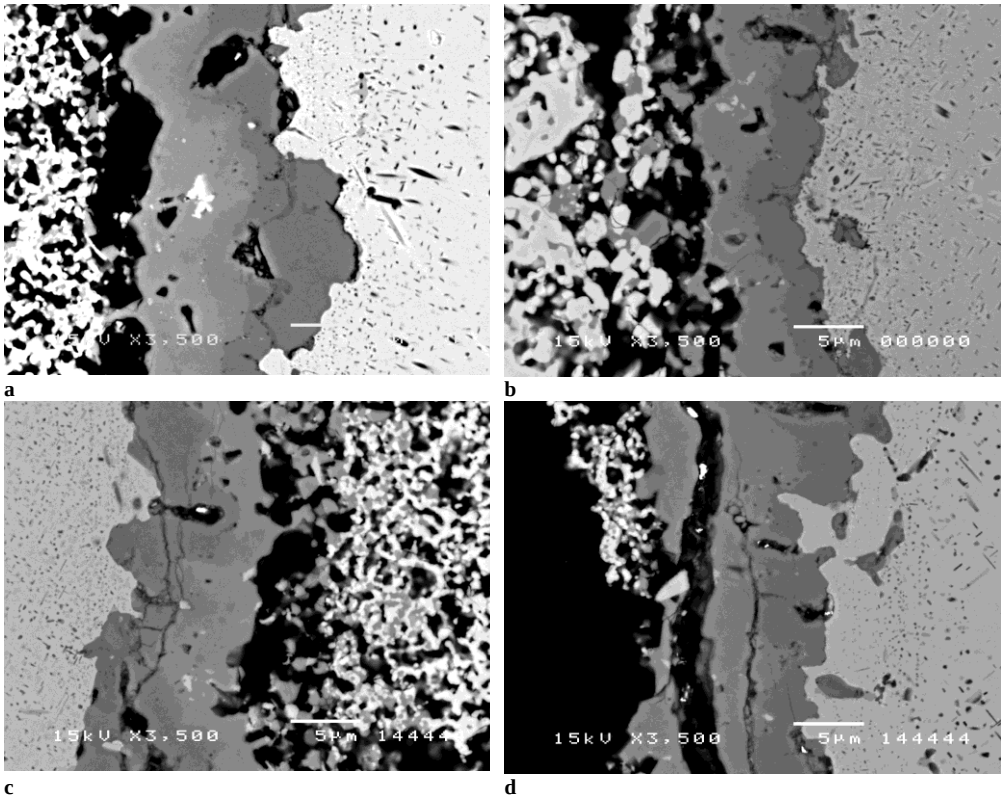

Figure 6.7. Micrographs of oxide scales grown in the 900˚C interconnect-stack after 1000 hours oxidation with and without an electrical load on Crofer 22APU samples coated with a) 15 µm Co_3O_4 + 15 µm LSM – only mechanical load, b) 15 µm Co_3O_4 + 15 µm LSC – only mechanical load, c) 15 µm Co_3O_4 + 15 µm LSM – fuel cell direction, and d) 15 µm Co_3O_4 + 15 µm LSM – electrolysis direction.

When comparing the oxide scales grown on the Co_3O_4 + LSM coated Crofer 22APU samples oxidized free-hanging at 900˚C and 950˚C in figure 6.5.c and 6.5.e respectively, it is found that the oxide scale thickness increases with increased oxidation temperature. The scale thickness has doubled, c.f. table 6.4, which is in agreement with the increase in the oxidation rate in table 6.2. It was also observed that the inner Co_3O_4 coating layer tended to be almost consumed when the oxidation temperature was raised.

When a mechanical load was applied during oxidation the oxide scale thickness increased while the inner Co_3O_4 coating layer was consumed. This is seen when comparing the oxide scales grown on Co_3O_4 + LSM and Co_3O_4 + LSC coated Crofer 22APU samples oxidized free-hanging at 900˚C in figure 6.5.c-d with the oxide scales grown on the Co_3O_4 + LSM and Co_3O_4 + LSC coated Crofer 22APU samples oxidized under a mechanical load in the 900˚C interconnect-stack in figure 6.7.a-b.

The oxide scales grown on the different sides of the coated Crofer 22APU samples in the 950˚C interconnect-stack are compared in figure 6.6. It is found that the direction of the electrical current does not appear to affect the microstructure of the oxide scales. The presence of an electrical current did not appear to have any effect at all on the microstructures of the oxide scales. This was observed when comparing the oxide scales grown on the Co_3O_4 + LSM coated samples under a mechanical load in the 900˚C interconnect-stack, figure 6.7.a, with the oxide scales grown on the Co_3O_4 +

LSM coated samples under an electrical load in the 900˚C interconnect-stack, figure 6.7.c-d.

The oxide scale thicknesses were measured on the different samples. They are listed in table 6.4.

The coatings appeared to have fallen of the LSM coated sample in the 950˚C interconnect-stack and partly on the Co_3O_4 + LSM coated sample under an electrical load in the 900˚C interconnect-stack. It is quite likely that this has happened during the demounting of the interconnect-stacks for cross-section preparation.

Table 6.4.a. Measured oxide scale thicknesses on BSE micrographs of the cross-sections on LSM, LSC, Co_3O_4 + LSM, and Co_3O_4 + LSC coated Crofer 22APU samples oxidized free-hanging for 1000 hours at 900˚C.

Free-hanging - 900°C	**Scale thickness [µm]**
15 µm LSM[a]	6.5±1.7
15 µm LSC[b]	4.3±1.6
15 µm Co_3O_4[b] + 15 µm LSM[a]	5.2±1.4
15 µm Co_3O_4[b] + 15 µm LSC[b]	3.6±0.9
(Heavy oxidation areas)	(27.3±3.4)

Table 6.4.b. Measured oxide scale thicknesses on BSE micrographs of the cross-sections on Co_3O_4 + LSM coated Crofer 22APU samples oxidized free-hanging for 1000 hours at 950˚C.

Free-hanging - 950°C	**Scale thickness [µm]**
15 µm Co_3O_4[f] + 15 µm LSM[d]	10.3±2.5

Table 6.4.c. Measured oxide scale thicknesses on BSE micrographs of the cross-sections on Co_3O_4 + LSM and Co_3O_4 + LSC coated Crofer 22APU samples oxidized for 1000 hours at 900˚C and under a mechanical load in the 900˚C interconnect-stack.

900°C interconnect-stack mechanical load	**Scale thickness [µm]**
15 µm Co_3O_4[e] + 15 µm LSM[c]	11.9±3.2
15 µm Co_3O_4[e] + 15 µm LSC[e]	9.8±3.2

Table 6.4.d. Measured oxide scale thicknesses on BSE micrographs of the cross-sections on Co_3O_4 + LSM coated Crofer 22APU samples oxidized for 1000 hours at 900˚C and under a mechanical and an electrical load in the 900˚C interconnect-stack.

900°C interconnect-stack mechanical and electrical load	**Scale thickness [µm]**
15 µm Co_3O_4[e] + 15 µm LSM[c]	
Fuel cell direction	11.4±3.1
Electrolysis direction	9.9±2.3

Table 6.4.e. Measured oxide scale thicknesses on BSE micrographs of the cross-sections on LSM, LSC, Co_3O_4 + LSM, and Co_3O_4 + LSC coated Crofer 22APU samples oxidized for 1000 hours at 950˚C under a mechanical and an electrical load in the 950˚C interconnect-stack.

950°C interconnect-stack mechanical and electrical load	**Scale thickness [µm]**
30 µm LSM[a]	
Fuel cell direction	11.6±5.7
Electrolysis direction	9.6±2.7
20 µm LSC[a]	
Fuel cell direction	9.5±1.8
Electrolysis direction	9.6±1.5
20 µm Co_3O_4[b] + 18 µm LSM[a]	
Fuel cell direction	12.9±2.6
Electrolysis direction	13.1±3.8
20 µm Co_3O_4[b] + 18 µm LSC[b]	
Fuel cell direction	16.2±3.2
Electrolysis direction	13.6±3.8

As described and discussed in chapter 4 and 5 the 15 µm Co_3O_4 + 15 µm LSC coated Crofer 22APU samples oxidized free-hanging at 900˚C forms heavily oxidized areas on a few spots along the cross-section. In table 6.4 the average thickness of these areas is included within brackets below the average thickness of the otherwise generally thin oxide scale on this sample. For the 15 µm Co_3O_4 + 15 µm LSC coated samples under mechanical load in the 900°C-stack no such heavily oxidized areas were observed.

6.3.3 Oxide compositions

Point analyses were performed in the outer oxide scales on the oxidized samples described above and based on these EDS measurements spinel compositions could be calculated. To visualize what "the outer oxide scale" concept entails, this area is marked on a micrograph of the 15 µm Co_3O_4 + 15 µm LSM coated Crofer 22APU sample oxidized in 900˚C under a mechanical load in figure 6.8 below.

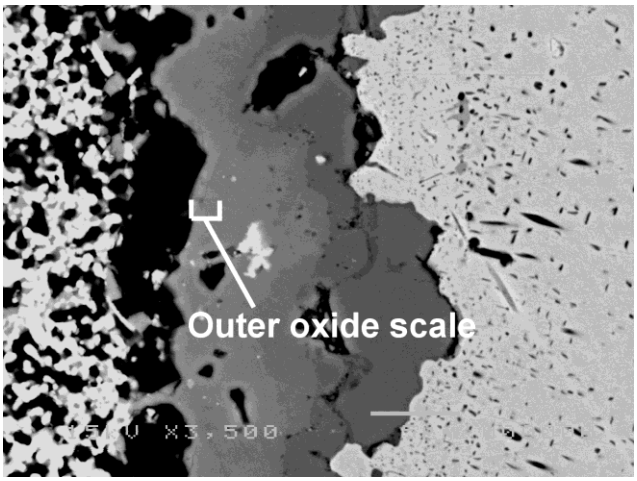

Figure 6.8. Micrographs of oxide scales grown on the 15 µm Co_3O_4 + 15 µm LSM coated Crofer 22APU sample in the 900˚C interconnect-stack under a mechanical load after 1000 hours oxidation.

The spinel compositions are listed in table 6.5.

Table 6.5.a. Spinel compositions found in the outer oxide scale on LSM, LSC, Co_3O_4 + LSM, and Co_3O_4 + LSC coated Crofer 22APU samples oxidized free-hanging for 1000 hours at 900˚C.

Free-hanging - 900°C	**Cr**	**Mn**	**Co**	**Fe**
15 μm LSM[a]	1.5±0.2	1.4±0.2		
15 μm LSC[b]	1.5±0.4	0.5±0.2	0.9±0.2	0.1±0.1
15 μm Co_3O_4[b] + 15 μm LSM[a]	0.4±0.1	0.9±0.2	1.7±0.2	0.1±0.0
15 μm Co_3O_4[b] + 15 μm LSC[b]	0.4±0.1	0.7±0.1	1.7±0.1	0.2±0.1

Table 6.5.b. Spinel compositions found in the outer oxide scale on Co_3O_4 + LSM coated Crofer 22APU samples oxidized free-hanging for 1000 hours at 950˚C.

Free-hanging - 950°C	**Cr**	**Mn**	**Co**	**Fe**
15 μm Co_3O_4[f] + 15 μm LSM[d]	0.1±0.0	0.8±0.1	1.9±0.1	0.2±0.0

Table 6.5.c. Spinel compositions found in the outer oxide scale on Co_3O_4 + LSM and Co_3O_4 + LSC coated Crofer 22APU samples oxidized for 1000 hours at 900˚C and under a mechanical load in the 900˚C interconnect-stack.

900°C interconnect-stack mechanical load	**Cr**	**Mn**	**Co**	**Fe**
15 μm Co_3O_4[e] + 15 μm LSM[c]	0.5±0.5	1.2±0.4	1.2±0.2	0.1±0.0
15 μm Co_3O_4[e] + 15 μm LSC[e]	0.6±0.3	1.0±0.2	1.3±0.1	0.1±0.0

Table 6.5.d. Spinel compositions found in the outer oxide scale on Co_3O_4 + LSM coated Crofer 22APU samples oxidized for 1000 hours at 900˚C and under a mechanical and an electrical load in the 900˚C interconnect-stack.

900°C interconnect-stack mechanical and electrical load	**Cr**	**Mn**	**Co**	**Fe**
15 μm Co_3O_4[e] + 15 μm LSM[c]				
Fuel cell direction	0.8±0.6	0.9±0.4	1.2±0.2	0.1±0.2
Electrolysis direction	0.7±0.4	1.1±0.3	1.1±0.1	0.1±0.0

Table 6.5.e. Spinel compositions found in the outer oxide scale on LSM, LSC, Co_3O_4 + LSM, and Co_3O_4 + LSC coated Crofer 22APU samples oxidized for 1000 hours at 950˚C under a mechanical and an electrical load in the 950˚C interconnect-stack.

950°C interconnect-stack mechanical and electrical load	**Cr**	**Mn**	**Co**	**Fe**
30 μm LSM[a]				
Fuel cell direction	1.3±0.1	1.6±0.1		0.2±0.0
Electrolysis direction	1.5±0.1	1.4±0.1		0.1±0.1
20 μm LSC[a]				
Fuel cell direction	1.4±0.3	0.7±0.2	0.9±0.1	0.1±0.0
Electrolysis direction	1.6±0.5	0.5±0.3	0.8±0.2	
20 μm Co_3O_4[b] + 18 μm LSM[a]				
Fuel cell direction	0.1±0.0	1.0±0.1	1.8±0.1	0.1±0.0
Electrolysis direction	0.1±0.0	0.9±0.1	1.9±0.1	0.1±0.0
20 μm Co_3O_4[b] + 18 μm LSC[b]				
Fuel cell direction	0.3±0.2	0.4±0.0	2.3±0.2	0.1±0.0
Electrolysis direction	0.3±0.1	0.4±0.1	2.2±0.1	0.1±0.0

The spinel composition found in the outer oxide scales on Co_3O_4 + LSM and Co_3O_4 + LSC coated Crofer 22APU samples oxidized at 900˚C did not appear to change

significantly when a mechanical or an electrical load was applied. There might be a slight trend towards increased chromium content when a mechanical load was applied, but the standard deviations were too large to make any certain conclusions.

Comparing the spinel composition in the outer oxide scale on the different sides of the coated Crofer 22APU samples in the 950˚C and the 900˚C interconnect-stacks under an electrical load no effect of the direction of the electrical current could be found.

Considering the spinel compositions found in the outer oxide scales on the Co_3O_4 + LSC coated samples in the 950˚C and the 900˚C interconnect-stacks it was observed that the manganese content tend to decrease when the temperature was raised from 900˚C to 950˚C.

For the Co_3O_4 + LSM coated Crofer 22APU samples oxidized either free-hanging or in an interconnect-stack with or without an electrical load at 900˚C the chromium content in the spinel phase in the outer oxide scale was found to be between 13-27%. When Co_3O_4 + LSM coated Crofer 22APU samples on the other hand was oxidized free-hanging or in an interconnect-stack under an electrical load at 950˚C the chromium content had decreased to negligible 3%.

The spinel compositions found in the outer oxide scales on LSM and LSC coated Crofer 22APU samples oxidized free-hanging at 900˚C and oxidized in the 950˚C interconnect-stack only differed slightly. This indicates that an increased temperature and the presence of a mechanical and an electrical load on the LSM and LSC coated sample do not affect the composition of the growing oxide scales. However, complementary experiments where the oxidation parameters are varied, as for the Co_3O_4 + LSM and Co_3O_4 + LSC coated samples in this study, would have to be performed before any conclusions can be made for the LSM and LSC coated samples.

6.4 Discussion

6.4.1 Effect of mechanical and electrical load on oxide scale growth

In the 900˚C interconnect-stack set-up in this study one Co_3O_4 + LSM coated Crofer 22APU sample was mounted under an electrical load and one without. Comparing the scale thicknesses and the spinel compositions in the outer oxide scales on these two Co_3O_4 + LSM coated samples no significant difference could be found. This indicates that the presence of an electrical load across the forming oxide scale does not affect the oxide scale growth. The direction of the electrical current running through the oxide scales on the two sides of the Co_3O_4 + LSM coated sample does not appear to affect the microstructure or compositions of the growing oxide scales. The same is observed for the coated Crofer 22APU samples included in the 950˚C interconnect-stack.

Crofer 22APU samples coated with Co_3O_4 + LSM and Co_3O_4 + LSC oxidized at 900˚C free-hanging presented thin oxide scales and significant residues of the inner Co_3O_4 coating layer. Crofer 22APU samples with the same coatings under a mechanical load but no electrical load in the 900˚C interconnect-stack presented thicker oxide scales, and the inner Co_3O_4 coating layers were basically completely consumed. The increased scale thickness and the consumption of the inner Co_3O_4 coating layer for dual coated Crofer 22APU sample under a mechanical load are

probably linked. As described and discussed in chapter 3 and 4 the inner Co_3O_4 coating layer undergoes a $Co_3O_4 \rightarrow CoO$ phase transition around 900˚C [5-7]. This phase transition leads to a volume decrease. However, when the CoO phase reacts with the outward diffusing Mn- and Cr-cations originating from the alloy and the inward diffusing Mn-cations from the LSM coating a $(CrMnCo)_3O_4$ spinel phase is formed (cf. figure 3.10) which subsequently leads to a volume increase. This should ensure formation of a dense spinel phase, as discussed in chapter 4, and the particles of the Co_3O_4 coating layer might become closer packed. When a mechanical load is applied onto the Co_3O_4 + LSM/LSC coated samples the particles in the inner Co_3O_4 coating layer might be packed even closer during the $Co_3O_4 \rightarrow CoO$ phase transition, and the densifying process of the Co_3O_4 coating layer and the growing oxide scale might become enhanced. This ultimately results in the total consumption of the inner Co_3O_4 coating layer.

The spinel composition in the outer oxide scale on the LSM and LSC coated Crofer 22APU samples oxidized free-hanging at 900˚C and in the 950˚C interconnect-stack were similar. This might indicate that neither a mechanical load nor a raised oxidation temperature from 900˚C to 950˚C affects the spinel compositions in the outer oxide scale on these samples. However, as mentioned earlier complementary oxidation experiments on the LSM and LSC coated samples where the oxidation temperature and eventual mechanical load are varied separately have to be performed to support this theory. The Co_3O_4 + LSM coated Crofer 22APU sample were oxidized both free-hanging and in interconnect-stacks at 900˚C and 950˚C, and it was found that it was the oxidation temperature that affected the spinel composition in the outer oxide scale on the dual coated samples. As seen in table 6.5 both free-hanging oxidation samples and samples inserted in an interconnect-stack oxidized at 950˚C show significantly lower chromium content in the spinel phase in the outer oxide scale compared to the corresponding Co_3O_4 + LSM coated samples oxidized at 900˚C. A possible explanation to why the increased temperature leads to lowered chromium content could be that the $Co_3O_4 \rightarrow CoO$ phase transition is ensured, since the temperature should be well above the phase transition temperature at 950˚C. The fast outward and inward diffusing Mn-cations reacts with the CoO phase and form a $(MnCo)_3O_4$ spinel phase resulting in low chromium mobility [8].

Crofer 22APU samples coated with Co_3O_4 + LSM and Co_3O_4 + LSC present lower ASR values than LSM and LSC coated Crofer 22APU samples in the 950˚C interconnect-stack as seen in table 6.3. At the same time the thicknesses of the oxide scales on the Co_3O_4 + LSM and Co_3O_4 + LSC coated samples are thicker than the corresponding oxide scales on the LSM and LSC coated samples in the 950˚C interconnect-stack as seen in table 6.4. That is an inner Co_3O_4 coating layer below a perovskite coating appears to improve the conductivity of the forming oxide scales. Considering the spinel compositions listed in table 6.5 the cobalt content in the forming spinel phase on the Co_3O_4 + LSM and Co_3O_4 + LSC coated samples are higher than in the LSM and LSC coated samples. A higher amount of cobalt in the spinel phase in the outer oxide scale thus results in lower ASR for the oxide scale which agrees with observations in the literature indicating that Co-containing spinels, especially in combination with manganese, present high electrical conductivity [9]. The positive effect on an inner Co_3O_4 coating layer below a perovskite coating layer was the most pronounced when the perovskite coating consisted of LSM. The ASR went from 9.1 $m\Omega*cm^2$ to 6.5 $m\Omega*cm^2$ i.e. a decrease of almost 30%. The cobalt

content in the spinel phase in the outer oxide scale on the LSM coated sample was zero while the Co_3O_4 + LSM coated sample presented a spinel containing ca. 66% cobalt in the 950˚C interconnect-stack. For the LSC and Co_3O_4 + LSC coated Crofer 22APU samples in the 950˚C interconnect-stack the change in cobalt content was not as drastic, and the same could be said about the ASR values for these two samples. It might also be possible that changes in the chromia phase in the oxide scale caused by the presence of a cobalt rich coating explains why the samples with a cobalt rich coating presents the lowest ASR values [10, 11]. The chromia phase probably becomes doped with inward diffusing Co-cations originating from the Co-rich coatings. Chromia doped with cations with lower valence than Cr^{3+} is generally expected to achieve an improved electrical conductivity, and assuming the Co-cations incorporated in the chromia scale has a valence of two this would be in agreement with findings in literature [12]. The effect of incorporated cobalt in the growing oxide scales might also be argued for when comparing the activation energies of the resistivities in the oxide scales in table 6.3. The activation energy found for the oxide scales grown on the LSC, Co_3O_4 + LSM, and Co_3O_4 + LSC coated samples in the 950˚C interconnect-stack were almost identical, indicating that the resistivity determining property of these oxide scales might be the same. The LSM coated samples in the 950˚C interconnect-stack had lower activation energy than the other three samples in the 950˚C interconnect-stack indicating that the resistivity limiting properties in the oxide scale on the LSM coated sample were different. This might indicate that the cobalt incorporated into the oxide scale due to the presence of cobalt rich coating affects or determines the resistivity limiting property in the oxide scale. Comparing the spinel compositions found on the LSC, Co_3O_4 + LSM, and Co_3O_4 + LSC coated samples in the 950˚C interconnect-stack they all have high amounts of cobalt, but otherwise they differ quite strongly. This might indicate that it is the resistivity limiting properties in the chromia scale that determines the activation energy. The activation energy for the Co_3O_4 + LSM coated sample in the 900˚C interconnect-stack was lower than the activation energy for the corresponding sample in the 950˚C interconnect-stack, but still higher than the activation energy for the LSM coated sample in the 950˚C interconnect-stack. A possible explanation to this observation might be that not enough cobalt is able to become incorporated into the chromia phase in the oxide scale during oxidation at 900˚C, to reach the same activation energy as the oxide scales grown in at 950˚C. Not enough EDS measurements were performed to support this theory though.

When the temperature in the 950˚C and the 900˚C interconnect-stacks was step-wise lowered the ASR of the oxide scales grown on the included samples increase as seen in table 6.3. This is expected since the resistance of bulk oxide is found to decrease with higher temperatures [13]. However, the ASR for the oxide scale grown on the Co_3O_4 + LSM coated Crofer 22APU sample in the 900˚C interconnect-stack was lower than the ASR for the corresponding sample and oxide scale in the 950˚C interconnect-stack. This is in direct contrast to the expected behaviour of the oxide resistance. In equation 6.5 a mathematical expression for the ASR of oxide scale was described. In the expression it is visible that the ASR is balanced by the activation energy for the oxidation process and the activation energy for the resistivity. At high temperatures the activation energy for the resistivity is high and should lead to a low ASR value for the growing oxide scale. However, if the activation energy for the oxidation process is significantly lower at high temperatures, the total ASR of the oxide scale might still become higher during oxidation at 950˚C than during oxidation

at 900˚C due to a thicker scale. This is probably what is observed for the Co_3O_4 + LSM coated samples in the 950˚C and 900˚C interconnect-stacks. For example it is visible in table 6.4 that the oxide scales on the Co_3O_4 + LSM coated samples in the interconnect-stacks are thicker at the higher oxidation temperature. The increased oxidation rate due to the increased oxidation temperature for the Co_3O_4 + LSM coated Crofer 22APU sample is also shown in the oxidation experiment with free-hanging samples. In figure 6.4 and table 6.2 it is visible that oxidation at 950˚C leads to a more than 50% faster oxidation rate than at 900˚C.

6.5 Conclusions

The composition and microstructure of the oxide scales do not appear to be affected by the presence of or the direction of an electrical current on LSM, LSC, Co_3O_4 + LSM, and Co_3O_4 + LSC coated Crofer 22APU samples.

A mechanical load of 0.3 MPa on Co_3O_4 + LSM and Co_3O_4 + LSC coated Crofer 22APU samples appears to increase the thickness of the forming oxide scales and the consumption of the inner Co_3O_4 coating layer during oxidation at 900°C and 950°C.

The spinel compositions in the outer oxide scales on the Co_3O_4 + LSM coated Crofer 22APU samples was significantly affected when the oxidation temperature was raised from 900˚C to 950˚C. The chromium content was lowered in the spinel phase in the outer oxide scale to a negligible level of 3%.

The Co_3O_4 + LSM and Co_3O_4 + LSC coated Crofer 22APU samples presented lower ASR values than the LSM and LSC coated Crofer 22APU samples in the 950˚C interconnect-stack as seen in table 6.3. The dual layer coated samples presented thicker oxide scales than the single layer coated samples and the composition of the formed spinel phase changed. The cobalt content in the spinel phase was increased while the chromium and to some degree the manganese contents were lowered in the presence of an inner Co_3O_4 coating layer. Higher cobalt content in the growing oxide scale results in lower ASR of the oxide scales.

6.6 Reference List

1. Zhu, W. Z. and Deevi, S. C., Materials Research Bulletin, 38, 957 (2003)

2. Kofstad P, *High Temperature Corrosion* (Elsevier Applied Science Publishers LTD, 1988)

3. Dönitz, W., Erdle, E., and Streicher, R., in *Electrochemical Hydrogen Technologies Electrochemical Production and Combustion of Hydrogen*, Edited by H. Wendt (Elsevier Science Publishers B. V., 1990),p. 213

4. Hauch, A., Jensen, S. H., Ramousse, S. and Mogensen, M., Journal of the Electrochemical Society, 153, A1741-A1747 (2006)

5. Oneill, H. S. C., Physics and Chemistry of Minerals, 12, 149 (1985)

6. Mocala, K., Navrotsky, A. and Sherman, D. M., Physics and Chemistry of Minerals, 19, 88 (1992)

7. Xing, L. and Prewitt, C. T., Physics and Chemistry of Minerals, 17, 168 (1990)

8. Yang, Z. G., Xia, G. G. and Stevenson, J. W., Electrochemical and Solid State Letters, 8, A168-A170 (2005)

9. Petric, A. and Ling, H., Journal of the American Ceramic Society, 90, 1515 (2007)

10. Kadowaki, T., Shiomitsu, T., Matsuda, E., Nakagawa, H., Tsuneizumi, H. and Maruyama, T., Solid State Ionics, 67, 65 (1993)

11. Hansson, A. N., Linderoth, S., Mogensen, M. and Somers, M. A. J., Journal of Alloys and Compounds, 433, 193 (2007)

12. Huang, K., Hou, P. Y. and Goodenough, J. B., Materials Research Bulletin, 36, 81 (2001)

13. Hou, P. Y., Huang, K. and Bakker, W. T., in 6th International Symposium on Solid Oxide Fuel Cells (SOFC-VI), Singhal S.C., Editor, p. 737

7. Closure

7.1 Summary

In this Ph.D. project high temperature oxidation of slurry coated ferritic alloy is studied in atmospheres resembling the atmosphere found at the cathode in an SOFC. The aim was to study and formulate possible interaction mechanisms between the slurry coatings and the growing oxide scale on the alloy surface. With knowledge of these mechanisms it would be possible to design coating/alloy combinations that display low growth rate, low chromium content, and low electrical resistance of/in the inevitable forming oxide scales on the alloy surfaces during high temperature oxidation.

Oxidation experiments with single layer coated Crofer 22APU samples were performed in air containing 1% water at 900˚C. The single layer slurry coatings consisted of LSM, LSC, Co_3O_4, $MnCo_2O_4$, ZrO_2, and Al_2O_3. With the exception of the $MnCo_2O_4$ coating, the presence of these single layer coatings decreased the oxidation rate of the alloy samples compared to uncoated Crofer samples. Four possible contributions were suggested to explain the lowered oxidation rate:

- Lowered inward oxygen diffusion due to increased spinel ratio in the oxide scale
- Decrease of the concentration profile of manganese across the oxide scale, when the coating contains manganese
- Geometrical protection by incorporated coating particles or reaction products in the growing oxide scale
- Spinel compositions in the reaction layer that display low cation diffusion properties

In the presence of a single layer coating the spinel ratio in the growing oxide scales was increased. Due to the presumed fully occupied oxygen lattice in a spinel phase, oxygen is unable to diffuse via anion vacancies in a spinel phase. The presence of such a spinel phase on top of the chromia phase in the grown oxide scales on the coated, oxidizing Crofer 22APU samples, would ensure that the oxidation process is dominated by outwardly diffusing cations, and that inwardly diffusing oxygen is suppressed. As a result the oxidation rate is decreased.

By applying a coating containing manganese, the concentration gradient of manganese across the growing oxide scale is decreased. Most likely this affects the chemical potential gradient of manganese across the oxide scale, whereby the driving force for outwardly diffusing manganese is lowered and indirectly also the oxidation rate of the alloy sample.

Incorporation of coating particles and/or reaction products in the growing oxide scale would implement a geometrical diffusion barrier that does not loose its effect as the oxide scale grows thicker, and would therefore continuously decrease the oxidation rate of the Crofer sample.

The specific spinel compositions in the formed spinel phase in the oxide scales might possess particularly low cation diffusion properties that would result in a decreased oxidation rate.

Probably, all four suggested contributions to the lowered oxidation rate contribute to different extent, depending on the coating type.

Based on the weight increase data and the microstructure and compositions of the oxide scales found on the single layer coated Crofer 22APU samples in the oxidation experiment, three different interaction mechanisms between a slurry coating and the growing oxide scale on a ferritic alloy were established. The three interaction mechanisms are:

A Surface covering coating
B Surface covering coatings with chemical reaction with the forming oxide
C Incorporation of coating particles in the oxide scale

In interaction mechanism A, the coating particles are pushed in front of the outwardly growing oxide scale. Coatings with this interaction mechanism mainly give a geometrical protection against oxidation by blocking oxygen access at the surface of the oxide scale. The protection effect is gradually lost when the oxide scale grows thicker than the diameter of the coating particles. Interaction mechanism B entails a chemical reaction between the growing oxide scale and the coating particles at the same time as these are pushed in front of the growing oxide scale. The chemical reaction leads to a change in the oxide composition. In the third and last interaction mechanism, C, the coating particles are incorporated into the growing oxide scale. The incorporated coating particles create geometrical protection against oxidation that should not loose their effect after the oxide scale has grown thicker than the diameter of the coating particles. The Co_3O_4 and $MnCo_2O_4$ coated Crofer 22APU samples showed an interaction mechanism of type B at the oxide/coating interface while the ZrO_2 and Al_2O_3 coated samples presented indication on an interaction mechanism of type C at the oxide/coating interface. For the LSM and LSC coated Crofer samples a combination of interaction mechanisms were found. For the LSM coated samples a combination of type A and B appears to characterize the interaction between the coating and the growing oxide scale. On the LSC coated Crofer samples interaction mechanisms B and C appeared to describe the interaction at the coating/oxide scale interface the best. The lowest weight gain rate and the lowest chromium in the outer oxide scales on the coated Crofer 22APU samples were found for the LSM and LSC coated samples. This suggests that a coating with multiple interaction mechanisms with the growing oxide scale is the most successful protection against oxidation and high chromium content in the outer oxide scale.

An inner coating layer of Co_3O_4 below a coating layer of LSM or LSC on Crofer 22APU samples decreased the oxidation rate and the chromium content in the outer oxide scale more successful in comparison to single layer coatings of LSM, LSC, and Co_3O_4 during oxidation. The dual layer coatings, Co_3O_4 + LSM and Co_3O_4 + LSC, also increased the spinel ratio in the oxide scale compared to the single layer coatings, LSM, LSC, and

Co_3O_4. The beneficial effect of an inner Co_3O_4 coating layer is believed to be caused by the $Co_3O_4 \rightarrow CoO$ phase transition that takes place around 900˚C. The phase transition initially leads to a volume decrease, but when the CoO reacts with the Cr- and Mn-ions diffusing into the CoO phase from both the alloy and the second layer of coating a $(Mn,Cr,Co)_3O_4$ spinel is formed and a volume increase follows. The total volume changes in the original Co_3O_4 coating layer, result in a densification of the forming spinel phase in the outer oxide scale. The interaction mechanisms between the dual coatings and the growing oxide scale appeared to be an enhancement of the interaction mechanisms found for the corresponding single layer coatings. The Co_3O_4 + LSM coated samples seemed to present an interaction mechanism of type A and B while the Co_3O_4 + LSC coated samples showed indications of an interaction mechanism consisting of a combination of type B and C.

Of the Co_3O_4 + LSM and Co_3O_4 + LSC coated Crofer 22APU samples the Co_3O_4 + LSC coated samples presented the lowest oxidation rate. Based on the microstructure, the composition of the growing oxide scales and the residues of the coating layers visible in the cross-sections of the oxidized samples, it was concluded that the Co_3O_4 + LSC coating has higher reactivity with the growing oxide scale than the Co_3O_4 + LSM coating. This indicates that coating with large reactivity should provide the best protection against oxidation. However, a few heavily oxidized spots along the 15 µm Co_3O_4 + 15 µm LSC coated Crofer samples' surfaces were observed, and these contained high amounts of iron as well as chromium. Areas like this would provide fast and easy diffusion paths for chromium that would be detrimental for an SOFC. On the 7/15 µm Co_3O_4 + 15 µm LSM and 7 µm Co_3O_4 + 15 µm LSC coated Crofer 22APU samples no signs of heavily oxidized areas were observed. This would indicate that even if a large reactivity of the coating layer is favorable for decreasing the oxidation rate of the alloy sample, there is a level at which the reactivity becomes damaging instead.

Dual layer coatings consisting of an inner Co_3O_4 coating layer below a LSM or LSC perovskite coating only induced lowered oxidation rate on Sandvik 1C44Mo20 samples compared to the single layer coated versions, when the second coating layer consisted of LSM. However, only a slight decrease in the oxidation rate was observed when Sandvik 1C44Mo20 samples were coated with Co_3O_4 + LSM instead of a single layer of LSM or Co_3O_4. The Co_3O_4 + LSC coated Sandvik 1C44Mo20 samples displayed significantly higher oxidation rate than the LSC and Co_3O_4 coated Sandvik 1C44Mo20 samples. The growing oxide scale and the coating layers on these Co_3O_4 + LSC coated Sandvik 1C44Mo20 samples became totally merged via a chromium rich $(CoCr)_3O_4$ phase during oxidation in air containing 1% water at 900˚C. In the oxide scales on the Co_3O_4 + LSC coated and the LSC coated Sandvik 1C44Mo20 samples only small amounts of Mn were detected. In the oxide scales grown on the LSC and Co_3O_4 + LSC coated Crofer 22APU a significantly higher manganese content was detected, and the growing oxide scales and the residues of the applied coatings were well discernable and easily separated on these samples. From these observations it was suggested that a certain amount of manganese was needed to ensure a slower growth rate of the oxide scale in the presence of a cobalt rich coating. The lower Mn access on the Sandvik 1C44Mo20 (0.1 wt.% Mn) samples compared to the Mn access on the Crofer 22APU (0.4 wt.%) samples could explain the

difference in oxidation behavior for the LSC and more importantly the Co_3O_4 + LSC coated samples. The weight gain data and the microstructure of the oxide scales grown on Co_3O_4 + LSC coated Sandvik OYC44 (0.3 wt.% Mn), Sandvik 350 (0.1 wt.% Mn), Sandvik 433 (0.6 wt.% Mn), Sandvik 434 (5.1 wt.% Mn), and Sandvik 515 (0.3 wt.% Mn) oxidized in air containing 1% water at 900˚C supported the theory of a need for a certain amount of manganese in the alloy to stabilize a cobalt rich coating. An optimum manganese content in an Fe-22Cr alloy is believed to be around 0.3-0.5 wt.%, since a too high amount of manganese increases the oxidation rate.

The oxide scale growth on Co_3O_4 + LSM and Co_3O_4 + LSC coated Crofer 22APU samples was found to be unaffected by the presence and the direction of an electrical current. A mechanical load of 0.3 MPa on the other hand increased the thicknesses of the growing oxide scales as well as the consumption of the inner Co_3O_4 coating layer on the Co_3O_4 + LSM and Co_3O_4 + LSC coated Crofer samples. The increased scale thickness and increased consumption of the inner Co_3O_4 coating layer are probably linked together.

Oxidation experiments of Co_3O_4 + LSM coated Crofer 22APU samples in air containing 1% water at both 900˚C and 950˚C showed that the chromium content in the spinel phase in the outer oxide scale decreased from ca. 13% down to ca. 3% when the oxidation temperature was raised from 900˚C to 950˚C. It could be that the higher oxidation temperature assures a fast $Co_3O_4 \rightarrow CoO$ phase transition and indirectly enables a fast $(MnCo)_3O_4$ spinel formation with a composition close to $MnCo_2O_4$ when the CoO phase reacted with Mn-cations originating from both the alloy and the LSM coating. A low diffusivity of chromium in the $MnCo_2O_4$ spinel would then explain the low chromium content.

Measurements of the electrical resistance in the oxide scales grown on LSM, LSC, Co_3O_4 + LSM, and Co_3O_4 + LSC coated Crofer 22APU samples during oxidation in technical air at 950˚C showed that the dual coated samples presented the lowest ASR values. The dual coated samples also had higher cobalt content in the oxide scale than the oxide scales grown on the LSM and LSC coated samples. This suggests that higher cobalt content in the oxide scale ensures a better electrical conductivity across the scale.

To summarize all these observations, a successful coating/alloy combination for SOFC use should have:

- High reactivity (not too high) and preferably several interaction mechanisms
- Volume change/expansion
- Incorporation of coating particles/reactions products in the growing oxide scale
- High cobalt content
- Optimal manganese content in the alloy to control the growth rate of the oxide scale in the presence of a cobalt rich coating

These qualities are accomplished to a different degree in the dual coating systems Co_3O_4 + LSM and Co_3O_4 + LSC discussed above. The choice and combinations of multi layer coating combinations can be refined even more, and a patent application regarding this

type of multi layer coatings of slurry coatings has also been submitted in January 2007, EP37840.

7.2 Future work

The favorable effects of Co-rich coatings were displayed in this project, but to understand in detail how to optimize the use of these coatings and how to control the oxide formation more studies would have to be conducted. Already available information sources could be used in this quest. For example would the comparison between coated Crofer 22APU and Sandvik 1C44Mo20 samples be completed by analyzing the microstructure and composition of the oxide scales formed on the Co_3O_4 coated Sandvik 1C44Mo20. This might give information that could explain why the dual coatings perform so badly on the Sandvik 1C44Mo20 samples compared to the Crofer 22APU samples. The heavily oxidized areas along the cross-section of the Co_3O_4 + LSC coated Sandvik 434 samples could also be analyzed further in SEM. This might provide information about why and how heavily oxidized areas can form along the oxide scale on alloy samples that should have enough manganese to stabilize the cobalt rich coating.

In the thesis results indicating higher oxidation rates during the initial oxidation compared to long term oxidation of uncoated and LSM and Co_3O_4 + LSM coated Crofer 22APU samples were displayed. A fast initial spinel formation, not visible in the weight gain data collected in the cycling oxidation experiment, was suggested as an explanation to the faster initial oxidation rate. To support this theory SEM investigation of the cross-sections of the TGA samples should be conducted. If evidence of a faster spinel formation during the initial stage of the oxidation is found this substantiates the description of the interaction mechanisms between the slurry coatings and the growing oxide scales.

In this thesis, low chromium content in the outer oxide scale on Co_3O_4 + LSM coated Crofer 22APU sample was found when the spinel phase formed in this outer oxide scale showed a composition close to $MnCo_2O_4$. This would indicate a low diffusion rate of chromium ions in $MnCo_2O_4$ spinel. It would therefore be of great interest to measure the tracer diffusion coefficient of chromium in $MnCo_2O_4$ spinel. Initial experiments, accounted for in appendix 5, to develop a reliable method to measure this tracer diffusion coefficients have been made based on a pulsed laser deposition/secondary ion mass spectrometry, PLD/SIMS, technique. On single crystal MgO a thin layer of $MnCo_2O_4$ was deposited via PLD at 750˚C. On top of the spinel layer a Cr_2O_3 layer was applied, also via PLD, at room temperature to avoid thermally activated diffusion during deposition. The $MgO/MnCo_2O_4/Cr_2O_3$ sandwich was heat treated at 900˚C in technical air. A concentration profile of the chromium ions in the sandwich sample was then attempted to be measured via SIMS. However, the concentration profiles achieved from the SIMS analysis were too complicated to interpret satisfactorily. When studying the cross-sections of the $MgO/MnCo_2O_4/Cr_2O_3$ sandwich samples in a focused ion beam field emission gun-SEM, FIB-FEG-SEM, it was also found that there were some epitaxy and deposition effects during PLD deposition that would have to be corrected, to achieve dense $MnCo_2O_4$ and Cr_2O_3 depositions. However, with a refined PLD deposition of

$MnCo_2O_4$ and Cr_2O_3 on single crystallite MgO, a tracer diffusion experiment measuring the chromium diffusion coefficient should be possible to perform. To avoid the complex concentration profiles achieved via SIMS analysis, the concentration profile of chromium in the $MnCo_2O_4$ phase is recommended to be analyzed via EDS techniques on a transmission electron microscope, TEM. An additional step would be to develop the technique to measure the tracer diffusion coefficients of manganese and cobalt in the $MnCo_2O_4$ phase as well, to relate to the tracer diffusion coefficient for chromium.

Appendix 1: Definition of k_p

In this study the weight gain has been plotted against time$^{1/2}$ to calculate the parabolic rate constant, since this facilitates an accurate determination of the true parabolic rate constant as described by B. Pieraggi in Oxidation of Metals, 27, 177 (1987). The slope in the weight gain-time$^{1/2}$ will be equal to the square rote of the rate constant if the start of the oxidation process, $t_{t,0}$, is set to zero, $t_{t,0} = 0$.

For the cyclic oxidation experiment $t_{t,0} = 0$ is assigned to the moment the heating ramp of the first 250 hours cycle is started. However, the weight gain during the first 250 hours oxidation for the samples was ignored in the cyclic oxidation experiment due to organic burn off. This was compensated for by a correction factor in the integration constant, C, in equation 2.1.

For the TGA experiments the continuously collected data made it possible to set $t_{t,0} = 0$ at the point where the furnace reached the oxidation temperature.

To summarize the definition of k_p in this study, equation 2.1 is derived:

$$\frac{d\Delta w}{dt_t} = \frac{k_p'}{\Delta w}$$

$$\int_{\Delta w_0}^{\Delta w} \Delta w d\Delta w = \int_{t_{t,0}}^{t_t} k_p' dt_t$$

$$\frac{1}{2}\left(\Delta w^2 - \Delta w_0^2\right) = k_p'\left(t - t_{t,0}\right)$$

$$if \quad 2k_p' = k_p$$

$$\left(\Delta w^2 - \Delta w_0^2\right) = k_p\left(t - t_{t,0}\right)$$

Generally

$$k_p = \frac{d\left(\Delta w^2 - \Delta w_0^2\right)}{d\left(t - t_{t,0}\right)}$$

By simplifying the rate equation to

$$\Delta w^2 = k_p t_t + C \quad \text{with} \quad C = -k_p t_{t,0} + \Delta w_0^2$$

the parabolic rate constant becomes

$$k_p = \frac{d\left(\Delta w^2\right)}{d\left(t\right)}$$

thereby implicitly taking $\Delta w_0 = 0$ and $t_{t,0} = 0$

Δw is the weight increase for the oxidation samples and Δw_0 is the weight increase of the oxidation sample before the oxidation process has started. t_t is the oxidation time and $t_{t,0}$ is the time for the start of the oxidation process. k_p is the parabolic rate constant and $k_p^{'}$. The above equations show that the values used for Δw_0 and $t_{t,0}$ in the evaluation of the parabolic rate constant have an influence on this value.

Appendix 2: Line scans across oxide scales on oxidized samples

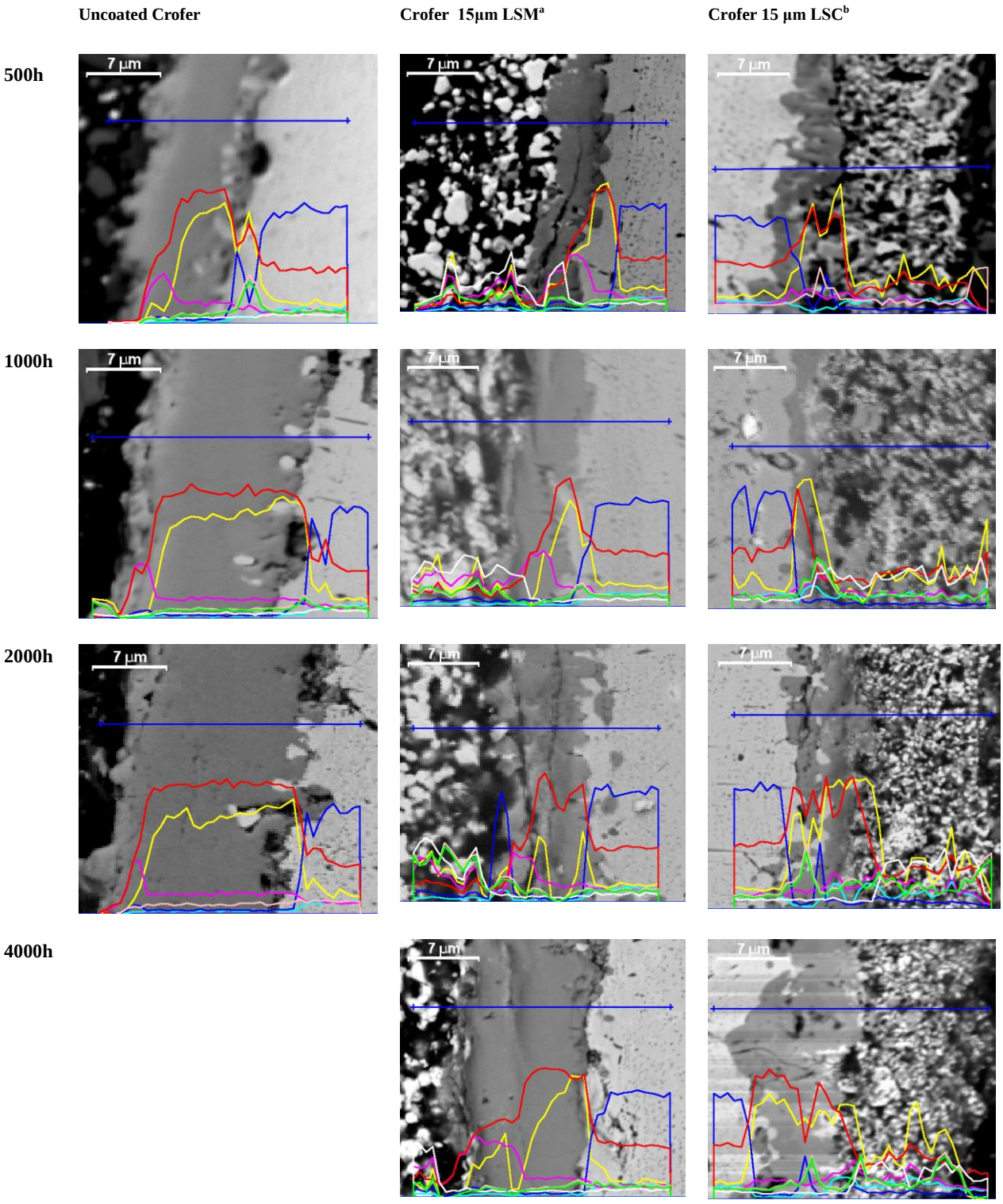

Fig. 1. Line scans over the oxide scale with the oxidation time to the left.

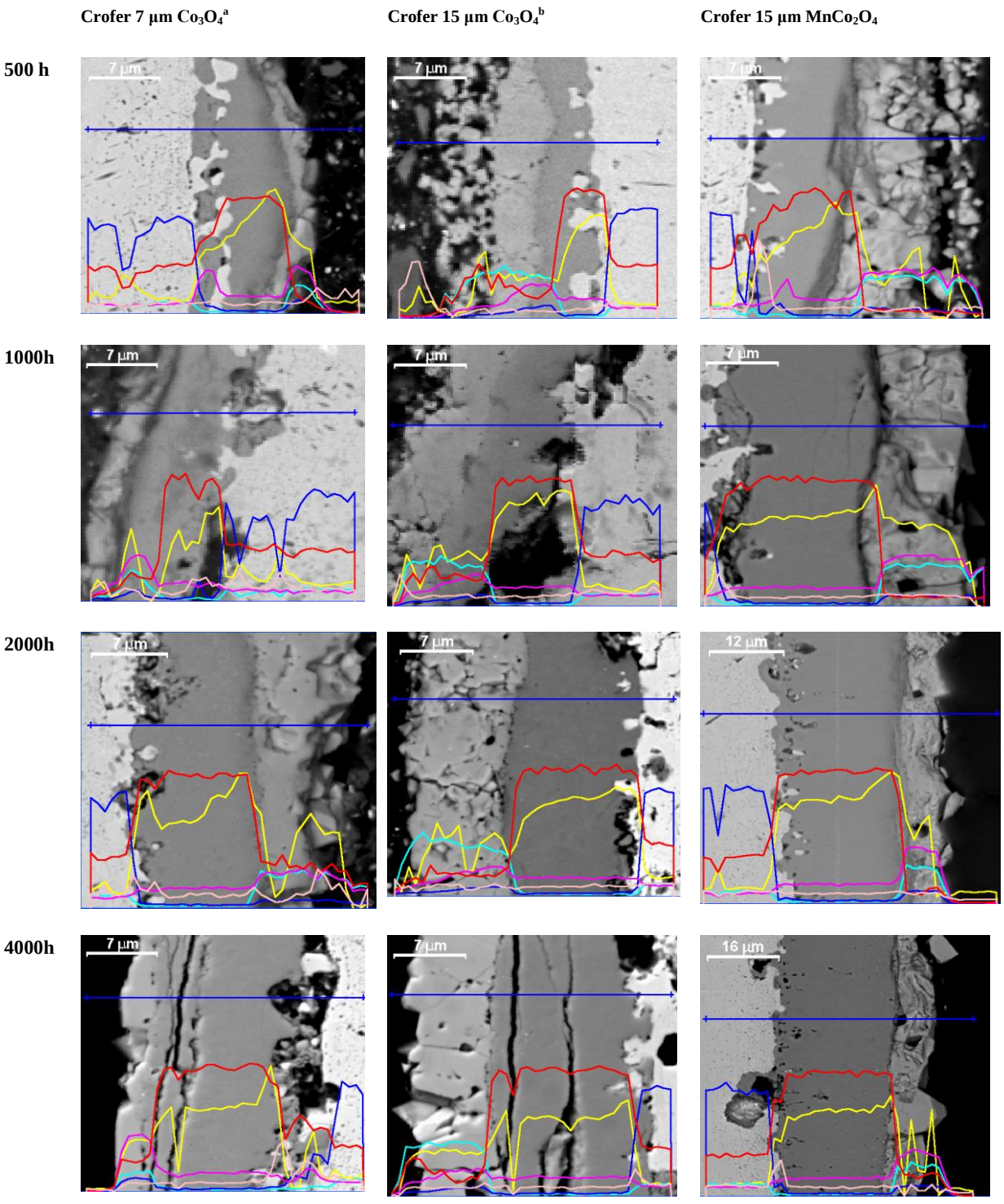

Fig. 2. Line scans over the oxide scale with the oxidation time to the left.

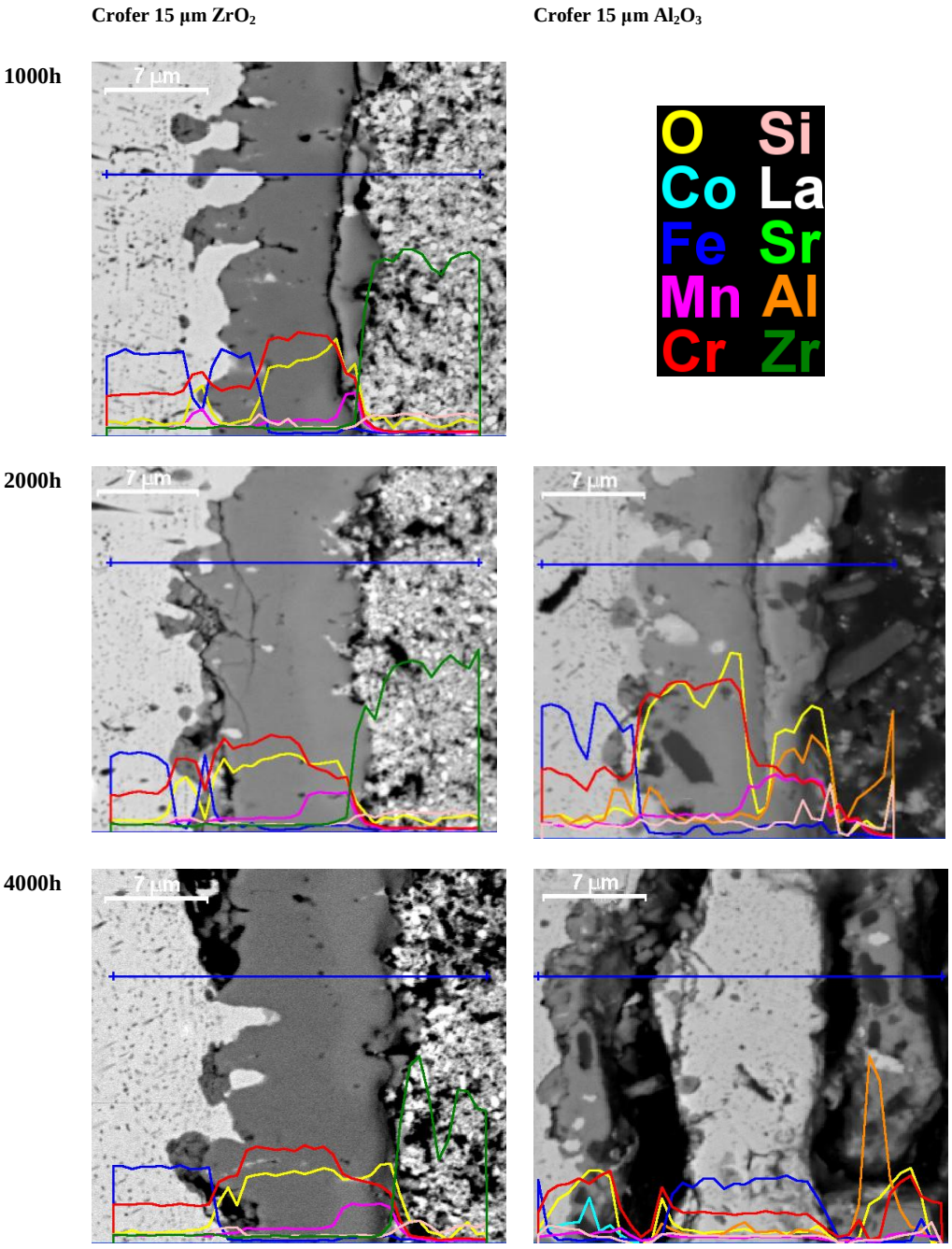

Fig. 3. Line scans over the oxide scale with the oxidation time to the left.

Appendix 3: The effect of oxygen uptake from the coating on the oxide scale growth

Crofer 22APU alloy has been shown to follow a parabolic oxidation behavior as described by equation 3.1. The weight gain corresponds to the oxygen uptake. For the spinel formation on uncoated Crofer the entire oxygen uptake originates from the atmosphere as illustrated in reaction 1 below.

$$Mn + 2Cr + 2O_2 \rightarrow MnCr_2O_4 \qquad \text{reac. 1}$$

The measured weight gain, Δw, of an oxidized sample consists of contributions from the spinel phase, Δw_s, and the chromia phase, Δw_c, in the oxide scale as illustrated in equation 1a below. The weight gain of the spinel and the chromia growth could be expressed in the total weight gain of the sample by using the spinel ratio in the oxide scale, cf. table 3.3, as illustrated in equation 1b-c. To simplify, the chromia and spinel are presumed to have identical specific volumes in the equations.

$$\Delta w_s + \Delta w_c = \Delta w \qquad \text{eq. 1a}$$

$$\Delta w_s = spinel\,ratio \cdot \Delta w \qquad \text{eq. 1b}$$

$$\Delta w_c = (1 - spinel\,ratio) \cdot \Delta w \qquad \text{eq. 1c}$$

For LSM coated Crofer it was noticed that the formed spinel phase had ca. 17% extra Mn-content, which is assumed to originate from the LSM coating. Since the manganese in the Mn_2O_3 phase undergoes a reduction when incorporated into the spinel phase, a certain oxygen contribution from the coating to the oxide scale growth is possible, and it is not registered in the weight gain of the sample. To ensure that the lowered weight gain of the LSM coated sample compared to the uncoated Crofer sample is not only an effect of oxygen uptake from the coating instead of the atmosphere, the possible oxygen contribution from the coating is transformed into the weight gain the sample would have experienced if the oxygen had originated from the atmosphere. In reaction 2 the oxygen contribution from the coating has been taken into consideration, and the term $MnO_{1.5}$ illustrates the oxide contribution from the Mn_2O_3 phase.

$$\frac{1}{2}MnO_{1.5} + Mn + \frac{3}{2}Cr + \frac{13}{8}O_2 \rightarrow Mn_{1.5}Cr_{1.5}O_4 \qquad \text{reac. 2}$$

By dividing the oxygen uptake from the atmosphere in reaction 1 and 2, as shown below, a factor is achieved that should be multiplied with the weight gain of the spinel phase in equation 1a-b to incorporated the weight gain of the oxygen originating from the coating. The resultant weight gain is a calculated theoretical weight gain, $\Delta w_{theo.}$.

$$2 \Big/ \left(\frac{13}{8}\right) = 1.23 \qquad 1.23 \cdot \Delta w_s + \Delta w_c = \Delta w_{theo.}$$

By expressing the weight gain of the spinel phase and the chromia phase in the total weight gain using the spinel ratio found in oxide scale grown on LSM coated Crofer 22APU samples, cf. table

3.3, the theoretical weight gain can be expressed in the measured weight gain of the oxidized sample. The spinel ratio in the oxide scale was found to be about 40% on the LSM coated samples.

$$1.23 \cdot 0.4 \cdot \Delta w + 0.6 \cdot \Delta w = \Delta w_{theo.} \quad \Rightarrow \quad 1.09 \cdot \Delta w = \Delta w_{theo.}$$

For LSC coated Crofer 22APU sample a spinel with the composition $Cr_{1.5}Mn_{0.5}CoO_4$ is formed. The cobalt is originating from the LSC coating and undergoes a reduction when reacting with the oxide scale to form the spinel described above. This leads to an oxygen uptake from the coating made visible in reaction 3 where the $CoO_{1.56}$ term illustrates the oxidation step of Co in the LSC perovskite and the oxide contribution from the coating. The lanthanum and strontium ions do not change oxidation the step when the LSC perovskite is reacting/dissociating into $LaCrO_3$, $SrCrO_4$ and $Cr_{1.5}Mn_{0.5}CoO_4$.

$$CoO_{1.56} + \frac{1}{2}Mn + \frac{3}{2}Cr + \frac{61}{50}O_2 \rightarrow Cr_{1.5}Mn_{0.5}CoO_4 \qquad \text{reac. 3}$$

A spinel ratio of ca. 40% was found in the oxide scale on the LSC coated Crofer 22APU sample, cf. table 3.3, and by using this ratio the theoretical weight gain of the LSC coated Crofer 22APU sample could be calculated. For simplicity the specific volumes for $CoO_{1.56}$ and $Cr_{1.5}Mn_{0.5}CoO_4$ are assumed to be similar.

$$2 \Big/ \left(\frac{61}{50}\right) = 1.64 \qquad 1.64 \cdot \Delta w_s + \Delta w_c = \Delta w_{theo.}$$

$$1.64 \cdot 0.4 \cdot \Delta w + 0.6 \cdot \Delta w = \Delta w_{theo.} \quad \Rightarrow \quad 1.26 \cdot \Delta w = \Delta w_{theo.}$$

In figure 1 the measured weigh gain of the single layer coated Crofer samples and the calculated theoretical weight gain for LSM and LSC coated Crofer samples are plotted against time$^{1/2}$. This plot shows that the oxygen uptake from the applied coatings is an almost negligible effect on the lowered weight increase on the coated samples.

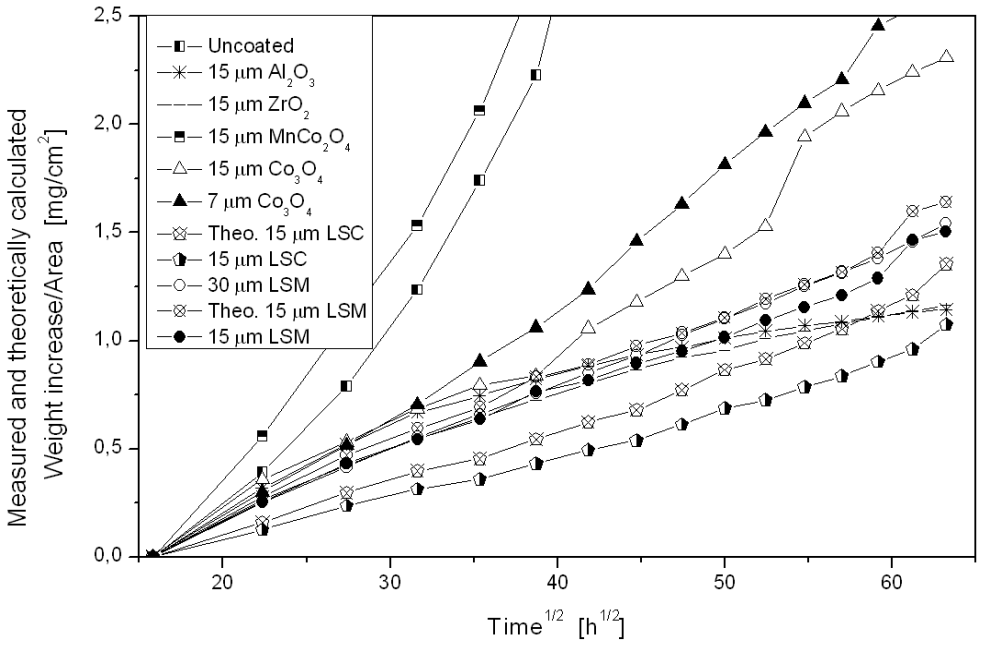

Figure 1. The measured weight gain for the uncoated and single layer coated Crofer samples and the theoretically calculated weigh gain for the LSM and LSC coated Crofer samples in the long term, cyclic oxidation experiment at 900˚C in air containing 1% water plotted against time$^{1/2}$.

Appendix 4: Line scans across oxide scales on oxidized samples

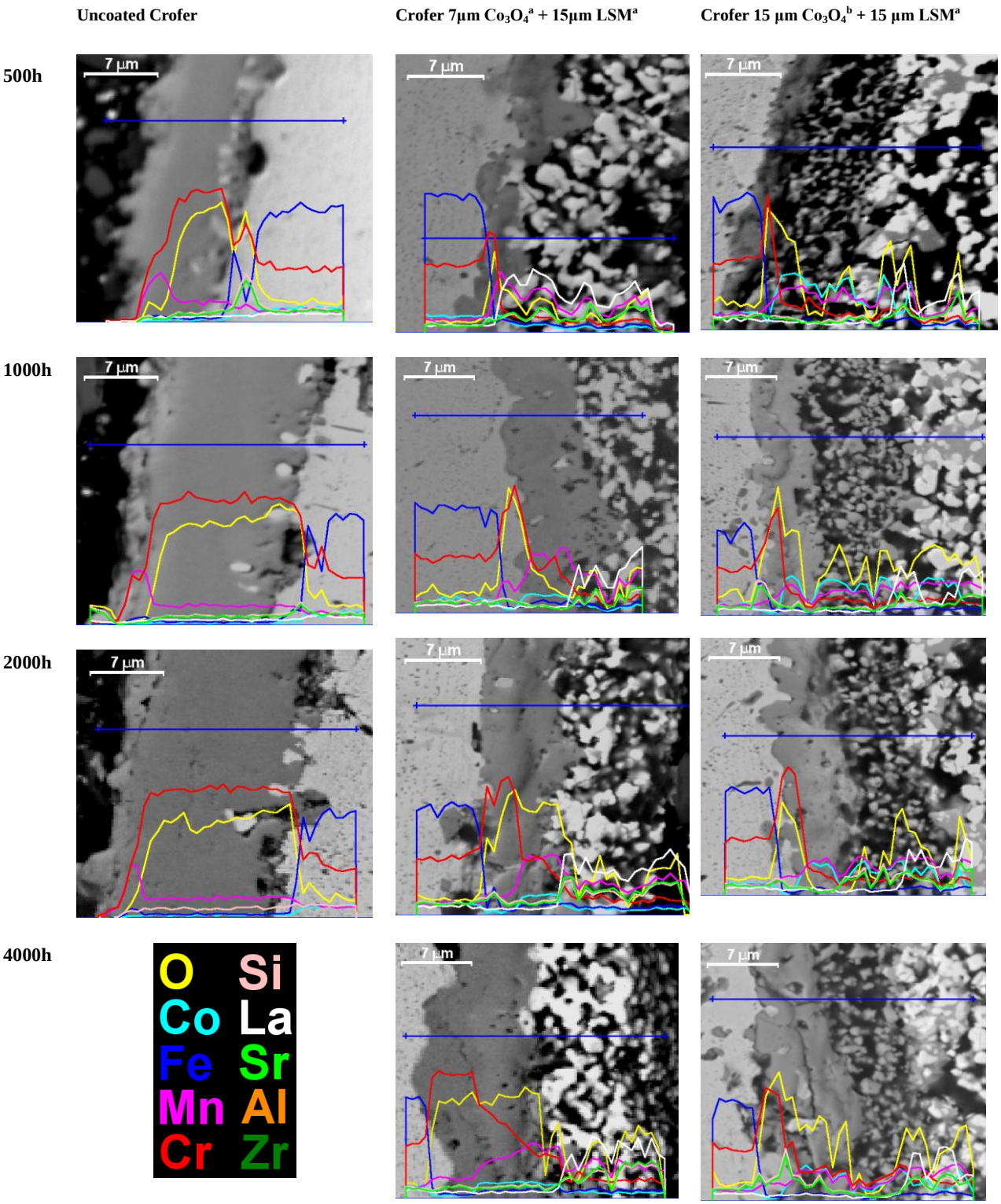

Fig. 1. Line scans over the oxide scale with the oxidation time to the left.

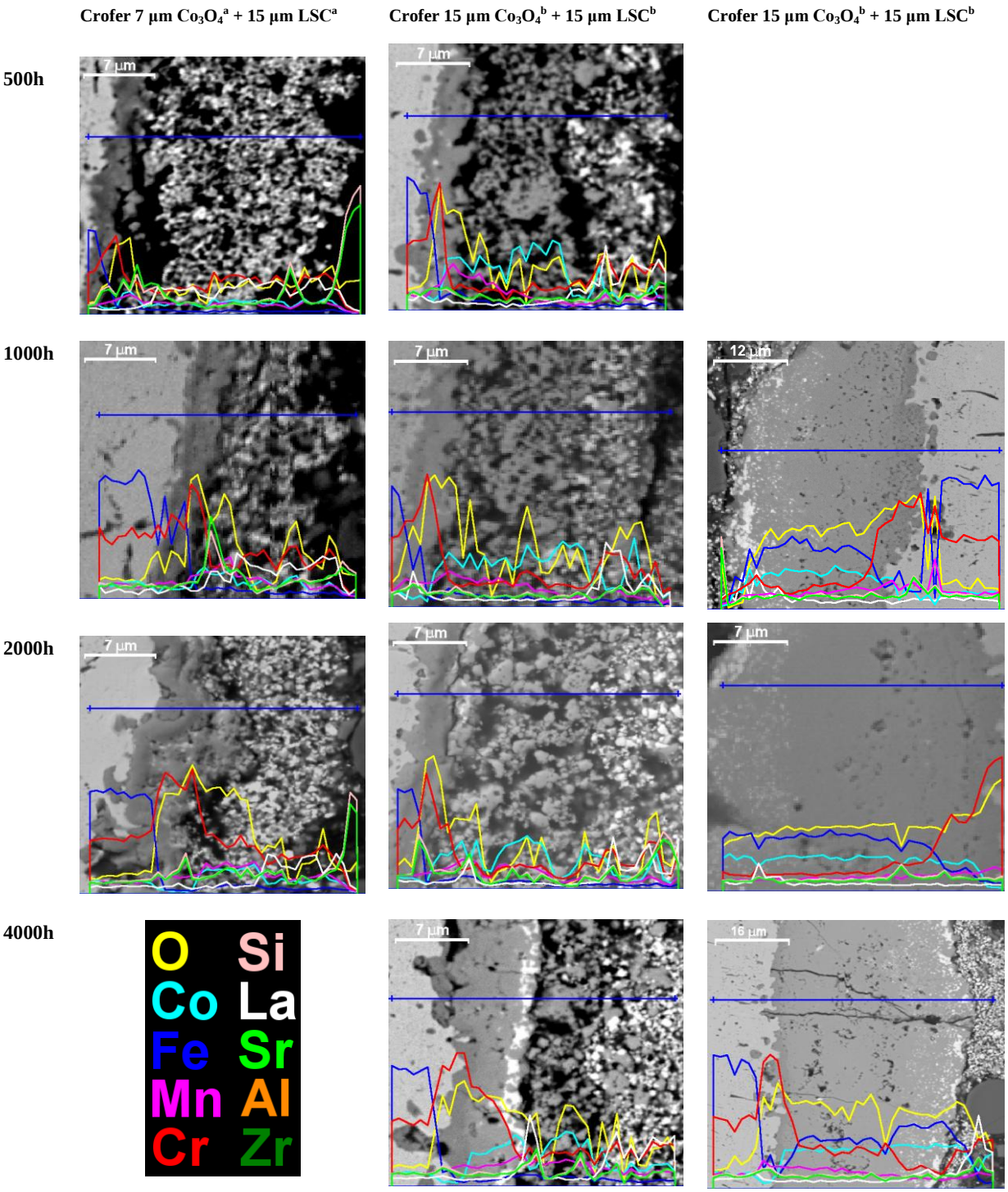

Fig. 2. Line scans over the oxide scale with the oxidation time to the left.

Appendix 5: Tracer diffusion coefficient of chromium in $MnCo_2O_4$

1. Introduction

In the thesis it is shown that the reaction products formed below successful coatings on the interconnect alloy mainly consist of a spinel phase. One of the most interesting spinel phases was found to form as a reaction product on Co_3O_4 + LSM coated Crofer 22APU samples at 950˚C in air containing 1% water. The phase consisted of a $(Mn,Co)_3O_4$ spinel phase, with a composition close to $MnCo_2O_4$ and only a small content of chromium. The coating, and indirectly the formed spinel phase, appeared to be successful in decreasing the oxidation rate of the Crofer sample. The formed $(Mn,Co)_3O_4$ spinel phase also appeared to be successful in decreasing the outward diffusion of chromium based on the low chromium content found in the outer oxide/spinel scale. Due to these promising observations a value for the tracer diffusion coefficient of chromium in a $MnCo_2O_4$ spinel in air at the temperature used in the oxidation experiments, as performed in the thesis, became of interest.

The experimental idea was to deposit a dense layer of $MnCo_2O_4$ spinel with a layer of Cr_2O_3 on top by pulse laser deposition, PLD. By heat treating the oxide double layer the chromium ions in the chromia scale would diffuse into the spinel phase creating a concentration profile, which then was measured by using SIMS. From the slopes of the chromium concentration profile a tracer diffusion coefficient for chromium in $MnCo_2O_4$ could be calculated.

2. Experimental

2.1 PLD target preparation

$MnCo_2O_4$ powder was produced via a glycine-nitrate synthesis using Mn- and Co-nitrate solutions. The produced powder was analysed with X-ray diffraction, XRD, to verify whether the produced powder consisted of a single phase $MnCo_2O_4$. The instrument used was a STOE (θ- θ) diffractometer equipped with Cu-Kα radiation.

One batch of the powder was calcinated for 8 hours in air at 750°C and one batch for 8 hours in air at 800°C. The heating and cooling ramps were set to 100°C/h during both calcination processes. The powder calcinated at 750°C was wet milled for 4 days until the average size of the powder particles was ca. 0.85 μm. The powder calcinated at 800°C was wet milled for 10 days until the average size of the powder particles was ca. 0.95 μm.

For production of target disks, 22-28 g portions of $MnCo_2O_4$ powder were weighed in per target. To achieve an optimal density of the target disks, 30% of the powder portions consisted of $MnCo_2O_4$ powder calcinated at 750°C while the remaining 70% of the $MnCo_2O_4$ powder portions consisted of powder calcinated at 800°C. The target disks were pressed using pressure tools with a diameter of 47 mm. The targets were pressed for 30 seconds at 1 ton. The exact dimensions of the two targets produced are presented in table 1. A target thickness over 6 mm is recommended during PLD deposition [1].

Table 1. Dimensions of produced PLD targets.

Disk	ø as prepared [mm]	Thickness – as prepared [mm]	ø Iso-statically pressed [mm]	Thickness – Iso-statically pressed [mm]
1	47.5	6.03	41.93	5.29
2	48.1	6.90	42.48	6.38

The targets were thereafter iso-statically pressed for 20 seconds at 55 ton, and the final dimensions of the target disks are shown in table 1. The target disks were sintered for 6 hours at 1000°C in air. The sintering process had heating and cooling ramps set to 100°C/h. The surfaces of the targets were polished using 1000 μm SiC abrasive paper. XRD analyses of the polished surfaces were performed to confirm that the targets still consisted of single phase $MnCo_2O_4$.

2.2 *Pulse Laser Deposition - PLD*

To ensure that the PLD deposition method does not change the crystallography or the composition of the $MnCo_2O_4$ spinel, three PLD depositions of $MnCo_2O_4$ onto three Si-wafers substrates were performed. Si-wafers were used as substrates since they are amorphous and should not insert any preferred orientation in the deposited layers. Significant texture was found when PLD deposition was performed on single crystal MgO substrates, which was made visible when only one reflection direction was detected during XRD analysis of the deposited film. With only one diffraction reflection it was impossible to determine whether the correct spinel phase composition was deposited. The three PLD depositions of $MnCo_2O_4$ on the Si-wafer substrates had a thickness of ca. 0.13 μm. All three depositions were made at 750°C, but at different pressures. The first Si-substrate sample was deposited at 0.05 mbar air, the second at 0.1 mbar air and the third at 0.2 mbar air. The absence of epitaxy in the deposited films ensured the presence of several reflection directions in the film during analysis in grazing incidence wide angle X-ray scattering, GIWAXS. The presence of several reflection directions made it possible to determine whether the deposited film consisted of a single phase of $MnCo_2O_4$ spinel with the correct composition. As will be described in the results section, the deposition in 0.1 mbar air resulted in single phase $MnCo_2O_4$.

Single crystals of MgO were used as substrates during the PLD deposition of the diffusion samples since MgO was assumed to be chemically inert in contact with $MnCo_2O_4$ and would be stable during heating to 950˚C. Two single crystals of MgO with a diameter of 25.4 mm and thickness of 1 mm were ultrasonically cleaned in ethanol for 10 minutes before insertion into the chamber of the PLD equipment. Note that the two MgO substrates were mounted and PLD coated in the PLD equipment at two different occasions, but under the exact same conditions as will be described as follows. On the polished side of the MgO substrate a film of $MnCo_2O_4$ was deposited for a total of 8 hours in 100% air with a total pressure of 0.1 mbar at 750°C. The PLD chamber was cooled, and at room temperature a target of Cr was used to apply a Cr_2O_3 layer on top of the $MnCo_2O_4$ film for 5 hours. The atmosphere was still 0.1 mbar air which should be enough to oxidize the chromium during the deposition, and the low deposition temperature should avoid any thermally activated diffusion of chromium into the spinel phase. With an EDS based method for measuring the thickness of PLD depositions [2], the thicknesses of the applied $MnCo_2O_4$ and Cr_2O_3

layers were measured to ca. 400 nm and 100 nm respectively in a JEOL JSM 5310 LV microscope at high vaccum.

2.3 Heat treatment

A duration time of the heat treatments at the different heat treatment temperatures had to be set. The duration time had to be long enough for a concentration profile of the inward diffusing chromium ions to build up, and short enough to avoid the chromium ions to diffuse all the way through the spinel phase. To calculate the duration times of the heat treatments a diffusion coefficient for chromium in $MnCo_2O_4$ at each temperature would have to be known so that the diffusion distances could be calculated.

In the literature few diffusion experiments of chromium in spinel phases are presented, and no direct value of the tracer diffusion coefficient for chromium in $MnCo_2O_4$ spinel was found. Instead estimated values of diffusion coefficients for chromium in $MnCo_2O_4$ had to be calculated. Based on tracer diffusion experiments of Mn, Co, Fe, and Cr in $(Cr_xFe_{1-x})_{3-\delta}O_4$ spinels at 1200˚C, it was found that cation vacancies are the majority defects at atmospheric pressure, and it appears that the logarithm of the diffusion coefficients for chromium tends to be an order of 3 lower than the logarithm of the diffusion coefficients for the Mn, Fe, and Co cations [3]. Combining this with the results from a tracer diffusion experiment of Mn, Co, and Fe in $(Co_xMn_{1-x})_{3-\delta}O_4$ spinels at 1200˚C [4], and the assumption that the diffusion coefficients in $MnCo_2O_4$ would be in the same region as the diffusion coefficients in $CoMn_2O_4$ had the $MnCo_2O_4$ spinel been stable at 1200˚C, an estimation of the diffusion coefficient for chromium in $MnCo_2O_4$ at 1200˚C in air could be calculated to ca. $10^{-16.5}$ m^2/s. The activation energy for cation diffusion via vacancies of Cr in $MnCo_2O_4$ was then assumed to be in the same region as for iron and cobalt in $(Co_xFe_{1-x})_{3-\delta}O_4$ as calculated by F.H. Lu, S. Tinkler and R. Dieckmann [5], that is about 140 kJ/mol. An estimation of the tracer diffusion coefficients of chromium in $MnCo_2O_4$ at different temperatures were calculated using the Arrhenius equation that connects the activation energy for cation diffusion via vacancies and diffusion coefficients, cf. equation 1.

$$D_{Cr}^{*} = D_0^{*} \exp\left(\frac{-Q_V}{RT}\right) \qquad \text{eq. 1}$$

Where D_{Cr}^{*} is the diffusion coefficient, D_0^{*} is a constant term referred to as the pre-exponential factor or frequency factor, Q_V is the activation energy for cation diffusion via vacancies, R is the gas constant, and T is the temperature in Kelvin [6].

Table 2. Estimated values of tracer diffusion coefficient for chromium in $MnCo_2O_4$ spinel at 855, 900, and 950˚C.

Temperature [˚C]	D_{Cr}^{*} **[m^2s^{-1}]**
855	$10^{-18.02}$
900	$10^{-17.77}$
950	$10^{-17.52}$

By using a simplification of Fick's second law, as seen in the equation 2 below, preliminary calculation of the time acquired for the chromium cations to diffuse a certain distance in $MnCo_2O_4$ could be made.

$$x_p = (D^*_{Cr} \cdot t_t)^{1/2} \quad \Rightarrow \quad t_t = \frac{x_p^2}{D^*_{Cr}} \qquad \text{eq. 2}$$

In equation 2 x_p is the diffusion distance the cation has diffused [6].

The first MgO substrate provided with a duplex $MnCo_2O_4/Cr_2O_3$ film, disk A, was inserted in a furnace with stagnant air for heat treatment at 900°C for 4 hours. The heating and cooling ramps were set to 100°C/h. The sample was thereafter broken into smaller pieces to fit into the SIMS sample holder by breaking the sample by hand along deep scratches made by a diamond crystal.

The second MgO substrate provided with a duplex $MnCo_2O_4/Cr_2O_3$ film, disk B, was broken into smaller pieces to fit into the SIMS sample holder by breaking the sample by hand along deep scratches made by a diamond crystal directly after PLD deposition. One of the pieces was heat treated at 855°C for 7.5 hours, and one piece was heat treated at 950°C for 2.7 hours. The heating and cooling ramps were set to 100˚C/h. During both heat treatments the samples were exposed to stagnant air. A third piece was left un-treated to function as a reference sample in the following SIMS analysis.

2.4 SIMS analysis

The diffusion profiles of the chromium ions in the spinel phases on the diffusion samples were measured via SIMS analysis performed[I] on an ATOMIKA Instruments ION MICROSCOPE; MacSIMS 2.1.13. Cs-ions were used as sputtering ions, and the samples were mounted so that the sputtering ions hit the samples with and an angle of 130° making the ion beam slightly grazing. The instrument was set to detect Cr-50, Mn-55, Co-59, and Mg-26. The ion beam was set to scan an area with the dimension 300*300 μm^2. The depth of the formed craters were measured using a Dektak 8 Stylus Profiler, and by assuming a constant sputtering rate through the samples, the time axis in the counts-time plots collected were transformed into counts-distance plots. These are presented in section App.5.3.2-3.

By applying the one-dimensional thin film diffusion equation, cf. equation 3, a least squares fit procedure could be used on the collected concentration profile for chromium to achieve a value of the diffusion coefficient.

$$\frac{S}{S_0} = 1 - erf\left(\frac{\Delta x}{2\sqrt{D^*_{Cr} \cdot t_t}}\right) \Rightarrow S = S_0\left(1 - erf\left(\frac{\Delta x}{2\sqrt{D^*_{Cr} \cdot t_t}}\right)\right) \qquad \text{eq. 3}$$

[I] Performed via assistance from Peixiong Shi at Danchip, Technical Univeristy of Denmark

S_0 stands for the Cr-concentration at the surface and the S for the Cr-concentration after a diffusion process into the sample after a time t_t, Δx is the diffusion distance, and D^*_{Cr} the diffusion coefficient of chromium [7].

One piece of the heat treated disk A was analyzed on an isolated occasion, while a second piece of the heat treated disk A was analyzed at the same time as the as-prepared and heat treated pieces of disk B. This would give information about the reproducibility of the SIMS measurement of the diffusion profile.

2.5 FIB-FEG-SEM analysis of cross-sections

The surfaces and the cross-sections of the diffusion samples were analysed using a field emission gun secondary electron microscopy equipped with a focused ion beam, FIB-FEG-SEM, Zeiss Cross-beam 1540X. The surfaces of the diffusion samples were carbon coated to avoid charging in the microscope. Via back-scatter electrons, BSE, and secondary electrons, SE, micrographs of the sample surfaces were collected, whereafter cross-sections in the diffusion samples were created via sputtering with Ga-ions. Due to removal of the carbon coating during these sputtering processes, the samples had to be carbon-coated again before BSE micrographs of the cross-sections could be collected.

3. Results

3.1 GIWAXS analysis

The background signal in the data collected from the GIWAXS analysis was quite high, presumably because of a significant contribution from the amorphous substrate. A background subtraction algorithm improved the images somewhat. The data from the three Si-substrate samples were varied. For sample 1, where the pressure had been 0.05 mbar, the collected diffraction peaks corresponded relatively well with the expected peaks for $MnCo_2O_4$. The anisotropic distribution of the collected intensities indicated several populations of different preferred orientations. For sample 2, where the pressure had been 0.1 mbar, the collected diffraction data showed an isotropic distributed cubic $MnCo_2O_4$. Sample 3 which had been deposited in 0.2 mbar presented data that indicated the presence of a second phase besides $MnCo_2O_4$, possibly tetragonal $CoMn_2O_4$. In the PLD depositions of the diffusion samples a pressure of 0.1 mbar were used.

3.2 SIMS analysis of 900°C sample from disk A

In figure 1 the two SIMS profiles for the two pieces from disk A, which has been heat treated at 900°C for 4 hours, are presented.

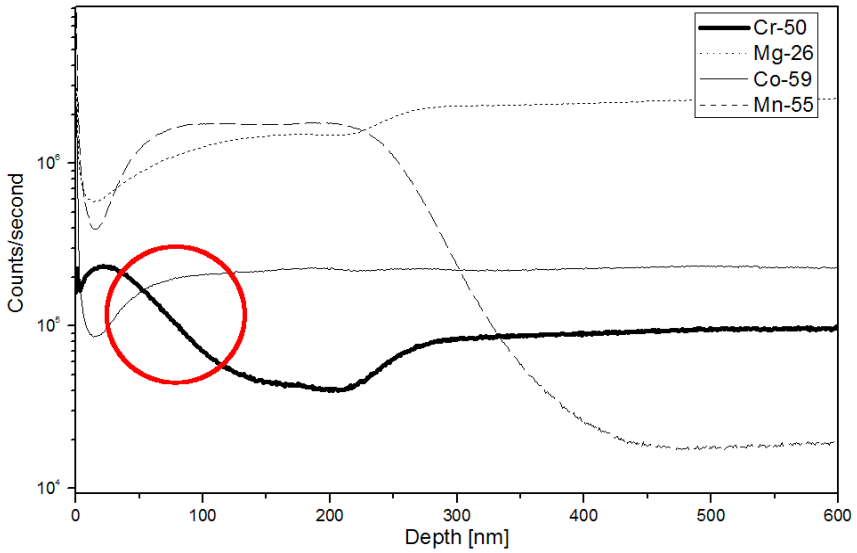

Figure 1.a. SIMS profiles of the Cr-50, Mn-55, Co-59, and Mg-26 ions on sample 1 from disk A, which was heat treated at 900°C for 4 hours.

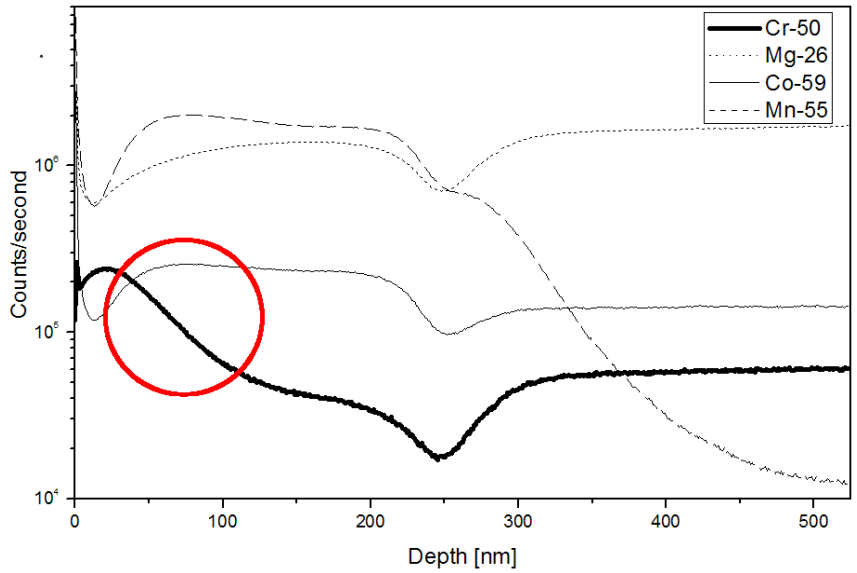

Figure 1.b. SIMS profiles of the Cr-50, Mn-55, Co-59, and Mg-26 ions on sample 2 from disk A, which was heat treated at 900°C for 4 hours.

In figure 2 the assumed phase boundaries between the Cr_2O_3 and $MnCo_2O_4$ layers and the MgO crystal in the diffusion sample are marked in the SIMS profiles of sample 1 from disk A which was heat treated at 900˚C fro 4 hours.

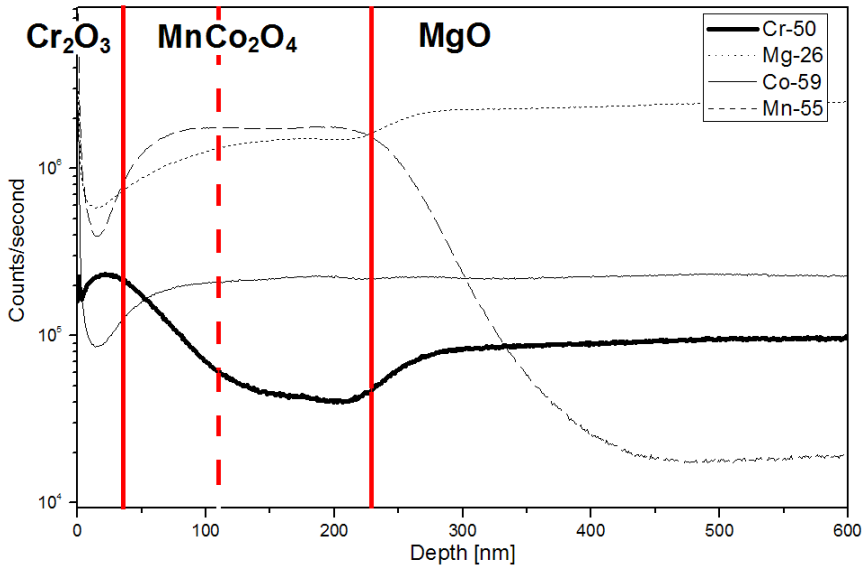

Figure 2. SIMS profiles of the Cr-50, Mn-55, Co-59, and Mg-26 ions on sample 1 from disk A, which was heat treated at 900°C for 4 hours.

Where the Mn- and Co-signals goes abruptly up the $MnCo_2O_4$ phase is assumed to start and the Cr_2O_3 to end. The Cr-signal does however not go down equally abruptly as the Mn- and Co-signal go up, since chromium ions probably have diffused inward in the spinel phase creating a concentration profile. Note however that the steep slope of the Mn- and Co-signals in the assumed Cr_2O_3 phase in the $Cr_2O_3/MnCo_2O_4$ interface indicate the outward diffusion of Mn- and Co-cations into the Cr_2O_3 phase. Going further into the sample the Mg signal goes up at the same time as the Mn-signal goes abruptly down suggesting that this is where the MgO crystal starts. With an EDS-based thickness measurement method of PLD films, the thicknesses of the $MnCo_2O_4$ and Cr_2O_3 layers were measured to be about 400 nm and 100 nm respectively. The SIMS data above indicate that these depth measurements might be slightly off.

Studying the Mn-signal more closely in figure 1 it becomes apparent that it seems to be significantly high on the surface of the diffusion sample. This is probably not completely explained by the initial extensive dive/increase during the first few nm in the intensity measurements caused by charging of the sample and impurities, for example different organic impurities absorbed from the atmosphere. Instead it is realistic to also assign this to Mn that has diffused fast and easy through the chromia layer just as observed on chromia forming ferrous alloys containing small amounts of Mn such as Crofer 22APU. The increase in the Co-signal where the spinel phase is assumed to start is expected. But when the Mn-signal is abruptly decreasing after ca. 250 nm, indicating the end of the spinel phase and the start of the MgO crystal, no change is observed in the Co-signal. Through-out the spinel phase an increasing Mg signal is detected. Reaching the MgO crystal the increase becomes more abrupt.

Studying the Cr-signal in figure 1 in more detail there is a small decrease on the surface of the diffusion sample, where the Mn-signal was elevated. This is to be expected if a Mn,Cr –spinel is formed due to the fast outward diffusion of Mn through the chromia layer. Disregarding this small area of forming spinel phase on the surface

of the sample, there is a ca 25 nm broad Cr-peak in the top area of the sample. This is probably indicating the chromia layer. As noted above, the Mn- and Co-signals go abruptly up after this broad Cr-peak while the Cr-signal has a much flatter slope when going down. This is the diffusion profile. In figure 2 a dashed vertical line illustrates where the concentration profile of the Cr-ions starts to even out, indicating how far chromium has been able to diffuse inward during the heat treatment.

In the SIMS profile in figure 1b an unexpected decrease in all signals is observed just where the MgO crystal would be assumed to start. The decrease seems to be equal in all signals, and a possible explanation for this could be a void between the PLD deposited film and the MgO crystal.

However, since no earlier experience with SIMS analysis of oxide sample of the same type as the diffusion samples were available, the interpretations of the cation profiles in figure 1 above is only based on guess-work and logical thinking. The complexity of the SIMS profiles would make it unwise to try and perform a least square fit of an erf-function on a SIMS profile not completely understood since the reliability of the result would be questionable. Furthermore, errors, that would lessen the accuracy of the analysis, might be implemented on the concentration profiles during SIMS analysis, and some of them are listed below [8]:

- Interlayer mixing
- Surface and interface roughness affects the intensity of the different ions
- Matrix effect - the intensity of the different isotopes are different in different chemical environment
- Hydride formation during SIMS analysis
- Preferential sputtering

The SIMS technique creates an error in the profiles since it promotes interlayer mixing, which means that when the ion beam hits the sample surface, material under it is pressed into the sample. The phenomenon is illustrated in figure 3. Some of the effect might be removed during the sputtering, but as the analysing probe reaches deeper and deeper into the sample, the effect of the interlayer mixing becomes increasingly worse.

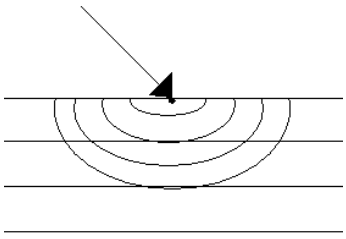

Figure 3. The illustration of interlayer mixing.

The intensities of the isotopes are different in different chemical environments, and the intensities of the isotopes are therefore not comparable in between two different chemical environments. The diffusion samples consist of at least three different chemical environments, the Cr_2O_3 layer, the $MnCo_2O_4$ layer, and the MgO crystal.

After heat treatment a reaction phase in between the Cr_2O_3 layer and the $MnCo_2O_4$ layer has probably developed. One example of the effect of the chemical environment on the intensities of the different isotopes might be the increase in the chromium signal when the sputtering probe has reached the MgO crystal, cf. figure 2. A second example might for example be the large intensity of the magnesium signal in the chromia phase compared to the rest of the sputtering depth in the SIMS profiles of the samples from disk B in figure 4.

Hydride formation during the SIMS analysis could create clusters that by mistake are registered as another element than it actually is which would create false intensities. This might however not be any significant problem during this particular case.

Preferential sputtering can take place when a multicomponent substrate is bombarded with an ion-beam. If the energy from the ion-beam is more efficiently transferred to one of the components in the substrate, this component might sputter more efficiently than the others. As a result a miss-leading enrichment of the less efficiently sputtered components would form, and this would implement errors on the concentration profiles.

The assumption that the sputtering rate through the chromia layer and the spinel layer is the same also implements error in the concentration profiles.

3.3 SIMS analysis of as-prepared, 855°C and 950°C samples from disk B

In figure 4 the SIMS profiles of the as-prepared piece from disk B and the 855°C and 950°C heat treated pieces from disk B as well are presented.

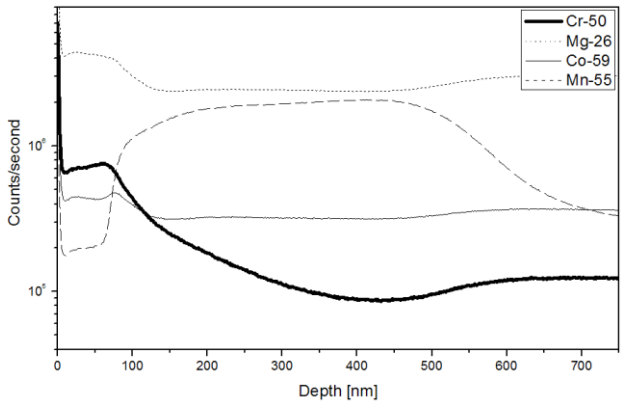

Figure 4.a. SIMS profile of the Cr-50, Mn-55, Co-59, and Mg-26 ions on the as-prepared sample from disk B.

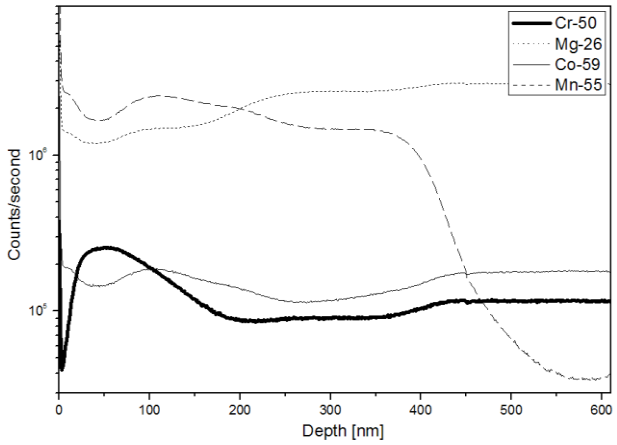

Figure 4.b. SIMS profile of the Cr-50, Mn-55, Co-59, and Mg-26 ions on the 855°C heat treated sample from disk B.

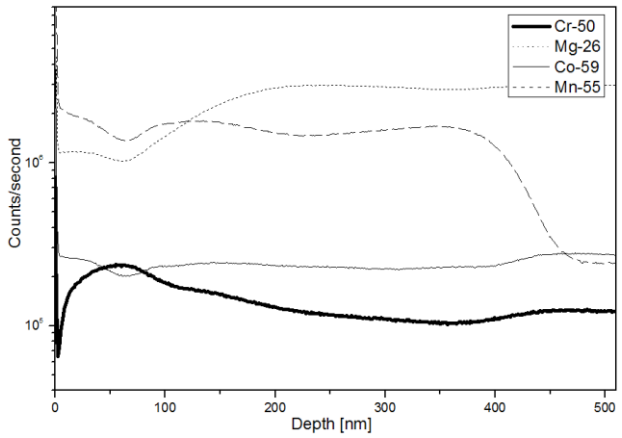

Figure 4.c. SIMS profile of the Cr-50, Mn-55, Co-59, and Mg-26 ions on the 950°C heat treated sample from disk B.

In figure 4.a it is visible that the initial broad chromium peak, indicating the chromia layer, is significantly flatter on the as-prepared sample than on the heat treated samples in figure 1. No peak of manganese appears to be detected on the diffusion sample surface. This is expected since no real outward diffusion of Mn should have taken place at room temperature. At this temperature no inward diffusion of Cr should have taken place either. But the chromia/spinel interface that should have been sharper and more discernable on the un-heated sample, than on the heat treated sample in figure 1, instead consists of a chromium profile with a rather flat slope. This would suggest that an inward diffusion of chromium would have taken place already at room temperature.

For the two diffusion samples heat treated at 950˚C and 855˚C from disk B the SIMS profiles in figure 4.b-c are even more flattened than on the as-prepared sample, and the interfaces can hardly be discerned in the profiles.

3.4 Cross-sections of the diffusion samples

In figure 5-7 below micrographs of the surfaces and the cross-sections of the as-prepared sample and the samples heat treated at 900˚C and 950˚C are presented.

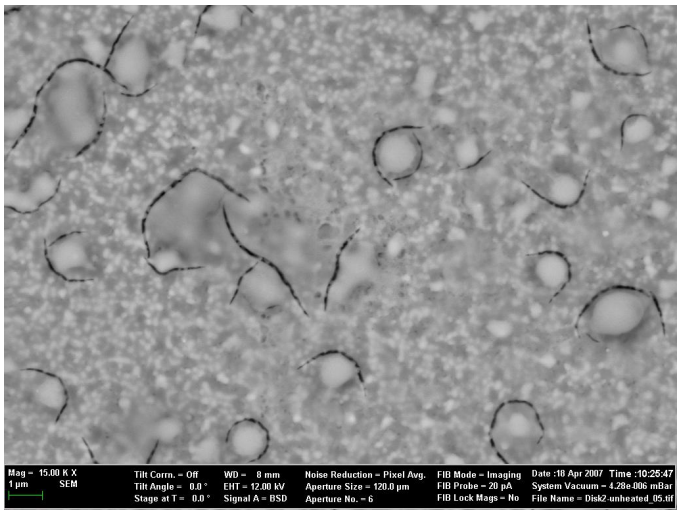

a

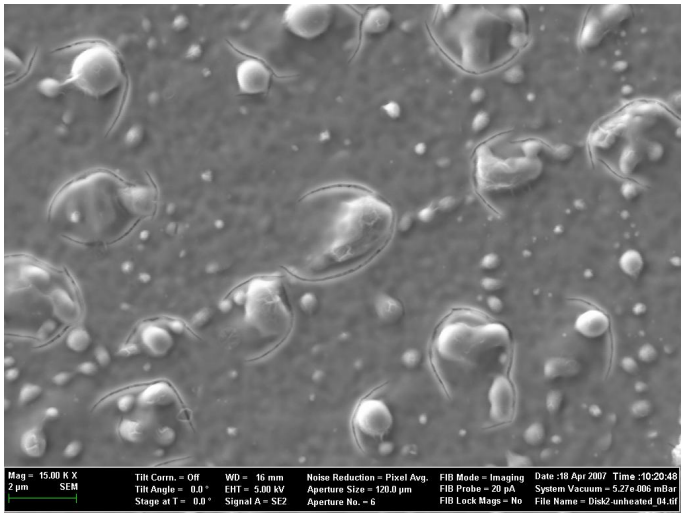

b

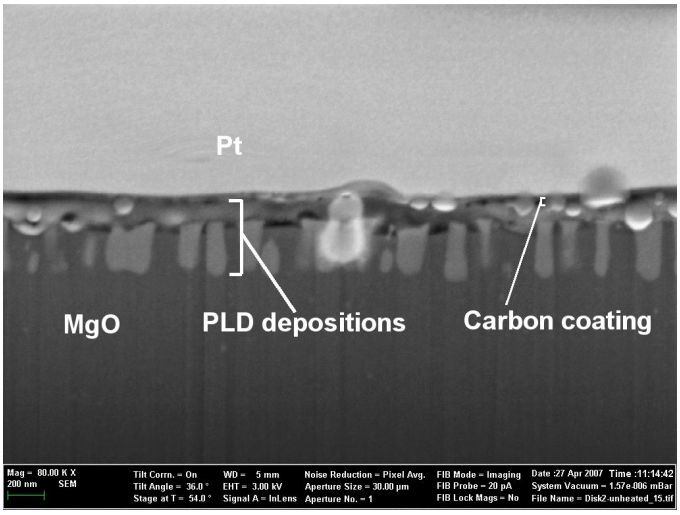

c

Figure 5. BSE micrographs of a) the surface via BSE, b) the surface via SE, b) the cross-section via BSE of the as-prepared diffusion sample.

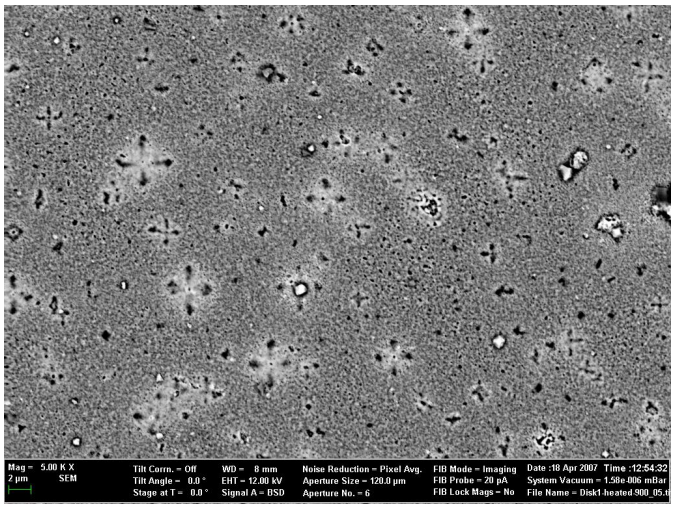

a

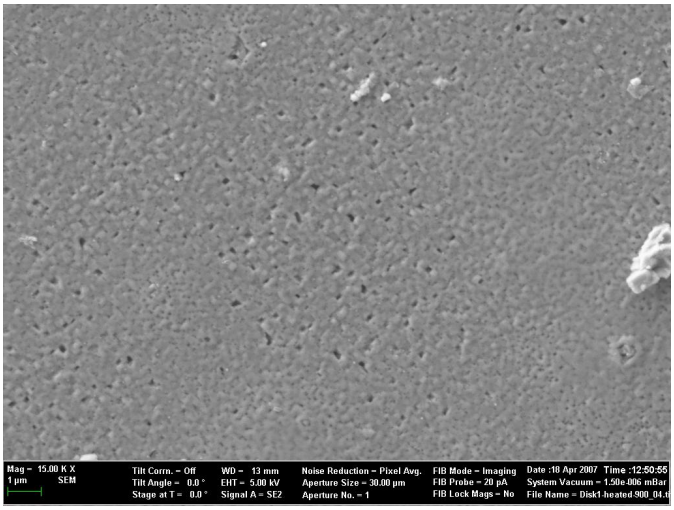

b

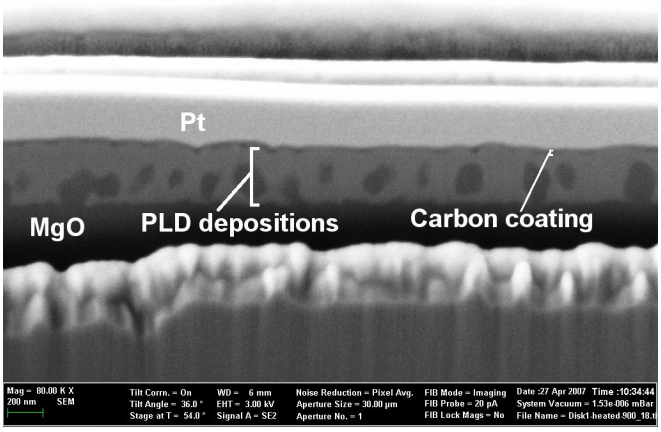

c

Figure 6. Micrographs of a) the surface via BSE, b) the surface via SE, b) the cross-section via BSE of the diffusion sample heat treated at 900˚C.

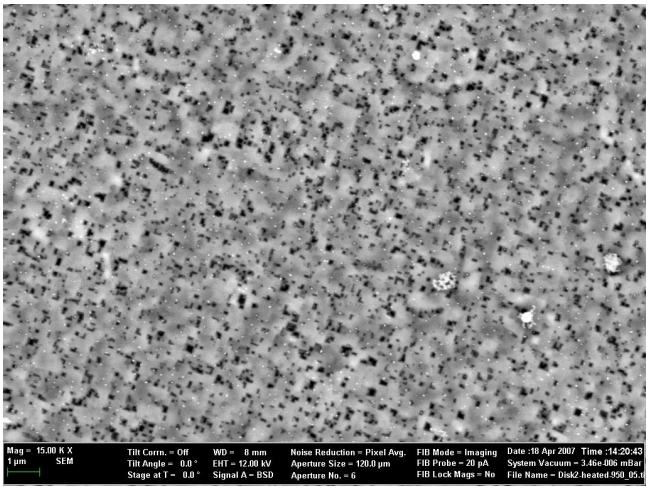

a

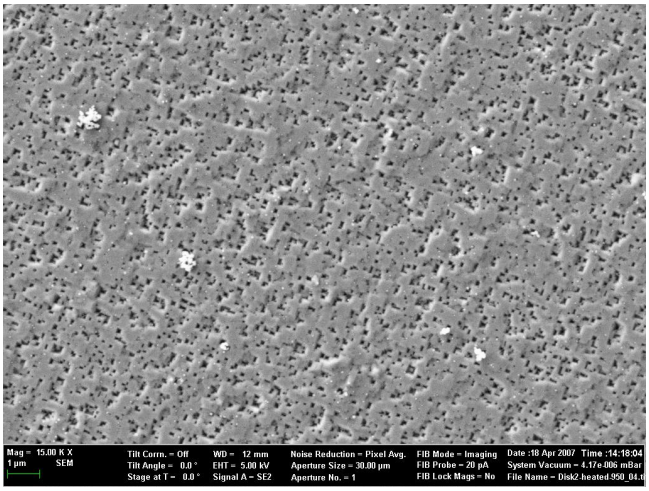

b

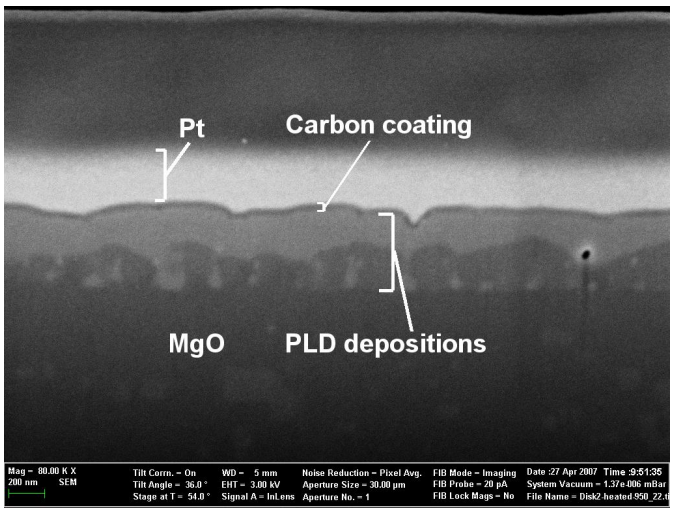

c

Figure 7. BSE micrographs of a) the surface via BSE, b) the surface via SE, b) the cross-section via BSE of the diffusion sample heat treated at 950˚C.

4. Discussion

4.1 SIMS profiles

The chromium signals on the two SIMS profiles collected from the two samples from disk A, which had been heat treated at 900˚C, indicated that SIMS analysis might be a successful method to analyse the concentration profiles in the diffusion samples since interfaces and concentration slopes etc. appeared to be discernable. However, when considering the complexity of the concentration profiles for the four cations in the SIMS profiles, and the unexpected variations in these signals the reliability of SIMS analysis was questioned. Considering the list of possible errors implemented by SIMS analysis on the concentration profiles the difficulties in using the technique appeared even larger. An understanding of the size and characteristics of these errors could be achieved by performing multiple SIMS analysis on similar PLD systems. Only, the characteristics of the PLD systems would have to be known. These investigations of SIMS analysis of known PLD deposited oxide systems might become very extensive and time consuming.

In figure 5 the SIMS profiles on the as-prepared, the 950˚C, and the 855˚C samples appeared different from the SIMS profiles collected on the 900˚C sample. Even on the as-prepared samples, a concentration profile of chromium in the spinel phase was detected, which would indicate that inward chromium diffusion would take place at room temperature. If this was the case, no useful information would be possible to achieve from the tracer diffusion experiments.

When studying the concentration profiles of chromium on the 855˚C and 950˚C samples, which also originated from disk B just as the as-prepared sample, the slope of the chromium concentration profile appeared to decrease as the heat treatment temperature increased. The slopes of the cations, and especially the chromium concentration profile, were however much smaller on all three samples originating from disk B compared to the 900˚C sample from disk A. This indicates that there is a difference in the PLD samples.

Based on the micrographs in figure 5-7 some of the differences between the samples were visualized. The density of the deposited PLD films is questionable when studying the micrographs of the cross-sections.

In figure 5 lumps of varying sizes are observed scattered on the surface of the as-prepared sample from disk B. In the micrograph of the cross-section of the as-prepared sample, light grey columns appear to be inserted into the dark grey phase assumed to consist of the MgO crystal. On top of the light grey columns a more dense and continuous phase is observed. The light grey columns are believed to consist of the deposited spinel phase, and the continuous phase on top of this of the applied chromia. The spinel deposition does not appear dense and continuous on this micrograph, and the un-even chromia/spinel interface and the holes between the spinel columns might explain why a concentration profile of chromium is detected on the as-prepared sample in figure 5a.

In figure 6 no lumps were observed on the surface of the 900˚C sample from disk A. Some type of structural distribution appeared to have taken place on the sample, since the BSE micrographs display a repeating pattern of crosses on the surface. In the

micrograph of the cross-section it is visible that the deposited films appear more dense and continuous than on the as-prepared sample. No columns of the spinel phase are displayed in the micrographs. Some darker areas, possibly holes or incorporated MgO, are observed though in the assumed PLD deposition layer. The residue of the chromia layer was difficult to discern from the micrographs.

In figure 7 of the 950˚C sample from disk B a repeating pattern is observed in the micrographs of the sample's surface. It appears as if heat treatment of the diffusion samples favours a structural re-distribution of the deposition into a more ordered pattern since no such structural order was observed on the surface of the as-prepared sample in figure 5. The as-prepared sample and the 950˚C sample both originate from disk B, and no larger differences in PLD depositions is possible between these two samples. Studying the cross-section of the 950˚C sample in figure 7c a light grey, dense phase is observed in the upper half of what is assumed to be the PLD deposition film. In the lower half of the PLD deposition, thin columns of the lighter grey phase are observed with dark spaces in between. These darker spaces are assumed to consist of MgO.

The variations in the microstructure of the diffusion samples show that the PLD deposition technique also affects the concentration profiles of the cations in the diffusion samples. If the $MnCo_2O_4$ deposition hits the surface of the MgO substrate with a significant velocity, the spinel phase might penetrate into the MgO substrate as the columnar formation in figure 5c illustrates. The deposition of the chromia layer might also implement errors in the concentration profiles. If for example the pulsing laser sputter away larger clusters of chromium atom/ions from the chromium target, or chromium atoms/ions with a significant velocity during the PLD deposition, the chromium atoms/ions might hit the surface of the $MnCo_2O_4$ deposition with such a large energy that they penetrate into the spinel phase creating a false concentration profile.

Based on all these observations it is found that the PLD deposition of the $MnCo_2O_4$ films would have to be refined so that dense, continuous films without false concentration profiles can be produced. To avoid the complexity of the SIMS analysis it could be recommended to use EDS analysis in TEM on the cross-sections of the diffusion samples to measure the concentration profiles of the cations in the oxide system. The use of TEM also has the advantage of giving visual information of the structure of the deposited and heat treated films at the same time as the concentration profiles are collected.

5. Conclusions

The PLD/SIMS method of measuring the tracer diffusion coefficient for chromium in a $MnCo_2O_4$ did not turn out to be usable in the current design. The PLD deposition has to be refined so that dense continuous films of $MnCo_2O_4$ and Cr_2O_3 can be applied onto a MgO substrate. Analysis of the concentration profiles in the diffusion samples via SIMS analysis proved to be more complex than expected, and to be able to interpret the SIMS profiles correctly a large number of SIMS analysis of known spinel depositions would have to be performed to measure and understand the different characteristics and implemented errors by the SIMS technique. For those who do not already possess experience of SIMS analysis of PLD deposited spinel and corundum structures, EDS measurements in TEM could be an alternative. Not only are the

concentration profiles easier to interpret, but visual information of the diffusion samples is achieved at the same time as a concentration profile of the cations are collected.